Università Ca' Foscari Venezia

Dottorato di ricerca in *SCIENZE CHIMICHE*, 22° ciclo

(A. A. 2006/2007 – 2008/2009)

Infrared Spectroscopy of Atmospherical and Astrophysical relevant Molecules: Spectral analysis, Line parameter retrievals and Study of collisional decay processes

Settore Scientifico-Disciplinare di afferenza: CHIM02, Chimica Fisica

Tesi di dottorato di ***NICOLA TASINATO***, 955380

Coordinatore del dottorato	Tutore
Prof. ***Paolo Ugo***	Prof. ***Paolo Stoppa***

To my Mum Nadia
and my Dad Olivio...

Index

Part II: Experimental and Computational Work

Bibliographic Information & Appendices

Introduction and Thesis Outline

Introduction

Spectroscopy is a field of chemical physics which studies the interaction of the electromagnetic radiation with matter. Infrared gas phase molecular spectroscopy uses the infrared light, which spans the electromagnetic spectrum from 14300 to 10 cm^{-1} [1], to probe a molecular gas sample. The interactions observed in the IR spectrum involve principally the energies associated with molecular structure change, and hence IR spectroscopy is widely used to infer information about the molecular structural parameters. Hence in the last decades the study of IR spectra has led to a fundamental understanding of molecular structures [2].

Although gas phase molecular spectroscopy dates back to the beginning of the 1800s, when it was used to explore the composition of the sun, it remains an active field, which during last years has become of essential importance in many disciplines, such as atmospheric chemistry and astrophysics [3]. Indeed, since the earlier experiments in the second half of the 1900, the study of Earth's and planetary atmospheres and of the interstellar medium by means of spectroscopic techniques has rapidly grown up. Nowadays, remote sensing techniques are widely used to probe the atmosphere and retrieve the concentration profiles of a number of species. For instance, the satellites used for sounding the terrestrial atmosphere (e.g. AIRS, SCISAT-1) and to explore the solar system (Voyager1, Cassini-Huygens, ISO) mount spectrometers which provide large amount of spectral information at ever increasing quality in terms of spectral coverage, resolution and signal-to-noise ratio [4]. Among the various spectroscopic techniques which cover the whole spectral range from microwave to UV-visible, infrared spectroscopy plays a very significant role, in particular for remote sensing of the terrestrial atmosphere. Indeed, IR remote sensing permits to monitor and accurately retrieve the concentrations of the atmospheric constituents and trace pollutants, since almost all these molecules have strong vibration-rotation bands in the infrared spectral domain [5].

Further, IR molecular spectroscopy is playing a primary role in the study of the atmospheres of the so-called exo-planets, which are planets in solar systems other than the our. By using spectral retrieval methods, it is possible to determine aspects such as dayside temperature

profiles and atmospheric composition, from which information about their habitability can be obtained [6, 7]. Up to now, several exo-planets have already been discovered and their number is growing steadily [8]. In the coming decades many space- and ground- based facilities are planned, in order to search for new exo-planets of all dimensions, from massive young “hot Jupiters”, through large rocky super-Earths, down to the discover of exo-Earths [9]. Very recently, the presence of methane and water vapour in the atmosphere of the hot Jupiter HD189733b has been detected by infrared spectroscopy [10, 11].

On these bases, spectroscopic parameters turn out to be of fundamental importance for the remote sensing applications used in atmospheric and climate research, environmental monitoring, gas-phase analytics and astronomy. Indeed, only their accurate knowledge allows an accurate retrieval of concentrations and distributions of the gas phase molecular species. The spectroscopic parameters include either line by line parameters, i.e line positions, line strengths, pressure broadening coefficients and pressure induced shifts, or absorption cross sections when a line by line approach is not possible [12, 13].

On the other hand, the growing concern of scientific communities and international politicians about climate changes and environmental degradation related to the human activities has even more highlighted the requirements for a deeper knowledge of atmospheric chemistry and physics, in order to understand and predict the evolution of the Earth atmosphere. These studies are carried out by using radiative transfer models which, in addition to an atmospheric profile, require as input a set of spectroscopic data for an increasing number of molecules [14]. The existing spectroscopic data are collected into a number of different databases, among which there are HITRAN [15], GEISA [16], JPL [17]. Given the absorber amount and the atmospheric pressure and temperature profiles, the spectroscopic parameters allow the molecular absorption or emission to be computed at any frequency, assuming a reliable line shape function [14].

Within this framework, the aim of laboratory spectroscopy is to provide spectroscopic parameters for a wide variety of species of atmospheric, astrophysical and industrial importance. Furthermore, given the advances in infrared spectroscopy instrumentation, the spectral parameters require to be determined with the highest possible accuracy. This represents a significant amount of work, which can be performed by combining laboratory measurements and theoretical models [5, 18].

Besides, thanks to the increasing sensitivity of modern laboratory measurements, the study of spectral line shapes, either in the frequency or in the time domain, allows the investigation of smaller and smaller details of the electromagnetic radiation – molecule interaction and of the relevant relaxation processes [19 – 21]. From this point of view, the proper modelling of the

experimental absorption line shapes requires detailed theoretical models, which take into account a number of processes. These experiments, which can benefit of the high resolution and signal-to-noise ratio offered by laser spectrometers, gives new insight into the identification of the different mechanisms that affect the appearance of a spectral line. This requires a constant improvement in understanding and modelling the processes which take place in a gas phase sample and are intimately related to the kind of molecular collisions, intermolecular potentials, and energy transfers occurring during the scattering event.

Objectives and Thesis Outline

The main target of this PhD thesis is the line shape analysis of the infrared ro-vibrational absorption lines, arising when a molecular gas sample is investigated by means of infrared radiation. As stated in the previous section, the interest in line parameter determinations is twofold. First, the line shape parameters represent the basic information needed by remote sensing retrievals; second, they constitute a basic tool to investigate the collisional processes and the related relaxation rates and interaction potentials.

During these three PhD years the entire procedure for line profile analysis and retrieval of the line parameters has been set up, both experimentally and computationally. From the experimental point of view, the work has been directed to the definition of a proper operative procedure. In order to minimize the instrumental contribution to the spectral line shapes, the instrumental function of the tunable diode laser spectrometer has been studied and characterized. In addition, the spectrometer has been appropriately adapted for this purpose. From the computational point of view, a new software for fitting the experimental absorption profiles has been projected and implemented.

I have also been involved in some of the research works carried out by my Research Group. These ranged from the vibrational study of low and medium resolution spectra to the analysis of high resolution spectra.

Besides, I spent seven months working in the QCL Spectroscopy Group of Professors Geoffrey Duxbury and Nigel Langford, at the Physics Department of the University of Strathclyde of Glasgow, Scotland.

Therefore, although the main scope of the present thesis is the line profile analysis, it encompasses a variety of aspects in the research field of infrared spectroscopy. In a certain sense, the subject of the thesis is the gas phase infrared spectroscopy as a whole.

The thesis is subdivided into two main parts: Part I summarizes the theory behind infrared spectroscopy, and Part II deals with the experimental and computational work. Concerning the Part I, Chapter 1, "*Principles of Quantum Mechanics*", gives a brief summary of the Quantum Mechanics upon which ro-vibrational spectroscopy is based. Chapter 2 and 3 review the theoretical knowledge required for the interpretation and the analysis of the experiments. The rotational and vibrational motions are described in Chapter 2, "*Molecular Rotations and Vibrations*", together with the developments of the effective Hamiltonians, which are used to predict the energies of the ro-vibrational transitions of an isolated molecule. Chapter 3, "*Molecular Collisions and Spectral Line Shapes*", is about the coupling between molecules and IR electromagnetic radiation, and the effect of perturbation due to molecular collisions which lead to characteristic spectral line shapes. Finally, Chapter 4, "*Ab initio Calculations in Infrared Spectroscopy*" gives a brief description of the computational *ab initio* approach used to determine the harmonic and anharmonic force fields, from which molecular parameters and structures can be calculated.

Part II starts with Chapter 5, "*Instrumentation*", where the infrared spectrometers which have been employed are described. These include both the tunable diode laser spectrometer and the Fourier Transform spectrometer of the Molecular Spectroscopy Group of Università Ca' Foscari Venezia, as well as a Quantum Cascade laser based spectrometer used at the University of Strathclyde.

The program implemented to fit the spectral lines is described in Chapter 6, "*Visual Line-Shape Fitting Program*". It performs the fit of the absorption features on the basis of different theoretical profiles. Besides the Gaussian and Lorentz functions, the spectral lines can be fitted employing the Voigt profile as well as other models, including the collisional narrowing effect. The fitting procedure, based on the Levenberg-Marquardt algorithm, allows the user to fit the experimental lines individually or simultaneously. The program, written combining C# and Visual Basic languages, presents a standard graphical interface, from which the lines to be fitted can be specified together with their input parameters.

The determination of the sulphur dioxide line parameters is the subject of Chapter 7, "*Sulphur Dioxide Line Parameters in the 9.2 μm Atmospheric Spectral Window*". Self-broadening and integrated absorption coefficients have been measured for several lines in the ν_1 band spectral region around 9.2 μm. Besides the parameters of the lines belonging to the ν_1 fundamental of $^{32}SO_2$, also those for some ro-vibrational lines of the $\nu_1 + \nu_2 - \nu_2$ hot band of the $^{32}SO_2$ isotopologue and the ν_1 band of the $^{34}SO_2$ isotopic species have been determined. The measurements have been carried out at 297 K using a tunable diode laser spectrometer. The self broadening parameters have also been theoretically determined, employing a semi-classical formalism based on the Anderson –

Tsao – Curnutte approximation. The study has been completed with the determination of the vibrational cross sections of the three fundamental bands, measured from spectra recorded at a resolution of 0.2 cm^{-1} using a FT-IR spectrometer.

The line parameter investigations are extended to vinyl fluoride in Chapter 8, "*Vinyl Fluoride Spectroscopy: Vibrational Analysis, Ab initio calculations and Line parameters determination*". The high resolution spectra of CH_2CHF, in the ν_7 band region around 1123 cm^{-1}, have been acquired using a tunable diode laser spectrometer with pressures ranging from 5 to 300 Pa. In spite of the employed low pressures, the absorptions due to the hot bands heavily contribute to the spectra, which appear very crowded. Nevertheless, the integrated line intensities and the self-broadening parameters for a number of spectral lines have been determined for the first time. The line shapes also show deviations from the Voigt profile which can be well modelled by using a Dicke narrowed line function. In addition, a detailed analysis of the infrared spectral features of vinyl fluoride has been carried out both experimentally and theoretically. Experimentally, the gas-phase vibrational spectra have been investigated at low and medium resolution in the range 400 – 8000 cm^{-1}. The spectra have been recorded using a Fourier transform spectrometer, with a gas sample pressure in the range 0.37 – 40 kPa. The integrated absorption cross sections have been determined for the first time. Theoretically, *ab initio* calculations have been performed using the coupled cluster theory within the singles and doubles approximations, augmented by a perturbative treatment of triple excitations, CCSD(T). The Dunning's hierarchy of correlation consistent basis sets have been used to obtain anharmonic force constants and optimized geometry.

In Chapter 9, "*Jet-Cooled Diode Laser Spectrum and FTIR Integrated Band Intensities of CF_3Br*", the high resolution infrared diode laser spectrum of CF_3Br (Halon 1301) with natural isotopic abundance has been investigated in the region 1090 – 1130 cm^{-1}, characterized by the presence of the $2\nu_5$ and $\nu_2 + \nu_3$ absorptions and several weaker hot bands. The rovibrational analysis of the data, obtained employing a slit-jet system together with those recorded at 200 K, has led to a complete and accurate set of spectroscopic constants for the bands of both bromine isotopologues. Integrated band intensities have been obtained for all the absorptions in the spectral range 450 – 2500 cm^{-1}.

Chapters 10 and 11 are devoted to the experiments carried out at the University of Strathclyde and designed to investigate the physics of the interaction of chirped infrared laser radiation with low pressure gases. In these experiments the sweep rate of the laser frequency may be faster than the inter-molecular collision frequency, thus allowing the build up of a strong molecular alignment within the gas. The obtained results provide a clear evidence for the chirp rate dependence of scattering processes. In Chapter 10, "*Frequency Down-Chirped QCL Spectroscopy:*

Time Dependent Measurements of Collisional Processes in a Dicke Narrowed Spectral Line of Water Vapour", the frequency down-chirped radiation, emitted by a Quantum Cascade Laser (QCL) spectrometer used in the intra-pulse method, has been employed to investigate the collisional processes responsible for the observed line shape of the unresolved K-doublet $15_{0,15} \leftarrow 16_{1,16}$ and $15_{1,15} \leftarrow 16_{0,16}$, which belong to the ν_2 bending mode of water vapour. The study has been carried out by analyzing the behaviour of this line using different chirp rates, while collisionally perturbing the water molecules by means of a range of atomic and molecular collision partners. The experimental results indicate that the frequency down-chirped technique may be employed to infer information about the physics of the absorption process itself, as well as that of intermolecular collisions. The study about the rapid passage signals and the time dependence of collisional processes is extended to nitrous oxide and carbon dioxide in Chapter 11, "*Frequency Down-Chirped QCL Spectroscopy: Time Dependent Measurements of Nitrous Oxide and Carbon Dioxide Collisional Relaxations*". The time dependence of the collisional cross sections, which has been studied by the use of different chirp rates, has been clearly demonstrated for the strong ν_1 transitions observed in the 7.8 μm spectral region. The investigation has been carried out by perturbing the nitrous oxide molecules with different atomic and molecular collisional partners and using different chirp rates, which in turns lead to different observation times. Among the considered collisional partners, carbon dioxide shows very unusual behaviour. It induces a much more efficient broadening of the absorption lines of nitrous oxide than N_2 and noble gas atoms, causing symmetrical line shapes to be observed at relatively low partial pressures. These large effects are reciprocated in the rapid quenching and broadening of the rapid passage signals of unsymmetrical $^{16}O^{12}C^{18}O$ isotopomer, which have been detected in the same spectral region. The CO_2 absorptions have been compared with the signals obtained from the solution of the optical Bloch equations.

Finally, "*Conclusions and Outlook*" summarizes the work and the obtained results, and it also addresses possible future developments and improvements.

Part I: Theory

1. Principles of Quantum Mechanics

Spectroscopy is basically an experimental subject which is concerned with the study of the interaction of light with matter. Nevertheless, the interpretation of a spectroscopy experiment seeks its basis in quantum mechanics. Spectroscopy and quantum theories are consequently strongly interrelated. In a sense, spectroscopy is applied quantum mechanics.

Toward the end of the 19th century the success of the classical physics was impressive. All the known physical phenomena seemed to found their explanation to the extent that many scientists thought that physics was virtually a closed book. In *A History of Science*, Sir William C. Dampier wrote: "It seemed as though the main framework had been put together once for all, and that little remained to be done but to measure physical constants to the increased accuracy represented by another decimal point".

It was rather the beginning of a profound upset of classical physics. Indeed a series of experimental observations demonstrated the inadequacy of classical mechanics to describe the properties of matter on molecular, atomic and subatomic scale. This revolution promoted the development of the quantum mechanics which was born in 1925 – 1926 when Werner Heisenberg and Erwin Schrödinger formulate Matrix Mechanics and Wave Mechanics, respectively. Both the methods are equivalent and have as their basis the same set of assumptions. Combining the elements of the two approaches has proven to be useful for spectroscopists.

1.1 Wave Equation and Approximations

According to Schrödinger's wave mechanics, the dynamical state of a quantum system is completely identified, by its wave function $\Psi(\mathbf{r}_1, \mathbf{r}_2, ..., \mathbf{r}_N, t)$ which is the solution of the proper wave equation:

$$\hat{H}\Psi(\mathbf{r}_1, \mathbf{r}_2, ..., \mathbf{r}_N, t) = -\frac{\hbar}{i}\frac{\partial\Psi(\mathbf{r}_1, \mathbf{r}_2, ..., \mathbf{r}_N, t)}{\partial t} \tag{1.1}$$

where $\mathbf{r}_i$ denotes the position of the i-th particle and $\hat{H}$ is the Hamiltonian of the system. For conservative systems, the Hamiltonian does not explicitly depend upon the time and the quantized stationary energy levels of the system are the eigenvalues of the time – independent Schrödinger equation:

$$\hat{H}\psi(\mathbf{r}_1,\mathbf{r}_2,...,\mathbf{r}_N) = E\psi(\mathbf{r}_1,\mathbf{r}_2,...,\mathbf{r}_N) \tag{1.2}$$

where $\psi(\mathbf{r}_1,\mathbf{r}_2,...,\mathbf{r}_N)$ is the time – independent wave function. The latter is usually called the wave function of the system, although it differs from the true wave function by a phase factor.

Unfortunately, for "complex" systems such as molecules, the Schrödinger equation has no analytical solutions and so it is necessary to adopt approximations. The solution of the wave equation is in general simplified by the Born – Oppenheimer approximation which is valid, at least as starting point, in the majority of quantum chemical calculations. It states that, since nuclei are much heavier than electrons, they move much more slowly. This permits to separate the nuclear and electronic motions so that, the total wave function, which is a function of both electronic and nuclear coordinates, can be written as the product of an electronic and a nuclear wave function. From now on, the validity of the Born – Oppenheimer approximation will always be assumed.

The allowed ro-vibrational energies, E_{RV}, of a molecule are the eigenvalues of the time – independent wave equation:

$$\hat{H}_{RV}\psi_{RV} = E_{RV}\psi_{RV} \tag{1.3}$$

where $\hat{H}_{RV}$ and ψ_{RV} are the ro-vibrational Hamiltonian and wave function, respectively. Another approximation which is usually adopted consists in neglecting the interaction between the rotational and vibrational motions. Doing so it is possible to break equation (1.3) into two separated wave equations. One of these describes the rotational motion of a rigid rotating body; the other describes the vibrational motion of the non-rotating molecule. However, in some circumstances the latter approximation lead to very poor results and hence the interaction between rotations and vibrations must be treated, usually by means of perturbation methods.

1.2 APPROXIMATION TECHNIQUES

There are two principal methods for the approximate determination of the energy levels and wave functions of a quantum system: the variational method and the perturbation method.

The variation method is a very general one which is based on the variation theorem. The latter states that, given a system whose Hamiltonian operator $\hat{H}$ is time independent and whose lowest energy eigenvalue is E_0, if ϕ represents any normalized, well-behaved function of the coordinates of the particles of the system that satisfy the boundary conditions of the problem, then

$$\langle E \rangle = \frac{\int \phi^* \hat{H} \phi \, d\tau}{\int \phi^* \phi \, d\tau} \geq E_0 \tag{1.4}$$

where $\langle E \rangle$ and ϕ are called the variation integral and the trial or variation function, respectively.

The significance of the variation theorem is that, whatever trial function is used, the energy calculated from it is never less than the true energy of the ground state of the system. Put in another way, the smaller the value of the energy obtained from ϕ, the closer it is to the true energy and therefore the more closely ϕ resembles the ground state wave function.

A special kind of variation function widely used in quantum chemistry is the linear variation function, which is a linear combination of *n* linearly independent basis functions f_i:

$$\phi = \sum_{i=1}^{n} c_i f_i \tag{1.5}$$

where the coefficients c_i are parameters to be determined minimizing the energy, while the functions f_i are frozen during the calculation. These functions, which constitute what is called the basis set, must satisfy the boundary conditions of the problem. The advantage of the linear variation theory is that it is not limited to the ground state energy. The coefficients c_i that give a minimum energy $\langle E \rangle$ satisfy the secular equation:

$$\sum_{i=1}^{n} c_i \left(H_{ki} - S_{ki} \langle E \rangle \right) = 0 \qquad k = 1, 2, \ldots, n; \tag{1.6}$$

where H_{ki} and S_{ki} are shorthand notations for the following expressions:

$$H_{ki} = \int f_k^* \hat{H} f_i \, d\tau ; \qquad S_{ki} = \int f_k^* f_i \, d\tau \tag{1.7}$$

A solution for equation (1.6) exists only if the secular determinant vanishes:

$$\det\left| H_{ki} - S_{ki} \langle E \rangle \right| = 0 ; \tag{1.8}$$

solving this equation leads to a set of *n* roots for the energy, $\langle E_0 \rangle \leq \langle E_1 \rangle \leq \ldots \leq \langle E_n \rangle$. Each of these roots represents an upper bound to the energy of the corresponding state, namely $E_i \leq \langle E_i \rangle$. For each solution $\langle E_i \rangle$, there is a particular set of coefficients that identifies the corresponding wave functions ϕ_i. Back substituting the values of $\langle E_i \rangle$ into equation (1.6) leads, after normalization, to the coefficients c_i's and then to the determination of the wave functions ϕ_i that better approach the true ones.

The time-independent perturbation theory makes use of the fact that the Hamiltonian for the true system, $\hat{H}$, is only slightly different from an Hamiltonian, $\hat{H}^{(0)}$, whose eigenvalues and eigenfunctions are known:

$$\hat{H}^{(0)} \psi_n^{(0)} = E_n^{(0)} \psi_n^{(0)} \tag{1.9}$$

where the eigenfunctions $\psi_n^{(0)}$ form a complete orthonormal basis set. It is then assumed that the Hamiltonian $\hat{H}$ of the perturbed system can be written as the sum of the unperturbed Hamiltonian $\hat{H}^{(0)}$ and a perturbation term $\lambda \hat{H}'$

$$\hat{H} = \hat{H}^{(0)} + \lambda \hat{H}' ; \tag{1.10}$$

λ is just a time-independent parameter used to keep track of the order of perturbation. At the end of the calculation it is set to one to turn the perturbation on. The wave equation for the perturbed state is

$$\left(\hat{H}^{(0)} + \lambda\hat{H}'\right)\psi_n = E_n\psi_n \tag{1.11}$$

where ψ_n and E_n are the perturbed wave function and energy, respectively. By expanding ψ_n and E_n as Taylor series in powers of λ:

$$\psi_n = \psi_n^{(0)} + \lambda\psi_n^{(1)} + \lambda^2\psi_n^{(2)} + \ldots + \lambda^k\psi_n^{(k)} + \ldots$$
$$E_n = E_n^{(0)} + \lambda E_n^{(1)} + \lambda^2 E_n^{(2)} + \ldots + \lambda^k E_n^{(k)} + \ldots$$

equation (1.11) can be written as

$$\begin{aligned}&\hat{H}^{(0)}\psi_n^{(0)} + \lambda\left(\hat{H}'\psi_n^{(0)} + \hat{H}^{(0)}\psi_n^{(1)}\right) + \lambda^2\left(\hat{H}'\psi_n^{(1)} + \hat{H}^{(0)}\psi_n^{(2)}\right) + \ldots \;= \\ &= \; E_n^{(0)}\psi_n^{(0)} + \lambda\left(E_n^{(1)}\psi_n^{(0)} + E_n^{(0)}\psi_n^{(0)}\right) + \lambda^2\left(E_n^{(2)}\psi_n^{(0)} + E_n^{(1)}\psi_n^{(1)} + E_n^{(0)}\psi_n^{(2)}\right) + \ldots\end{aligned} \tag{1.12}$$

For the two series on each side of equation (1.12) to be equal to each other for all values of λ, the coefficients of like powers of λ must be equal. By equating the coefficients of the λ^k terms and solving, one obtains the *k*th-order corrections to the wave function and energy.

In the case of perturbation of an energy level whose degree of degeneracy is *d*, the treatment is analogous, but the zeroth-order wave functions are expressed as a linear combination of the degenerate wave functions:

$$\phi_n^{(0)} = \sum_{i=1}^{d} c_i\psi_i^{(0)}, \qquad 1 \le n \le d\,. \tag{1.13}$$

In the latter case the perturbation can remove the degeneracy and hence split the energy levels. In some circumstances, it may have no effect or may only partly remove the degeneracy.

In order for the perturbation approach to be useful, the series expansions of the wave function and energy must converge and the *k*th-order correction should be larger than the (*k* + 1)th-order correction.

1.3 TIME-DEPENDENT PERTURBATION THEORY

A molecule exposed to electromagnetic radiation experiences an oscillating electromagnetic field. Time-dependent perturbation theory is the most convenient approximate approach to treat such problems and it is used to calculate the transition probabilities and the intensities of spectral lines.

The time-independent wave equation of the unperturbed system is given by equation (1.9), where the $E_n^{(0)}$ and $\psi_n^{(0)}$ are the stationary-state energies and wave functions. These functions are related to the time-dependent unperturbed wave functions $\Psi_n^{(0)}(t)$ by

$$\Psi_n^{(0)}(t) = \psi_n^{(0)} e^{-i\frac{E_n^{(0)}t}{\hbar}}. \tag{1.14}$$

The time-dependent wave equation of the perturbed system is

$$\left[\hat{H}^0 + \hat{H}'(t)\right]\Psi = -\frac{\hbar}{i}\frac{\partial\Psi}{\partial t} \tag{1.15}$$

where $\hat{H}'(t)$ is a time-dependent operator. At any time the true wave function can be expressed as a linear combination of the $\Psi_n^{(0)}$ functions according to:

$$\Psi = \sum_k b_k(t) e^{-\frac{iE_k^{(0)}t}{\hbar}} \psi_k^{(0)} \tag{1.16}$$

where the expansion coefficients b_k are also time-dependent.

Upon substitution of equation (1.16) into (1.15), multiplication by $\left(\psi_m^{(0)}\right)^*$ and integration over the spatial coordinates one gets:

$$\frac{\mathrm{d}b_m(t)}{\mathrm{d}t} = -\frac{i}{\hbar}\sum_k b_k e^{i\frac{\left(E_m^{(0)} - E_k^{(0)}\right)t}{\hbar}} \left\langle \psi_m^{(0)} \middle| \hat{H}' \middle| \psi_k^{(0)} \right\rangle. \tag{1.17}$$

in which Dirac's notation $\left\langle \psi_i \middle| \hat{H} \middle| \psi_j \right\rangle = \int \psi_i^* \hat{H} \psi_j$ has been used.

The above expression is simplified by considering that the system is in an initial state $|n\rangle$ and assuming that the perturbation is small and acts only for a short time. Under these conditions, the change in the expansion coefficients from their initial values is small and to a good approximation at time *t*' they are given by

$$b_m(t') \approx \delta_{mn} - \frac{i}{\hbar}\int_0^{t'} e^{i\frac{\left(E_m^0 - E_n^0\right)t}{\hbar}} \left\langle \psi_m^{(0)} \middle| \hat{H}' \middle| \psi_n^{(0)} \right\rangle dt \tag{1.18}$$

where δ_{mn} is the Kronecker's delta.

The time-dependent wave function of the perturbed system is obtained employing the coefficients given by the previous expression. At the end of the perturbation, the state function is:

$$\Psi = \sum_m b_m(t') e^{-\frac{iE_m^{(0)}t}{\hbar}} \psi_m^{(0)} \tag{1.19}$$

The time-dependent perturbation changes the state of the system from $\Psi_n^{(0)}$ to a superposition of states $\sum_m b_m(t')\Psi_m^{(0)}$. The net result is a transition from the stationary state $|n\rangle$ to the stationary state $|m\rangle$, with a probability given by $|b_m(t')|^2$.

1.4 ANGULAR MOMENTUM OPERATORS

In quantum mechanics, as in classical mechanics, the rotation of a system finds its description in the angular momentum, which is a constant of the motion for an isolated system. Differences with classical mechanics arise in that the angular momentum is not an ordinary vector but a vector operator. Classically, the angular momentum of a system of *N* particles about an arbitrary origin is given by

$$\mathbf{L} = \sum_{n=1}^{N} \mathbf{q}_n \wedge \mathbf{p}_n \tag{1.20}$$

where $\mathbf{q}_n$ and $\mathbf{p}_n$ are the position and the instantaneous linear momentum of the n-th particle. In a space fixed reference frame, (X, Y, Z), equation (1.20) can be expanded as

$$\mathbf{L} = \ell_x \mathbf{i} + \ell_y \mathbf{j} + \ell_z \mathbf{k} =$$
$$= \sum_{n=1}^{N} \left[\left(Y\, p_Z - Z\, p_Y \right)_n \mathbf{i} + \left(Z\, p_X + X\, p_Z \right)_n \mathbf{j} + \left(X\, p_Y - Y\, p_X \right)_n \mathbf{k} \right] \tag{1.21}$$

where $(X,Y,Z)_n$ and $(p_X, p_Y, p_Z)_n$ are the components of $\mathbf{q}_n$ and $\mathbf{p}_n$, respectively. The quantum mechanical equivalent of equation (1.20) is obtained upon replacement of $\mathbf{q}$ and $\mathbf{p}$ with their corresponding operators, leading to the following components of the quantum mechanical angular momentum operator:

$$\hat{J}_X = \sum_{n=1}^{N} \frac{\hbar}{\mathrm{i}} \left[Y\left(\frac{\partial}{\partial Y} \right) - Z\left(\frac{\partial}{\partial Z} \right) \right]_n$$
$$\hat{J}_Y = \sum_{n=1}^{N} \frac{\hbar}{\mathrm{i}} \left[Z\left(\frac{\partial}{\partial X} \right) - X\left(\frac{\partial}{\partial Z} \right) \right]_n \tag{1.22}$$
$$\hat{J}_Z = \sum_{n=1}^{N} \frac{\hbar}{\mathrm{i}} \left[X\left(\frac{\partial}{\partial Y} \right) - Y\left(\frac{\partial}{\partial X} \right) \right]_n$$

where the symbol for the general angular momentum operator, $\hat{J}$, has been used instead of $\hat{L}$, which is usually employed to denote the orbital angular momentum operator.

In the matrix mechanics approach, the basic information is carried in the commutation properties, which hold among the various operators representing the observables associated with the relevant problem. The commutator of two operators $\hat{A}$ and $\hat{B}$ is defined as

$$\left[\hat{A}, \hat{B} \right] = \hat{A}\hat{B} - \hat{B}\hat{A} \tag{1.23}$$

and two situations are of particular interest: $\left[\hat{A}, \hat{B} \right] = 0$ and $\left[\hat{A}, \hat{B} \right] = k\hat{B}$ where k is a scalar number. In the former case the two operators are said to commute and it follows that functions exist which are simultaneous eigenfunctions of both operators. In the latter case, it is possible to generate complete sets of functions which are eigenfunctions of $\hat{A}$, according to

$$\hat{A}\left(\hat{B}\left|A\right\rangle\right)=\left(a+k\right)\left(\hat{B}\left|A\right\rangle\right) \tag{1.24}$$

where $\left|A\right\rangle$ is an eigenfunction of $\hat{A}$ with eigenvalue *a*. Equation (1.24) implies that the effect of the operation of $\hat{B}$ on $\left|A\right\rangle$ is to generate a new eigenfunction of $\hat{A}$ with eigenvalue (*a* + *k*).

The above defined Cartesian components of $\hat{\mathbf{J}}$, satisfy the following commutation relations:

$$\left[\hat{J}_X,\hat{J}_Y\right]=i\hbar\hat{J}_Z \qquad \left[\hat{J}_Y,\hat{J}_Z\right]=i\hbar\hat{J}_X \qquad \left[\hat{J}_Z,\hat{J}_X\right]=i\hbar\hat{J}_Y \tag{1.25}$$

This commutation relations can be considered as the quantum conditions which define the space fixed components of a generalized angular momentum operator, i.e. a general angular momentum obeys these commutation rules.

Of particular interest for the treatment of rotational motion is the square of the total angular momentum:

$$\hat{\mathbf{J}}^2=\hat{J}_X^2+\hat{J}_Y^2+\hat{J}_Z^2 \tag{1.26}$$

whose commutation properties are

$$\left[\hat{\mathbf{J}}^2,\hat{J}_i\right]=0 \tag{1.27}$$

with *i* standing for *X*, *Y* or *Z*. This result is understandable by considering that $\hat{\mathbf{J}}^2$ is a scalar quantity and thus it is independent of the orientation. Since $\hat{\mathbf{J}}^2$ commutes with all the components of $\hat{\mathbf{J}}$ but these components do no commute with themselves, it follows that only $\hat{\mathbf{J}}^2$ and one component of $\hat{\mathbf{J}}$ (by convention $\hat{J}_Z$) are simultaneously measurable and there exist functions which are simultaneously eigenfunction of both $\hat{\mathbf{J}}^2$ and $\hat{J}_Z$.

The angular momentum operator of a rotating body can be expressed as well with respect to a molecular fixed reference frame, (*x*, *y*, *z*). The two systems of coordinates are related to each other by the direction cosine matrix and hence the components of $\hat{\mathbf{J}}$ in the two reference systems are linked by

$$\begin{bmatrix} \hat{J}_X \\ \hat{J}_Y \\ \hat{J}_Z \end{bmatrix} = \begin{bmatrix} \Phi_{Xx} & \Phi_{Xy} & \Phi_{Xz} \\ \Phi_{Yx} & \Phi_{Yy} & \Phi_{Yz} \\ \Phi_{Zx} & \Phi_{Zy} & \Phi_{Zz} \end{bmatrix} \begin{bmatrix} \hat{J}_x \\ \hat{J}_y \\ \hat{J}_z \end{bmatrix} \tag{1.28}$$

with $\Phi_{i\alpha} = \cos(i\alpha)$, where $i\alpha$ represents the angle between the space fixed i axis and the molecule-fixed α axis. The space- and molecule- fixed components of $\hat{\mathbf{J}}$ commute, and the latters obey commutation rules similar to that of the space fixed components:

$$\left[\hat{J}_x, \hat{J}_y\right] = -i\hbar\hat{J}_z \qquad \left[\hat{J}_y, \hat{J}_z\right] = -i\hbar\hat{J}_x \qquad \left[\hat{J}_z, \hat{J}_x\right] = -i\hbar\hat{J}_y . \tag{1.29}$$

Because $\hat{J}_Z$ and $\hat{J}_z$ commutes each other and both commute with $\hat{\mathbf{J}}^2$, there exist functions, $|J \quad k \quad m\rangle$, which are simultaneously eigenfunctions of the three operators. It can be shown that

$$\begin{aligned} \hat{J}^2|J \quad k \quad m\rangle &= \hbar^2 J(J+1)|J \quad k \quad m\rangle \\ \hat{J}_z|J \quad k \quad m\rangle &= \hbar k|J \quad k \quad m\rangle \\ \hat{J}_Z|J \quad k \quad m\rangle &= \hbar m|J \quad k \quad m\rangle \end{aligned} \tag{1.30}$$

from which it follows that $\hbar^2 J(J+1)$, $\hbar k$ and $\hbar m$ are the eigenvalues of $\hat{\mathbf{J}}^2$, $\hat{J}_z$ and $\hat{J}_Z$, respectively, while J, k, m are three quantum numbers such that

$$\begin{aligned} &J = 0, 1, 2, \ldots \\ &k = J, J-1, J-2, \ldots, -J \\ &m = J, J-1, J-2, \ldots, -J. \end{aligned} \tag{1.31}$$

Since $\hat{\mathbf{J}}^2$, $\hat{J}_z$ and $\hat{J}_Z$ are Hermitian, their eigenfunctions are orthogonal and they can be normalized such that $\langle J' \quad k' \quad m'|J'' \quad k'' \quad m''\rangle = \delta_{J'J''}\delta_{k'k''}\delta_{m'm''}$.

1.5 THE HARMONIC OSCILLATOR

In classical mechanics, a simple one-dimensional harmonic oscillator is described as a particle constrained to move along the *x* axis and subject to a restoring force given by the Hooke's law, $F = -kx$ where *k* is called the force constant. Denoting with $q = x$ and *p* the position coordinate and the linear momentum of the particle, the Hamiltonian of such system is given by

$$\mathcal{H} = \frac{1}{2m}\left(p^2 + m^2\omega^2 q^2\right), \tag{1.32}$$

where $\omega = (k/m)^{1/2}$ is the angular frequency of the motion and *m* represents the mass of the particle. The corresponding quantum mechanical Hamiltonian can be written as

$$\hat{H} = \frac{\hat{\mathcal{H}}}{\hbar\omega} = \frac{1}{2}\left(\frac{\hat{p}^2}{m\hbar\omega} + \frac{m\omega}{\hbar}\hat{q}^2\right). \tag{1.33}$$

Defining $\hat{q} = \left(\frac{\hbar}{m\omega}\right)^{1/2}\hat{Q}$ and $\hat{p} = \left(\frac{\hbar}{m\omega}\right)^{1/2}\hat{P}$, the above Hamiltonian can be put in the more compact form:

$$\hat{H} = \frac{1}{2}\left(\hat{P}^2 + \hat{Q}^2\right) \tag{1.34}$$

where the Hermitian operators $\hat{Q}$ and $\hat{P}$ satisfy the commutation relation $\left[\hat{Q}, \hat{P}\right]$ = i. The problem of finding the eigenvalues of the operator (2.34) can be conveniently tackled by making use of the so called annihilation and creation operators, which are respectively defined as

$$\begin{aligned} \hat{a} &= \frac{\sqrt{2}}{2}\left(\hat{Q} + i\hat{P}\right) \\ \hat{a}^\dagger &= \frac{\sqrt{2}}{2}\left(\hat{Q} - i\hat{P}\right) \end{aligned} \tag{1.35}$$

where the upper script † is used to denote the complex conjugate transpose. Using these two operators, the quantum mechanical Hamiltonian can be rewritten as

$$\hat{H} = \hat{N} + \frac{1}{2} \tag{1.36}$$

with $\hat{N} = \hat{a}^{\dagger}\hat{a}$. The eigenvalue problem associated with the harmonic oscillator is thus equivalent to the problem of constructing the eigenvectors of the operator $\hat{N}$. By making use of the commutation relation between $\hat{a}$ and $\hat{a}^{\dagger}$, $\left[a, a^{\dagger}\right] = 1$, the following equations can be derived:

$$\hat{N}\hat{a} = \hat{a}\left(\hat{N} - 1\right); \qquad \hat{N}\hat{a}^{\dagger} = \hat{a}^{\dagger}\left(\hat{N} - 1\right).$$

It can be proved that if $\left|\mathrm{v}\right\rangle$ is an eigenvector of $\hat{N}$ and v is the corresponding eigenvalue, then:

(i) necessarily $\mathrm{v} \geq 0$;

(ii) if $\mathrm{v} = 0$, $\hat{a}\left|\mathrm{v}\right\rangle = 0$; if $\mathrm{v} \neq 0$, $\hat{a}\left|\mathrm{v}\right\rangle$ is a non-zero vector of norm $\mathrm{v}\left\langle \mathrm{v}\middle|\mathrm{v}\right\rangle$ and it is an eigenvector of $\hat{N}$ belonging to the eigenvalue $\mathrm{v} - 1$;

(iii) $\hat{a}^{\dagger}\left|\mathrm{v}\right\rangle$ is certainly non-zero with norm equals to $\left(\mathrm{v}+1\right)\left\langle \mathrm{v}\middle|\mathrm{v}\right\rangle$ and it is an eigenvector of $\hat{N}$ corresponding to the eigenvalue $\mathrm{v} + 1$.

By normalization of the eigenvectors[1], it follows that

$$\hat{a}\left|\mathrm{v}\right\rangle = \sqrt{\mathrm{v}}\left|\mathrm{v}-1\right\rangle \qquad \hat{a}^{\dagger}\left|\mathrm{v}\right\rangle = \sqrt{\mathrm{v}+1}\left|\mathrm{v}+1\right\rangle. \tag{1.37}$$

which show that the creation operator can be used to generate the infinite set of eigenvectors, each separated by an energy quantum of ω.

The energy levels of the harmonic oscillator can be written as

$$E_{\mathrm{v}} = \left(\mathrm{v} + \frac{1}{2}\right)\hbar\omega \tag{1.38}$$

[1] It should be mentioned that the normalization constants are defined within an arbitrary phase.

where the quantum number v can assume integer values within the interval [0, +∞[. The relations given in (1.37) can be used to derive the matrices of $\hat{p}$ and $\hat{q}$ which diagonalize $\hat{H}$ in the basis $|\mathrm{v}\rangle$. This matrices are not diagonal but they are Hermitian.[i]

[i] The chapter has been written by consulting Refs. [22 – 30].

2. Molecular Rotations and Vibrations

In the prediction of molecular absorptions and spectral lines in the infrared region it is common practice to use an effective Hamiltonian approach. An effective Hamiltonian is one which may be derived from the complete Hamiltonian by using a perturbation theory approach. As seen in the previous chapter, almost all the effective Hamiltonians are based upon the separation of electron, vibrational and rotational motion. Hence, the complete vibration-rotation Hamiltonian is expanded in terms of the rotational and vibration Hamiltonians,

$$\hat{H}_{RV} = \hat{H}_R + \hat{H}_V \tag{2.1}$$

and the complete wave function is expressed as the product

$$\psi_{RV} = \psi_R \psi_V \tag{2.2}$$

where ψ_R and ψ_V are the rotational and vibrational wave functions, respectively [3].

The vibration-rotation Hamiltonian was originally derived by Wilson and Howard [31], but most of the theoretical treatment relating it to observed vibration-rotation spectra was developed by Nielsen [32]. Further developments were made by Hougen's work on symmetry classification, Oka's order of magnitude classification of the various terms, and culminated with the Watson's work on the general Hamiltonian [33].

2.1 Molecular Vibrations

The motion of a molecule consisting of N atoms is completely described by $3N$ coordinates, i.e. $3N$ degrees of freedom. The translational motion of the molecule as a whole is described by 3 coordinates which specify its centre of mass. The remaining $3N - 3$ coordinates are sufficient to fix the relative position of all the N atoms with respect to the centre of mass: they represent the internal

degrees of freedom. The rotation may be described by two or three coordinates, depending on whether the molecule is linear or not. The remaining coordinates describe the vibrational motion: linear molecules have $3N - 5$ vibrational degrees of freedom, whereas non-linear molecules possess $3N - 6$ vibrational degrees of freedom.

During the vibrational motions all the atoms are usually displaced to some extent from their equilibrium positions. The resulting complex motion is called Lissajous motion. Nevertheless, it can be decomposed into simpler vibrations, which are called normal modes of vibration. They are characterized by the fact that each atom carries out a simple harmonic motion and that all particles have the same frequency of oscillation. The number of normal modes is always equal to the number of the vibrational degrees of freedom, that is $3N - 5$ and $3N - 6$ for linear and non-linear molecules, respectively. Any vibrational motion of the system may be represented as a superposition of these normal modes.

The treatment of molecular vibrations can be conveniently tackled by the so-called normal coordinates analysis. A fortunate outcome of this method is an exactly solvable Schrödinger equation, provided that the potential is assumed to be harmonic. An alternative, but equivalent method is the use of the internal coordinates and of the Wilson's **F** and **G** matrices.

Within the normal coordinate analysis approach, with each atom of a molecule is associated a Cartesian coordinate system having its origin at the equilibrium position of the atom. At any time, the geometry of the molecule can be specified by $3N$ atomic displacement coordinates:

$$\begin{aligned}&\{(\Delta x_1, \Delta y_1, \Delta z_1), (\Delta x_2, \Delta y_2, \Delta z_2), \ldots (\Delta x_N, \Delta y_N, \Delta z_N)\} = \\ &= \{(q_1, q_2, q_3), (q_4, q_5, q_6), \ldots (q_{3N-2}, q_{3N-1}, q_{3N})\} = \{q_i\}.\end{aligned} \tag{2.3}$$

By defining the mass-weighted Cartesian displacements as[2],

$$\eta_i = \sqrt{m_j}\, q_i \tag{2.4}$$

the classical kinetic energy, which comprises the translational, rotational and vibrational degrees of freedom, is

$$T = \frac{1}{2} \sum_{i=1}^{3N} \left(\frac{d\eta_i}{dt} \right)^2 . \tag{2.5}$$

[2] The masses m_j are intended to run over the $3N$ nuclei and therefore a set of three displacement coordinates, for example (q_1, q_2,q_3), is associated with the same mass.

If the vibrational displacements are restricted to small amplitudes, the potential energy can be expanded around the equilibrium position. Within the harmonic oscillator approximation the series is truncated after the quadratic terms, so that the potential energy can be expressed as[3]

$$V = \sum_{i=1}^{3N} \sum_{j \geq i} b_{ij} \eta_i \eta_j \tag{2.6}$$

where $b_{ij} = \frac{1}{(m_i m_j)^{1/2}} \left(\frac{\partial^2 V}{\partial q_i \partial q_j} \right)_0$ are the elements of the force constant matrix, **B**.

There exists a particular coordinate system in which the matrix **B** and hence the potential energy turn out to be diagonal. This system is called normal coordinate system. A normal coordinate can be expressed as a linear combination of the mass weighted Cartesian coordinates,

$$Q_i = \sum_{k=1}^{3N} l_{ki} \eta_k \ , \tag{2.7}$$

where l_{ik} are the elements of the matrix **L** which diagonalizes the force constant matrix as follows: $\mathbf{L}^{\mathrm{T}}\mathbf{B}\mathbf{L} = \mathbf{\Lambda}$. $\mathbf{\Lambda}$ is a diagonal matrix whose elements are related to the frequencies of the normal vibrations ω_i through $\sqrt{\lambda_i} = 2\pi\omega_i$. It has to be pointed out that two (for linear molecules) or three (for non-linear molecules) of these frequencies turn out to be zero, since they correspond to non-genuine vibrations in which the molecule is simply translating or rotating.

The kinetic and the potential energies written as functions of the normal coordinates become, respectively

$$T = \frac{1}{2} \sum_{i=1}^{3N} \left(\frac{\partial Q_i}{\partial t} \right)^2 , \tag{2.8}$$

$$V = \frac{1}{2} \sum_{i=1}^{3N} \lambda_i Q_i^2 \ . \tag{2.9}$$

---

[3] At the equilibrium position, $\frac{\partial V}{\partial q_i} = 0$; the equilibrium value V_0 can be taken as reference potential energy, and therefore it can be put equal to zero without loss of generality.

The quantum mechanical vibrational Hamiltonian in terms of normal coordinates is therefore (for non-linear molecules)

$$\hat{H}_{\mathrm{v}} = \sum_{i=1}^{3N-6}\left(-\frac{\hbar}{2}\frac{\partial^2}{\partial Q_i^2} + \frac{1}{2}\lambda_i Q_i^2 \right) \tag{2.10}$$

which is the sum of one-dimensional harmonic oscillator Hamiltonians. Since for non-genuine vibrations ω_i = 0, they do not contribute to the vibrational energy and hence they have been dropped from the summation. The total wavefunction is the product of the individual harmonic oscillator wavefunctions

$$\psi_{\mathrm{v}}(\mathbf{Q}) = \prod_{i=1}^{3N-6}\phi_{v_i}(Q_i) \tag{2.11}$$

and hence the total energy is the sum of the individual energies

$$G(\mathrm{v}_1, \mathrm{v}_2, ..., \mathrm{v}_{3N-6}) = \sum_{i=1}^{3N-6}\tilde{\nu}_i\left(\mathrm{v}_i + \frac{1}{2}\right), \qquad \mathrm{v}_i = 0,\ 1,\ 2, ... \tag{2.12}$$

where G is called vibrational term value and the frequencies $\tilde{\nu}_i$ are expressed in wavenumber units (i.e. $\tilde{\nu}_i = \nu_i / c$). A vibrational state is then designated by specifying all the $3N - 6$ (or $3N - 5$) vibrational quantum numbers v_i, each of which varies independently over the range 0 to $+\infty$.

It may happen that two or more vibrational frequencies coincide, in which case the corresponding vibrations are said degenerate with one another. In this case the vibrational energy may be written as

$$G(\mathrm{v}_1, \mathrm{v}_2, ...) = \sum_i \tilde{\nu}_i\left(\mathrm{v}_i + \frac{d_i}{2}\right), \tag{2.13}$$

where d_i is the degree of degeneracy of the vibration $\tilde{\nu}_i$ (d_i = 1 means no degeneracy).

The concept of normal vibrations rests on the assumption of infinitesimal amplitude oscillations when only the quadratic terms in the potential energy need to be considered. Actually, the amplitudes of the quantized oscillations are by no means infinitesimal and therefore cubic,

quartic (and higher terms) in the potential energy must be considered, meaning that the molecular vibrations are anharmonic. For polyatomic molecules, if cubic and quartic order terms are introduced into the vibrational wave equation, it no longer resolves into a number of independent equations and the resolution of the vibrational motion into normal vibrations is not possible. In consequence the energy is no longer a sum of the energies of the individual oscillators, but it has cross terms containing the vibrational quantum numbers of two or more normal vibrations.
The vibrational term values for a polyatomic anharmonic oscillator with only non-degenerate vibrations modify from equation (2.12) to

$$G(\mathrm{v}_1, \mathrm{v}_2, ..., \mathrm{v}_{3N-6}) = \sum_{i=1}^{3N-6} \tilde{\nu}_i \left(\mathrm{v}_i + \frac{1}{2} \right) + \sum_{i=1}^{3N-6} \sum_{j \geq i} x_{ij} \left(\mathrm{v}_i + \frac{1}{2} \right) \left(\mathrm{v}_j + \frac{1}{2} \right) + ... \qquad (2.14)$$

where the $x_{i,j}$ are anharmonic force constants.

For an anharmonic oscillator with degenerate vibrations the term values are

$$G(\mathrm{v}_1, \mathrm{v}_2, ...) = \sum_i \tilde{\nu}_i \left(\mathrm{v}_i + \frac{d_i}{2} \right) + \sum_i \sum_{j \geq i} x_{ij} \left(\mathrm{v}_i + \frac{d_i}{2} \right) \left(\mathrm{v}_j + \frac{d_j}{2} \right) + \sum_i \sum_{j \geq i} g_{ij} \ell_i \ell_j \qquad (2.15)$$

where $g_{ij} \ell_i \ell_j$ is an additional anharmonic term.

2.2 VIBRATIONAL SELECTION RULES

In general, for a transition to be active (i.e. observable with a given technique) two selection rules must be satisfied. The gross selection rules are statements about the properties that a molecule must possess in order to be capable of showing a particular type of transition; the specific selection rules state the changes in quantum numbers that may occur during such a transition.

In the process of absorption or emission of infrared radiation involving transitions between two vibrational states of a molecule, the interaction is mainly between the molecule and the electric, rather than the magnetic, component of the electromagnetic radiation. For this reason infrared selection rules are also referred to as electric dipole, or simply dipole, selection rules.

The vibrational transition moment for a v' $\leftarrow$ v" transition is defined by the following expression

$$\boldsymbol{\mu}_{\mathrm{v'v''}} = \langle \mathrm{v'} | \hat{\boldsymbol{\mu}} | \mathrm{v''} \rangle \tag{2.16}$$

where $\hat{\boldsymbol{\mu}}$ is the dipole moment operator of the molecule in a given electronic state. The transition moment is a vector whose components are

$$\mu^{\alpha}_{\mathrm{v'v''}} = \langle \mathrm{v'} | \hat{\mu}_{\alpha} | \mathrm{v''} \rangle, \qquad \alpha = x, y, z \tag{2.17}$$

where $\hat{\mu}_{\alpha}$ is the component of the electric dipole moment along the α axis. Therefore, the square of the transition moment can be written as

$$\left|\boldsymbol{\mu}_{\mathrm{v'v''}}\right|^2 = \left|\mu^{x}_{\mathrm{v'v''}}\right|^2 + \left|\mu^{y}_{\mathrm{v'v''}}\right|^2 + \left|\mu^{z}_{\mathrm{v'v''}}\right|^2 . \tag{2.18}$$

Since the intensity of a transition is proportional to the square of the transition moment, $\left|\boldsymbol{\mu}_{\mathrm{v'v''}}\right|^2$, it follows that the transition is forbidden if the transition moment vanishes, whereas the transition is allowed if the transition moment is non-zero, i.e. at least one of the components among the $\mu^{\alpha}_{\mathrm{v'v''}}$ is non-zero.

If the amplitudes of normal vibrations are small, then the components of $\boldsymbol{\mu}_{\mathrm{v'v''}}$ can be expanded as a converging series

$$\mu_{\alpha} = \mu_e^{\alpha} + \sum_k \left(\frac{\partial \mu_{\alpha}}{\partial q_k} \right)_e q_k + \frac{1}{2} \sum_k \sum_{l \geq k} \left(\frac{\partial^2 \mu_{\alpha}}{\partial q_k \partial q_l} \right)_e q_k q_l + \ldots \tag{2.19}$$

where μ_e^{α} is the component of the permanent dipole moment along the α axis and all the partial derivatives are referred to the equilibrium configuration of the molecule. To a first approximation, the quadratic and higher order terms in the expansion are neglected; they give rise to the so-called electrical anharmonicity. Due to the orthogonality of the eigenfunctions, the components of the transition moment can be expressed as

$$\mu^{\alpha}_{\mathrm{v'v''}} = \sum_k \left(\frac{\partial \mu_{\alpha}}{\partial q_k} \right)_e \langle \mathrm{v'} | q_k | \mathrm{v''} \rangle . \tag{2.20}$$

It follows that the gross selection rule states that for an electric dipole transition to be infrared active there must be a change of the dipole moment during the vibrational motion. In addition, the specific selection rule requires that the vibrational quantum number changes according to $\Delta v = \pm 1$, and if anharmonicity is considered, $\Delta v = \pm 2, \pm 3, \ldots$ is allowed as well.

There are symmetry requirements for equation (2.16) to be non-zero and therefore for a transition to be infrared allowed. The requirement is that the symmetry species of the integrand contains the totally symmetric representation:

$$\Gamma(\psi_{v'}) \times \Gamma(\hat{\boldsymbol{\mu}}) \times \Gamma(\psi_{v''}) \supset A \tag{2.21}$$

where ψ_v is the vibrational function, Γ stands for "representation of …" and A denotes the totally symmetric representation of the point group to which the molecule belongs. The dipole moment vector belongs to the same symmetry species as a translation of the molecule in the same direction,

$$\Gamma(\mu_\alpha) = \Gamma(T_\alpha), \qquad \alpha = x, y, z; \tag{2.22}$$

therefore, given equation (2.18), it follows that (2.21) can be recast as

$$\begin{aligned} &\Gamma(\psi_{v'}) \times \Gamma(T_x) \times \Gamma(\psi_{v''}) \supset A \quad \text{and/or} \\ &\Gamma(\psi_{v'}) \times \Gamma(T_y) \times \Gamma(\psi_{v''}) \supset A \quad \text{and/or} \\ &\Gamma(\psi_{v'}) \times \Gamma(T_z) \times \Gamma(\psi_{v''}) \supset A, \end{aligned} \tag{2.23}$$

Fundamental vibrations, or normal modes, are transitions between the ground vibrational states and the first excited vibrational state, $v_i = 1$ (Figure 2.1 a). Since the ground vibrational state belongs to the totally symmetric representation, $\Gamma(\psi_{v''}) = A$, a fundamental vibration is infrared active if the wave function which describes the excited state belongs to the same representation of one or more translations, $\Gamma(\psi_{v'}) \supset \Gamma(T_\alpha)$.

The anharmonicity causes vibrations other than the fundamental ones to be observable. The classification of these vibrational transitions, and their symmetry species are as follow.

Overtone vibrations are transitions in which the molecule gains more than one vibrational energy quantum within the same vibrational mode (Figure 2.1 b). The transition v' = 2 ← v'' = 0 gives rise to the first overtone, the transition v' = 3 ← v'' = 0 gives rise to the second overtone and so on: the transition v' = *n* ← v'' = 0 gives rise to the (*n* – 1)-th overtone. The symmetry species of an *n*-th overtone can be determined by taking (*n* + 1) times the direct product of the irreducible representation to which the involved normal mode belongs.

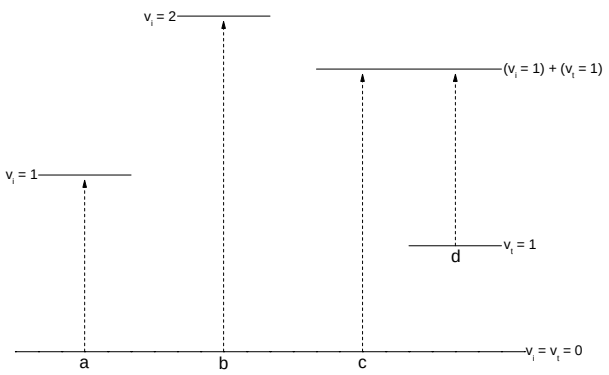

Figure 2.1. Schematic representation of vibrational transitions: (a) fundamental; (b) overtone; (c) combination band; (d) hot band.

Combinations bands arise when the molecule gains two or more vibrational quanta over two or more normal vibrational modes (Figure 2.1 c). The symmetry species of the combination bands can be obtained by taking the direct product of the irreducible representations to which the involved normal modes belong.

Hot bands are due to transitions between an excited vibrational level and another excited vibrational level of higher energy (Figure 2.1 d). They are called hot band because their intensity increases with the temperature. The symmetry species can be determined as for the combination bands.

2.3 MOMENTS OF INERTIA

The rotational properties of molecules can be described according to their principal moments of inertia. With respect to any set of Cartesian axes whose origin is at the centre of mass of the molecule, the angular momentum is

$$\mathbf{J} = \mathbf{I} \cdot \boldsymbol{\omega} \tag{2.24}$$

where **J** is the angular momentum vector, **I** is the second order tensor of inertia and **ω** is the angular velocity vector. Written explicitly, equation (2.24) takes on the form

$$\begin{bmatrix} J_x \\ J_y \\ J_z \end{bmatrix} = \begin{bmatrix} I_{xx} & I_{xy} & I_{xz} \\ I_{yx} & I_{yy} & I_{yz} \\ I_{zx} & I_{zy} & I_{zz} \end{bmatrix} \begin{bmatrix} \omega_x \\ \omega_y \\ \omega_z \end{bmatrix}; \tag{2.25}$$

(J_x, J_y, J_z) and (ω_x, ω_y, ω_z) are the components of the angular momentum and angular velocity, respectively; I_{xx}, I_{yy} and I_{zz} are the moments of inertia along the axis indicated as subscript, while the non-diagonal elements of the tensor of inertia are called products of inertia:

$$\begin{cases} I_{xx} = I_x = \sum_i m_i \left(y_i^2 - z_i^2 \right) \\ I_{yy} = I_y = \sum_i m_i \left(x_i^2 - z_i^2 \right) \\ I_{zz} = I_z = \sum_i m_i \left(x_i^2 - y_i^2 \right) \end{cases} \tag{2.26}$$

$$\begin{cases} I_{xy} = I_{yx} = -\sum_i m_i x_i y_i \\ I_{yz} = I_{zy} = -\sum_i m_i y_i z_i \\ I_{xz} = I_{zx} = -\sum_i m_i x_i z_i \end{cases} \tag{2.27}$$

where m_i is the mass of the i-th atom whose coordinates are (x_i, y_i, z_i) and the summation is taken over all the particles of the body. Among all the various axes going through the centre of mass, there are always three mutually perpendicular directions, for which the products of inertia vanish and hence the tensor of inertia becomes diagonal,

$$\mathbf{I} = \begin{bmatrix} I_x & 0 & 0 \\ 0 & I_y & 0 \\ 0 & 0 & I_z \end{bmatrix},$$

and there are a maximum and a minimum value of the moments of inertia. The axes representing these directions are called the principal axes, and the corresponding moments of inertia the principal moments of inertia. In spectroscopy, this unique set of parameters carry the subscript A, B and C, and the order is determined by the convention $I_A \leq I_B \leq I_C$.

There are six possible ways of identifying the axes x, y and z with the principal axes of inertia A, B and C. These are listed in Table 2.1 according to the notation of King, Hainer and Cross [34].

Table 2.1. King, Hainer and Cross notation: r and l denotes a Cartesian axes system right- and left- handed, respectively.

	$\mathbf{I}^r$	$\mathbf{II}^r$	$\mathbf{III}^r$	$\mathbf{I}^l$	$\mathbf{II}^l$	$\mathbf{III}^l$
x	B	C	A	C	A	B
y	C	A	B	B	C	A
z	A	B	C	A	B	C

According to the values assumed by the principal moments of inertia, molecules are subdivided into four different classes of rotors. If one of the principal moments is zero, while the remaining two are equal, the molecule is classified as a linear rotor; if two of the principal moments of inertia are equal and the third is non zero, it is called a symmetric top; if all the three moments of inertia are equal, the molecule is classified a spherical top and if the three moments are all different, the molecule is said to be an asymmetric top. This classification is summarized in Figure 2.2.

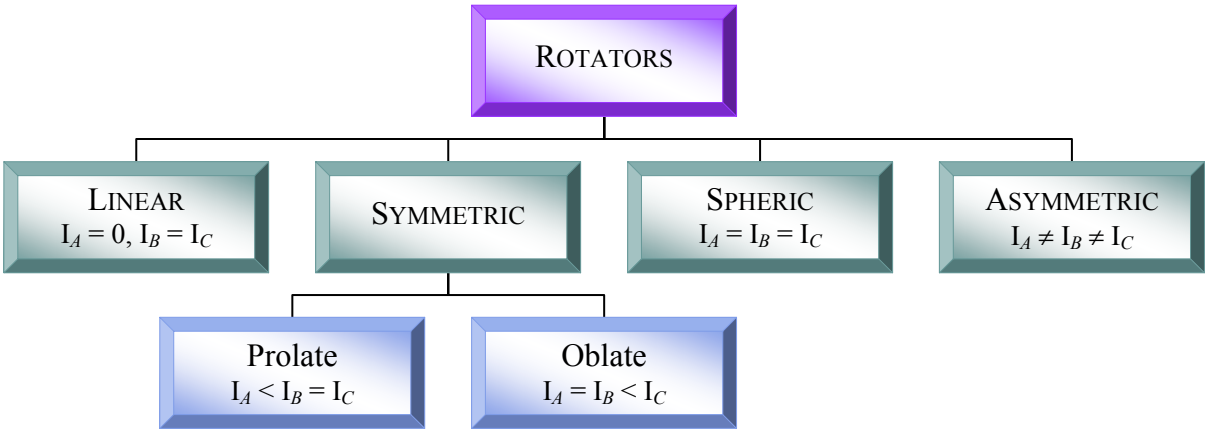

Figure 2.2. Classification of rotators on the basis of the principal moments of inertia.

Each class of rotators is characterized by an its own spectroscopic behaviour.

2.4 THE RIGID SYMMETRIC AND ASYMMETRIC ROTORS

The quantum mechanical Hamiltonian of a rigidly rotating molecule referred to the principal axes of inertia is

$$\hat{H}_r^0 = B_x \hat{J}_x^2 + B_y \hat{J}_y^2 + B_z \hat{J}_z^2 \tag{2.28}$$

where $\hat{J}_x$, $\hat{J}_y$, $\hat{J}_z$ are the components of the angular momentum operator and B_x, B_y, B_z are the rotational constants of the molecule, which are given by:

$$B_\alpha = \frac{h}{8\pi^2 I_\alpha c}; \tag{2.29}$$

in which the B_α's are expressed in cm^{-1}, I_α is the moment of inertia about the α-axis and c is the speed of light. Usually, the rotation constants are denoted A, B, C depending on whether they refer to the principal moment of inertia I_A, I_B or I_C, respectively.

The rotational Hamiltonian may conveniently be expressed in terms of the so-called shift operators; in the molecule- and space-fixed axis systems these operators are defined respectively as

$$\hat{J}^{\mp} = \hat{J}_x \pm i\hat{J}_y, \qquad \hat{J}_{\pm} = \hat{J}_X \pm i\hat{J}_Y. \tag{2.30}$$

Rewriting the rotational Hamiltonian (2.28) by using the $\hat{J}^{\mp}$ operators, one obtains

$$\hat{H}_r^0 = \frac{1}{2}\left(B_x + B_y\right)\hat{\mathbf{J}}^2 + \left[B_z - \frac{1}{2}\left(B_x + B_y\right)\right]\hat{J}_z^2 + \frac{1}{4}\left(B_x + B_y\right)\left[\left(\hat{J}^+\right)^2 + \left(\hat{J}^-\right)^2\right]. \tag{2.31}$$

The eigenvalues of the Hamiltonian operator represent the quantized rotational levels of the molecule. If the Hamiltonian operator commutes with the angular momentum operators, then it results diagonal in the representation in which those operators are diagonal.

The symmetric top rotor has a component of its angular momentum about the internal symmetry axis of inertia which is a constant of the motion. The symmetric-top representation is of particular importance, since the rotational Hamiltonian commutes with the angular momentum operators, which are diagonal in the J, k, m representation. The non-zero elements of the angular momentum operators in the molecule-fixed and space-fixed axes are listed in Table 2.2 using the symmetric rotor basis function $|J,k,M\rangle$; in the expressions $K = |k|$ and $M = |m|$ and the quantum numbers J, k and m are given by the relations (1.31).

As can be seen from equations (2.28) and (2.31), in finding the eigenvalues of the rotational Hamiltonian, the squared operators $\hat{J}_z^2$, $\hat{J}_x^2$ and $\hat{J}_y^2$ are needed. They can be found from the above expressions giving the $\hat{J}_\alpha$ matrix elements by applying the properties of the product of matrices[4]. The matrix associated with $\hat{J}_z^2$ results diagonal, while matrices $\hat{J}_x^2$, $\hat{J}_y^2$ have both diagonal and non-diagonal elements. The involved non-zero matrix elements of the three squared operators are also given in Table 2.2.

Table 2.2. Non-zero matrix elements of the angular momentum operators of the symmetric rotor basis functions.

Molecule-fixed axes: *x*, *y*, *z*

$$\langle J \quad k \quad m|\hat{J}^2|J \quad k \quad m\rangle = \hbar^2 J(J+1)$$

$$\langle J \quad k \quad m|\hat{J}_z|J \quad k \quad m\rangle = \hbar K$$

$$\langle J \quad k \pm 1 \quad M|\hat{J}^{\mp}|J \quad k \quad M\rangle = \left[J(J+1) - k(k \mp 1)\right]^{1/2}$$

Space-fixed axes: *X*, *Y*, *Z*

$$\langle J \quad k \quad m|\hat{J}^2|J \quad k \quad m\rangle = \hbar^2 J(J+1)$$

$$\langle J \quad k \quad m|\hat{J}_Z|J \quad k \quad m\rangle = \hbar M$$

$$\langle J \quad k \quad M \pm 1|\hat{J}_{\pm}|J \quad k \quad M\rangle = \left[J(J+1) - M(M \pm 1)\right]^{1/2}$$

Squared Operators

$$\langle J \quad k \quad m|\hat{J}_z^2|J \quad k \quad m\rangle = \hbar^2 k^2$$

$$\langle J \quad k \quad m|\hat{J}_x^2|J \quad k \quad m\rangle = \langle J \quad k \quad m|\hat{J}_y^2|J \quad k \quad m\rangle = \frac{\hbar^2}{2}\left[J(J+1) - k^2\right]$$

$$\langle J \quad k \mp 2 \quad m|\hat{J}_x^2|J \quad k \quad m\rangle = -\langle J \quad k \mp 2 \quad m|\hat{J}_y^2|J \quad k \quad m\rangle =$$

$$= -\frac{\hbar^2}{4}\left[J(J+1) - k(k \pm 1)\right]^{1/2}\left[J(J+1) - k(k \pm 1)(k \pm 2)\right]^{1/2}$$

As stated above, the rotational Hamiltonian of a symmetric rigid rotor is diagonal in the *J*, *k*, *m* representation, with matrix elements given by

$$E_{J,k} = \langle J \quad k \quad m|\hat{H}_r^0|J \quad k \quad m\rangle = B_x J(J+1) + (B_z - B_x)K^2 \qquad (2.32)$$

These diagonal elements are independent of *m*, in agreement with the classical principle that the rotational energy in the absence of torques is independent of the spatial orientation of the angular

[4] $\langle J' \quad k' \quad m'|\hat{J}_\alpha^2|J \quad k \quad m\rangle = \sum_{J'',k'',m''} \langle J' \quad k' \quad m'|\hat{J}_\alpha|J'' \quad k'' \quad m''\rangle\langle J'' \quad k'' \quad m''|\hat{J}_\alpha|J \quad k \quad m\rangle$.

momentum vector. Further, states whose only difference is the sign of k have the same energy: classically, they correspond to the two opposite direction of rotation. Thus all states with $K > 0$ are doubly degenerate.

While for a symmetric rotor the Hamiltonian matrix is already diagonal and there exist analytic expressions for the rotational energy levels, the asymmetric rotor Hamiltonian matrix is not diagonal and it is not possible to obtain a general closed-form expression for the energy levels. The diagonalization of the asymmetric rotor Hamiltonian matrix is usually carried out by using as basis functions the symmetric rotor wave-functions, and by factorizing the matrix according to the transformation introduced by Wang [35]:

$$\begin{cases} \left|J \quad K \quad M \quad \gamma\right\rangle = \dfrac{1}{\sqrt{2}}\left[\left|J \quad k \quad M\right\rangle + (-1)^{\gamma}\left|J \quad -k \quad M\right\rangle\right] & K > 0 \\ \left|J \quad 0 \quad M \quad 0\right\rangle = \left|J \quad 0 \quad M\right\rangle & K = 0 \end{cases} \tag{2.33}$$

where $\gamma = 0$ or 1. The $\gamma = 0$ functions are the symmetric Wang functions, while the $\gamma = 1$ functions are the anti-symmetric Wang functions. By using the Wang's transformation, the Hamiltonian matrix for each value of J other than 0 or 1 may be partitioned into four independent tridiagonal matrices labelled $\mathbf{E}^{+}$, $\mathbf{E}^{-}$, $\mathbf{O}^{+}$ and $\mathbf{O}^{-}$, whose dimensions are given in Table 2.3.

Table 2.3. Dimensions of the $\mathbf{E}^{\pm}$, $\mathbf{O}^{\pm}$ matrices.

	$J = n$	$J = 2n+1$
$\mathbf{E}^{+}$	$\frac{J}{2}+1$	$\frac{J+1}{2}$
$\mathbf{E}^{-}$	$\frac{J}{2}$	$\frac{J-1}{2}$
$\mathbf{O}^{+}$	$\frac{J}{2}$	$\frac{J+1}{2}$
$\mathbf{O}^{-}$	$\frac{J}{2}$	$\frac{J+1}{2}$

The notation E, O refers to the evenness or oddness of the K values involved in the matrix elements and +,– to the evenness or oddness of γ. An example of the form of the four matrices for $J = 8$ is given in Table 2.4. Each of these matrices may be diagonalized independently, thus simplifying the problem of finding the rotational energies of an asymmetric rotor.

Table 2.4. Form of the $\mathbf{E}^{\pm}$, $\mathbf{O}^{\pm}$ matrices for $J = 8$. $E_{i,j} = \langle J,i,M \,|\hat{H}_r|\, J,j,M \rangle$

$$E^{+} = \begin{bmatrix} \mathrm{E}_{0,0} & \sqrt{2}\mathrm{E}_{0,2} & 0 & 0 & 0 \\ \sqrt{2}\mathrm{E}_{0,2} & \mathrm{E}_{2,2} & \mathrm{E}_{2,4} & 0 & 0 \\ 0 & \mathrm{E}_{2,4} & \mathrm{E}_{4,4} & \mathrm{E}_{4,6} & 0 \\ 0 & 0 & \mathrm{E}_{4,6} & \mathrm{E}_{6,6} & \mathrm{E}_{6,8} \\ 0 & 0 & 0 & \mathrm{E}_{6,8} & \mathrm{E}_{8,8} \end{bmatrix} \qquad \mathbf{E}^{-} = \begin{bmatrix} \mathrm{E}_{2,2} & \mathrm{E}_{2,4} & 0 & 0 \\ \mathrm{E}_{2,4} & \mathrm{E}_{4,4} & \mathrm{E}_{4,6} & 0 \\ 0 & \mathrm{E}_{4,6} & \mathrm{E}_{6,6} & \mathrm{E}_{6,8} \\ 0 & 0 & \mathrm{E}_{6,8} & \mathrm{E}_{8,8} \end{bmatrix}$$

$$\mathbf{O}^{+} = \begin{bmatrix} \mathrm{E}_{1,1} + \mathrm{E}_{-1,1} & \mathrm{E}_{1,3} & 0 & 0 \\ \mathrm{E}_{1,3} & \mathrm{E}_{3,3} & \mathrm{E}_{3,5} & 0 \\ 0 & \mathrm{E}_{3,5} & \mathrm{E}_{5,5} & \mathrm{E}_{5,7} \\ 0 & 0 & \mathrm{E}_{5,7} & \mathrm{E}_{7,7} \end{bmatrix} \qquad \mathbf{O}^{-} = \begin{bmatrix} \mathrm{E}_{1,1} - \mathrm{E}_{-1,1} & \mathrm{E}_{1,3} & 0 & 0 \\ \mathrm{E}_{1,3} & \mathrm{E}_{3,3} & \mathrm{E}_{3,5} & 0 \\ 0 & \mathrm{E}_{3,5} & \mathrm{E}_{5,5} & \mathrm{E}_{5,7} \\ 0 & 0 & \mathrm{E}_{5,7} & \mathrm{E}_{7,7} \end{bmatrix}$$

2.5 THE EFFECTIVE VIBRATIONAL – ROTATIONAL HAMILTONIAN

High order corrections for vibrational-rotational interactions and anharmonicity need to be introduced into the Hamiltonian in order to fully describe all the features observable in the experimental spectra. The perturbation approach is generally adopted, in which the vibrational-rotational Hamiltonian is expanded in terms of the normal coordinates, their conjugate momenta and the components of the rotational angular momentum. The harmonic oscillator and rigid rotor wavefunctions are used as basis functions. This leads to effective rotational Hamiltonians for individual vibrational states or "polyads" of vibrational states. The perturbation theory is usually applied in the form of the method of contact transformations. By this method it is possible to achieve a kind of separation of the vibration-rotation Hamiltonian, which makes it possible to discuss the effective rotational Hamiltonian for an individual vibrational level or a block of nearly-degenerate vibrational levels.

The complete quantum mechanical Hamiltonian of a vibrating-rotating molecule following Watson's simplifications [39] can be expressed as

$$\hat{H}_{\mathrm{vr}} = \frac{\hbar^2}{2} \sum_{\alpha,\beta=x,y,z} \mu_{\alpha\beta} \left(\hat{J}_\alpha - \hat{\pi}_\alpha\right)\left(\hat{J}_\beta - \hat{\pi}_\beta\right) + \frac{1}{2}\sum_k \hat{P}_k^2 + V(\mathbf{Q}). \tag{2.34}$$

where Q_k represents the k-th normal coordinate, $\hat{P}_k = -i\hbar\partial/\partial Q_k$ is its conjugate momentum, $\hat{\pi}_\alpha$ is the component of the vibrational angular momentum along the direction α, $\mu_{\alpha\beta}$ represents the

component of a modified reciprocal inertia tensor $\boldsymbol{\mu}$ and $V(\mathbf{Q})$ is the potential energy. The vibrational angular momentum is given by

$$\hbar\hat{\pi}_\alpha = \sum_{k,l} \zeta_{k,l}^{(\alpha)} Q_k \hat{P}_l \tag{2.35}$$

where $\zeta_{k,l}^{(\alpha)}$ is the Coriolis zeta constant, coupling the normal coordinates Q_k and Q_l through a rotation about the α axis. The reciprocal inertia tensor can be obtained from the following expression

$$\boldsymbol{\mu} = \left(\mathbf{I}''\right)^{-1} \mathbf{I}^{\mathrm{e}} \left(\mathbf{I}''\right)^{-1}, \qquad I''_{\alpha\beta} = I''_{\beta\alpha} = I^{\mathrm{e}}_{\alpha\beta} + \frac{1}{2}\sum_k a_k^{\alpha\beta} Q_k, \qquad a_k^{\alpha\beta} = \left(\frac{\partial I_{\alpha\beta}}{\partial Q_k}\right)_{\mathrm{e}}$$

where $\mathbf{I}^{\mathrm{e}}$ is the inertia tensor in the equilibrium configuration of the molecule.

In the perturbation approach, the Hamiltonian (2.34) can be expanded in a power series of products of vibrational and rotational operators, by expanding $\boldsymbol{\mu}$ and $V(\mathbf{Q})$ in terms of the normal coordinates $\mathbf{Q}$ about the points of equilibrium configuration of the atomic nuclei. The expanded Hamiltonian can then be conveniently arranged using the $\hat{H}_{mn}$ notation:

$$\begin{aligned}
\hat{H}_{\mathrm{vr}} &= \sum_{m,n} \hat{H}_{mn} = \\
&= \hat{H}_{20} + \hat{H}_{30} + \hat{H}_{40} + \ldots + && \text{(vibrational terms)} \\
&+ \hat{H}_{21} + \hat{H}_{31} + \hat{H}_{41} + \ldots + && \text{(Coriolis terms)} \\
&+ \hat{H}_{02} + \hat{H}_{12} + \hat{H}_{22} + \ldots && \text{(rotational terms).}
\end{aligned} \tag{2.36}$$

The first subscript refers to the degree in the vibrational operators (coordinates and momenta) and the second subscript is the degree in the components of the total angular momentum. In the expansion, the term $\hat{H}_{11}$ turns out to be zero; the terms $\hat{H}_{00}$ and $\hat{H}_{10}$ give a small contribution, which is indistinguishable from the effects of the breakdown of the Born – Oppenheimer approximation and hence they can be ignored. The perturbation method procedure takes the harmonic oscillator $\hat{H}_{20}$ as the unperturbed Hamiltonian, and then $\hat{H}_{\mathrm{vr}}$ is reduced to a block

diagonal form by a succession of contact transformations[5]. At each stage of the contact transformation procedure, the equation to solve is of the form

$$\tilde{H}_{mn}^{(j)} = \tilde{H}_{mn}^{(j-1)} + i\left[\hat{S}_{mn}, \hat{H}_{20}\right]$$

where $\tilde{H}_{mn}^{(j-1)}$ results from the previous transformation and $\hat{S}_{mn}$ is the Hermitian operator that performs the unitary transformation. Both $\tilde{H}_{mn}$ and $\hat{S}_{mn}$ can be expressed as power series of the vibrational ladder operators defined as

$$\hat{\mathrm{L}} = \hat{q}_k - i\sigma\hat{p}_k, \qquad \sigma = + \text{ or } -$$

in which the dimensionless normal coordinate $\hat{q}_k$ and conjugate momentum $\hat{p}_k$ are related to the corresponding dimensional operators by

$$\hat{Q}_k = \gamma_k^{-1/2}\hat{q}_k, \qquad \hat{P}_k = \hbar\gamma_k^{1/2}\hat{p}_k, \qquad \gamma_k = \frac{hc\omega_k}{\hbar^2}.$$

By using the commutation relations, it can be shown that $\tilde{H}_{mn}^{(i-1)}$ and $\hat{S}_{mn}$ assume the general forms:

$$\tilde{H}_{mn}^{(i-1)} = \sum C\left(k^{(i-1)}, \sigma_{k^{(i-1)}}; k^{(i-2)}, \sigma_{k^{(i-2)}}; k^{(i-3)}, \sigma_{k^{(i-3)}}; \ldots\right)\hat{\mathrm{L}}_{k^{(i-1)}}^{\sigma_{k^{(i-1)}}}\hat{\mathrm{L}}_{k^{(i-2)}}^{\sigma_{k^{(i-2)}}}\hat{\mathrm{L}}_{k^{(i-3)}}^{\sigma_{k^{(i-3)}}}\cdots$$

$$\hat{S}_{mn} = \sum{}^{*}\frac{C\left(k^{(i-1)}, \sigma_{k^{(i-1)}}; k^{(i-2)}, \sigma_{k^{(i-2)}}; k^{(i-3)}, \sigma_{k^{(i-3)}}; \ldots\right)}{\sigma_{k^{(i-1)}}\omega_{k^{(i-1)}} + \sigma_{k^{(i-2)}}\omega_{k^{(i-2)}} + \sigma_{k^{(i-3)}}\omega_{k^{(i-3)}} + \ldots}\hat{\mathrm{L}}_{k^{(i-1)}}^{\sigma_{k^{(i-1)}}}\hat{\mathrm{L}}_{k^{(i-2)}}^{\sigma_{k^{(i-2)}}}\hat{\mathrm{L}}_{k^{(i-3)}}^{\sigma_{k^{(i-3)}}}\cdots$$

where the coefficients $C\left(k^{(i-1)}, \sigma_{k^{(i-1)}}; k^{(i-2)}, \sigma_{k^{(i-2)}}; k^{(i-3)}, \sigma_{k^{(i-3)}}; \ldots\right)$ are generally rotational operators and the asterisk on the summation means that the terms for which the denominator vanishes, or nearly, are omitted.

Detailed derivations of the constants appearing in the effective Hamiltonian are given for example by Mills [33], Aliev and Watson [36], Papoušek and Aliev [37].

In particular, the terms $\tilde{H}_{0n}$ (n = 2, 4, 6,…) in the effective Hamiltonian represent the pure rotational and centrifugal contributions to the energy. Among these, the term $\tilde{H}_{02}$ is the rigid rotor

[5] A general description of the contact transformation technique is given in Appendix A.

Hamiltonian, while $\widetilde{H}_{04}$ and $\widetilde{H}_{06}$ represent the second and third order contributions to the effective Hamiltonian, respectively. They can be put into the form

$$\widetilde{H}_{04} = \frac{1}{4} \sum_{\alpha,\beta,\gamma,\delta} \tau_{\alpha\beta\gamma\delta} \hat{J}_\alpha \hat{J}_\beta \hat{J}_\gamma \hat{J}_\delta \tag{2.37}$$

$$\widetilde{H}_{06} = \frac{1}{4} \sum_{\alpha,\beta,\gamma,\delta,\varepsilon,\eta} \tau_{\alpha\beta\gamma\delta\varepsilon\eta} \hat{J}_\alpha \hat{J}_\beta \hat{J}_\gamma \hat{J}_\delta \hat{J}_\varepsilon \hat{J}_\eta \tag{2.38}$$

where $\alpha, \beta, \gamma, \delta, \varepsilon, \eta$ can be x, y or z, and the τ's include the coefficients resulting from the contact transformation procedure.

The operators $\widetilde{H}_{22}$, $\widetilde{H}_{42}$, $\widetilde{H}_{24}$,… describe the dependence of the rotational and centrifugal constants on the vibrational quantum numbers. In addition, in the case of degenerate or near-degenerate vibrational states, these terms provide the resonance parameters connecting the interacting levels. The leading term $\widetilde{H}_{22}$ describes the dependence of the rotational constants on the vibrational quantum numbers. It has the following general form

$$\widetilde{H}_{22} = -\frac{1}{2} \hat{\sum_{klrs}} \left(\hat{q}_k \hat{q}_l + \hat{p}_k \hat{p}_l \right) \alpha_{kl}^{(rs)} \hat{J}_r \hat{J}_s$$

where the summation implies a restriction to terms with $\omega_k \approx \omega_l$ and $\alpha_{kl}^{(rs)} = \alpha_{kl}^{(sr)} = \alpha_{lk}^{(rs)} = \alpha_{lk}^{(sr)}$. For $k = l$ and $r = s$, one can derive the α constants which enter into the expression for the vibrational dependence of the rotational constants:

$$B_r^{(V)} = B_r^e - \sum_k \alpha_k^r \left(\mathrm{v}_k + \frac{1}{2} \right) \tag{2.39}$$

where B_r^e is the value of the rotational constant in the equilibrium configuration of the molecule. When k and l are the components of a degenerate mode, the rotational l-doubling constants are obtained. These are the q_t constants of linear molecules, or the $q_t^{\pm}$ and r_t constants of symmetric top molecules.

The $\tilde{H}_{40}$ terms are the principal sources of information on the quartic potential constants. The non-resonant contributions to this term give the anharmonic constant $x_{i,j}$ in the formula for the vibrational term value given in equation (2.14).

By means of the contact transformation method the Hamiltonian is brought to block-diagonal form and it can be expressed as a power series in the vibrational and rotational operators. However, not all the coefficients of the series can unequivocally be determined[6] but only some their linear combinations can be obtained. These are called determinable combinations of coefficients. Watson has shown that it is possible to choose $\hat{S}$ so that particular terms or matrix elements vanish [40]. The effective Hamiltonian then takes a special form which is called reduced Hamiltonian or "Watsonian".

2.6 INTERACTIONS

In a polyatomic molecule, it may happen that two or more ro-vibrational states belonging to different vibrations may have nearly the same energy. If the involved vibrations have the proper symmetry, an interaction takes place whose effect is to shift the energy levels and change the intensity of the spectral absorptions. The levels which have nearly the same energy repel each other as shown in Figure 2.3: the level having the higher energy is shifted up whereas the lower energy level is shifted down. At the same time a mixing of the eigenfunctions of the two states occurs. Consequently, not only the spectral transitions are shifted from their unperturbed positions, but there is also a perturbation in their intensity.

Two kinds of resonance there exists: (i) anharmonic resonances which arise from the anharmonic potential; (ii) Coriolis resonances which are caused by the interaction between the rotational and vibrational motions.

The magnitude of the perturbation depends on the value of the matrix element W_{ij} of the perturbation operator $\hat{W}$ connecting the accidentally degenerate states:

$$W_{ij} = \int \psi_i^{0,*} \hat{W} \psi_j^0 d\tau \qquad (2.40)$$

[6] Because the contact transformation $\tilde{H}' = e^{i\hat{S}} \tilde{H} e^{-i\hat{S}}$ has the effect of changing the coefficients of the expansion but it leaves the eigenvalues invariant.

where ψ_i^0 and ψ_j^0 are the unperturbed wavefunctions of the involved states.

For anharmonic resonances, the perturbation operator $\hat{W}$ is related to the anharmonic (cubic, quartic,…) terms in the potential energy. Since $\hat{W}$ belongs to the totally symmetric representation, ψ_i^0 and ψ_j^0 must belong to the same symmetry representation in order for the matrix element W_{ij} to be non-zero:

$$\Gamma\left(\psi_i^0\right)\times\Gamma\left(\psi_j^0\right)\supset A\,. \tag{2.41}$$

It follows that anharmonic resonance can occur only between vibrational levels which belong to the same symmetry species.

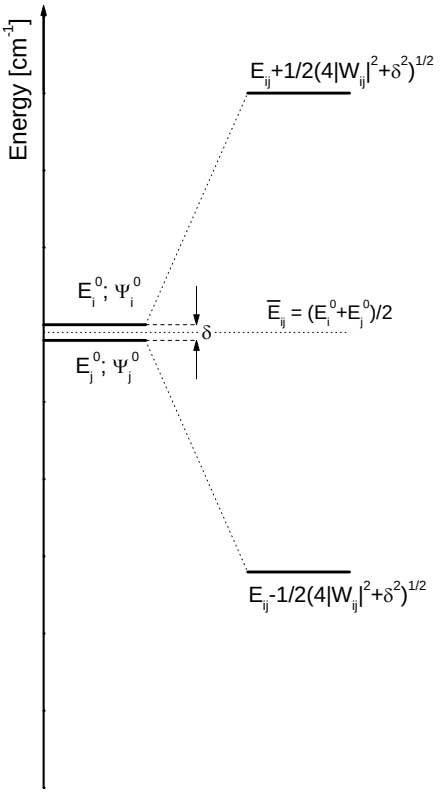

Figure 2.3. Schematic representation of the effect on the energy levels caused by anharmonic resonances between two accidentally degenerate vibrational levels.

The anharmonic resonance comprises two kinds of interactions: Fermi and Darling – Dennison resonances. The Fermi resonance takes place between fundamental and overtone, or combination, vibrations. The Darling – Dennison resonance can exist only between overtone and overtone, or combination, vibrations. Both of them involve ro-vibrational levels having the same value of J and K ($\Delta J = 0$, $\Delta K = 0$). In addition, anharmonic resonance may also occur for $\Delta K = \pm 2$, ± 4, ± 6,… These are called high order anharmonic interactions and they can take place between fundamental vibrations, as well.

According to first order perturbation theory, if the resonance is fairly close, the magnitude of the shift is given by the secular determinant

$$\begin{vmatrix} E_i^0 - E & W_{ij} \\ W_{ji} & E_j^0 - E \end{vmatrix} = 0 \tag{2.42}$$

where E_i^0 and E_j^0 are the energy of the unperturbed levels. The perturbed energies results to be

$$E = \overline{E}_{ij} \pm \frac{1}{2}\sqrt{4\left|W_{ij}\right|^2 + \delta^2} \qquad (2.43)$$

with $\overline{E}_{ij} = \frac{1}{2}\left(E_i^0 + E_j^0\right)$ is the mean energy and $\delta = E_j^0 - E_i^0$ is the energy separation. From equation (2.43) two considerations can be drawn: (i) the magnitude of the interaction is stronger the larger is the matrix element W_{ij}; (ii) the shift of the energy levels and the mixing of the wavefunctions is the stronger the smaller is the energy difference between the interacting levels. Figure 2.4 shows the position of the perturbed levels as a function of their energy separation (for constant values of W_{ij} and $\overline{E}_{ij}$). The shift produced by the perturbation is given by the separation between the black curve and the nearest green line.

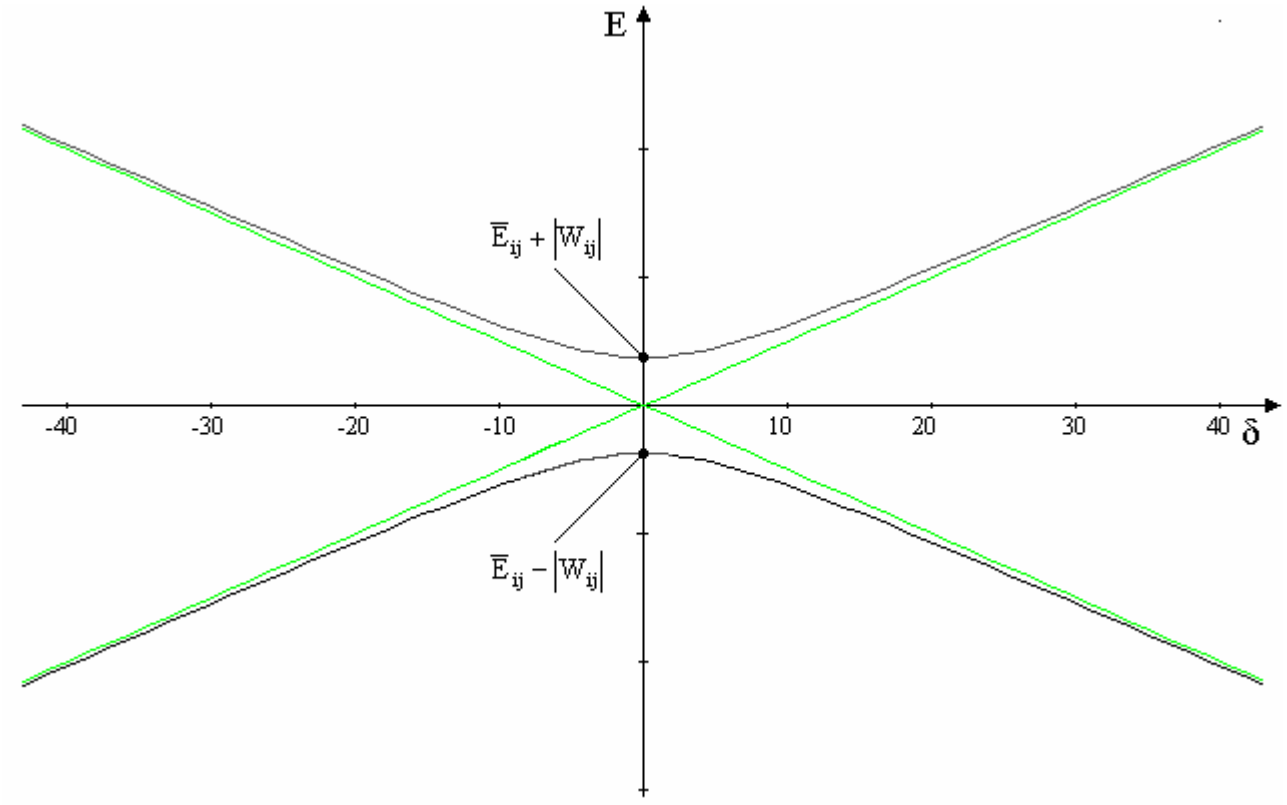

Figure 2.4. Plot of the energy of the perturbed levels (—) with respect to the unperturbed positions (—) as a function of their energy separation. The plot has been obtained for constant and arbitrary value of W_{ij} and $\overline{E}_{ij}$.

2.7 NUCLEAR SPIN STATISTICAL WEIGHT

The total wave function including the contribution of the nuclear spins is to a first approximation expressed by

$$\psi = \psi_e \psi_v \psi_r \psi_n$$

where ψ_e, ψ_v, ψ_r are the electronic, vibrational and rotational wave functions and ψ_n is the nuclear spin wave function.

For an exchange of identical nuclei, the overall wave function ψ must either remain unchanged or change sign. Those which remain unchanged are designated as symmetric wave functions and those which change sign as antisymmetric. In any molecule containing two or more identical nuclei of non-integer spin, exchange of any two of them results in a change of sign of the total wave function, which is therefore antisymmetric. The nuclei are said fermions. On the other hand, when the nuclear spin takes integer values, ψ is symmetric to nuclear exchange and the nuclei are bosons.

The transition moment between two states i and j vanishes, unless the wave functions representing the two states have the same symmetry. Therefore the parity selection rules are[7]:

$$\text{symmetric} \leftrightarrow \text{symmetric}; \qquad \text{antisymmetric} \leftrightarrow \text{antisymmetric};$$
$$\text{symmetric} \leftarrow|\rightarrow \text{antisymmetric}$$

The presence of identical nuclei in a molecule can have important consequences for the statistical weights of the energy levels and the relative intensities of spectroscopic transitions. When the molecule has no symmetry all the ro-vibrational levels have the same weights. However, there are symmetries that cause inequivalent statistical weights, arising from the requirement that the total wave functions must be symmetric or antisymmetric with respect to an exchange of two identical bosons and fermions, respectively.

In general, for molecules in the electronic and vibrational ground states, both the corresponding wave functions are symmetric, and hence $\psi_e \psi_v$ is symmetric. When the nuclear spin is zero, the nuclear spin wave functions are all symmetric, and therefore only symmetric rotational wave functions give the symmetric overall wave function required for Bose particles. In this

[7] The symbols $\leftrightarrow$ and $\leftarrow|\rightarrow$ indicate allowed and forbidden transitions, respectively.

instance, the odd rotational levels are entirely missing. This is the case of molecules such as $S^{16}O_2$ in which a rotation about the symmetry axis exchanges the two atoms of oxygen.

When the nuclear spin is non-zero, the product $\psi_r\psi_n$ can be symmetric or antisymmetric whatever the symmetry of ψ_r. However, in general the number of symmetric and antisymmetric spin functions is not the same, and so it is for the number of rotational levels that can be matched with them to satisfy the required overall symmetry. For example, in molecules belonging to the point group C_{3v} and having three identical atoms of nuclear spin $I = ½$, there are eight different nuclear spin functions corresponding to the eight different orientations of the spins. Of these, four are totally symmetric (A) and the remaining form two doubly degenerate spin functions of symmetry E. As a consequence, for a non-degenerate vibrational state the rotational levels with $K = 3n$ ($\neq 0$) have a statistical weight which is double with respect to levels $K = 3n \pm 1$; that is, the ratio between the statistical weights of the A and E levels is 2:1.

2.8 LINEAR MOLECULES

Linear molecules belong to either the $D_{\infty h}$ or $C_{\infty v}$ point groups, depending on whether they have or not a centre of inversion. A linear molecule with N atoms has $3N - 5$ modes of vibration, and the bending modes are always double degenerate. In the non-rotating molecule these degenerate vibrations take place into perpendicular planes, say the xz and yz planes, respectively. In the rotating molecule, the two perpendicular modes of vibration are coupled by the Coriolis force and a vibrational angular momentum along the inter-nuclear axis arises.

The ro-vibrational energy levels of linear molecules in the absence of perturbation and up to the sixth power of rotational angular momentum are given by

$$\frac{E_{VR}}{hc} = \tilde{\nu}_{\mathrm{v}}^{0} + B_{\mathrm{v}}\left[J(J+1) - l^2\right] - D_{\mathrm{v}}\left[J(J+1) - l^2\right]^2 + H_{\mathrm{v}}\left[J(J+1) - l^2\right]^3 \qquad (2.44)$$

where D_{v} and H_{v} are the quartic and sextic centrifugal distortion constants and l, which is the quantum number for the vibrational angular momentum, can take the values:

$$l = \mathrm{v}, \mathrm{v} - 2, \mathrm{v} - 4, \ldots -\mathrm{v}.$$

The double degeneracy associated with the $\pm l$ levels is removed by the vibration-rotation interaction and, taking into account this *l*-type doubling, the energy levels modify according to

$$\frac{E_{VR}^{\pm}}{hc} = \nu_i^0 + \left[B_{\mathrm{v}} J(J+1) - l^2\right] \pm \frac{q_l}{4}(\mathrm{v}_i + 1) J(J+1) + \\ - D_{\mathrm{v}}\left[J(J+1) - l^2\right]^2 + H_{\mathrm{v}}\left[J(J+1) - l^2\right]^3 \qquad (2.45)$$

where q_l is the *l*-type doubling constant.

The types of the absorption bands observed depend upon the direction, in the rotating molecule, of the oscillating electric dipole moment induced by the electromagnetic radiation. In the fundamental vibrational bands the transition dipole moment lies either along or perpendicular to the inter-nuclear axis. In the former case the band is said to be a parallel band, whereas in the latter case the band is said perpendicular.

Following the discussion of Section 2.2, the active ro-vibrational transitions are those for which the vibrational and rotational selection rules are respectively:

$\Delta l = 0, \pm 1$; $\quad \Sigma^+ \leftarrow|\rightarrow \Sigma^-$; $\quad g \leftarrow|\rightarrow g$; $\quad u \leftarrow|\rightarrow u$;

$\Delta J = 0, \pm 1$; $\quad (J = 0 \leftarrow|\rightarrow J = 0)$; $\quad + \leftrightarrow -$; $\quad s \leftarrow|\rightarrow a$.

According to these selection rules the vibrational bands of a linear molecule can be classified as follows:

(1) Parallel bands, for which $l = 0$ and $\Delta l = 0$ ($\Sigma - \Sigma$ transitions). For these bands only $\Delta J = \pm 1$ can occur, that is they have only *P* ($\Delta J = -1$) and *R* ($\Delta J = +1$) branches.

(2) Perpendicular bands, for which $\Delta l = \pm 1$ ($\Pi - \Sigma$, $\Delta - \Pi$,… transitions). For these bands $\Delta J = 0, \pm 1$ is possible; therefore, in addition to the *P* and *R* branches, a *Q* branch appears which is stronger than either the *P* or *R* branch.

(3) Parallel bands, for which $\Delta l = 0$ but $l \neq 0$ ($\Pi - \Pi$, $\Delta - \Delta$,… transitions). For these bands $\Delta J = 0, \pm 1$ and as for the perpendicular bands they have a *Q* as well as a *P* and an *R* branch. Here, however, the *Q* branch is weak.

In the standard notation, the quantum number l is written as a superscript to the degerate bending mode: for example, the vibrational levels of a linear triatomic molecule are specified as $(\mathrm{v}_1\mathrm{v}_2^l\mathrm{v}_3)$.

2.9 Symmetric Top Molecules

In a symmetric top molecule two of the principal axes of inertia are equal and different from the third which is non-zero. Molecules that are symmetric tops because of their symmetry possess a unique axis of rotational symmetry, which is usually taken as the z-axis, of threefold or higher degeneracy. According to the classification of Figure 2.2, prolate symmetric tops have $A > B$, whereas oblate symmetric tops have $C < B$. As with linear molecules, the fundamental bands of a symmetric top are either parallel or perpendicular bands. Parallel bands arise when the transition moment is parallel to the molecular axis of highest symmetry, whereas when the transition moment is perpendicular to this axis, perpendicular bands occur. For a parallel band the selections rules are

$$\Delta K = 0, \qquad \Delta J = 0, \pm 1, \qquad \text{for } K \neq 0;$$

$$\Delta K = 0, \qquad \Delta J = \pm 1, \qquad \text{for } K = 0;$$

and for a perpendicular band they are

$$\Delta K = \pm 1, \qquad \Delta J = 0, \pm 1.$$

In addition there are also selection rules which are concerned with the symmetry properties of the rotational levels:

$$+ \leftrightarrow -; \qquad + \leftarrow|\rightarrow +; \qquad - \leftarrow|\rightarrow -;$$

where + and – refer to the overall symmetry with respect to the inversion of all the particles about the origin.

For a non-degenerate vibrational state, the ro-vibrational energy levels of a prolate symmetric top up to the forth power of rotational angular momentum are given by

$$\frac{E}{hc} = \tilde{\nu}_{\mathrm{v}}^{0} + \left(A_{\mathrm{v}} - B_{\mathrm{v}}\right)K^2 + B_{\mathrm{v}}J(J+1) + \\ - D_J^{\mathrm{v}}J^2(J+1)^2 - D_{JK}^{\mathrm{v}}J(J+1)K^2 - D_K^{\mathrm{v}}K^4 . \qquad (2.46)$$

As for linear molecules, for degenerate states the influence of the Coriolis force may produce an interaction between the two components of a degenerate pair of vibrations. The result of this interaction is the splitting of the degenerate vibrational levels, whose separation increases with increasing K and is zero when K is zero.

The ro-vibrational transitions in symmetric tops are usually indicated by ${}^{\Delta K}\Delta J_K(J)$, in which ΔK and ΔJ are expressed with a letter (… O, P, Q, R, S,… → …, -2, -1, 0, +1, +2,…), and J, K refer to the ro-vibrational level from which the transition takes place.

2.10 Asymmetric Top Molecules

In an asymmetric rotor the three principal moments of inertia are different and none of them is zero. A measure of the degree of asymmetry of a molecule is given by the Ray's asymmetry parameter, which is defined as

$$\kappa = \frac{2B - A - C}{A - C} \qquad (2.47)$$

where A, B and C are the rotational constants. The asymmetry parameter takes values between –1 and +1, which correspond to the prolate ($B = C$) and oblate symmetric ($A = B$) tops, respectively.

In asymmetric top molecules, the levels $+k$ and $-k$, which are degenerate in symmetric rotors, are no longer degenerate due to the so-called asymmetry splitting. Therefore, the rotational energy levels of asymmetric rotors are identified by the quantum number J and two pseudo-quantum numbers K_a and K_c which take the values:

$K_a = 0, 1, \ldots J$; $\qquad K_c = 0, 1, \ldots J$

provided that $K_a + K_c = J$ or $J + 1$. Following the notation introduced by King, Hainer and Cross [42] the energy levels are conveniently indicated as $J_{K_aK_c}$.

The ro-vibrational selection rules depend upon the orientation of the molecular transition moment with respect to the principal axes of inertia. The vibrational bands of asymmetric top molecules are therefore classified as follows [43].

(i) *A*-type bands, in which the transition moment lies along the *A*-axis. The rotational selection rules are:

$\Delta J = \pm 1;$ $\Delta K_a = 0, \pm 2, \pm 4, \ldots$ $\Delta K_c = \pm 1, \pm 3, \pm 5, \ldots$ for $K_a = 0;$

$\Delta J = 0, \pm 1;$ $\Delta K_a = 0, \pm 2, \pm 4, \ldots$ $\Delta K_c = \pm 1, \pm 3, \pm 5, \ldots$ for $K_a \neq 0.$

These bands are characterize by a central *Q* branch and well defined *P* and *R* branches.

(ii) *B*-type bands, in which the transition moment lies along the *B*-axis. The rotational selection rules are:

$\Delta J = 0, \pm 1;$ $\Delta K_a = \pm 1, \pm 3, \pm 5, \ldots$ $\Delta K_c = \pm 1, \pm 3, \pm 5, \ldots$

These bands have two weak *Q*-branches which are often merged with the *P* and *R* branches [44].

(iii) *C*-type bands, in which the transition moment lies along the *C*-axis. The rotational selection rules are:

$\Delta J = \pm 1;$ $\Delta K_a = \pm 1, \pm 3, \pm 5, \ldots$ $\Delta K_c = 0, \pm 2, \pm 4, \ldots$ for $K_c = 0;$

$\Delta J = 0, \pm 1;$ $\Delta K_a = \pm 1, \pm 3, \pm 5, \ldots$ $\Delta K_c = 0, \pm 2, \pm 4, \ldots$ for $K_c \neq 0.$

These bands have a strong *Q* branch, whereas the *P* and *R* branches are relatively weak.

When the transition moment does not lie along a unique axis, hybrid bands occur. For example, vinyl fluoride, which belongs to the point group C_s, has hybrid *A*/*B* bands in which the transition moment lies in the (*AB*)-plane.

As also pointed out in Section 2.4, the ro-vibrational energy levels of asymmetric rotors can no longer be expressed by closed algebraic equations as can be done for linear or symmetric tops. Therefore a diagonalization of the Hamiltonian matrix is required. A particularly useful asymmetric rotor Hamiltonian has been developed by Watson [40]. This operator in the *A*-reduction and I^r representation, up to the second order perturbation terms, is given by:

$$\hat{H}_r^{(A)} = A^{(A)}\hat{P}_a + B^{(A)}\hat{P}_b + C^{(A)}\hat{P}_c +$$
$$-\Delta_J\hat{J}^4 - \Delta_{JK}\hat{J}^2\hat{J}_a^2 - \Delta_K\hat{J}_a^4 - 2\delta_J\hat{J}^2\left(\hat{J}_b^2 - \hat{J}_c^2\right) - \delta_K\left[\hat{J}_a^2\left(\hat{J}_b^2 - \hat{J}_c^2\right) + \left(\hat{J}_b^2 - \hat{J}_c^2\right)\hat{J}_a^2\right] +$$
$$+\Phi_J\hat{J}^6 + \Phi_{JK}\hat{J}^4\hat{J}_a^2 + \Phi_{KJ}\hat{J}^2\hat{J}_a^4 + \Phi_K\hat{J}_a^6 + 2\varphi_J\hat{J}^4\left(\hat{J}_b^2 - \hat{J}_c^2\right) +$$
$$+\varphi_{JK}\hat{J}^2\left[\hat{J}_a^2\left(\hat{J}_b^2 - \hat{J}_c^2\right) + \left(\hat{J}_b^2 - \hat{J}_c^2\right)\hat{J}_a^2\right] + \varphi_K\left[\hat{J}_a^4\left(\hat{J}_b^2 - \hat{J}_c^2\right) + \left(\hat{J}_b^2 - \hat{J}_c^2\right)\hat{J}_a^4\right] \qquad (2.48)$$

where Δ_J, Δ_{JK}, Δ_K, δ_J, δ_K are the quartic centrifugal distortion constants and Φ_J, Φ_{JK}, Φ_{KJ}, Φ_K, φ_J, φ_{JK}, φ_K are the sextic centrifugal distortion constants.

The ro-vibrationl transitions of asymmetric rotors can be indicated with a notation derived from the symmetric top one: ${}^{\Delta K}\Delta J_K^{\pm}(J)$ where the subscripts '+' and '–' refers to levels for which $K_a + K_c = J$ and $K_a + K_c = J + 1$, respectively. For near prolate asymmetric tops K refers to the value of the pseudo-quantum number K_a, whereas for near oblate asymmetric rotors it refers to K_c.[ii]

[ii] The chapter has been written by consulting Refs. [2, 3, 24, 28, 31 – 44].

3. Molecular Collisions and Spectral Line Shapes

The first parameters governing the interactions between molecules and electromagnetic fields are the internal energy levels and the optical transition moments, which are related to the frequencies and integrated intensities of the spectral transitions, respectively. These spectroscopic data are intrinsic features of molecules regardless of their environment.

In real gases, the optically active molecules, which are also referred to as radiators, interact with the surrounding environment so that they cannot be considered as isolated. Consequently, the intrinsic spectroscopic parameters are no longer sufficient for the modelling of the spectra. Indeed, the collisions with the surrounding particles, also called perturbers, lead to characteristic absorption line shapes, which depend on the physical-chemistry of the intermolecular interactions.

3.1 The Absorption Coefficient

At low radiation intensity, the transmission of monochromatic radiation through a homogeneous gas sample is described by the Beer – Lambert law:

$$I(\nu) = I_0 e^{-\kappa(\nu) n l} \tag{3.1}$$

where $I(\nu)$ and I_0 are the transmitted and unattenuated intensities, respectively; n is the concentration of the gas; l is the optical path length and $\kappa(\nu)$ is the absorption coefficient.

The integrated absorption coefficient, which represents the integrated intensity of the spectral line corresponding to the transition $j \leftarrow i$, is defined as

$$S_{ij} = \int_{-\infty}^{+\infty} \kappa(\nu) d\nu \tag{3.2}$$

and hence the absorption coefficient can be written in the form

$$\kappa(\nu) = S_{ij} f(\nu - \nu_0) \tag{3.3}$$

where $f(\nu - \nu_0)$ is the dimensionless normalized line shape function and ν_0 is the frequency of the line centre.

3.2 LINE INTENSITIES

The integrated absorption coefficient is related to the transition dipole moment of the transition $j \leftarrow i$ through the following equation

$$S_{ij} = \frac{8\pi^3}{3hc} \frac{N}{Q} \tilde{\nu}_{ij}^0 e^{-E_i/K_B T} \left(1 - e^{-hc\tilde{\nu}_{ij}^0/K_B T}\right) \left|\langle i | \hat{\boldsymbol{\mu}} | j \rangle\right|^2 \tag{3.4}$$

where N is the total number of radiating molecules per unit volume per unit pressure, Q is the total partition function, E_i is the lower state energy, $\tilde{\nu}_{ij}^0$ is the frequency (in wavenumbers) of the transition, c is the speed of light and K_B is the Boltzmann's constant.

The commonly employed measure units for the integrated line intensity and the corresponding conversion factors are listed in Table 3.1 [45].

Table 3.1. Commonly used integrated intensity units and conversion factors to $cm^{-2}atm^{-1}$ at 300 K.

Units	Factor for conversion to $cm^{-2}atm^{-1}$ at 300 K
$cm^{-2}atm^{-1}$ at 300 K	1.0
$cm^{-2}atm^{-1}$ at T	$3.3333T \cdot 10^{-3}$
$cm^{-2}atm^{-1}$ at STP ($cm^{-2}amagat^{-1}$)	$9.1053 \cdot 10^{-1}$
cm $mole^{-1}$	$4.0623 \cdot 10^{-5}$
cm $mmole^{-1}$ (dark)	$4.0623 \cdot 10^{-2}$
km $mole^{-1}$	4.0623
cm $molecule^{-1}$	$2.4464 \cdot 10^{-19}$

In an isotropic medium the space fixed *X*, *Y*, *Z* directions are equivalent and therefore the transition moment can be calculated as

$$\left|\left\langle j\left|\hat{\boldsymbol{\mu}}\right|i\right\rangle\right|^2 = \sum_j \sum_i 3\left|\left\langle j\left|\hat{\mu}_F\right|i\right\rangle\right|^2 \tag{3.5}$$

where $\hat{\mu}_F$ is the component of the dipole moment operator relative to one of the space fixed axes. Apart from the nuclear spin degeneracy function, the transition moment integral between the ro-vibrational basis functions may be subdivided into vibration-rotation products. Therefore, the transition moment is conveniently factorized as

$$\left\langle \mathrm{v}' \quad J' \quad r'\left|\hat{\boldsymbol{\mu}}\right|\mathrm{v}'' \quad J'' \quad r''\right\rangle = S_{n'n''}S_{\mathrm{v}'\mathrm{v}''}S_{r'r''} = \beta\left\langle \mathrm{v}'\left|\hat{\boldsymbol{\mu}}\right|\mathrm{v}''\right\rangle \sum_{r',r''}\left\langle J' \quad r'\left|\Phi_{Fg}\right|J'' \quad r''\right\rangle \tag{3.6}$$

where v' and v'' are the quantum numbers of the upper and lower vibrational states, respectively; *r*' and *r*'' represent appropriate rotational quantum numbers other than the total angular momentum quantum number *J*; the nuclear spin degeneracy factor, $\beta = S_{n'n''}$, is usually included as a part of the rotational line strength factor $S_{r'r''}$. In the expression, Φ_{Fg} is the element of the direction cosine matrix, i.e. the direction cosine of the angle between the molecule fixed *g* axis and the space fixed *F* axis.

In the symmetric rotor basis set, $\left|J \quad k \quad M\right\rangle$, the matrix elements of the direction cosines can be separated as follows

$$\begin{aligned}\left\langle J' \quad k' \quad M'\left|\Phi_{Fg}\right|J'' \quad k'' \quad M''\right\rangle = \\ = \left\langle J'\left|\Phi_{Fg}\right|J''\right\rangle\left\langle J' \quad k'\left|\Phi_{Fg}\right|J'' \quad k''\right\rangle\left\langle J' \quad M'\left|\Phi_{Fg}\right|J'' \quad M''\right\rangle;\end{aligned} \tag{3.7}$$

the corresponding matrix elements are summarized in Table 3.2 [3].

In an isotropic medium the summation over *F* of the square elements of the dipole moment may be achieved by multiplying the squared elements of any given *F* (usually *Z*) by three and performing a summation over all possible transitions between the *M* components. However, in anisotropic conditions, such as those caused by the use of linearly polarized light, the contribution coming from the different *M* components must be calculated explicitly.

Table 3.2. Direction cosine matrix elements in the symmetric rotor basis set.

Matrix element	J'		
	$J+1$	J	$J-1$
$\langle J\lvert\Phi_{Fg}\rvert J'\rangle$	$\left[4(J+1)\sqrt{(2J+1)(2J+1)}\right]^{-1}$	$\left[4J(J+1)\right]^{-1}$	$\left[4J\sqrt{(2J-1)(2J+1)}\right]^{-1}$
$\langle J,k\lvert\Phi_{Fz}\rvert J',k\rangle$	$2\sqrt{(J+1)^2-k^2}$	$2k$	$2\sqrt{J^2-k^2}$
$\langle J,k\lvert\Phi_{Fz}\rvert J',k\pm1\rangle$ $\pm i\langle J,k\lvert\Phi_{Fy}\rvert J,k\pm1\rangle$	$\mp\sqrt{(J\pm k+1)(J\pm k+2)}$	$\sqrt{(J\mp k)(J\pm k+1)}$	$\pm\sqrt{(J\mp k)(J\mp k-1)}$
$\langle J,M\lvert\Phi_{Zg}\rvert J',M\rangle$	$2\sqrt{(J+1)^2-M^2}$	$2M$	$2\sqrt{J^2-M^2}$
$\langle J,M\lvert\Phi_{Xg}\rvert J',M\pm1\rangle$ $\pm\langle J,M\lvert\Phi_{Yg}\rvert J,M\pm1\rangle$	$\mp\sqrt{(J\pm M+1)(J\pm M+2)}$	$\sqrt{(J\mp M)(J\pm M+1)}$	$\pm\sqrt{(J\mp M)(J\mp M-1)}$

In the absence of perturbation, the integrated absorption coefficient of a ro-vibrational transition can be expressed as

$$S_{ij} = S_{\mathrm{v}}^{0} R_i \tag{3.8}$$

where R_i is the rotational factor including the square of the transformed direction cosines; S_{v}^{0} is the vibrational band intensity which is related to square of the vibrational transition dipole moment by

$$S_{\mathrm{v}}^{0} = \frac{8\pi^3}{3hc}\tilde{\nu}_0 \frac{N}{Q_{\mathrm{v}}}\langle \mathrm{v}'|\hat{\boldsymbol{\mu}}|\mathrm{v}''\rangle \tag{3.9}$$

where $\tilde{\nu}_0$ is the band centre in wavenumbers and Q_{v} is the vibrational partition function.

3.3 DIPOLE AUTOCORRELATION FUNCTION

For weak optical fields and for non-reactive collisions at local thermodynamic equilibrium, the line shape function of a spectral absorption is given by the Fourier transform

$$f(\nu) = \frac{1}{\pi}\mathcal{R}e\left[\int_0^{+\infty} e^{i\nu t}\Phi(t)dt\right] = \frac{1}{\pi}\mathcal{R}e\left[\int_0^{+\infty} e^{-i\nu t}\Phi(-t)dt\right] \tag{3.10}$$

where $\Phi(t)$ is the dipole autocorrelation function, which is defined by

$$\Phi(t) = \left\langle \boldsymbol{\mu}^*(t'+t) \cdot \boldsymbol{\mu}(t') \right\rangle . \tag{3.11}$$

The dipole autocorrelation function thus describes how the dipole $\boldsymbol{\mu}$ at time t' correlates with itself at a later time $t' + t$. It must be normalized such that $\Phi(0) = 1$, because a function is correlated with itself at zero time.

It follows from equation (3.10) that an infinitely narrow spectral line corresponds to a stationary correlation function, i.e. $\Phi(t)$ does not decay with time. However, there are a number of processes which cause the autocorrelation function to decay, resulting in a broadening of the spectral line: the faster $\Phi(t)$ decays, the broader the line.

Line broadening mechanisms in low pressure gases can be classified as homogeneous or inhomogeneous. Homogeneous processes are associated with the time – energy uncertainty relation: they cause the radiator to remain in a given state for only a finite time; they are called homogeneous because they equally affect all the radiating particles. On the other hand, inhomogeneous broadening processes are associated with some property whose values vary according to a statistical distribution, and therefore the line shape reflects this distribution.

In the infrared region, where spontaneous emission is negligible, the time decay of the dipole autocorrelation function is mainly caused by the translational motion of the radiator and its collisions with perturbers. Therefore, the observed spectral line shape is strictly related with the gas phase dynamics and collisional processes. The line shape functions describing the different decay processes are always obtained within some simplifying assumptions.

The binary and impact approximations underlie the majority of collision theories. The binary approximation assumes that the relaxation is dominated by binary collisions. The impact approximation relies upon the assumption that the average duration of a collision, τ_c, is negligible with respect to the average time, τ, between two successive collisions and with respect to the frequency detuning from line centre, ν_0 :

$$\begin{cases} \tau_c << \tau \\ \tau_c << \dfrac{1}{|\nu - \nu_0|} \end{cases} . \tag{3.12}$$

All the times of interest are therefore assumed much greater than τ_c.

3.4 DOPPLER BROADENING

At very low gas pressure, where the effects of collisions can be disregarded, the main contribution to the spectral broadening comes from the thermal motion of the radiators. Indeed, according to the Doppler principle, in the molecular reference frame the frequency of the incident radiation is shifted by an amount

$$\nu_{radiator} = \nu_{radiation}\left(1 - \frac{v_z}{c}\right) \tag{3.13}$$

where the electromagnetic wave, having frequency $\nu_{radiation}$, propagates in the $+z$ direction and v_z is the z component of the radiator velocity. The frequency of the absorbed radiation is higher than the frequency of resonance if the molecule moves in the same direction of the wave, and lower if it moves in the opposite sense. Therefore, the Doppler effect mirrors the Maxwell – Boltzmann distribution of velocities thus resulting in an inhomogeneous broadening of the line, which is symmetric since the velocities $+v_z$ and $-v_z$ are equally probable.

If the velocity of the radiator does not vary in time, or remains constant during a sufficiently long time [46], the autocorrelation function for the radiator translational motion is

$$\Phi_{ext}(t) = \left\langle e^{-i(\mathbf{k}\cdot\boldsymbol{v})t} \right\rangle = e^{-\left(\frac{\Delta\nu_D t}{2}\right)^2} \tag{3.14}$$

where **k** is the propagation vector of the electromagnetic wave and the average has been performed using the Maxwell – Boltzmann distribution; $\Delta\nu_D$ is related to the resonant frequency ν_{fi} through

$$\Delta\nu_D = \frac{\nu_{fi}\langle v \rangle}{c} \tag{3.15}$$

where

$$\langle v \rangle = \left(\frac{2K_B T}{m}\right)^{1/2} \tag{3.16}$$

is the most probable speed at temperature T for a radiator of mass m.

The Doppler profile is the Fourier transform of $\Phi_{ext}(t)$:

$$f_D(\nu-\nu_0)=\frac{1}{\pi}\mathcal{R}e\left[\int_0^{+\infty}e^{i(\nu-\nu_0)}\Phi_{ext}(t)dt\right]=\frac{1}{\sqrt{\pi}\Delta\nu_D}e^{-\left(\frac{\nu-\nu_0}{\Delta\nu_D}\right)^2} \tag{3.17}$$

where $\Delta\nu_D$ is the (1/e) half width of the resulting Gaussian function. Its relation with the Doppler half width at half maximum (HWHM), γ_D, is

$$\Delta\nu_D=\frac{c\gamma_D}{\sqrt{ln\,2}}; \tag{3.18}$$

the molecular Doppler half width is given by

$$\gamma_D=\frac{\nu_{fi}}{c}\left(\frac{2K_BN_AT\ln 2}{m}\right)^{1/2} \tag{3.19}$$

where ν_{fi} is the resonant frequency, N_A is the Avogadro's number and m is the mass of the absorbing gas. In the infrared region, typical values of γ_D are a few 10^{-3} cm^{-1} at room temperature.

3.5 COLLISIONAL BROADENING: THE LORENTZ PROFILE

At high pressure the spectral line shape is dominated by the broadening due to molecular collisions. This broadening mainly comes from the intermolecular energy exchange which takes place during the collisions between the radiator and the perturber. The energy transfers include both internal and external degrees of freedom and their effect is to shorten the lifetimes of the initial and final optical levels. According to the time dependent perturbation theory, the collisional width of the spectral line corresponding to the $f \leftarrow i$ transition, due only to the population decay of the two levels, is

$$\Gamma_1 \approx \frac{1}{\Delta t_i}+\frac{1}{\Delta t_f}$$

where Δt represents the lifetime of the involved states. To a first approximation each collision can be considered a state-changing collision and hence the lifetimes Δt_i and Δt_f may be approximated by the free time of flight, τ_0, of the radiator; hence the collisional half width at half maximum is $\gamma \approx 1/\tau_0$. This simple description is justified by the efficiency of the rotational energy transfer, since the energy spacing between the rotational levels is generally smaller than the thermal energy, $K_B T$.

However, collisions can destroy the coherence of the system without changing its internal state. These collisions are called dephasing collisions, since their effect is to interrupt the phase of the oscillating dipole.

If all the collisional effects are treated as dephasing processes, the correlation function describing the relaxation due to the collisions between the radiator and the perturber is

$$\Phi_{int}(t) = e^{i\langle\varphi(t)\rangle} \tag{3.20}$$

where $\langle\varphi(t)\rangle$ is the average collisional phase shift of the radiator dipole for the optical transition. Within the framework of the binary impact approximation, $\langle\varphi(t)\rangle$ is a complex quantity whose imaginary part determines the decay rate, γ, of the radiating dipole and the real part its frequency shift, δ:

$$\Phi_{int}(t) = e^{-(\gamma + i\delta)t} . \tag{3.21}$$

The Fourier transform of this correlation function leads to the Lorentz profile:

$$f_L(\nu - \nu_0) = \frac{1}{\pi} \frac{\gamma}{(\nu - \nu_0 - \delta)^2 + \gamma^2} ; \tag{3.22}$$

γ and δ are the collisional HWHM and the collisional line shift, respectively, which depend on the total pressure through

$$\gamma = \gamma^0_{self} P_{radiator} + \sum_i \gamma^0_{r,i} P_i \tag{3.23}$$

$$\delta = \delta^0_{self} P_{radiator} + \sum_i \delta^0_{r,i} P_i \tag{3.24}$$

where γ^0_{self} and δ^0_{self} are the self- broadening and shifting coefficients, respectively; $\gamma^0_{r,i}$ and $\delta^0_{r,i}$ are the foreign- broadening and shifting coefficients between the radiator and the perturber *i*; $P_{radiator}$ and P_i denote the partial pressures of the radiator and the *i*-th perturbing species, respectively.

3.6 THE VOIGT PROFILE

At intermediate gas pressure, both the translational motion and the collisional damping contribute to the shape of the ro-vibrational absorption profiles. The autocorrelation function is given by the product of $\Phi_{ext}(t)$ and $\Phi_{int}(t)$ (equations 3.14 and 3.20, respectively) and therefore the line shape is described by the convolution of the Doppler and Lorentz profiles:

$$f_V(x,y) = \int_{-\infty}^{+\infty} f_D(x') f_L(x-x',y)dx' .$$

The resulting function is the Voigt profile, which can be conveniently expressed as the real part of the complex probability function, $w(x+iy)$:

$$f_V(x-s,y) = \frac{1}{\sqrt{\pi}} \Re e[w(x-s+iy)] = \frac{y}{\pi^{3/2}} \int_{-\infty}^{+\infty} \frac{e^{-t^2}}{(x-s-t)^2+y^2} dt \qquad (3.25)$$

where, for simplicity, the following dimensionless parameters have been defined [47]:

$$x = \frac{\nu-\nu_0}{\Delta\nu_D}; \qquad y = \frac{\gamma}{\Delta\nu_D}; \qquad s = \frac{\delta}{\Delta\nu_D}. \qquad (3.26)$$

Despite the number of effects which lead to departures from the Voigt profile (see for example [48 – 53]), this remains a reference model and a basis for more sophisticated approaches. The Voigt profile is compared with other line shape functions in Figure 3.1.

3.7 COLLISIONAL NARROWING: GALATRY AND NELKIN-GHATAK PROFILES

When the collisions do not affect the internal state of the radiator and the mean free path is smaller than the wavelength, λ, of the radiation [54], there is a contraction of the Doppler broadened contour. This effect, which was first described by Dicke [48], is referred to as collisional narrowing.

A collision which changes the velocity of the radiator from $\boldsymbol{v}$ to $\boldsymbol{v}'$, causes a change $\nu_{fi} v_z' c^{-1} \leftarrow \nu_{fi} v_z c^{-1}$ of the Doppler shift, and therefore it modifies the line profile. In order to maintain the velocity equilibrium distribution, the probability density per unit time, $A(\boldsymbol{v}' \leftarrow \boldsymbol{v})$, of velocity changing collisions must satisfy the principle of detailed balance [19]:

$$A(\boldsymbol{v}' \leftarrow \boldsymbol{v}) f_M(\boldsymbol{v}) = A(\boldsymbol{v}' \rightarrow \boldsymbol{v}) f_M(\boldsymbol{v}')$$

where $f_M(\boldsymbol{v})$ is the Maxwell – Boltzmann velocity distribution. Given the velocity isotropy of the gas, it follows that the velocity component along the direction z of propagation of the electromagnetic wave must, in turn, satisfy the relation

$$A(v_z' \rightarrow v_z) = A(v_z' \leftarrow v_z) \frac{f_M(v_z)}{f_M(v_z')} = A(v_z' \leftarrow v_z) e^{-\frac{m}{2K_B T}\left[(v_z)^2 - (v_z')^2\right]};$$

as a result, collisions inducing a decrease of $|v_z|$ are more probable than the reverse case. Thus, in the corresponding Doppler frequency profile, the frequency transfers induced by collisions are more probable from the wing to the centre, causing a narrowing of the Doppler distribution.
The effect of velocity changing collisions is also to increase the mean time taken to move a distance $\lambda/2\pi$, thus hindering the movement of the oscillators [46]. For this reason the Dicke narrowing is sometimes called motional (or confinement) narrowing.

In the IR region, early observations of Dicke narrowing were found on light molecules with rotational levels separated by more than the thermal energy, $K_B T$ [55]. Its effect is illustrated in Figure 3.1 in which the departures from the Voigt profile are highlighted. The residuals clearly exhibit the typical w-shaped signature.

The effect of velocity changing collisions (VCC) have been tacked analytically in two limiting cases depending on the strength of the collisions themselves. A very comprehensive

treatment has been give by Rautian and Sobel'man [46] who also introduced the statistical correlation between velocity changing- and dephasing-internal state changing collisions.

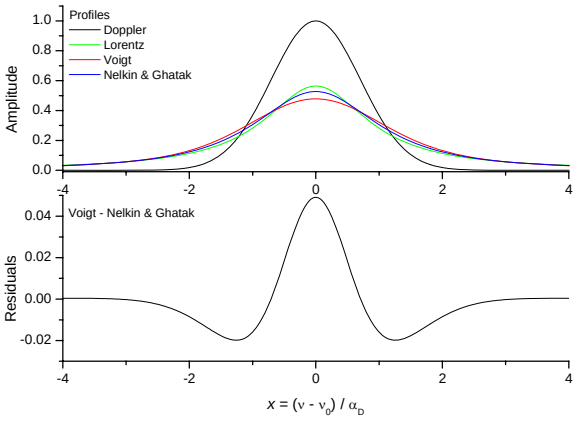

Figure 3.1. Upper panel: Adimensional line shape models ($\alpha_D = y = 1$; $\varsigma = 1$). The Nelkin – Ghatak profile is reported as an example of Dicke narrowed profile. Lower panel: deviations from the Voigt profile when collisional narrowing is acting.

The first model, called *weak collision model*, was developed by Galatry assuming a Brownian movement of the particles [56]. Within the framework of this approach the effects of the single collisions are assumed negligible. As a consequence a large number of collisions is required to completely randomize a given velocity distribution probability. The correlation function taking into account the Doppler effect as well as the Dicke narrowing is

$$\Phi_{ext}^{weak} = e^{-\frac{\Delta\omega_D}{2\beta}\left(\beta t - 1 + e^{-\beta t}\right)} \tag{3.27}$$

where $\beta = \nu_{VC}^{weak}$ is the speed independent effective velocity changing collision rate[8] for this weak collision model. Since VCC and dephasing-, internal state changing-collisions are assumed to be statistically uncorrelated, the autocorrelation function is the product of Φ_{ext}^{weak} and $\Phi_{int}(t)$, whose Fourier transform leads to the Galatry profile, which in dimensionless units is

$$f_G(x-s,y,z) = \frac{1}{\pi}\mathcal{R}e\left\{\int_0^{+\infty} \mathrm{e}^{-t\left[y+\mathrm{i}(x-s)\right]+\left(2z^2\right)^{-1}\left[1-zt-\mathrm{e}^{-zt}\right]}dt\right\} \tag{3.28}$$

where x, y and s are defined in (3.26) and

$$z = \frac{\beta}{\Delta\nu_D}. \tag{3.29}$$

This function can also be expressed in terms of the confluent hyper-geometric function [47].

The second limiting case, denoted *strong collision model*, was first introduced by Nelkin and Ghatak to describe Mössbauer line shapes [57]. Later Rautian and Sobel'man considered, in

[8] It is also called dynamical friction coefficient.

addition, the effect of pressure broadening [46]. This model assumes that the velocity after a single collision is completely uncorrelated to the velocity prior to the collision, i.e. after each collision the velocity memory is lost and the velocity distribution is Maxwellian.

The line shape is derived by solving the kinetic equation for the probability density, $f(\mathbf{r},\boldsymbol{v},t)$, of finding the radiator at position $\mathbf{r}$ with velocity $\boldsymbol{v}$ at time t. The resulting Nelkin – Ghatak profile (sometimes also called Rautian – Sobel'man profile) is given by

$$f_{NG}(x-s,y,\varsigma)=\frac{1}{\sqrt{\pi}}\mathrm{Re}\left[\frac{w(x-s,y+\varsigma)}{1-\sqrt{\pi}\varsigma w(x-s,y+\varsigma)}\right] \tag{3.30}$$

with x, y and s as in equation (3.26) and

$$\varsigma=\frac{\Omega}{\Delta\nu_D} \tag{3.31}$$

where $\Omega=\nu_{VC}^{strong}$ is the frequency of the velocity changing collisions.

It should be noted that both the Galatry and Nelkin – Ghatak profiles have the proper limiting behaviour: the Doppler profile when s, y and z tends to zero; the Voigt profile for z equal to zero. Further, both the models assume that there is no statistical correlation between dephasing-internal state changing collisions and velocity changing collisions.

Formally, the weak collision approximation underlying the Galatry profile is more appropriate for collisions in which the radiator is much heavier than the perturber [47, 58]. On the other hand, the strong collision model seems more suitable when the mass of the radiating species is much lower than the mass of the collisional partner [58]. However, this simple picture of heavy radiators and light perturbers is somewhat excessive for strong collisions [19].

3.8 Speed Dependence and Line Mixing

Another effect which gives rise to deviations from the collisional broadened line shapes is the dependence of the relaxation rates on the radiator speed. Coy made distinction between two types of speed dependences [59]: the first is the dependence of the relaxation rate on the relative speed of the colliding particles. Indeed, the relative translational kinetic energy participates in the energy transfers, implying that both radiator and perturber speeds are involved. By denoting with

$\sigma(v_{rel})$ the collisional cross section averaged over all relative orientations of absorbers and perturbers for a particular relative speed, v_{rel}, and a given Boltzmann population, the relaxation rate for the absorber species in collisions where the partners have this relative speed is $\sigma(v_{rel})v_{rel}$. When averaged over the Boltzmann distribution of relative speeds, this quantity becomes the total relaxation rate for the system.

The second quantity is the dependence of the relaxation rate on the speed of molecules in the absorber population. This quantity can be calculated by averaging the relaxation rate as a function of the relative speed over the distribution $f(v_{rel}, v_a)$, which gives the probability of a relative speed v_{rel} in an absorber – perturber pair with absorber speed v_a [59]. Anyway, the dependence of the collisional relaxation rates on the speed of the absorbing molecule is a consequence of the fact that they generally depend on the relative speed of the colliding molecules [60].

Consequently, the collisional profiles may be thought as inhomogeneously distributed according to radiator speed groups in the range $[v, v + dv]$, each group being weighted by the thermal equilibrium probability $f_M(v)dv = 4\pi v^2 f_M(\boldsymbol{v})dv$. In the frequency domain, the consequences of the speed dependent line widths $\gamma(v)$ and shifts $\delta(v)$ are departures of the line shapes from the Voigt (or Lorentz) profile, which reflect the non-exponential decay behaviour in the time domain [60].

The speed dependent profiles take into account two sources of inhomogeneous broadening: the Doppler shift and the speed distribution of $\gamma(v)$ and $\delta(v)$. The speed dependent effects occur both in the collisional broadening regime and in the Dicke narrowing pressure range. Therefore, subtle effects can arise from the combination of velocity changing collisions and speed dependencies of the collisional cross sections.

Line mixing effects arise when collisions are enough efficient for some lines to be considered no longer collisionally isolated one from the others. A simple illustration of line mixing consists of two vibrational levels (usually, the ground state and an excited vibrational one) coupled by rotationally inelastic collisions, as schematically shown in Figure 3.2.

The two vibrational transitions undergoing collisional interference $f \leftarrow i$ and $f' \leftarrow i'$ have resonant frequencies $\nu_{f \leftarrow i}$ and $\nu_{f' \leftarrow i'}$, respectively. The coupling occurs because each transition can take place via two possible paths: one path is the optical transition, whereas the second path involves collision induced population transfers. When subjected to a radiation field, a molecule in internal state i can be excited to level f on absorption of a photon with frequency $\nu_{f \leftarrow i}$. Alternatively, the molecule can be transferred to state i' by collisions. From this level it can be

excited to level f' by a photon of frequency $\nu_{f'\leftarrow i'}$ and finally relax collisionally to state f (the reverse path $i' \xrightarrow{collisions} i$; $i \xrightarrow{\nu_{f\leftarrow i}} f$; $f \xrightarrow{collisions} f'$ is possible, as well). This path from i to f via i' and f' shows that a molecule initially in state i can contribute to the $f' \leftarrow i'$ absorption line, through population transfer induced by the collision interaction of radiator with perturbers. Hence, in line mixing effects, inelastic collisions induce a coupling of ro-vibrational levels (i, i') and (f, f') causing the optical transitions to be mixed, since population is exchanged between them.

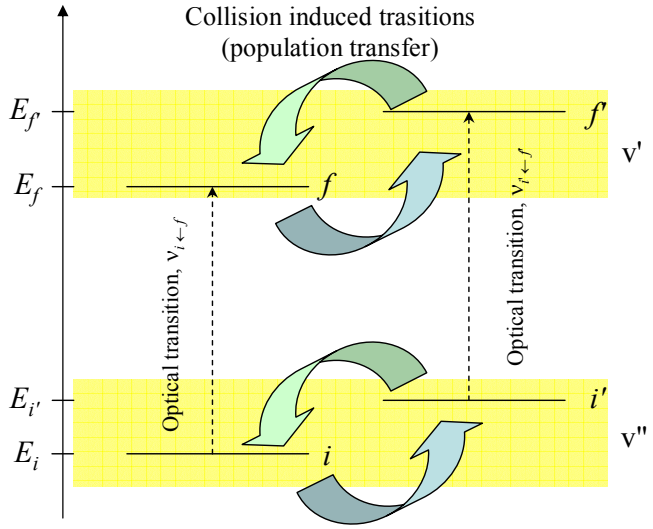

Figure 3.2.Schematic representation of collisional line mixing.

Three necessary conditions are required for the line mixing process to exist: (i) the $i \leftrightarrow i'$ and $f \leftrightarrow f'$ transitions must be allowed; (ii) the lines have to be closely spaced, $\left|\nu_{f'\leftarrow i'} - \nu_{f\leftarrow i}\right| <\approx 2\gamma$ and the radiator-perturber interactions have to be efficient in inducing the $i \leftrightarrow i'$ and $f \leftrightarrow f'$ transitions; (iii) population transfers have to satisfy the detailed balance relation.

In the spectra, line mixing effects lead to transfers from regions where absorptions are weak to those of strong absorption, and hence they reduce the absorption in the wings and enhance that in the centre of spectral lines.

3.9 SEMICLASSICAL THEORY OF PRESSURE BROADENING

The theoretical treatment of pressure broadening must express the macroscopic effect of a thermal bath composed of perturbers on the spectral lines in terms of the microscopic collision parameters. Over the years the problem has been extensively dealt by various authors: a quantum theory of pressure broadening has been formulated independently by Baranger [61] and by Kolb and Griem [62]. A general impact theory has been given by Fano [63] and then extended by Ben-Reuven [64].

The most applied approach to the pressure broadening of ro-vibrational spectral lines has been first proposed by Anderson in 1949 [65] and then generalized by Tsao and Curnutte [66]. The resulting formalism is generally known as ATC theory or ATC approximation. Basically, it is a

time-dependent perturbative treatment of the deviations from the radiator's unperturbed Hamiltonian caused by collisions.

Within the impact approximation, the collisional line shape is described by a Lorentzian function whose line width and line shift are linear with respect to the density N of the gas:

$$\Gamma = N\bar{v}\sigma_{\Gamma}$$
$$\Delta = N\bar{v}\sigma_{\Delta}$$

where $\bar{v}$ is the average relative velocity in the collisions and σ_{Γ}, σ_{Δ} are effective broadening and shifting cross sections, respectively.

The effect of a collision is described by the scattering matrix $\hat{\mathbf{S}}$:

$$\hat{\mathbf{S}} = \vartheta \exp\left[-\frac{i}{\hbar}\int_{-\infty}^{+\infty} e^{i\hat{H}_0 t/\hbar}\hat{V}(t)e^{-i\hat{H}_0 t/\hbar}dt\right] \tag{3.32}$$

where ϑ is the time ordering operator[9], $\hat{H}_0$ is the unperturbed Hamiltonian of internal degrees of colliding molecules, and $\hat{V}(t)$ represents the time dependent collisional interaction.

The radiating molecule, which absorbs a photon, gives rise to the optical transition $u \leftarrow l$ between the lower state l and the upper state u; collisions take action on both these states inducing transitions $u \rightarrow u'$ and $l \rightarrow l'$. On the other side the collisions also change the internal state p of the perturber into p'. On the whole two different kinds of transitions are involved: the optical transition $u \leftarrow l$ and the collision induced transitions $u \rightarrow u'$, $l \rightarrow l'$ and $p \rightarrow p'$.

The relaxation efficiency of a collision, P, is described in terms of the scattering matrix by the following function

$$P(p,k) = 1 - \sum_{p'}\sum_{k'}\langle l \quad p \quad k|\hat{\mathbf{S}}|l \quad p' \quad k'\rangle\langle u \quad p' \quad k'|\hat{\mathbf{S}}^{\dagger}|u \quad p \quad k\rangle \tag{3.33}$$

where k and k' denote the translational states.

A full quantum mechanical calculation of the scattering matrix can be made only for atoms or very simple molecular systems, such as linear molecules colliding with atoms. For more

[9] The time ordering operator makes an operator to act in the order prescribed by the time of their argument, with time increasing from right to left.

complicated molecules simplifying approximations are used. The semiclassical approximation restricts the quantum treatment to the internal degrees of freedom of the colliding species and assumes that the translational motion follows classical mechanics, so that the translational state is described by the impact parameter b and the relative velocity v.

Within this framework, the calculation involves an average on b, on v and over the internal states of the perturber. The line width and shift are then connected to the real and imaginary parts of P:

$$\Gamma + i\Delta = N\sum_p \rho_p \int_0^{+\infty} v\ f_M(v)dv \int_0^{+\infty} 2\pi P(b,v,p)db \tag{3.34}$$

where ρ_p is the population of the state p of the perturber, and $P = P(b,v,p)$ is now the semiclassical relaxation efficiency function.

Even in the frame of the semiclassical approximation an exact calculation of the scattering matrix is not easily realized and further approximations are introduced by the ATC treatment: straight line trajectories and, for weak collisions occurring at large impact parameter[10], lowest order (second order) perturbative expansion in Eq. (3.32). This yields a relaxation efficiency function $P^{weak}(b,v,p)$ which, for an intermolecular potential dominated by dipole – dipole interaction, is given by

$$P^{\text{weak}}(b,v,p) = \frac{4}{9v^2\hbar^2 b^4}\sum_{p'}\left(\sum_{l'}\left|\langle l|\boldsymbol{\mu}_l|l'\rangle\right|^2 f_{\text{dd}}(x_l + x_p) + \sum_{u'}\left|\langle u|\boldsymbol{\mu}_u|u'\rangle\right|^2 f_{\text{dd}}(x_u + x_p)\right)\times$$
$$\times\left|\langle p|\boldsymbol{\mu}_p|p'\rangle\right|^2 \tag{3.35}$$

in which only rotational transitions are included in the summations over p', l' and u' because the vibrational contribution is generally negligible; $\boldsymbol{\mu}_p$ is the dipole moment of the perturber, while $\boldsymbol{\mu}_l$ and $\boldsymbol{\mu}_u$ are the dipole moments in the lower and uppers states of the radiating molecule, respectively. They are slightly different because of the different vibrational state. In Eq. (3.35) x_l, x_u and x_p are proportional to the energy changes induced by collisions:

$$x_l = \frac{b}{v\hbar}(E_{l'} - E_l), \qquad x_u = \frac{b}{v\hbar}(E_{u'} - E_u), \qquad x_p = \frac{b}{v\hbar}(E_{p'} - E_p); \tag{3.36}$$

[10] The intermolecular potential $V(t)$ is a small perturbation of H_0.

$f_{\mathrm{dd}}(x)$, which is plotted in Figure 3.3, is the dipole – dipole resonance function defined by Tsao and Curnutte [66]: it is an even function of x. When the collision is resonant ($x_l + x_p = 0$ or $x_u + x_p = 0$) $f_{\mathrm{dd}} = 1$, whereas it goes to zero when the overall change of rotational energy is large.

The efficiency function P^{weak} is asymptotically exact for $b \to \infty$. From Figure 3.3 it can be deduced that the broadening and shifting effect is strongly reduced when x is large, that is when the energy transferred by a collision from translational to internal degrees of freedom is large in comparison to the duration of the collision.

For strong collisions, occurring at small impact parameters, every coherence is lost and the outgoing rotational state of the absorber is assumed to be completely uncorrelated to the ingoing one. Consequently, $\langle i \quad p \quad k|\hat{\mathbf{S}}|i \quad p' \quad k'\rangle$ and $\langle f \quad p' \quad k'|\hat{\mathbf{S}}^{\dagger}|f \quad p \quad k\rangle$ in Eq. (3.33) are small and with a completely random phase. This yields

$$P^{strong}(b, v, p) = 1, \tag{3.37}$$

hence, strong collisions give full contribution to the line width and no contribution to the line shift.

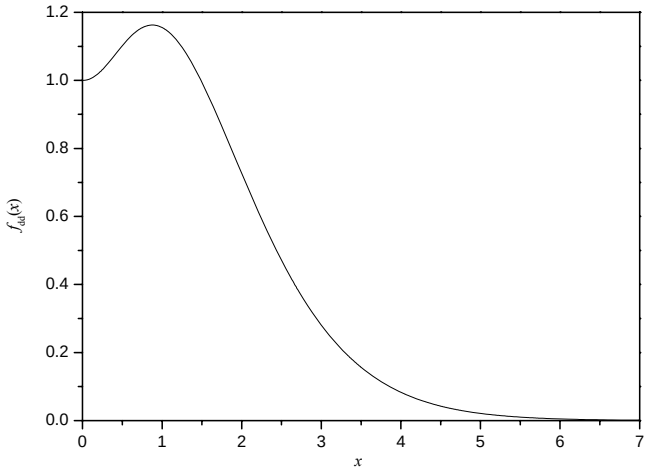

Figure 3.3. Dependence on x of the dipole-dipole resonance function $f_{dd}(x)$.

For intermediate b values, different approximations can be found in the literature. Some authors [65, 66] resort to a cutoff impact parameter $b_0(v, p)$: P^{weak} is extended to all values larger than b_0, while P^{strong} is used when $b < b_0$. The cutoff impact parameter is defined by imposing a unitary bound to the perturbative approach used for weak collisions. The bound can be imposed either on the real part, $\mathcal{R}e\left[P^{\mathrm{weak}}(b, v, p)\right] = 1$ or to its absolute value [67], $\left|P^{\mathrm{weak}}(b, v, p)\right| = 1$.

Another interpolation is obtained by omitting the time ordering operator, $\mathcal{T}$, in Eq. (3.32) [68, 69]. This yields a smooth relaxation efficiency function,

$$P(b, v, p) = 1 - e^{-P^{\mathrm{weak}}(b, v, p)} \tag{3.38}$$

which have the desired behaviour for both strong and weak limits. The choice of one or another interpolation method can change the calculated broadening and shifting parameters by a small extent, around 10 – 20 %.

The ATC approximation leads to reasonable results for gases whose molecules mainly interact through strong dipolar interaction. For all the other cases the application of this formalism is questionable, due to the major role played by the impact parameter cutoff in the electronic cloud overlap region for the two colliding partners.

3.10 Coherent Transients and Rapid Passage Signals

Fast passage effects are defined as the coherent spontaneous radiation of gas molecules through excitation by radiation with fast frequency sweep over the absorption line [70]. The first evidences of the rapid passage effects were observed in nuclear magnetic spectroscopy as wiggles [71].

Since the advent of the laser in 1960s, there has been considerable interest in optical analogues of the many transient phenomena observed in pulsed nuclear magnetic resonance experiments on spin systems. In the optical regions, these phenomena are referred to as coherent transients and the interest in them is twofold [20]. First, they exhibit the dynamics involved in the interaction of radiation and matter; second, they can be used as probe to study collisional decay processes. By now, every effect seen in magnetic resonance has been observed in the optical region, along with several new phenomena which have no NMR analogues [72, 73].

In the period from 1970 to 1980, one of the main method developed to rapidly turn molecules into resonance with the radiation field was laser Stark spectroscopy. In Stark switching experiments, which allow the use of stable continuous-wave lasers, a differential electric field is used to tune the M_J ($\equiv M$) components of a vibration-rotation transition on a particular laser emission line [3].

Later, the use of high power tunable lasers gave the opportunity of producing coherent transient phenomena in a variety of other methods [74]. In particular, it has been shown that linear optical techniques such as frequency chirping can produce laser pulses with a moderately linear frequency sweep [74]. When the sweeping time of the laser frequency across an optical resonance is shorter that the optical depopulation time and the dephasing time of the resonance, the transient process is a coherent phenomenon [75].

Moving from the density matrix formalism [20], the method of treating rapid passage and coherent transient problems is based on the Bloch vector approach used in magnetic spectroscopy: a detailed analysis of the rapid passage process in NMR and ESR magnetic resonances has been given by Ernst [76] and Stoner et al. [77], respectively. A similar treatment of the fast passage signals observed in gas phase microwave spectroscopy has been carried out by McGurk at al. [78]. When the Bloch vector approach is applied to electric dipole transitions, it is usually called the optical Bloch, or Maxwell – Bloch, approach [20, 73, 79].

The coupled Maxwell – Bloch equations are derived by treating each transition as a two level system with resonance frequency ω_0. In these equation the electric field may be represented by a plane polarized wave travelling along the *z* axis

$$E(t) = 2E^0 \cos(\omega t - kz) \tag{3.39}$$

where *k* represents the wavenumber. The field induces a polarization of the sets of molecular two level systems in which the transitions take place. Assuming that the population of the upper level decays to the lower level at a rate γ_1 and that the induced dipole dephases from the driving field at a rate γ_2, the time evolution of the polarization, $P(t)$, and the population inversion, $w(t)$, for a molecular velocity component v_z is given by the set of differential equations:

$$\begin{aligned}
\frac{dP(t,v_z)}{dt} &= -[i\Delta(t) + \gamma_2]P(t,v_z) - \frac{iN\mu_{12}^2}{\hbar}E(t)w(t,v_z) \\
\frac{dw(t,w_z)}{dt} &= -\frac{2i}{N\hbar}\left[E(t)P(t,v_z)^* - E(t)^* P(t,v_z)\right] - \gamma_1\left[w(t,w_z) - w_{eq}\right] \\
\frac{dE(t)}{dz} &= \frac{ik}{2\varepsilon_0}\int P(t,v_z)dv_z
\end{aligned} \tag{3.40}$$

where $\Delta(t)$ is the frequency detuning, *N* is the number density of the two level system, γ_1 is called the population decay rate, γ_2 is called the polarization decay rate, μ_{12} is the transition dipole moment, w_{eq} is the equilibrium population difference and ε_0 is the permittivity of the free space.

According to the Bloch vector picture, the evolution of the sample polarization can be described by the vector $\mathbf{M} = [u(t),\ v(t),\ w(t)]$. The components $u(t)$ and $v(t)$ are respectively

related to real and imaginary parts of the complex refractive index of the gas: $u(t)$ is the dispersive part and $v(t)$ is the absorptive part; $w(t)$ represents the population difference between the upper and lower levels of the transition [80, 81].[iii]

[iii] The chapter has been written by consulting Refs. [3, 19, 20, 45 – 48, 54 – 63, 65 – 70, 72 – 81].

4. Ab initio Calculations in Infrared Spectroscopy

Ab initio calculations are computational methods based on Quantum Mechanics. The term "ab initio" means "from the beginning" and it is used to indicate that these methods use no experimental data other than the fundamental physical constants.

Ab initio quantum mechanical calculations have long promised to become a major tool for the study of chemical and physical properties of molecules, such as structures, dynamics, reaction mechanisms and spectroscopic quantities as well. The fundamental theory behind them dates back to the earliest days of Quantum Mechanics. However, quantitative and reliable applications have become possible in the last few decades, thanks to the huge progresses made by computer hardware and to the development of efficient programming techniques.

Nowadays the level of quantum mechanical calculations can be so refined that molecular spectroscopic parameters can be calculated with an accuracy of few wavenumbers.

4.1 Potential Energy Surface

In the framework of the Born – Oppenheimer approximation the electronic energy, at a given set of nuclear positions, represents the potential energy. The potential energy surface (PES) governs the displacements of the atoms, and hence the molecular vibrational motions. The knowledge of the potential energy surface is also important for the determination of the equilibrium structure and for a better understanding of the reaction kinetics, in particular the intramolecular vibration redistribution. The equilibrium structure of a molecule corresponds to the minimum of its potential energy surface and the changes in its geometry can be considered as movements on the PES.

For polyatomic molecules, the complete determination of the potential energy surface, from the equilibrium geometry to the dissociation limit, is a formidable task. Fortunately, for most spectroscopic applications, it is sufficient to know the PES around its minimum. This allow the expansion of the potential energy in a Taylor series as a function of the nuclear dimensionless nuclear coordinates around the equilibrium structure as done in Chapter 2, namely:

$$V(\mathbf{Q}) = \frac{1}{2}\sum_{r}\omega_r Q_r^2 + \frac{1}{6}\sum_{r,s,t}\phi_{rst}Q_r Q_s Q_t + \frac{1}{24}\sum_{r,s,t,u}\phi_{rstu}Q_r Q_s Q_t Q_u + \ldots \qquad (4.1)$$

The coefficients of this expansions are called the force field. Force fields are usually classified as harmonic and anharmonic: the harmonic force field involves the quadratic terms in the expansion, which are also called the second order (or quadratic) force constants; the anharmonic force field includes also the remaining terms, which represent high order corrections to the potential energy.

4.2 ELECTRONIC STRUCTURE CALCULATIONS

The PES is created by determining the electronic energy of a molecule while varying the positions of its nuclei. The electronic structure calculations, which are therefore required, involve the solution of the non relativistic, time-independent Schrödinger equation. For a molecule consisting of *N* nuclei and *n* electrons the Hamiltonian, in atomic units, obtained after applying the Born – Oppenheimer approximation is

$$\hat{H} = -\frac{1}{2}\sum_{i=1}^{n}\nabla_i^2 - \sum_{i=1}^{n}\sum_{\alpha=1}^{N}\frac{Z_\alpha}{r_{i\alpha}} + \frac{1}{2}\sum_{i=1}^{n}\sum_{j>i}^{n}\frac{1}{r_{ij}} + V(\mathbf{Q}) \qquad (4.2)$$

where the indexes *i* and *j* refer to electrons and α refers to nuclei. In molecular structure calculations it is conventional to use an electronic Hamiltonian, $\hat{H}_{el}$, which does not include the internuclear repulsion energy. The latter energy is added to the electronic energy, which is solution of $\hat{H}_{el}\psi_{el} = E_{el}\psi_{el}$, as a classical term at the end of the calculation.

The most convenient way to write the total electronic wavefunction ψ_{el} is by means of a Slater determinant[11], which for a system of *n* electrons in *n* spin-orbitals is given by:

[11] In this way the electronic wavefunction obeys the Pauli principle.

$$\psi_{el} = \begin{vmatrix} \chi_1(1) & \chi_2(1) & \ldots & \chi_n(1) \\ \chi_1(2) & \chi_2(2) & \ldots & \chi_n(2) \\ \vdots & \vdots & \vdots & \vdots \\ \chi_1(n) & \chi_2(n) & \ldots & \chi_n(n) \end{vmatrix} \equiv \left| \chi_1 \quad \chi_2 \quad \ldots \quad \chi_n \right| \tag{4.3}$$

where $\chi_i(e)$ denotes the spin-orbital χ_i occupied by electron *e*. A spin orbital is the product of a one-electron space orbital and a one-electron spin function, namely $\chi_i(e) = \psi_i(e)\sigma(e)$. The spatial part ψ_i describes the distribution of electron density in space, whereas the spin part σ defines the electron spin.

In the majority of quantum chemical calculations, the LCAO approach is used, where each molecular orbital is expressed as a Linear Combination of single electron Atomic Orbitals,

$$\psi_i = \sum_{m=1}^{k} c_{mi}\phi_m \tag{4.4}$$

where c_{mi} is a coefficient and the ϕ_m's are commonly called basis functions and often correspond to the atomic orbitals. The smallest number of basis functions for a molecular system is that which can accommodate all the electrons of the molecule.

According to the variational principle, the general problem to solve in electronic structure calculations is to seek those spin-orbitals which make the total energy $\langle \psi_{el} | \hat{H}_{el} | \psi_{el} \rangle$ a minimum. Therefore, for a given basis set and a given functional form of the wavefunction, the best set of coefficients is obtained when the energy is a minimum, as illustrated in Section 1.2.

4.3 THE HARTREE – FOCK SELF CONSISTENT FIELD

In the Hartree – Fock method the molecular electronic wavefunction is written as a Slater determinant of spin orbitals, Eq. (4.3), and the electron – electron repulsion is treated in an average way. Each electron is considered to move in the field of the nuclei and the average field of the remaining *n* – 1 electrons. The Hamiltonian operator, for one electron, e.g. 1, in the spin orbital χ_i contains three terms, corresponding to different contributions to the energy:

$$\hat{f}_i(1) = \hat{H}_{(1)}^{core} + \sum_{j=1}^{n}\left[\hat{J}_j(1) - \hat{K}_j(1)\right] \tag{4.5}$$

with

$$\hat{H}_{(1)}^{core} = -\frac{1}{2}\nabla_i^2 - \sum_{\alpha=1}^{N}\frac{Z_\alpha}{r_{1\alpha}} \tag{4.6}$$

$$\hat{J}_j(1) = \int \chi_j(2)\frac{1}{r_{12}}\chi_j(2)d\tau_2 \tag{4.7}$$

$$\hat{K}_j(1)\chi_i(1) = \left[\int \chi_j(2)\frac{1}{r_{12}}\chi_i(2)d\tau_2\right]\chi_j(1). \tag{4.8}$$

The operator $\hat{H}_{(1)}^{core}$ is called the core Hamiltonian and corresponds to the motion of a single electron moving in the field of the bare nuclei. The operators $\hat{J}_j$ and $\hat{K}_j$ are the Coulomb and exchange operators, respectively. The Coulomb operator takes into account in an average way the electrostatic repulsion between electrons; the exchange operator represents the contribution arising from the effects of spin correlations.

The Fock operator, $\hat{f}_i$, is an effective one electron Hamiltonian for an electron in a poly-electronic system. Each spin orbital must be obtained by solving the Hartree – Fock equation with the corresponding Fock operator,

$$\hat{f}_i\chi_i(1) = \varepsilon_i\chi_i(1). \tag{4.9}$$

However, since $\hat{f}_i$ depends on the spin-orbitals of all the other $n - 1$ electrons, an iterative solution strategy is used. First, a set of trial solutions χ_i' to the Hartree – Fock is defined. The Hartree – Fock equations are solved giving a second set of solutions χ_i'' which are used in the next iteration. The procedure thus gradually refines the individual electronic solutions, that correspond to lower and lower total energies, until the point is reached at which the results for all the electrons are unchanged. At this point the solutions are self-consistent.

Substituting the LCAO approximation (4.4) for the molecular orbitals into the Hartree – Fock equation (4.9), yields

$$\hat{f}_i \sum_{m=1}^{k} c_{mi} \phi'_m(1) = \varepsilon_i \sum_{m=1}^{k} c_{mi} \phi'_m(1), \tag{4.10}$$

where ϕ' is used to denote the spin orbitals corresponding to the basis functions. The Hartree – Fock equations can be transformed into the following matrix form, which is known as Roothaan equations:

$$\mathbf{FC} = \mathbf{SC}\boldsymbol{\varepsilon} \tag{4.11}$$

where **C** is the $k \times k$ matrix of the coefficients c_{mi}; $\boldsymbol{\varepsilon}$ is the $k \times k$ matrix of the orbital energies ε_i; **F** and **S** are called Fock matrix and overlap matrix, whose elements are respectively:

$$F_{lm} = \left\langle \phi'_l(1) \middle| \hat{f}_i \middle| \phi'_m(1) \right\rangle \qquad S_{lm} = \left\langle \phi'_l(1) \middle| \phi'_m(1) \right\rangle .$$

The Roothaan equations have a non-trivial solution only if the following secular equation vanishes,

$$\det|\mathbf{F} - \boldsymbol{\varepsilon}\mathbf{S}| = 0 ; \tag{4.12}$$

this cannot be solved directly because the Fock matrix depends on the wave equations, through the Coulomb and exchange integrals. Therefore, as before a self consistent field approach must be used: a new set of coefficients is obtained at each iteration and the process continues until convergence is reached, as schematically shown in Figure 4.1.

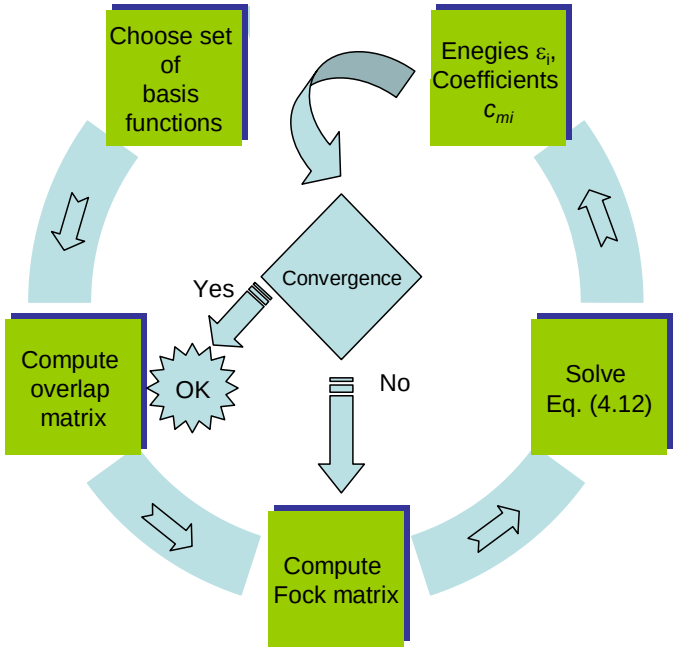

Figure 4.1. Schematic diagram of the Hartree – Fock Self Consistent procedure.

4.4 BASIS SETS

The use of an adequate basis set is an essential requirement for the success of the calculation. The basis sets most commonly used in quantum mechanical calculations are composed of atomic wavefunctions. The use of Slater-type atomic orbitals is computationally too expensive and therefore it is common practice to replace the Slater orbitals by functions based upon Gaussians, which gives the so-called Gaussian-type orbital (GTO).

A major advantage of Gaussian functions is that the product of two Gaussians can be expressed as a single Gaussian, and therefore Gaussian integral evaluation takes much less CPU time than Slater integral evaluation. A Cartesian Gaussian centred on a given atom is defined as

$$g^{ijk\alpha} = Nx^i y^j z^k e^{-\alpha r_\alpha^2} \tag{4.13}$$

where N is a normalization constant, i, j, k, are non-negative integers and α is a positive orbital exponent, which determines the radial extent of the function. The order of the Gaussian-type functions is determined by the powers of the Cartesian variables: a zeroth order function has $i + j + k = 0$ and it is called an *s*-type Gaussian; a first order function, which leads to the *p*-type Gaussians, has $i + j + k = 1$; when $i + j + k = 2$ one obtains the *d*-type Gaussians, which are second order functions. In the latter case five linear combinations can be formed, which have the same angular behaviour as the atomic *d* orbitals.

Since a single Gaussian function does not have the desired cusp at the nucleus, it is current practice to overcome this problem by representing each orbital as a linear combination of Gaussian functions of the form

$$\phi_i = \sum_{u=1}^{L} d_{ui} g_u^\alpha \tag{4.14}$$

where d_{ui} are the expansion coefficients of the g_u^α, which are primitive Gaussian functions centred on the same atom and having the same i, j, k as one another, but different orbital exponent α. When the expansion parameters (coefficients and exponents) are held fixed during the calculation, ϕ_i is called a contracted Gaussian-type function (CGTF).

The simplest type of basis set is a minimal basis set, in which one CGTF is used to represent each of the occupied orbitals. The minimal basis set, which is referred to as single-zeta[12] (SZ) basis set, is usually inadequate. A significant improvement is made by adopting a double-zeta basis set (DZ), which doubles the size of the basis set and therefore each basis function in the minimal basis set is replaced by two CGTF's. In triple-zeta (TZ) and quadruple-zeta (QZ) basis sets three or four CGTF's are respectively used to represent each of the orbitals.

A split-valence basis set (SV) is a compromise between the inadequacy of a minimal basis set and the computational demanding TZ and QZ basis sets. In a SV basis set the orbitals of the inner shells are represented by a single CGTF, whereas the valence orbitals are modelled using more CGTFs. For example, the 6-31G basis set is single-ζ for the core orbitals and double-ζ for the valence orbitals.

Since the charge distribution of an atom in a molecule is usually perturbed from that of the isolated atom, polarisation functions are introduced into the basis set. The polarisation functions have the angular quantum number higher than the maximum one of the occupied orbitals in the free atom: they correspond to *p* orbitals for hydrogen and *d* orbitals for the first and second row elements. The use of polarisation basis functions on heavy atoms is indicated by an asterics, e.g. 6-31G*. Two asterics (e.g. 6-31G**) indicate the use of polarisation functions also on hydrogen.

Several methods exist to form contracted Gaussian basis sets. One of these starts from Slater-type orbitals and the coefficients in the linear combination of Gaussian functions and their exponents are chosen to give the best fit to the STO's. Another method contracts Gaussian-type functions obtained from a SCF calculation. In the correlation-consistent basis sets developed by Dunning [84], the split valence basis sets are constructed by minimizing the energy of the atoms at the Hartree-Fock level with respect to the contraction coefficients and exponents. These basis sets, which are designated as cc-pV*N*Z (with *N* = D, T, Q,…standing for double, triple, quadruple,…) extract the maximum electron correlation energy for each atom. As *N* increases, the number of polarisation functions also increases. For example, the cc-pVTZ basis set is triple-zeta in the valence space and has two sets of *d* functions and a set of *f* functions. The cc-pVTZ basis set is described by a [4*s*3*p*2*d*1*f*/3*s*2*p*1*d*] contraction of a (10*s*5*p*2*d*1*f*/5*s*2*p*1*d*) primitive set for C, F/H atoms, whereas the cc-pVQZ basis set corresponds to a [5*s*4*p*3*d*2*f*1*g*/4*s*3*p*2*d*1*f*] contraction of a (12*s*6*p*3*d*2*f*1*g*/6*s*3*p*2*d*1*f*) primitive set.

[12] The term zeta reflects that each basis function mimics a single Slater type orbital (STO) which is defined by its exponent usually denoted by ζ.

4.5 COUPLED CLUSTER THEORY

The result of a Hartree – Fock calculation is a set of k molecular orbitals, where k is the number of basis functions employed. The n electrons are fed into these orbitals according to the Aufbau principle. The remaining orbitals, which do not contain any electron, are known as virtual orbitals. Alternative electronic configurations can be generated by exciting electrons to these orbitals. The excited configurations are used in more advanced calculations.

The accuracy of an electronic calculation is affected by four sources of error, which are: (i) incomplete treatment of electron correlation[13]; (ii) incompleteness of the basis set; (iii) relativistic effects; (iv) breakdown of the Born – Oppenheimer approximation. The last effect is usually negligible for molecules in the ground electronic state and, usually, relativistic effects arise only in heavy atoms. Therefore, in calculations on molecules without heavy atoms (i) and (ii) are the main sources of error.

Multiconfigurational methods are used to address the problem of electron correlation and also to permit orbital readjustments to occur. These methods basically rely on exciting electrons to the virtual molecular orbitals and express the wavefunction as a linear combination of determinants rather than a single one. Configurations produced by moving one electron from an occupied to a virtual orbital are singly excited relative to the Hartree – Fock configuration and are called singles; those where two electrons are excited are called doubles.

Coupled-cluster theory is a multiconfigurational approach which describes the wavefunction as [85]

$$\psi_{CC} = e^{\hat{T}} \psi_{el} \tag{4.15}$$

where ψ_{CC} is the exact non-relativistic ground state molecular electronic wavefunction, and the operator $e^{\hat{T}}$ is defined by the Taylor-series expansion:

$$e^{\hat{T}} = \sum_{m=0}^{+\infty} \frac{\hat{T}^m}{m!} = 1 + \hat{T} + \frac{\hat{T}^2}{2!} + \frac{\hat{T}^3}{3!} + \ldots ; \tag{4.16}$$

the cluster operator $\hat{T}$ is defined by:

[13] The Hartree – Fock method indeed ignores instantaneous electron – electron repulsion, which is know as electron correlation.

$$\hat{T} = \hat{T}_1 + \hat{T}_2 + ... + \hat{T}_n \tag{4.17}$$

where n is the number of electrons in the molecule and the operator $\hat{T}_i$ generates all the configurations with i excited electrons. The effect of $e^{\hat{T}}$ is to express ψ_{CC} as a linear combination of Slater determinants which comprise ψ_{el} and all possible excitations of electrons from occupied to virtual spin-orbitals.

The most important contribution to the coupled cluster operator is made by $\hat{T}_2$, but since the inclusion of $\hat{T}_1$ is only slightly computationally expensive, the expansion (4.17) is generally truncated after the second term. The coupled cluster singles and doubles (CCSD) method is the typical coupled cluster computation.

The one- and two-electron excitation operators are defined, respectively, as

$$\hat{T}_1\psi_{el} = \sum_{a=n+1}^{+\infty}\sum_{i=1}^{n} t_i^a \psi_i^a \qquad \hat{T}_2\psi_{el} = \sum_{b=a+1}^{+\infty}\sum_{a=n+1}^{+\infty}\sum_{j=i+1}^{n}\sum_{i=1}^{n-1} t_{ij}^{ab} \psi_{ij}^{ab} \tag{4.18}$$

where ψ_i^a is a singly excited Slater determinant with the occupied spin-orbital χ_i replaced by the virtual spin-orbital χ_a; ψ_{ij}^{ab} is a doubly excited Slater determinant with the occupied spin-orbitals χ_i and χ_j replaced by the virtual spin-orbitals χ_a and χ_b; t_i^a and t_{ij}^{ab} are numerical coefficients called amplitudes. The effect of the operator $\hat{T}_1$ and $\hat{T}_2$ is to transform a Slater determinant into a linear combination of all possible singly excited and doubly excited Slater determinants, respectively.

It can be shown [26, 86] that the coefficients appearing in Equations (4.18) can be obtained from a set of simultaneous non-linear equations, in which the coefficients are constant that involve orbital energies and electron-electron repulsion integrals over the basis functions.

Inclusion of the operator $\hat{T}_3$ is computationally demanding and therefore the triple excitations are included by a perturbative treatment in the CCSD(T) method. This has become the standard method used for high-level *ab initio* calculations which lead to the most accurate results. However, it requires significant computer resources and therefore it is limited to relatively small molecules.

4.6 HARMONIC AND ANHARMONIC FORCE FIELDS

The knowledge of the energy derivatives greatly facilitates the search for critical points, such as minima and saddle points, on the molecular potential energy surface. Besides, as shown in Chapter 2, the spectroscopic parameters can be calculated from the second and higher order derivatives of the molecular energy. Table 4.1 summarizes the connection between the energy derivatives up to the fourth order and some spectroscopic quantities [87].

Table 4.1. Molecular energy derivatives and related spectroscopic observables.

Derivative	Observable
$\frac{\partial E}{\partial q}$	Forces on the nuclei; critical points on the PES.
$\frac{\partial^2 E}{\partial q_r \partial q_s}$	Quadratic force constants; harmonic fundamental vibrational frequencies; Coriolis vibration-rotation couplings.
$\frac{\partial^3 E}{\partial q_r \partial q_s \partial q_t} = \phi_{rst}$	Cubic force constants; anharmonic constants; anharmonic resonances.
$\frac{\partial^4 E}{\partial q_r \partial q_s \partial q_t \partial q_u} = \phi_{rstu}$	Quartic force constants; anharmonic constants; anharmonic resonances.

Calculation of the derivatives from energy points can be done in two ways. In numerical methods a number of energy values is calculated close to the point where the derivatives need to be evaluated; then an analytical function, generally a polynomial, is fitted to these points. This method is usually plagued by numerical instability, unless the number of points greatly exceeds the number of derivatives to be calculated. Another numerical method is represented by the use of finite difference methods, which are free from the instability encountered when surfaces are fitted.
In analytical methods, the derivatives are directly calculated from quantum mechanical wavefunctions, for instance [88]

$$-\frac{\partial E}{\partial q_i} = -\left\langle \psi \left| \frac{\partial \hat{H}}{\partial q_i} \right| \psi \right\rangle - 2\left\langle \frac{\partial \psi}{\partial q_i} \left| \hat{H} \right| \psi \right\rangle . \tag{4.19}$$

In comparison to numerical methods, the analytical calculation of the energy derivatives is more efficient and numerically accurate. On the other hand, the analytical approach requires huge programming efforts for its implementation. Another drawback is that the calculation of a single derivative usually takes more computer resources than the energy calculation itself, in particular for

second and higher order derivatives. For these reasons the analytical calculations are usually limited to the gradient (i.e. the vector of the N first derivatives) and the Hessian matrix (i.e. the $N \times N$ matrix of the second derivatives). The third and fourth derivatives, which are important for predicting vibrational anharmonicity, are computed numerically.[iv]

[iv] The chapter has been written by consulting Refs. [26, 27, 38, 82 – 88].

Part II: Experimental & Computational Work

5. Instrumentation

During the last forty years there has been a revolutionary improvement in the instrumentation used to measure the infrared spectra of molecules. The spectrometers based on the Fourier Transform (FT) technique are nowadays the major tools used for infrared spectroscopy. Their success is mainly due to the large spectral interval which can be recorded during a single measurement in a relatively short time, which depends on the spectral resolution employed.

On the other hand, high precision quantitative absorption measurements are provided by Tunable Diode Laser (TDL) spectrometers as well. Precise line shape measurements are one of the most important applications of these spectrometers in high resolution molecular spectroscopy.

More recently, Quantum Cascade Laser (QCL) based spectrometers have become one of the most promising sources of infrared radiation, in particular for trace gas detection and monitoring [89 – 95]. Indeed, they have led to the development of compact and transportable spectrometers, which are free of the requirement for cryogenic cooling [96 – 101].

5.1 Tunable Diode Laser Spectrometer

In IR TDL spectrometers the source of light is a tunable semiconductor laser. Semiconductor lasers are generally based upon a p-n junction: the light emission is associated with the radiative recombination of electron and holes that occurs at the junction [102, 103]. A schematic picture of a heterojunction semiconductor laser is given in Figure 5.1. The excitation is provided by an external electric field applied across the p-n junction, which causes the two types of carriers to come together. In Fabry – Pérot lasers the optical feedback necessary for the laser cavity is usually obtained by cleaving and polishing the opposite facets of the semiconductor so that they result parallel.

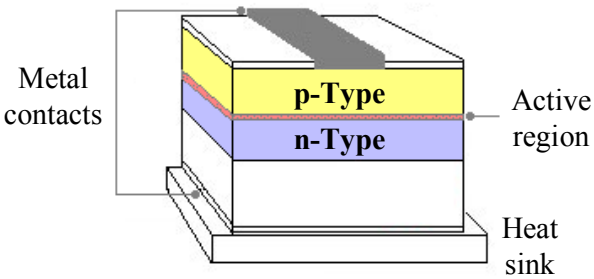

Figure 5.1. Schematic diagram of a heterojunction semiconductor laser

Within the infrared spectral region, the semiconductor lasers are based on lead salts, namely $Pb_{1-x}Sn_xTe$ and $Pb_{1-x}Sn_xSe$, and they provide a spectral coverage inside the interval 4 – 32 μm [3,

102]; the nominal frequency of the radiation emitted depends on the exact composition of the crystal. The typical size of such semiconductor lasers is around 0.1 × 0.04 × 0.02 cm. These lasers operate at cryogenic temperatures in the range between 77 and 120 K and hence, they must be attached to the cold finger of a Dewar at liquid nitrogen temperature.

For a given TDL, the bandwidth associated with spontaneous emission may be of the order 5 – 50 cm^{-1}, however laser action can only occurs at the wavelengths allowed by cavity modes which are dictated by the optical length of the Fabry – Pérot cavity.

The wavelength of the radiation emitted depends on the injection current, while fine tuning is usually achieved by changing the temperature. This alters the refractive index and hence the optical length of the cavity. The rate of change of the band gap with the temperature is of the order of 2 – 4 $cm^{-1}K^{-1}$, as shown in Figure 5.2(a). Nevertheless, there is no continuous tuning over the whole gain profile, because of mode hopping. An example of this discontinuous emission pattern is shown in Figure 5.2(b).

Lead salt diode lasers are generally multi-mode devices and therefore a monochromator is used to isolate a single mode. Typical single-mode output powers are between 10 and 100 μW.

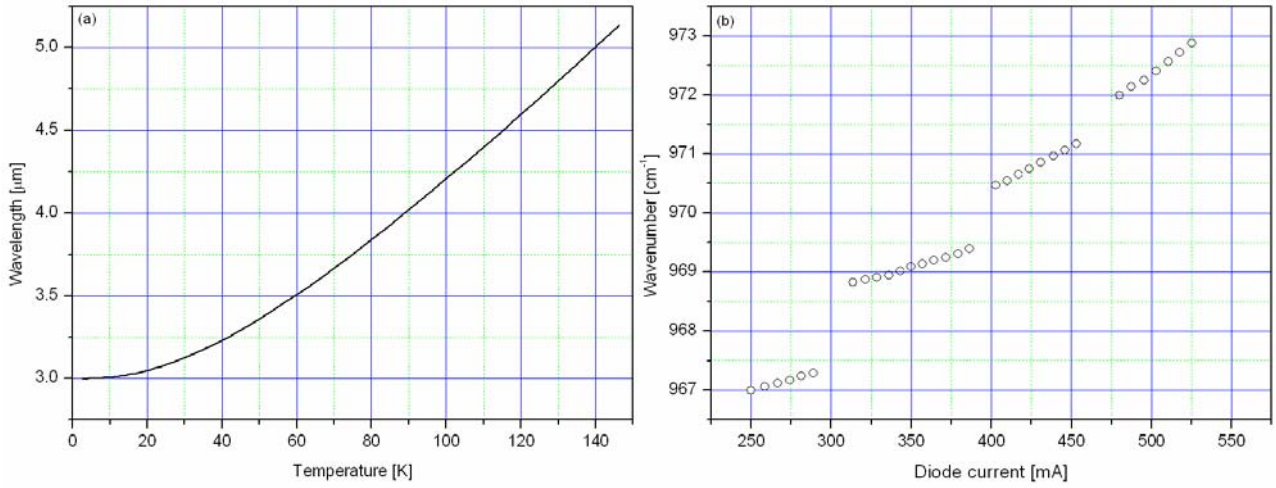

Figure 5.2. (a) Temperature tuning of TDLs. (b) Example of mode hops occurring in TDLs.

At the University Ca' Foscari Venezia, the high resolution measurements were carried out on a Laser Analytics tunable diode laser assembly model SP-5000. During the years the spectrometer has been upgraded and progressively improved: at present it works in a two or three channel configuration. The scheme of the instrument and its optical arrangement are shown in Figure 5.3. After being collimated, the IR radiation emitted by the laser is split into two distinct beams: one is sent through the absorption cell containing the gas sample; the other is directed into a Germanium etalon, having a free spectral range of about 0.48288 cm^{-1}, used for frequency calibration. When the spectrometer is operating in the three channel arrangement, the major beam is

further separated in two parts by another beamsplitter. One ray passes though the absorption cell, whereas the third beam is directed to a second cell which can be filled with a reference gas for calibration purposes. The emerging beams are then collected by different nitrogen cooled HgCdTe (MCT) photoconductive detectors. The electric signals produced by these detectors are simultaneously acquired by a 4 channel digital oscilloscope (Tektronix TDS 3014) and transferred to a personal computer for post processing, e.g. calibration and conversion to absorbance spectrum.

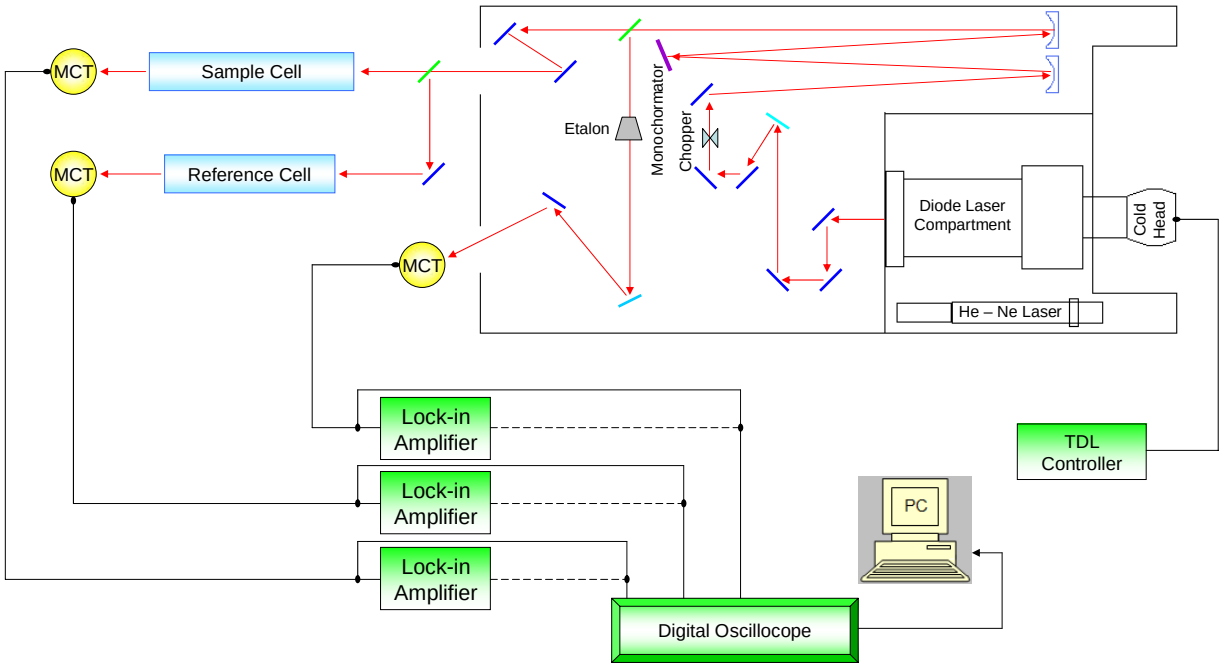

Figure 5.3. Scheme of the experimental setup of the TDL spectrometer employed at Università Ca' Foscari Venezia. In the phase-sensitive signal recovery the spectral acquisition is performed by lock-in amplifiers (dashed lines).

There are two ways in which the spectra can be acquired: sweep integration and phase-sensitive signal recovery. In the sweep integration method the laser output is scanned repetitively by using a sawtooth modulation to the current supply, and the detector signal is recovered by a signal averager. The scan times are short (~ 3 ms), so that the effects of laser instability are reduced and the signal-to-noise ratio is improved by averaging a large number of scans.

In the experimental setup adopted, the phase-sensitive signal recovery is obtained by modulating the laser output beam using a mechanical chopper. The laser is scanned slowly (generally several minutes), and the resulting AC signal at the detector is demodulated by using lock-in amplifiers.

For line parameter retrieval experiments, the first method is preferred, since in the phase-sensitive signal recovery the effects of modulation depth may be difficult to calculate and correct for [3].

5.2 FOURIER TRANSFORM SPECTROMETER

The majority of modern Fourier Transform Infrared (FTIR) spectrometers is based on the two beam interferometer originally designed by A. A. Michelson in 1891. The Michelson interferometer is a device that splits a beam of radiation into two paths, which are then recombined after introducing into one of them a path difference [104].

The simplest form of Michelson interferometer is schematically represented in Figure 5.4. It consists of a beamsplitter placed between two mutually perpendicular mirrors, one of which moves along an axis that is perpendicular to its plane. The operations of the interferometer are as follow: the energy from the infrared source is collimated and directed toward the beamsplitter, where the beam is partly reflected to the fixed mirror F and partly transmitted to the movable mirror M. The two beams are then reflected by the corresponding mirrors back to the beamsplitter, where they interfere and are again partly reflected to the source and partly transmitted to the detector.

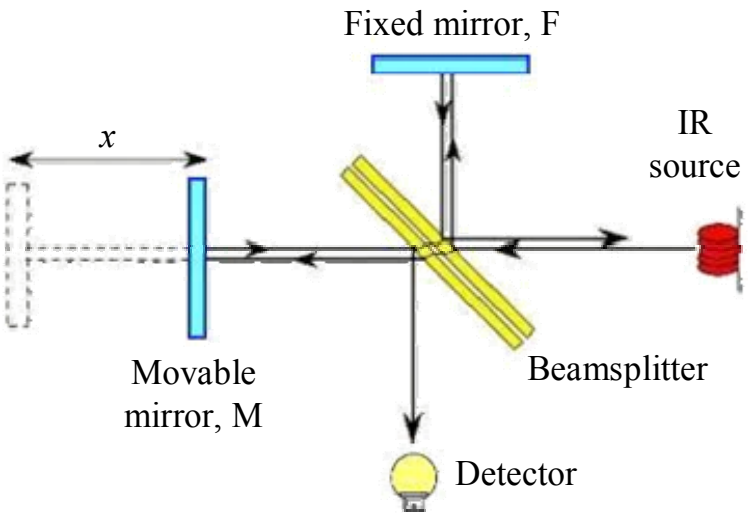

Figure 5.4. Scheme of a Michelson two mirror interferometer.

The energy reaching the detector is the sum of the beams, which recombine at the beamsplitter. If the distance of the two mirrors from the beamsplitter is the same, then the two beams travel equal distances and, once recombined, they interfere constructively since they are in phase. When the movable mirror is moved, the two beams travel unequal optical paths. Once recombined they can interfere either constructively or destructively depending on the path difference. The path difference introduced by the movable mirror is called optical path difference (OPD) or retardation and it is usually denoted by δ. If the movable mirror is displaced by x, the OPD is $\delta = 2x$.

The intensity of the beam that arrives at the detector is a function of the optical path difference, $I'(\delta)$, and it contains all the spectral information. If the movable mirror is translated back and forth at constant velocity, the signal at the detector varies sinusoidally. It has a maximum when the OPD is an integer multiple of the wavelength, λ, of the radiation, since the two beams recombine in phase; it has a minimum when the OPD equals an half-integer multiple of λ, since the two beams add out-of-phase [105].

The beam intensity $I'(\delta)$ is composed of a constant (DC) and a modulated (AC) component. Only the latter is important for spectroscopic measurements, and it is generally referred to as interferogram, $I(\delta)$. For an ideal interferometer, the interferogram $I(\delta)$ and the spectrum $B(\tilde{\nu})$ form an integral Fourier pair [104, 105]:

$$I(\delta) = 2\int_0^{+\infty} B(\tilde{\nu})\cos(2\pi\tilde{\nu}\delta)d\tilde{\nu} \tag{5.1a}$$

$$B(\tilde{\nu}) = 2\int_0^{+\infty} I(\delta)\cos(2\pi\tilde{\nu}\delta)d\delta\,, \tag{5.1b}$$

and hence the spectrum can be obtained from the interferogram by computing its cosine Fourier transform. In principle, according to equation (5.1a) the spectrum can be measured at infinitely high resolution[14], however equation (5.1b) shows that this would be possible only by scanning the movable mirror over an infinitely long distance. This is obviously impossible and therefore the finite OPD limits the resolution of the interferometers.

By denoting with δ_{max} the maximum optical path difference of an interferometer, the theoretical maximum limiting resolution, $\Delta\tilde{\nu}$ is

$$\Delta\tilde{\nu} = \frac{1}{\delta_{max}}\,. \tag{5.2}$$

In practice, however, this resolution is never attained because of truncation and apodization; in addition interferogram is digitized at finite, rather than infinitesimal, sampling intervals.

If the OPD ranges from –Δ to +Δ, this amounts to multiplying the complete interferogram by a boxcar function, $D(\delta)$, reproduced in Figure 5.5 (a) and defined as

$$D(\delta) = \begin{cases} 1 & \text{if} \quad -\Delta \le \delta \le +\Delta \\ \\ 0 & \text{if} \quad \delta > |\Delta|. \end{cases} \tag{5.3}$$

[14] There are various way to define the spectral resolution. One of the most employed is the use of the FWHM (Full Width Half Maximum): two spectral lines of equal intensity cannot be considered resolved if their separation is less than the FWHM.

The spectrum is then given by

$$B(\tilde{\nu}) = \int_{-\infty}^{+\infty} I(\delta) D(\delta) \cos(2\pi\tilde{\nu}\delta) d\delta \,; \tag{5.4}$$

this yield a spectrum that is the convolution of the FT of $I(\delta)$ from –∞ to +∞ and the FT of $D(\delta)$. The former is the complete spectrum, while the FT of $D(\delta)$ is the sinc function,

$$f_{FT}(\tilde{\nu}) = \mathrm{sinc}(2\pi\tilde{\nu}\Delta) = \frac{2\sin(2\pi\tilde{\nu}\Delta)}{2\pi\tilde{\nu}\Delta}, \tag{5.5}$$

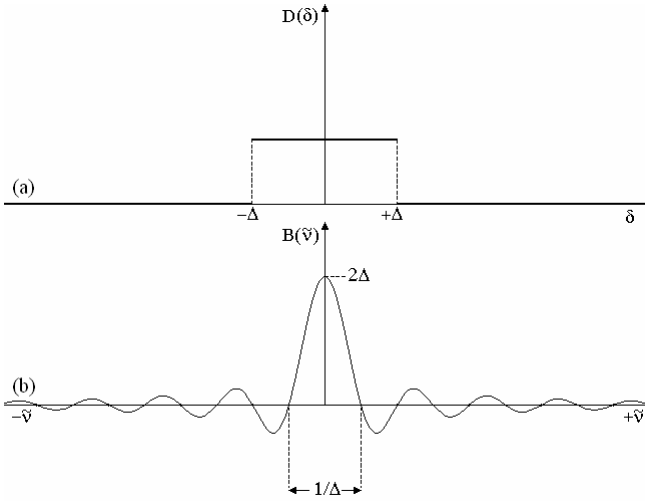

Figure 5.5. The boxcar function (a) and corresponding Fourier transform (b), i.e. the sinc function.

which is represented in Figure 5.5 (b). Since the sinc function has a FWHM of 0.605, an infinitely narrow spectral line broads to $0.605/\delta_{max}$ [104]. In addition, the sinc function causes each spectral line to be accompanied by a series of side lobes undulating positive and negative, with diminishing intensities on moving from the line centre[15]. The suppression of the magnitude of these oscillations is known as apodization and there exists a wide variety of apodization functions[16] [104]. However, while reducing the magnitude of the ringing, the apodization functions lead to a poorer spectral resolution.

One of the most serious drawbacks of the original Michelson interferometer is the slight rotation of the plane mirrors [106]. The tilt compensation can be achieved by the use of retroreflectors such as corner cube mirror systems. The simplest corner cube consists of three mutually perpendicular plane mirrors, as shown in Figure 5.6. An ideal corner cube works as a perfect retroreflector, indeed if the beam impinging on the corner cube moves in the +**k** direction, the outgoing beam will propagate in the –**k** direction as a result of the three successive reflections by the mirrors. Hence, the outcoming beam is exactly parallel to the incident one. The simplest

[15] This effect is called ringing.
[16] The boxcar function is usually called apodization function as well. Strictly speaking it is simply a truncation function. Indeed apodization derives from the Greek "apodos" which means "without feet" and therefore it refers to the removal of the side lobes caused by the truncation.

corner cube interferometer is a conventional Michelson interferometer in which both plane mirrors have been replaced by corner cube mirrors [106].

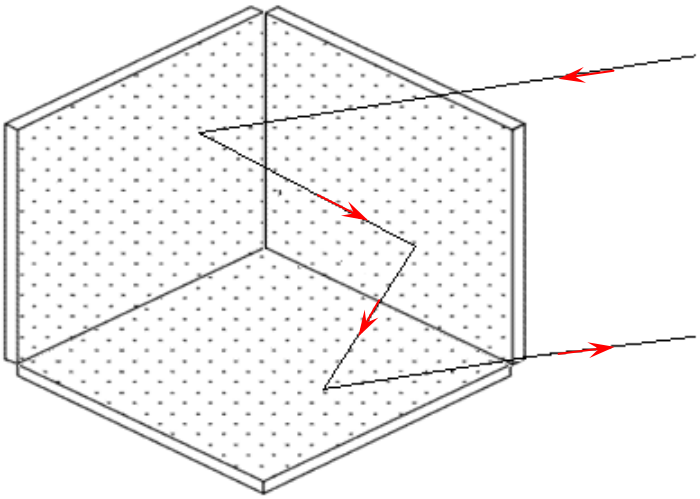

Figure 5.6. Corner cube retroreflector.

At Università Ca' Foscari Venezia the FTIR spectra were recorded on a Bruker Vertex 70 corner cube spectrometer. The scheme of the instrument is given in Figure 5.7. It can work at different spectral resolution and covers both the medium IR region (400 – 5000 cm^{-1}) and the near infrared region from 5000 to about 12000 cm^{-1}. For operations in the MIR region, the radiation is emitted by a Globar source, a KBr beamsplitter is used and the radiation is collected by DTGLas detector. When the instrument is working in the NIR region, the radiation emitted by a tungsten lamp is sent to a Si/CaF_2 beamsplitter and a InGaAs detector is used.

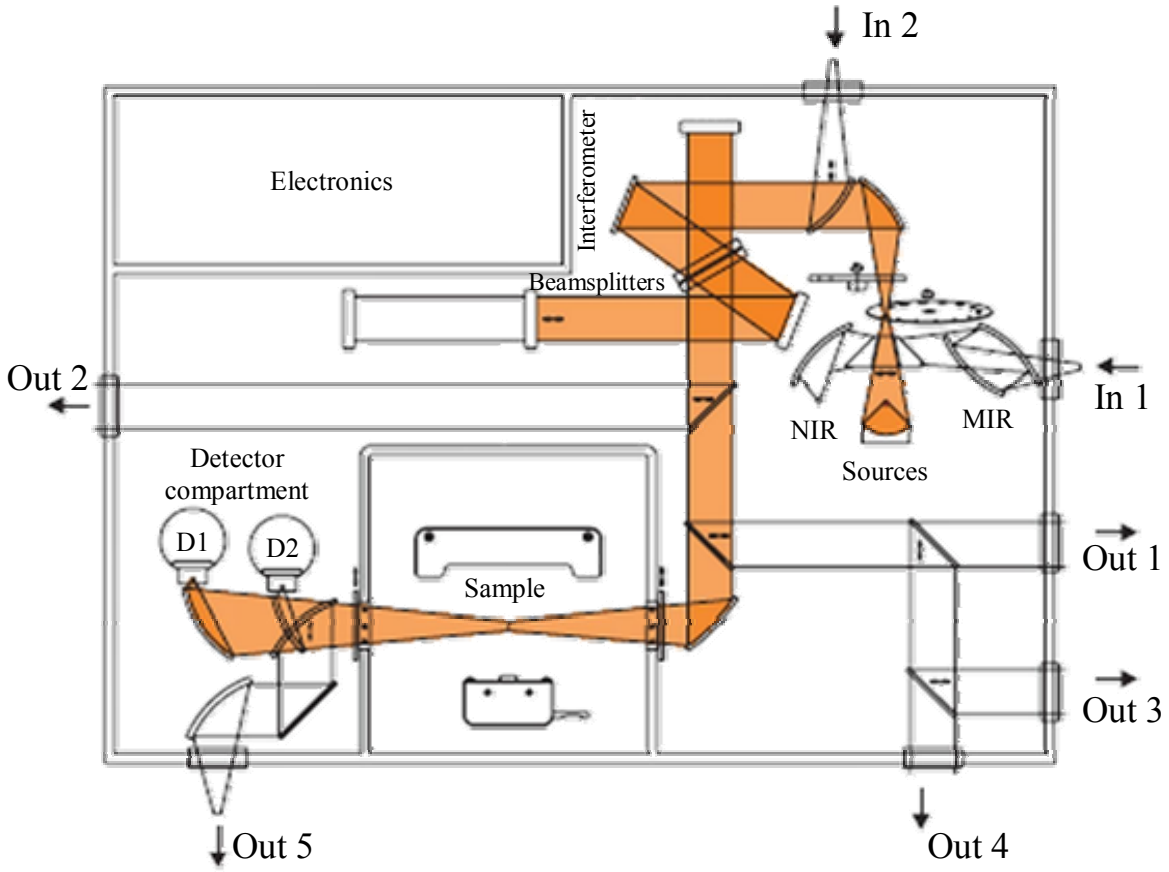

Figure 5.7. Diagram of the Bruker Vertex 70 FTIR spectrometer used for low and medium resolution measurements.

After the interferogram has been acquired by the proper detector, it is transferred to a PC, where it is Fourier transformed into the corresponding spectrum by the instrument control software (OPUS).

5.3 SUPERSONIC FREE JET EXPANSION

Infrared spectra provide a wealth of information on molecular energy levels and intramolecular dynamics. In order to obtain a reliable molecular Hamiltonian from the experimental spectra, the observed transitions must be properly assigned. The task is simplified by the use of high spectral resolution: an ideal gas sample would be thought as an ensemble of molecules, all in a given well defined quantum state (usually the vibronic ground state), travelling in free space with a narrow velocity distribution and at a sufficiently low density such that intermolecular interactions become unimportant [107]. However, for molecules with a number of heavy atoms, the spectral lines are so closely spaced that many of them overlap within their natural or Doppler widths. In addition, for molecules with low lying vibrational levels, the absorptions due to the hot bands significantly contribute to the spectrum, which thus appears as a continuum or a quasi-continuum at room temperature. Under these circumstances the spectral analysis is a very formidable, often prohibitive, task.

The spectral structure can be greatly simplified by means of the supersonic expansion of the molecular gas sample. In supersonic free jets, molecules at moderately high pressures (usually between 1 and 100 atm) are expanded either neat or in a carrier through a small orifice (nozzle) or a planar slit, into a region of relatively low pressure [108]. The expansion cools the translational degrees of freedom of the gaseous mixture, thus creating a cold translational bath. In order to obtain a supersonic jet, the diameter, D, of the orifice must be larger than the mean free path, λ_0, of the particles: $\lambda_0 / D << 1$. When this condition is met, there will be many collisions as the gas flows through the orifice and downstream of the orifice. Such a flow regime is called hydrodynamic. The hydrodynamic expansion converts the enthalpy associated with the random motion of the particles into direct mass flow. This process causes the mass flow velocity, u, to increase and the temperature T to decrease. The rate of cooling is governed by $\gamma = C_p / C_v$, that is the ratio of the specific heat at constant pressure and that at constant volume. If an ideal gas at pressure P_0, density ρ_0 and

temperature T_0 is expanded into a vacumm discharge chamber, the temperature T_1, density ρ_1 and pressure P_1 after the expansion satisfy the following relations:

$$\frac{T_1}{T_0} = \left(\frac{P_1}{P_0}\right)^{\gamma-1/\gamma} = \left(\frac{\rho_1}{\rho_0}\right)^{\gamma-1} = \left(1+\frac{\gamma-1}{2M^2}\right)^{-1}; \tag{5.6}$$

M is the Mach number, which is the ratio of the bulk flow velocity to the local speed of sound, a,

$$M = \frac{u}{a} = A\left(\frac{x}{D}\right)^{\gamma-1} \tag{5.7}$$

where x is the distance from the nozzle, A is a constant which depends on the type of gas (A = 3.26 for an atomic gas) and a is given by

$$a = \left(\frac{\gamma K_B T}{m}\right)^{1/2}. \tag{5.8}$$

As the temperature of the expanding gas drops, the speed of sound decreases and therefore M increases. When M exceeds 1, the expansion is called supersonic. Although M changes with the distance, it converges to a limiting value at which the temperature lowering stops.

After the expansion, the cold particles of the supersonic flow collide with the warm background molecules present in the vacuum chamber and a shock wave is formed around the beam. The structure of a free jet is shown in Figure 5.8. The supersonic jet occurs in the so called zone of silence, that is the spatial region enclosed by a barrel shock and the Mach disk. If a particle in the jet reaches the barrel shock or the Mach disk it is heated up. The Mach disk distance from the nozzle can be approximated by

$$x_M = 0.67D\left(\frac{P_0}{P_c}\right) \tag{5.9}$$

where P_c is the pressure of the vacuum chamber [108]. Within the zone of silence the two body collisions probability becomes small and no further significant cooling occurs. The cooled molecules in the jet are then isolated and stay in the prepared state until they encounter an obstacle.

Generally, the supersonic expansion is carried out employing a monoatomic gas carrier in which the radiators are seeded: in this way lower temperatures can be achieved because atoms do not store energy into internal degrees of freedom. The polyatomic molecules seeded into the expanding gas cool by means of two body collisions with the atoms of the carrier. The percentage of added molecules is generally so small that the conditions achieved in the expanding gas are nearly the same of the pure gas carrier.

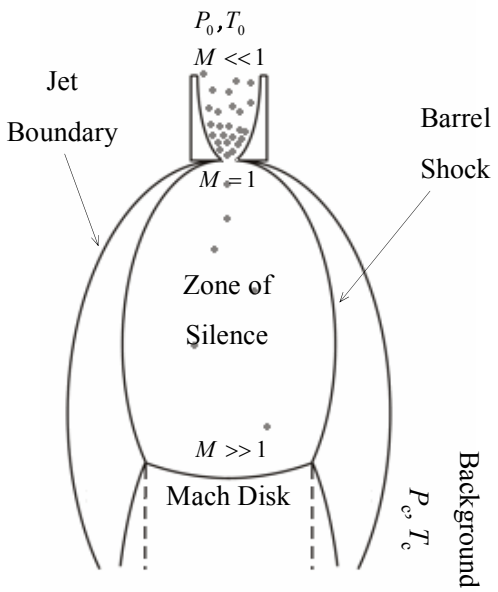

Figure 5.8. Structure of a free jet expansion.

Since the supersonic jet is in a non-equilibrium state, the equilibration rates of the different degrees of freedom are not the same. Generally, the rate of equilibration between translations and rotations is generally fast and therefore extensive rotational cooling takes place before the molecules enter the collision-free region. The rate of vibration – translation equilibration of a particular vibrational mode is generally slower. Therefore, vibrational cooling occurs to some extent, but it is not as complete as the rotational one [107]. It follows that $T_{\text{trans}} <\approx T_{\text{rot}} < T_{\text{vib}}$, where T_{trans}, T_{rot} and T_{vib} are the translational, rotational and vibrational temperatures, respectively [109, 110]. The rate of phase equilibration is very slow and the molecules persist for long time in the gas phase at temperatures far lower than those necessary to freeze the entire system into a solid [107]. The result is that, when the molecules enter the collision-free region, the system is translationally and rotationally very cold, vibrationally somewhat cold, but still consisting of single isolated gas phase molecules [107].

A schematic diagram of the home-built supersonic free jet system [111, 112] of the Molecular Spectroscopy group of Università Ca' Foscari Venezia is shown in Figure 5.9. The system is coupled to the TDL spectrometer presented in Section 5.1.

The radiation emitted by the lead salt laser, after being collimated and mode filtered, is subdivided into three parts by a couple of beamsplitters. The main part of the beam is directed into a 1.5 m^3 vacuum chamber. The radiation is focused onto a detector after a single passage through the supersonic jet. A set of large mechanic pumps, consisting of a 2000 m^3h^{-1} Roots blower, backed by a 500 m^3h^{-1} Roots blower and a 175 m^3h^{-1} double stage rotary vane pump, is employed to evacuate

the gas from the vacuum chamber. In order to minimize their vibrations, special vibration absorber are fitted under the pump system and a flexible pipe is used to connect the pumps to the chamber.
By using an electronic delay generator, an adjustable delay time between the first pulse (which initializes the valve orifice controller) and the second one (which starts the scan and initiates the oscilloscope) can be properly set. It is generally chosen such that the valve is fully opened during the recording time.

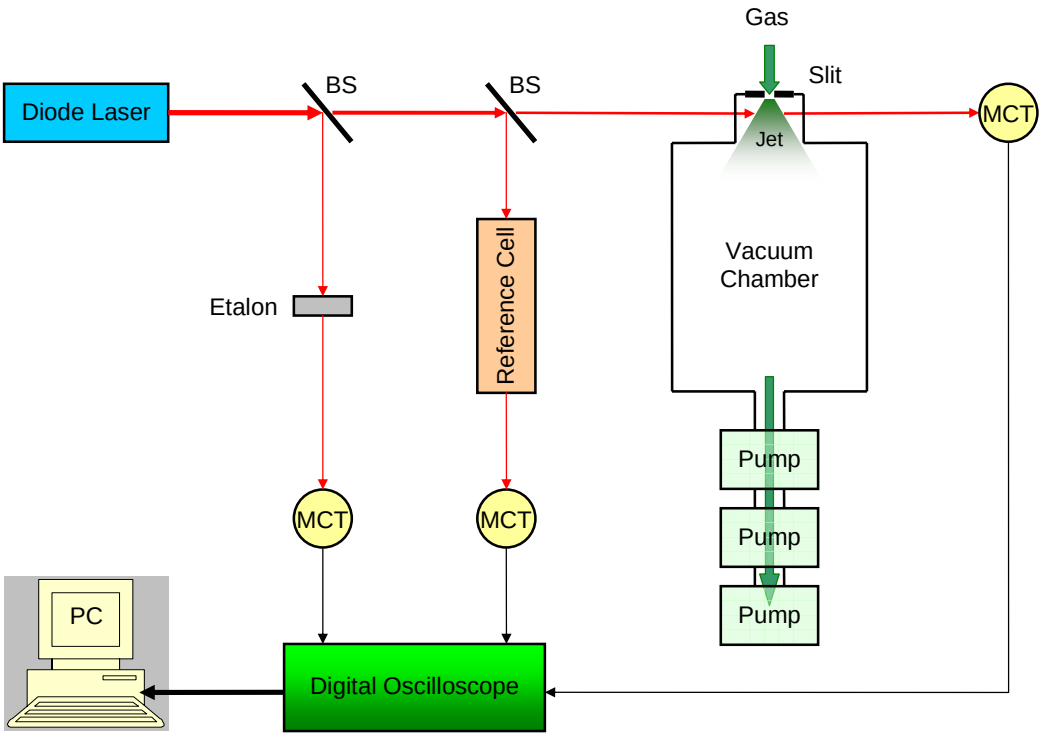

Figure 5.9. Block diagram of the home built free jet system at Università Ca' Foscari Venezia.

5.4 Quantum Cascade Laser Spectrometer

The main disadvantages of bipolar lead salt lasers are that they require cryogenic cooling to operate and their output power is usually low (some μW).

Over the last years, the invention of Quantum Cascade Lasers (QCLs) have led to the development of medium IR spectrometers which avoid the need of cryogenic cooling [94, 96 – 101]. These lasers, which are based upon the AlInAs, InGaAs and InP technologies developed for optical communications [113], have been first realized by Capasso's group [114], although the original idea of this type of laser was proposed by Kazarinov and Suris [115].

QCL's rely on transitions between the quantized conduction band states of a multi-quantum well device [113]. They are unipolar semiconductor lasers which have only electrons as type of

carrier. The electrons propagate through a potential staircase of coupled quantum wells, where the conduction band is split by quantum-confinement into a number of distinct subbands [114, 116]. The sets of different square well potentials are designed by band structure engineering and they are obtained by growing a semiconductor composed of alternating layers of different types of semiconductor materials.

The scheme of the conduction band structure of the laser active core is shown in Figure 5.10. A single stage of this device consists of an injector region and an active region. The light is generated by transitions between energy levels in the square well based potential. By applying an electric field, electrons are injected via an injector miniband into level 3, light is emitted by the transition from level 3 to level 2; then level 2 rapidly relaxes to level 1. The latter is coupled into the injector miniband which populates the upper level in the next stage of the cascade where the process is repeated again [117]. Therefore, by stacking a series of *m* stages (i.e. injector and active region) one electron is responsible for emitting *m* different photons [113].

QCLs cover the entire medium IR region and are of particular importance for the two atmospheric windows at 3 – 5 μm and 8 – 13 μm. The frequency of the emitted radiation depends on the energy spacing between the lasing subbands, i.e the $n = 3$ and $n = 2$ levels of the quantum well, and therefore it can be varied by changing the width of the quantum well [113]. The power levels available from these lasers can be three orders of magnitude greater than commercial lead salt lasers in this wavelength region; in addition, they have narrower emission linewidths. Generally, single mode QCLs adopt a distributed feedback (DFB) design for the longitudinal mode separation. The tuning mechanism of a DFB-QCL relies upon the variation of the refractive index of the waveguide with the temperature. This causes the apparent optical length of the frequency selection grating to change.

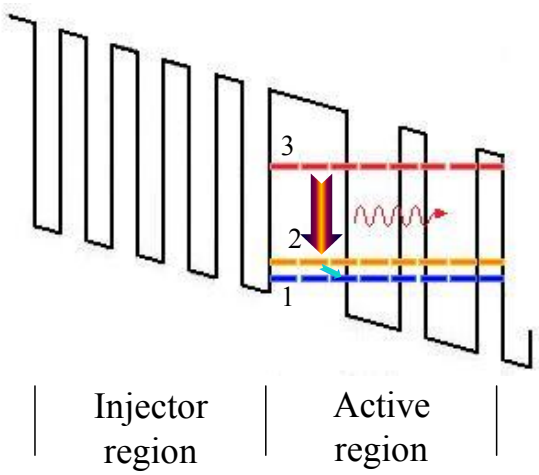

Figure 5.10. Schematic diagram of the QCL conduction band structure.

Quantum Cascade Lasers operate either continuously or in pulsed mode. In the latter case, when a current pulse is applied to a QCL, the laser output frequency sweeps to lower frequency as a function of time. Two types of instrument for pulsed operations have been developed: the inter-pulse [89, 91, 97, 118] and the intra-pulse [92, 98 – 100, 117, 119] methods.

In the inter-pulse method short current pulses (3 – 10 ns) are used in order to limit the frequency down-chirp. The current generates a pulse in the spectral domain, which is tuned through the

spectral features by the use of a sub-threshold current ramp [119]. The obtained spectra resemble those produced by a TDL spectrometer, the recorded spectral micro-window covering an interval of $0.2 – 0.8\ cm^{-1}$.

In the intra-pulse method, the frequency down-chirp is used to provide the scan through the absorption spectrum: a long current pulse is used so that the laser frequency rapidly sweeps to lower frequency [117]. In this way a complete spectral window covering some wavenumbers is recorded during each pulse. This method requires a very wide frequency bandwidth detector and amplifier combination, and also a fast and efficient digitiser [117].

The resolution limitations of the intra-pulse QCL spectrometers are not determined by the effective linewidth of the laser emission profile induced by the current pulse, but by the chirp rate of the frequency down-chirp and the temporal resolution of the detection system [98, 117]. For the latter, the bandwidth – time duration product of a signal can not be less than a certain minimum value; this is sometimes referred to as "uncertainty relation" [120]. It states that the product of the equivalent duration, Δt, and the equivalent bandwidth, $\Delta \nu$, must exceed or be equal to a constant C, which is determined by the pulse shape:

$$\Delta t \cdot \Delta \nu \geq C\ ; \tag{5.10}$$

for a rectangular time window $C = 0.886$, whereas for a Gaussian time window $C = 0.441$.

A peculiar feature of the intra-pulse method is that, when very low pressures of pure gas are used, the shapes of the absorption lines have a characteristic hook shape [80, 81, 117, 121, 122]. This line shape is analogous to the rapid passage signals of NMR [76] and ESR spectroscopy [77], the fast passage signals of microwave spectroscopy [70, 78] or the optical nutation signals observed in time dependent coherent transient experiments [20].

Most of the developments made on QCL spectrometers adopting the intra-pulse method have been carried out by the Strathclyde University group of Prof. G. Duxbury and Prof. N. Langford. The experimental arrangement of their laboratory-fixed spectrometer is shown in Figure 5.11.

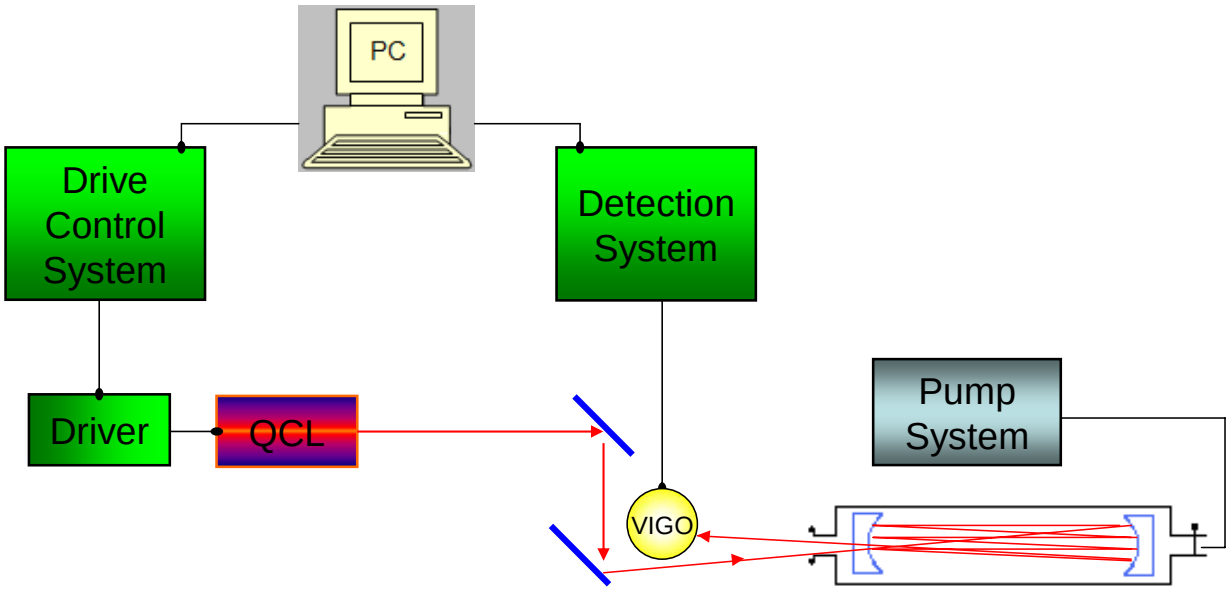

Figure 5.11. Schematic diagram of the experimental arrangement of the QCL laser spectrometer used at University of Strathclyde.

The DFB-QCL is excited by a rectangular pulse current of 3 – 2000 ns and repetition rate of up to 100 kHz. The laser heat sink is mounted upon a Peltier thermoelectric cooler, which allows the QCL substrate temperature to be maintained constant between –40 and +40 °C. The light emitted by the laser is coupled out through an anti-reflection coated ZnSe window and then collected by an off-axis parabolic mirror-germanium telescope arrangement to produce a beam of about 3 mm diameter. This beam is directed via a set of steering mirrors into a multipass cell containing an astigmatic Herriot mirror arrangement. After traversing the cell, the radiation is coupled onto a Peltier-cooled small area photovoltaic VIGO MCT detector operating close to 0°C. The electrical signal produced by the detector is amplified by a built-in trans-impedance amplifier; the effective bandwidth of the detector-amplifier combination is about 1 GHz. The amplified signals are recorded with a high-speed (500 MHz bandwidth, 2 GSample) computer-controlled digitiser with a digitisation step of 0.5 ns.

6. Visual Line-Shape Fitting Program

Thanks to the availability of always more powerful computers, the time consuming task of inverting the experimental spectra to extract spectroscopic parameters has become increasingly assisted by computer programs. Compared to the huge number of softwares available for extracting the Hamiltonian's parameters from the assigned line positions (a list of freely available devices is given in Ref. [123]), few programs specifically designed to perform line shape analysis by fitting experimental spectra have been presented (see, for example, Refs. [124 – 128]). These software rely upon the multi-spectrum fitting technique, introduced by Carlotti for the spectroscopic retrieval of concentration profiles of atmospheric constituents [129]. The basic idea underlying the multi-spectrum approach is to fit various spectra recorded in different conditions (e.g. pressure, temperature, path length, etc.) at once. This method is the best choice when the large number of lines recorded in a single scan by an FT interferometer needs to be analyzed. Hence these programs appear designed to deal mainly with the FTIR spectra. Indeed, during the fitting procedure they explicitly take into account the step of the parameterization of the FTIR instrumental line shape, which is generally modelled as a sinc function.

On the other hand, the spectrometers based on laser sources have simpler instrumental contributions, generally modelled as a Gaussian or Lorentzian function. Furthermore, the spectral region which can be recorded in a scan is of the order of some wavenumbers, thus greatly reducing the amount of lines to be accounted for in a single spectrum. In many cases, the line shape analysis is carried out by using home made programs which are sometimes designed to fit the experimental features to a single theoretical function. Further, some programs are able to fit only one absorption line at time and still run from a command line window, thus avoiding an immediate comparison between the experimental data and the theoretical model. Commercial packages, such as IGOR Pro [130] and Origin [131], can be employed as well, although they are not completely well suited for the purpose.

As a consequence, a new software for line shape fitting has been projected and implemented. The program, called "*Visual Line-Shape Fitting Program*" (VLSFP), can fit more lines simultaneously, using different theoretical line shape functions. It has a standard graphical interface and it runs under Microsoft Windows environment.

6.1. Visual-Line Shape Fitting Program Implementation: an Object Oriented Approach

VLSFP has been written combining Microsoft Visual Basic and C# for the graphical interface and the computational kernel, respectively.

The evaluation of the line parameters within a given theoretical model is performed through an iterative procedure using the Levenberg – Marquardt algorithm [132, 133]. The algorithm [134, 135] has been implemented in a box constrained version [136], thus permitting to set bounds to the variability of the parameters or to keep the parameter values constrained. The fitting routine runs as a background process, hence avoiding the program interface to be frozen during the execution of the fitting task.

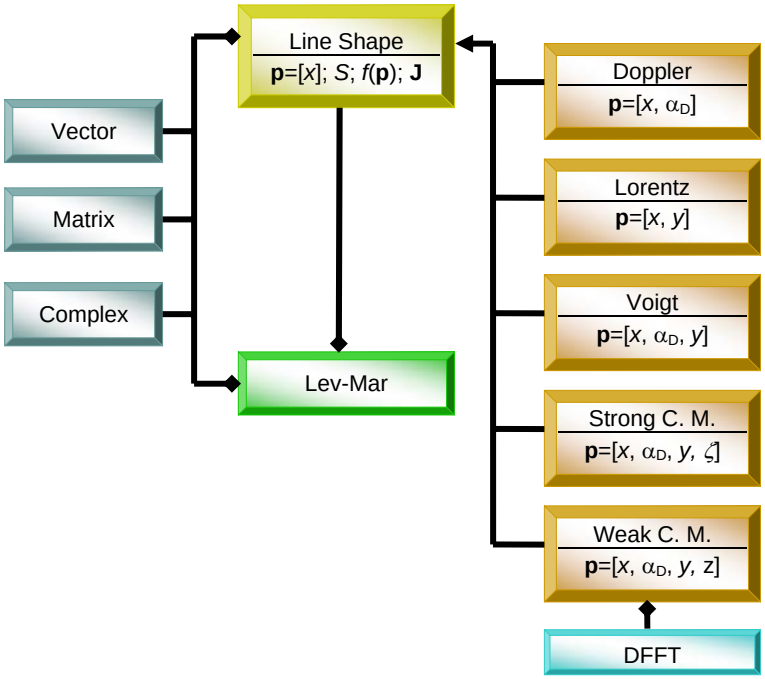

Figure 6.1. Block diagram representing the implementation of VLSFP. Each box represents a class referred to as Object (C. M. stands for collision model). The objects interact with each other to make the application: the arrow means "derives from", the diamond means "makes use of" (see text for discussion).

The computational kernel, schematically depicted in Figure 6.1, has been projected following an *Object Oriented Programming* (OOP) approach [137]. This programming technique, born around 1960s, uses objects and their interactions to design computer programs. An application is then composed by a collection of cooperating objects, rather than an ensemble of subroutines that compute specific tasks. Each box of Figure 6.1 is referred to as a class and it represents an "object". The class defines the properties (class variables) of the corresponding object and its behaviour (class methods). The object is able to process data and, mostly, to interact with other objects by receiving and sending messages. In a pictorial representation, every single object can be thought as a little machine with its own task. The distinct machines then cooperate to accomplish an objective: in this case the fit of the experimental line shape by means of different theoretical profiles.

The benefit of the OOP relies in that classes provide modularity and structure in a program. Further, objects can interact each other by just knowing their properties, while the specific implementation does not matter. This gives a large level of abstraction and the possibility of

modifying an object without changing the other ones. As a consequence the maintenance of a program becomes easier.

Referring to Figure 6.1, the classes Vector, Matrix and Complex implements vector, matrix and complex algebra, respectively. They are used by the other objects of the project to store and process the data. The matrices have been implemented as one-dimensional arrays and therefore they are allocated as a single chunk of computer memory, thus speeding up the access to their elements. The fitting routines have been encapsulated inside the class LevMar and they have been designed to deal with a generic object of the type Line Shape. Line Shape represents an abstract class, that is an abstract object which defines the common characteristics possessed by all the line shapes (for example, the computed line profile, the line parameter array and the Jacobian matrix). The single line shape functions have been derived from the main abstract class and within each line shape class a specific implementation of the methods has been made. As a consequence, new line shape functions, such as the speed-dependent profiles, can be implemented without changing neither the Line Shape nor the LevMar classes.

6.2. DESCRIPTION OF THE LINE-SHAPE FUNCTIONS

The line shape functions have been implemented in the normalized form: denoting a generic line function by $f(\mathbf{p})$, it is normalized to unitary area:

$$\int_{-\infty}^{+\infty} f(\mathbf{p})dx = 1 \tag{6.1}$$

where $\mathbf{p} = [x, y, z, \ldots]$ is the vector of dimensionless parameters which are described in Table 6.1 following the notation of Varghese and Hanson [47]. As can be seen, the line parameters are normalized by the effective Doppler half width (see also Eq. 3.18) defined as

$$\alpha_D = \frac{\gamma_D}{\sqrt{\ln 2}} \tag{6.2}$$

where γ_D is the dimensional Doppler half width as given by equation (4.19). Since the program has been projected to work in the infrared region, the dimensional quantities are expressed in wave numbers. Nevertheless, being all the profiles computed using dimensionless quantities, VLSFP

could be employed also in other spectral regions. During the fitting procedure, VLSFP refines the line centre frequency $\tilde{\nu}_0$, the line intensity S and the remaining line parameters, which clearly depend on the specific line shape function.

Table 6.1. List of the dimensionless parameters of the normalized line shape functions

Definition [a]	Dimensionless Parameter Description	Related Dimensional parameters
$x = \frac{\tilde{\nu} - \tilde{\nu}_0}{\alpha_D}$	Frequency detuning from resonance frequency	Wavenumber frequency $\tilde{\nu}$ and line centre $\tilde{\nu}_0$ [cm^{-1}].
$y = \frac{\gamma_L}{\alpha_D}$	Frequency of broadening collisions	Collisional half width, γ_L; Pressure broadening coefficient, γ_L^0 [$cm^{-1}atm^{-1}$]
$z = \frac{\beta}{\alpha_D}$	Effective frequency of velocity changing collisions (weak collision model)	Collisional narrowing, β; Collisional narrowing parameter, β^0 [$cm^{-1}atm^{-1}$].
$\zeta = \frac{\Omega}{\alpha_D}$	Frequency of velocity changing collisions (strong collision model)	Collisional narrowing, Ω; Collisional narrowing parameter, Ω^0 [$cm^{-1}atm^{-1}$].
$s = \frac{\delta}{\alpha_D}$	Effective frequency of shifting collision	Line shift, δ; Line shift coefficient, δ^0 [$cm^{-1}atm^{-1}$].

[a] α_D denotes the 1/e Doppler half width, eq. (6.2).

The normalized profiles, and the corresponding parameters, as implemented in VLSFP are presented in Table 6.2. For each profile the Jacobian matrix required by the Levenberg – Marquardt procedure is computed analytically or numerically.

The Doppler and Lorentz profiles are quite easily valuable, whereas the functions defining the Voigt, the Galatry and the Nelkin – Ghatak profiles can only be computed numerically. The calculations of the Voigt and the Nelkin – Ghatak profiles have been based on the algorithm proposed by Wells [138], while the Galatry function is computed following the Fourier transform method proposed by Ouyang and Varghese [139]. The algorithms are described in sections 6.4 and 6.5, respectively.

Table 6.2. Normalized line shape functions implemented in VLSFP

Profile and Physical features	Equation [a]
Doppler Broadening by random thermal motion.	$f(x)=\frac{1}{\sqrt{\pi}}\mathrm{e}^{-x^2}$
Lorentz Broadening by internal state perturbing collisions with negligible thermal motion contribution.	$f(x-s,y)=\frac{1}{\pi}\frac{y}{y^2+(x-s)^2}$
Voigt Broadening by thermal motion and internal state perturbing collisions.	$f(x-s,y)=\mathrm{Re}[w(\xi)]=\frac{y}{\alpha_D\pi^{3/2}}\int_{-\infty}^{+\infty}\frac{\mathrm{e}^{-t^2}}{[(x-s)-t]^2+y^2}dt$
Galatry Broadening by thermal motion and internal state perturbing collisions; weak collision model for VCC.	$f(x-s,y,z)=\frac{1}{\pi}\mathrm{Re}\left\{\int_0^{+\infty}\mathrm{e}^{-t[y+\mathrm{i}(x-s)]+(2z^2)^{-1}[1-zt-\mathrm{e}^{-zt}]}dt\right\}$
Nelkin & Ghatak / Rautian & Sobel'man Broadening by thermal motion and internal state perturbing collisions; strong collision model for VCC.	$f(x-s,y,\zeta)=\frac{1}{\sqrt{\pi}}\mathrm{Re}\left[\frac{w(x-s,y+\zeta)}{1-\sqrt{\pi}\zeta w(x-s,y+\zeta)}\right]$

[a] $w(x, y)$ is the complex probability function.

6.3. THE LEVENBERG – MARQUARDT ALGORITHM

Given a set of experimental data points, one is often involved in adjusting the parameters of an underlying theoretical model, that best describes the observations. The problem is generally known as least squares problem. In the case of the line parameters retrieval, the set of *n* data points represents the experimentally recorded absorption lines and the objective consists of determining the line parameter vector **p** (which also include the integrated intensity) that better reproduce the observed line contour within a given theoretical line shape function. Formally written, it consists of finding the parameters **p** ($\in \Re^m$) which minimize the residuals between experimental $\mathbf{y}_{exp}(\mathbf{x})$ and calculated $\mathbf{y}_{calc}$ observables:

$$\boldsymbol{\varepsilon}^T\boldsymbol{\varepsilon}(\mathbf{p})=\left\|\mathbf{y}_{exp}-\mathbf{y}_{calc}\right\|^2 \tag{6.3}$$

where $\boldsymbol{\varepsilon}(\mathbf{p})=\mathbf{y}_{exp}-\mathbf{y}_{calc}$ with $\mathbf{y}_{calc}=\mathbf{f}(\mathbf{x},\mathbf{p})$ and $\|\ \|$ denotes the Euclidean norm. For small parameter variations, $\|\boldsymbol{\delta}_\mathbf{p}\|$, the Taylor series expansion of the generic element of $f(x_i,\mathbf{p})$ leads to (omitting the x_i variable for clarity)

$$f(\mathbf{p}+\boldsymbol{\delta}_\mathbf{p}) = f(\mathbf{p}) + \boldsymbol{\delta}_\mathbf{p}^\mathrm{T}\nabla f(\mathbf{p}) + \frac{1}{2}\boldsymbol{\delta}_\mathbf{p}^\mathrm{T}\mathbf{H}(\mathbf{p})\boldsymbol{\delta}_\mathbf{P} + O\left(\|\boldsymbol{\delta}_\mathbf{P}\|^3\right) \tag{6.4}$$

where $\nabla f(\mathbf{p})$ and $\mathbf{H}(\mathbf{p})$ are, respectively, the gradient vector and the Hessian matrix:

$$\nabla f(\mathbf{p}) = f'(\mathbf{p}) = \frac{\partial f(\mathbf{p})}{\partial \mathbf{p}} \in \Re^{m\times 1}; \qquad \mathbf{H}(\mathbf{p}) = f''(\mathbf{p}) = \frac{\partial^2 f(\mathbf{p})}{\partial \mathbf{p}^2} \in \Re^{m\times m}.$$

The basis of the Levenberg – Marquardt method is a linear approximation of $\mathbf{f}(\mathbf{x},\mathbf{p})$ in the neighbourhood of $\mathbf{p}$, and hence the function is approximated by:

$$\mathbf{f}(\mathbf{p}+\boldsymbol{\delta}_\mathbf{p}) \approx \mathbf{f}(\mathbf{p}) + \mathbf{J}\boldsymbol{\delta}_\mathbf{P} \tag{6.5}$$

where $\mathbf{J} \in \Re^{n\times m}$ is the Jacobian matrix, whose elements are

$$[\mathbf{J}(\mathbf{p})]_{ij} = \frac{\partial f(x_i,\mathbf{p})}{\partial p_j}.$$

By substituting equation (6.5) into (6.3) it is possible to obtain an iterative procedure which, given a starting point $\mathbf{p}_0$, produces a series of vectors $\mathbf{p}_1$, $\mathbf{p}_2$,… that converge toward the local minima $\mathbf{p}^*$. The necessary condition for a minima in equation (6.3), is that its gradient is equal to zero. Since $\nabla\boldsymbol{\varepsilon}^\mathrm{T}\boldsymbol{\varepsilon} = -\mathbf{J}^\mathrm{T}\boldsymbol{\varepsilon}$, each step requires to solve the so-called normal equations to find the $\boldsymbol{\delta}_\mathrm{p}$ which minimizes equation (6.3):

$$\mathbf{J}^\mathrm{T}\mathbf{J}\boldsymbol{\delta}_\mathrm{P} = \mathbf{J}^\mathrm{T}\boldsymbol{\varepsilon}. \tag{6.6}$$

The Levenberg – Marquardt algorithm solves a variation of equation (6.6), referred to as augmented normal equations,

$$\mathbf{N}\boldsymbol{\delta}_\mathrm{P} = \mathbf{J}^\mathrm{T}\boldsymbol{\varepsilon} \tag{6.7}$$

with

$$\mathbf{N} = \lambda\mathbf{I} + \mathbf{J}^T\mathbf{J} \tag{6.8}$$

where $\mathbf{I}$ is the $m \times m$ identity matrix and λ is a positive number. That is, the off-diagonal elements of $\mathbf{N}$ are identical to the corresponding elements of $\mathbf{J}^T\mathbf{J}$, while the diagonal elements have been incremented by λ. The strategy of altering the diagonal elements of $\mathbf{J}^T\mathbf{J}$ is called damping and hence λ is called the damping term.

If the newer set of parameters $\mathbf{p} + \boldsymbol{\delta}_p$ obtained from equation (6.7) leads to a reduction of the error $\boldsymbol{\varepsilon}$, the update is retained and the process iterated with a decreased damping term. Otherwise, the update is rejected and the augmented normal equations are solved with an increased damping term, until a value of $\boldsymbol{\delta}_p$ that decreases the error is found. The process terminates when one of the following convergence conditions is fulfilled: (i) the magnitude of $\nabla\boldsymbol{\varepsilon}^T\boldsymbol{\varepsilon}$ drops below a threshold ε_1; (ii) the change in magnitude of $\boldsymbol{\delta}_p$ between two successive iterations drops below a threshold ε_2; (iii) $\boldsymbol{\varepsilon}^T\boldsymbol{\varepsilon}$ drops below a threshold ε_3; (iv) the maximum number of iterations is reached.

The Levenberg – Marquardt algorithm is adaptive, because it controls its own damping: the damping term is decreased if a reduction of the residuals is found, otherwise it is increased. Doing so, the algorithm is able to alternate between a slow approach, when the minimum is far away, and a fast convergence in proximity of the minima.

Once reached the minima, and hence the set of parameters which best describe the experimental data, their statistical errors are calculated from the covariance matrix.

6.4. Implementation of the Voigt Profile and the Complex Probability Function

The Voigt profile is widely used for modelling the spectral line profiles and in other scientific areas (for example, see [140] and references therein). As a consequence, the issue of its computation has been dealt over long time and intensive efforts have led to the development of many algorithms. A comprehensive survey of the different computational approaches has been reported by Schreier [141]. The most employed strategy consists in evaluating the complex probability function employing series and asymptotic expansions, rational approximations and Gauss – Hermite integrations [138, 142 – 147]. The computation of the imaginary part of the complex probability function is performed following the same methods [138, 145 – 147]. In particular, Humliček pointed out that rational approximations seems superior to other methods and

they may be very efficient once the parameters have been properly chosen [145, 146]. An *n*-term rational approximation is specified by 2*n* complex numbers

$$w(z) = \sum_{k=1}^{n} \frac{\alpha_k^{(n)} + i\beta_k^{(n)}}{z + \gamma_k^{(n)} + i\delta_k^{(n)}} \tag{6.9}$$

where α_k, β_k, γ_k and δ_k are real constants that have to be chosen in order to minimize the errors. The real parameters are related to the roots, $x_k^{(n)}$, and weights, $\lambda_k^{(n)}$, of the *n*-point Gauss – Hermite formula,

$$w(z) = \frac{1}{\pi} \sum_{k=1}^{n} \frac{\lambda_k^{(n)}}{z - x_k^{(n)}}, \tag{6.10}$$

by the following relations:

$$\alpha_k^{(n)} = -\frac{1}{\pi} \lambda_k^{(n)} \mathrm{e}^{\left[y_0^{(n)}\right]^2} \sin\left[2x_k^{(n)} y_0^{(n)}\right]$$

$$\beta_k^{(n)} = \frac{1}{\pi} \lambda_k^{(n)} \mathrm{e}^{\left[y_0^{(n)}\right]^2} \cos\left[2x_k^{(n)} y_0^{(n)}\right]$$

$$\gamma_k^{(n)} = x_k^{(n)}$$

$$\delta_k^{(n)} = y_0^{(n)}.$$

It follows that once the order of the approximation has been fixed, the only disposable constant is the real positive number $y_0^{(n)}$.

In VLSFP, the Voigt function is computed employing the optimized version of the Humliček's code proposed by Wells [138]. According to this implementation the variable domain of the function is subdivided into five different regions and within each of them a convenient expression for the real and imaginary parts of the complex probability function is used. The subdivision of the complex plane for y ≥ 0 is shown schematically in Figure 6.2. Far from the line centre, inside Region 0 where $|z| \to +\infty$, $w(z)$ is computed by a very simple expression:

$$w(z) = \frac{i}{\sqrt{\pi} z} \tag{6.11}$$

which gives adequate relative accuracy with a relative error less than 10^{-5}.

Within Region I and Region II, the function is computed by means of the following rational approximation of order 2 and 4, respectively:

$$w(z) = (-iz)^2 \frac{\sum_{k=1}^{n/2} c_k \left[(-iz)^2\right]^{k-1}}{(-iz)^n + \sum_{k=1}^{n/2} d_k \left[(-iz)^2\right]^{k-1}} \tag{6.12}$$

where the coefficients of the expansion are listed in Table 6.3 for $n = 2$ and 4 [146].

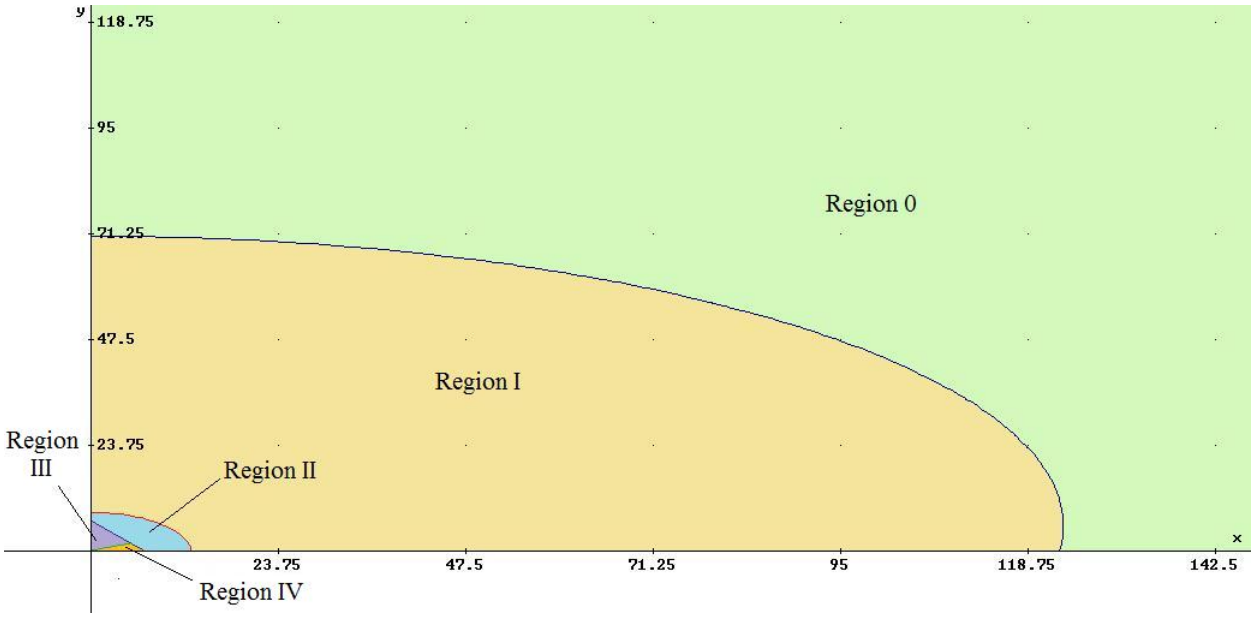

Figure 6.2. Schematic picture of the variable domain subdivision adopted to compute the complex probability function, $w(x, y)$.

Table 6.3. Coefficients of the approximation (6.12) for $n = 2$ and 4

n	*k*	*c*	*d*
2	1	0.56418958355	0.50000000000
4	1	1.4104739589	0.74999999999
	2	0.56418958355	3.0000000000

A slightly different rational approximation is adopted for region III:

$$w(z) = \frac{\sum_{k=1}^{5} a_k (-iz)^{k-1}}{(-iz)^5 + \sum_{k=1}^{5} b_k (-iz)^{k-1}} \tag{6.13}$$

with the coefficients a_k and b_k listed in Table 6.4 [146].

Table 6.4. Coefficients of the approximation (6.13)

k	*a*	*b*
1	16.4954955	16.4954955
2	20.2093334	38.8236274
3	11.9648172	39.2712051
4	3.77898687	21.6927370
5	0.0564223565	6.69939801

When high relative accuracy is required, the real part $u(z)$ of the complex probability function is most difficult to approximate by a rational function on the real axis. As a consequence, within region IV the imaginary part of $w(z)$ is computed employing the approximation (6.9) of the twelfth order, while the real part is approximated employing the following expression:

$$u(x,y) = e^{-x^2} + \sum_{k=1}^{n} \frac{y}{\left(x - x_k^{(n)}\right)^2 + \left(y_0^{(n)}\right)^2} \frac{\beta_k^{(n)}\left[\left(x - x_k^{(n)}\right)^2 - y_0^{(n)}\left(y - y_0^{(n)}\right)\right] - \alpha_k^{(n)}\left(x - x_k^{(n)}\right)\left(y + 2y_0^{(n)}\right)}{\left(x - x_k^{(n)}\right)^2 + \left(y + y_0^{(n)}\right)^2} \tag{6.14}$$

again with $n = 12$ and $y_0^{(12)} = -1.5$ [145].

The achieved relative error is between 10^{-4} and 10^{-5} and in general less than 10^{-5}, except for the region very close to the origin of the complex plane, where it starts to increase up to 10^{-2} at worst. Anyway the overall accuracy is properly adequate to describe the spectral line shapes, especially when both the Doppler and the Lorentz components contribute significantly to the resulting Voigt profile. Since the Well's algorithm computes also the imaginary part of the complex probability function, it can be conveniently used also for the computation of the Nelkin – Ghatak profile. Concerning the derivatives of the real part of the complex probability function, they have been computed following the supplementary algorithm given by Wells, with an accuracy suitable for line-by-line fitting purposes.

6.5. PROFILES INCLUDING DICKE NARROWING

As stated in Chapter 4, the Dicke narrowing is the contraction of the Doppler broadened width due to the effect of velocity changing collisions. Both the weak and strong collision models developed to treat this narrowing have been implemented in VLSFP.

The Nelkin – Ghatak profile, representing the strong collision limit, has been implemented employing the Well's algorithm described in the preceding section. The derivatives of the imaginary part of the complex probability function, $L(z)$, are derived from the derivatives of the real part by means of the Cauchy – Riemann conditions:

$$\frac{\partial K(z)}{\partial x} = \frac{\partial L(z)}{\partial y} \qquad \text{and} \qquad \frac{\partial K(z)}{\partial y} = -\frac{\partial L(z)}{\partial x}$$

where $K(z)$ denotes the real part of the complex probability function.

Concerning the Galatry profile, which is the expression for the weak collision limit, it is computed as the Fourier transform of its correlation function following the algorithm proposed by Ouyang and Varghese [139]:

$$f_G(x,y,z) = \frac{1}{\pi}\mathrm{Re}\{\Im[\Phi(y,z,t)]\} \tag{6.15}$$

where $\Im$ is the Fourier transform operator, $\Phi(y,z,t)$ is the correlation function and t the dimensionless time.

The actual evaluation of the Fourier transform is carried out employing a Discrete Fourier Transform (DFT), whose elements are equally spaced in time:

$$\Im[\Phi(y,z,t)] = \int_0^T \Phi(y,z,t)e^{-ixt}dt \approx \sum_{n=0}^{N-1} f_n e^{-ixn\Delta t} \tag{6.16}$$

with $\Delta t = \frac{T}{N-1}$, where T is the dimensionless time limit and N is the number of DFT points. The integrals f_n are given by:

$$f_n = \begin{cases} \int_0^{1/2} \Phi(y,z,t) \approx \dfrac{\Delta t}{6}\left[2\Phi(0) + \Phi\left(\dfrac{1}{2}\Delta t\right)\right] & \text{for } n = 0 \\ \int_{n-1/2}^{n+1/2} \Phi(y,z,t) \approx \dfrac{\Delta t}{6}\left[\Phi(n\Delta t - 0.5\Delta t) + 4\Phi(n\Delta t) + \Phi(n\Delta t + 0.5\Delta t)\right] & \text{for } n > 0 \end{cases}$$

(6.17)

It follows that the DFT of an array of N of equally spaced, discrete points of frequency x is given by:

$$F(x_k) = \sum_{n=0}^{N} f_n e^{-i\frac{2\pi kn}{N}} \qquad k = 0, 1, 2, \ldots, N-1 \tag{6.18}$$

with $x_k = \dfrac{2\pi k}{T}$; at an arbitrary frequency $x \neq x_k$ the Galatry function is obtained by interpolation.

The derivatives of the Galatry profile are computed following the same procedure, since they can be expressed as Fourier transforms, as well:

$$\frac{\partial f_G(x,y,z)}{\partial x} = \frac{1}{\sqrt{\pi}} \mathrm{Re}\{\Im[\Phi_x(y,z,t)]\}, \qquad \Phi_x(y,z,t) = -it\Phi(y,z,t) \tag{6.19}$$

$$\frac{\partial f_G(x,y,z)}{\partial y} = \frac{1}{\sqrt{\pi}} \mathrm{Re}\{\Im[\Phi_y(y,z,t)]\}, \qquad \Phi_y(y,z,t) = -t\Phi(y,z,t) \tag{6.20}$$

$$\frac{\partial f_G(x,y,z)}{\partial z} = \frac{1}{\sqrt{\pi}} \mathrm{Re}\{\Im[\Phi_z(y,z,t)]\}, \qquad \Phi_z(y,z,t) = \frac{\partial \Phi(y,z,t)}{\partial z} \tag{6.21}$$

In VLSFP, the derivatives of the Galatry function with respect to y and z are computed using the relations (6.20) and (6.21), respectively, while the derivative with respect to x is obtained from $\partial f_G / \partial y$ according to

$$\frac{\partial f_G(x,y,z)}{\partial x} = -\frac{\partial f_G(x,y,z)}{\partial y}.$$

The evaluation of the DFT is demanded to the FFT class in which it is implemented the algorithm for the computation of the Discrete Fast Fourier Transform [135]. The accuracy of the algorithm depends on the number N of DFT points. This number is a compromise between accuracy and computation time and in the current implementation it is set to 2048. For this number the minimum precision achieved is 0.1% when y is comprised between 0 and 0.15, as stated by Ouyang and Varghese [139].

6.6. DESCRIPTION OF THE USER INTERFACE

The graphical interface of Visual Line Shape Fitting Program is shown in Figure 6.3. From this interface the user has a complete control of the program: indeed, it is possible to define a project and declare the lines to be fitted. Then, from the tool bar, it is possible to start and stop the fitting procedure.

A VLSFP project is composed of three files:

(i) the experimental spectrum file (.esf/.dat);
(ii) the synthetic spectrum file (.csf);
(iii) the line parameter file (.psf).

For sake of clarity, the files can be grouped together into a project file (.lsf). Doing so, all the files can be loaded and saved at once by loading and saving the corresponding project. Each files comes into standard ASCII format. The only input data required by the program is the file storing the observed spectrum; the computed spectrum is saved as an absorbance spectrum in a file having format wavenumber, intensity, residual.

By right clicking on the spectrum panel, a contextual menu appears. From this menu it is possible to declare or delete the lines to be fitted and to define some of their parameters (for example the line centre and the bounds of the line). The remaining parameters, as well as the line shape function, are input by using the input panel on the right side of the interface. The value of each line parameter can be typed into the corresponding text box, while the “numeric up – down” control may be used to specify its percentage variability; setting the variability to zero keeps the parameter constrained during the Levenberg – Marquardt refinement.

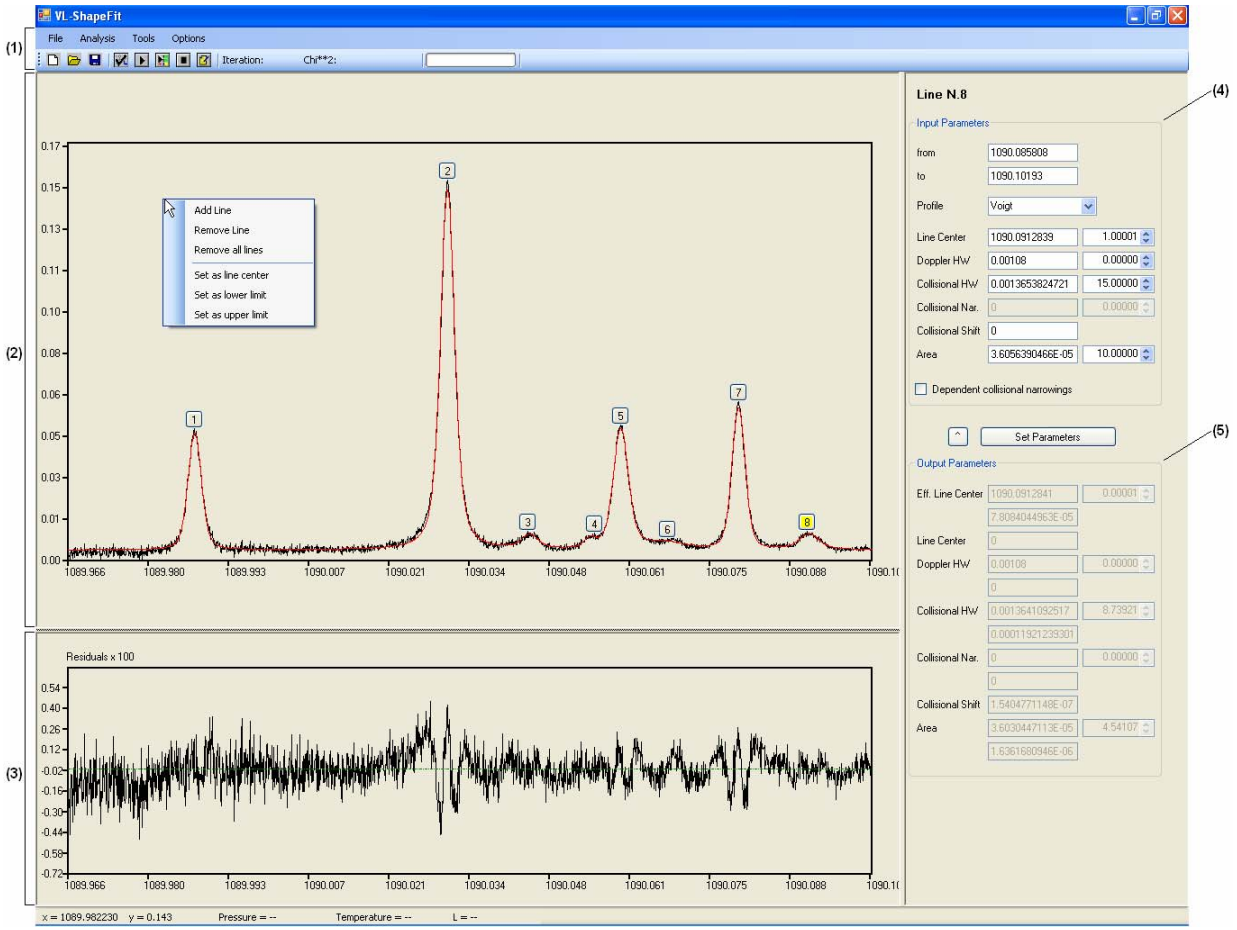

Figure 6.3. Graphical interface of VLSFP. The main regions are labelled: (1) menu and tool bars; (2) spectrum panel; (3) residual panel; (4) input panel; (5) output panel. In the spectrum panel the contextual menu for the declaration/delete of the lines is also shown.

Both the single line- and the multiple line- fitting procedures can be started (and stopped as well) by clicking on the appropriate button on the tool bar. The current status of the fit is displayed on the status bar as number of iterations and associated χ^2 value (sum of the squares, $\boldsymbol{\varepsilon}^T\boldsymbol{\varepsilon}$). The progress bar shows the overall advance of the fitting procedure. The program also presents useful tools to chose several options of the fit. For example, these features let the user to set the number of iterations, the convergence criteria of the fitting process and the field delimiters of the files.

At the end of the fit, the computed spectrum is plotted superimposed to the experimental one, while the residuals are shown into the relative panel. The resulting parameters are displayed into the output panel just under the input controls.

A number of additional features are accessible from the menu bar. For example, they allow the user to specify the experimental conditions, to set the range for the search of the maximum absorption when a line is declared, or to export the obtained parameters into a tab-delimited text file.

In the present implementation the maximum number of lines that can be declared and fitted is one thousand. Clearly, as the number of lines to be fitted increases, the fitting routine becomes

progressively slow, due to increased size of the matrices which the Levenberg – Marquardt algorithm deals with.

7. Sulphur Dioxide Line Parameters in the 9.2 μm Atmospheric Spectral Window

Sulphur dioxide is an important molecule which plays a significant role in many fields such as chemistry, biology and industry. It is of noticeable interest for the Earth's atmosphere since it actively enters into the sulphur cycle. The natural sources are biomass burning and volcanic eruptions. The latter are sporadic sources but they are capable to cause huge local fluctuations in the SO_2 concentration [148]. The main sources of sulphur dioxide arise from anthropogenic activities. Indeed it is widely employed by industry, in particular in winemaking and food preserving. Further, coal and petroleum often contain sulphur compounds which oxidize to SO_2 during their combustion. Once in the atmosphere, it is one of the main causes of acid rains. Sulphur dioxide is also of astrophysical importance: it has been identified in the interstellar medium, in particular in star forming regions [149], and it has also been detected on the surface of Io [150] and in the Venus atmosphere [151].

As a consequence, sulphur dioxide has always been widely studied using spectroscopic methods (see Refs. [152, 153] and references therein) and it is still the subject of considerable interest. Indeed, few years ago the ground state constants have been accurately re-determined as well as those of the excited vibrational state $\nu_2 = 1$ [154]. In the infrared region, the fundamental bands ν_1 and ν_3 of the $^{32}SO_2$ isotopologue have been deeply analyzed first by Guelachvili [155] and then re-investigated together with ν_2 and $2\nu_2 - \nu_2$ by Flaud et al. [156], taking also into account anharmonic and Coriolis resonances.

Great efforts have been devoted toward the determination of the broadening parameters of SO_2 whether self broadened [153, 157 – 159] or perturbed by air, nitrogen or noble gases [158 – 161]. Absolute line intensity measurements for some ro-vibrational transitions of ν_1 and ν_3 have been carried out through diode laser spectroscopy [153], while intensity determinations have been performed within the entire 950 – 1400 cm^{-1} spectral region by means of Fourier transform

spectroscopy [152]. Very recently, the line parameters of a number of transitions around 9 μm have been retrieved employing both continuous wave [162, 163] and pulsed Quantum Cascade lasers [164]. Further investigations within the range 1315 – 1395 cm^{-1} have been made using a difference frequency spectrometer [165].

The investigations have regarded not only the main isotopic species, but also $^{34}SO_2$. Very recently, Lafferty et al. [166] have carried out a complete analysis of the high resolution spectrum of $^{34}SO_2$ in the 19, 7 – 8 and 5 – 6 μm regions, whereas Flaud et al. [167] have measured a large number of individual line intensities for the ν_1, ν_3 and $\nu_1 + \nu_3$ bands determining expansions of the various transition moment operators.

Besides the experimental measurements, theoretical values of the self-broadening coefficients have been calculated several years ago by Tejwani [168] on the basis of the Anderson – Tsao – Curnutte (ATC) theory [65, 66]. A modification of this theory has been used by Lazarev et al. [161] to compute pressure broadening and shift coefficients of sulphur dioxide perturbed by noble gases.

Given the wide literature available about the subject, sulphur dioxide has been chosen as target molecule to define the experimental procedure for the retrieval of the line parameters by means of TDL spectroscopy and to test VLSFP as well. The present chapter deals with the determination of the line shape parameters for several ro-vibrational transitions of both $^{32}SO_2$ and $^{34}SO_2$ in the region around 9.2 μm. The self-broadening coefficients have also been determined theoretically using the ATC approximation. Further, the integrated band intensities of the three fundamental bands have been measured from medium resolution spectra recorded with a FT-IR spectrometer.

7.1. Experimental Procedure for Line Parameter Determinations: Characterization of Instrumental Distortions and Data Inversion

The SO_2 high resolution infrared spectra in the 9 μm region were recorded with the tunable diode laser spectrometer described in Chapter 5. The spectrometer was used in the two beams configuration: the main part of the laser radiation passed through the 92.3 cm path length cell (PLC), with KBr windows, containing the gas sample; the other part was directed into the Germanium etalon used for frequency calibration. Each experimental spectrum was the result of an average of 512 scans.

High-precision quantitative absorption measurements and detailed line shape determinations using TDL spectroscopy require a particular attention to the effect of the spectrometer instrumental function, because the measured spectrum is actually the convolution of the true spectrum with the instrumental function [169]. Each subsystem of a TDL apparatus and each step of the spectral acquisition and processing can introduce various sources of error, thus limiting both the precision and accuracy of the measurements. Amplitude and frequency noise, multimode and spontaneous emission from the laser, laser radiation astigmatism affect the quality of the spectra. Many factors limiting the precision of the determinations, such as optical feedback and interference from different optical elements, are related to the optics [170].

Indicatively, error sources can be grouped into two classes. The first one, involving the so-called technical errors, includes errors which can be eliminated by improving hardware and data processing procedure. The second class of error sources involves errors of fundamental nature (for example shot noise): they can be minimized, but not eliminated, by carefully checking at the experimental conditions [170]. It follows that each stage of the spectral acquisition and processing must be handled very prudently.

Therefore, the line shape distortions induced by the instrumental apparatus were accurately checked and minimized. In particular, it was discovered that the monochromator causes aberrations and asymmetries in the measured spectral profiles. The monochromator is responsible for a number of undesiderable effects among which there are: (i) an increase in the laser intensity noise due to the formation of optical feedback between the entrance slit of the monochromator and the laser; (ii) a significant increase in the instability of the power revealed by the photo detectors [170]. Consequently, the monochromator was employed just to find the frequency emission region of the laser, but it was removed during the measurements.

On the other hand, the absence of a frequency selecting element demanded severe requirements on the monochromaticity of the laser output radiation. In accordance, single mode and stability emission of the lead salt laser were accurately checked before data acquisition. The spurious emissions were detected by modulating the radiation emitted by the laser with the TDL chopper and locking the acquisition system to its reference signal. The radiation was considered as monochromatic only when the observed residual oscillations were below 1% of the detected laser emission power.

For the SO_2 measurements, each spectral micro-window was recorded at different pressures in the range 20 – 900 Pa; an example of the resulting series of spectra is given in Figure 7.1. The pressure was measured employing an Alcatel capacitance vacuum gauge with a full scale range of 1000 Pa and a quoted accuracy of 0.15%. Before each measurement the cell was evacuated down to

about 10^{-4} Pa by a diffusion pump backed by a double stage rotary pump. An elapsed time of 15 minutes between the filling of the cell and the recording of the spectra was adopted in order to promote the homogenization of the gas and avoid gradients of concentration and temperature. All measurements were carried out at 297 ± 1 K and the SO_2 sample provided by Sigma – Aldrich (99.9% purity) was used without further purification.

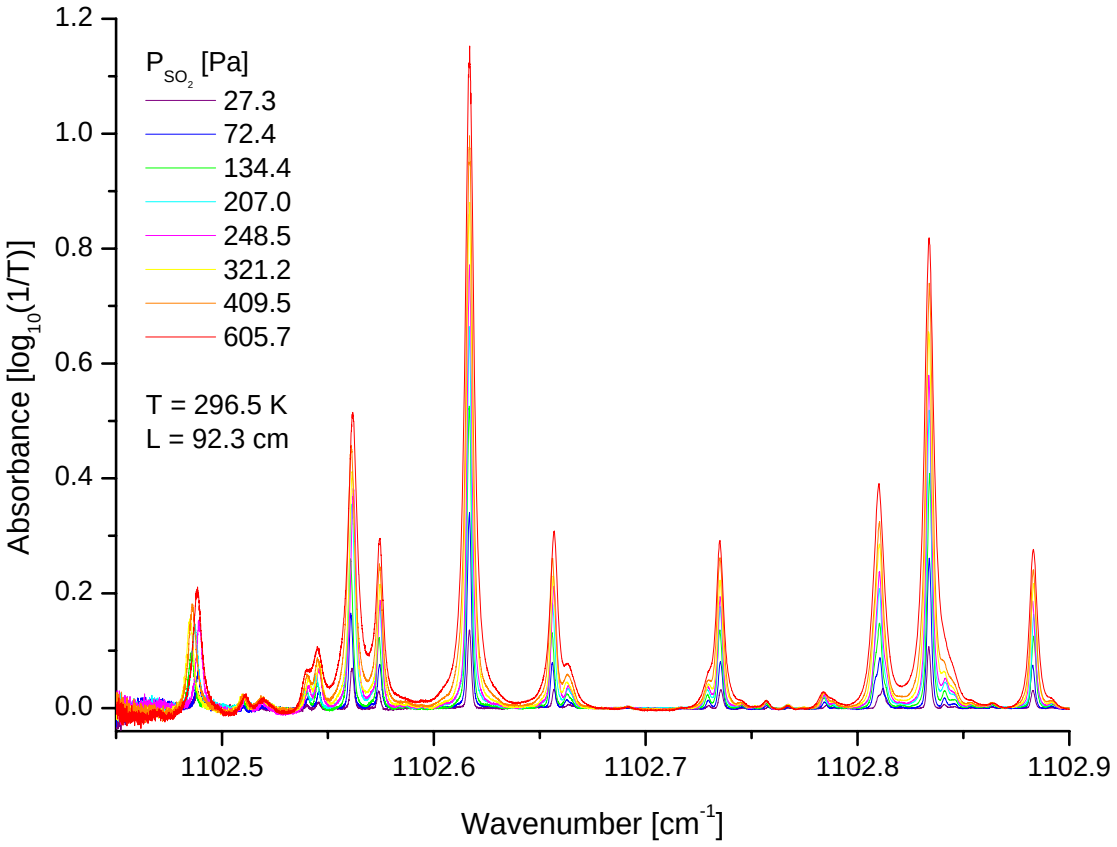

Figure 7.1. Example of the series of spectra recorded at different pressures of SO_2 in the region between 1102.45 and 1102.90 cm^{-1}. Details of the experimental conditions are given.

After being recorded, the spectra were first wavenumber calibrated and then transformed into the corresponding absorbance spectra. These operations were made by using an home-made package of programs written in MatLab [171]. The calibration was performed using the frequency of the SO_2 lines obtained from the high resolution FT-IR spectrum. The average wave number accuracy resulted about 5×10^{-4} cm^{-1}.

The experimental transmittance spectra were obtained according to the Beer – Lambert's law (equation 3.1) from the incident and transmitted radiation intensities, $I_0(\tilde{\nu})$ and $I(\tilde{\nu})$, respectively. As shown in Figure 7.2, the incident intensity was obtained by fitting the baseline to a high order polynomial or spline cubic function over the whole spectral region. In order to account

for a slight drift of the detector, the zero transmission level was fitted as well; this is also shown in Figure 7.2.

Baseline location is another crucial step which limits the accuracy of the retrieved line parameters. The experimental complications arise from the fact that in a real experiment $I(\tilde{\nu})$ and $I_0(\tilde{\nu})$ cannot be recorded neither simultaneously nor in the same conditions. Therefore the baseline is usually synthetized through a fitting procedure similar to that of Figure 7.2. This approach uses the spectral portions of negligible absorption to obtain a function which represents the synthetic baseline. For an error in the base line which is 1% of the absorption coefficient value at line centre, the errors in the retrieved parameters have been estimated to be 6%, 9% and 12% for the integrated absorption coefficient, the Gaussian line-width and the Lorentzian line-width, respectively [170].

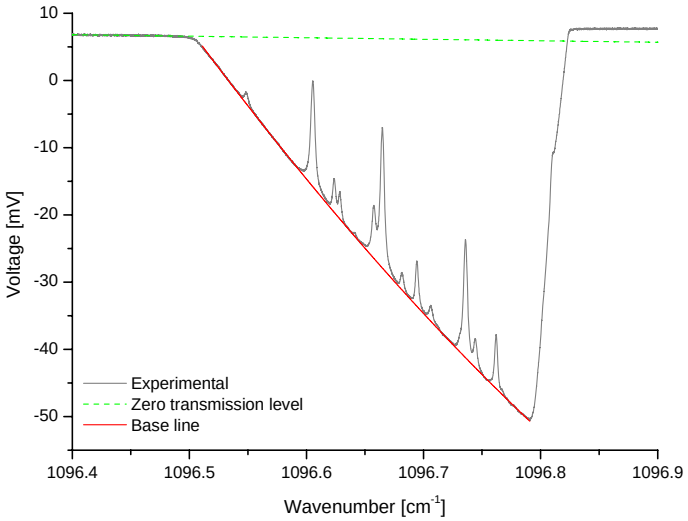

Figure 7.2. Data inversion procedure: the baseline is fitted to a polynomial function to obtain the spectral background; the maximum absorption level is fitted to account for the slight drift of the photo-detector.

The line parameters were retrieved by fitting the experimental features to the Voigt profile employing VLSFP: due to the overlap of different absorptions, the multi-line fitting approach was adopted. An example of the obtained results is given in Figure 7.3 (a). At this stage the contribution coming from the instrumental function must be explicitly taken into account. Unlike FTIR spectrometers whose instrumental response is determined by the geometry of the instrument itself, the shape of the instrumental function of a laser spectrometer is not well known and it is determined by the shape of the laser emission profile. The emission profiles and line widths of diode lasers vary from one device to another, depend on the instantaneous laser power and drive current noise characteristics and they have been described as nearly Gaussian or nearly Lorentzian ([169] and references therein). On a theoretical basis, the line shape of a laser emission profile can be thought as Lorentzian [113]. Nevertheless, there is a number of factors which lead to deviations from the Lorentzian line shape. For example, high-frequency broad-band noise on the laser current supply results in a Gaussian contribution to the instrumental function; a rectangular contribution arises from a linear drift of the laser tuning during a signal averaged measurement. Finally, low-frequency thermal and current drifts gives an irregular and unpredictable contribution. Given that the white noise Gaussian and the inherent Lorentz contributions are always present to some extent, the

instrumental function can be modelled as (nearly) Gaussian or (nearly) Lorentzian depending on the relative magnitude of each contribution.

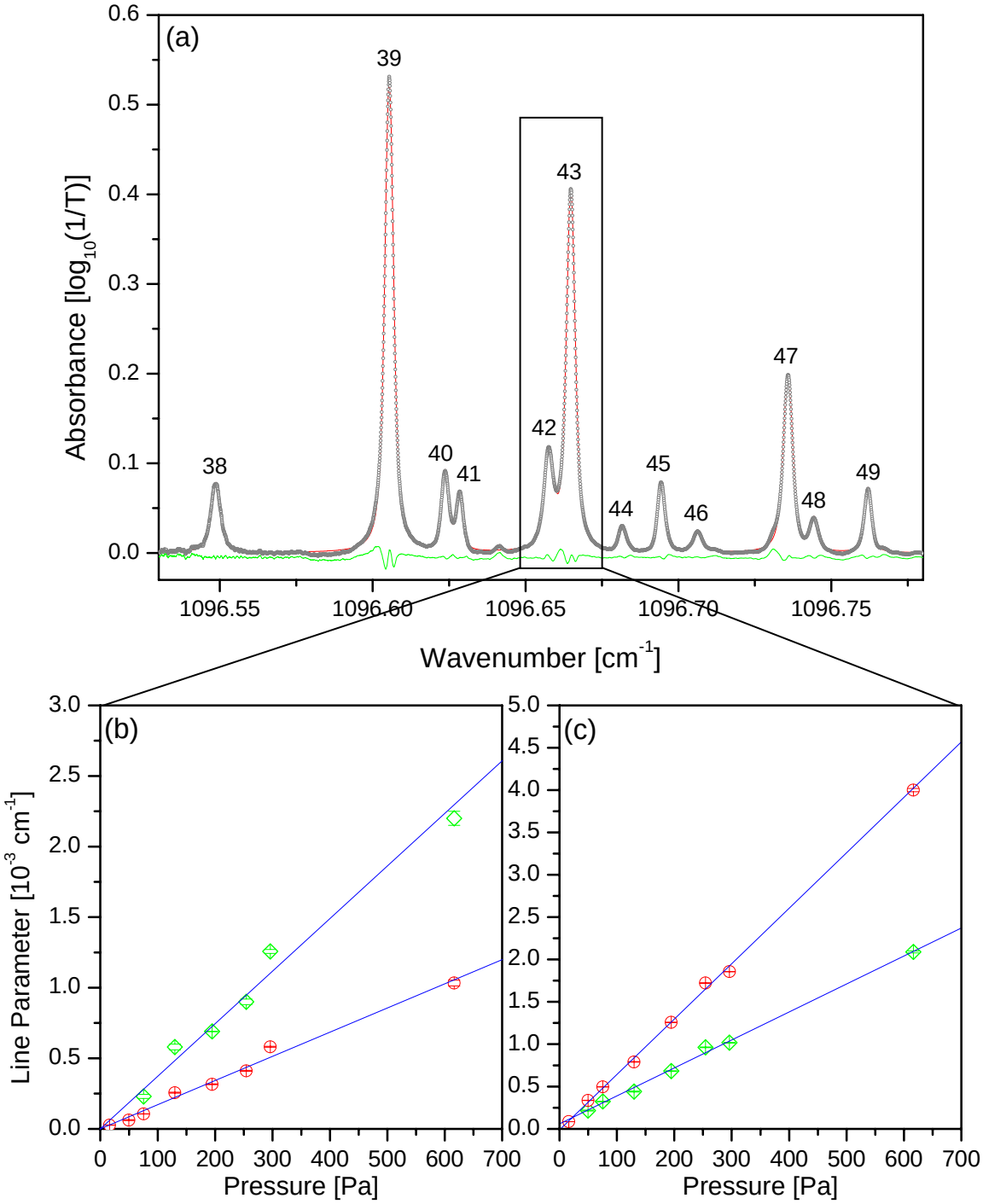

Figure 7.3. Panel (a) shows the SO_2 spectrum (○) between 1096.5 and 1096.8 cm^{-1} (P_{SO_2} = 296.0 Pa, PLC = 92.3 cm, T = 297 K). The synthetic spectrum (—), as obtained from the fit of the experimental absorption features to the Voigt profile, and the corresponding residuals (—) are also shown. Panels (b) and (c) give an example of the linear regressions performed on the retrieved line parameters as a function of the gas pressure for lines 42 and 43, respectively: (◇) collisional half width; (○) line intensity.

Strictly speaking, both contributions can be significant and hence the proper instrumental function of a TDL spectrometer is a Voigt function. In the small absorbance limit, modelling the effect of a Voigt instrumental function on a Voigt absorption line is quite simple, given that the convolution of two Voigt functions is still a Voigt function. The effective Gaussian width, γ_D^{eff}, of the measured Voigt profile is the square root of the sum of the squares of the molecular, $\gamma_D^{molecular}$, and instrumental, γ_D^{TDL}, Gaussian widths, respectively:

$$\gamma_D^{eff} = \sqrt{\left(\gamma_D^{molecular}\right)^2 + \left(\gamma_D^{TDL}\right)^2} \,. \tag{7.1}$$

The effective Lorentzian width, γ_L^{eff}, is the sum of the pressure broadened half width, γ_L, and the Lorentzian instrumental width, γ_L^{TDL}:

$$\gamma_L^{eff} = \gamma_L + \gamma_L^{TDL} \,. \tag{7.2}$$

The measured integrated absorption coefficient remains unaffected. However, if the small absorption limit is not met, the effect of a Voigt instrumental function is more complicated and the treatment above outlined is no longer valid [169].

As shown in Figure 7.4, a low pressure spectral line can be well reproduced by a Doppler profile, and hence in the present case the instrumental line shape function can be considered to a very good approximation as a Gaussian distribution. Therefore, the instrumental contribution to the absorption line shapes was taken into account by keeping the Doppler half width fixed to the value given by equation (7.1) during the fitting procedure. The effective Doppler half-width was obtained by fitting the experimental absorptions recorded at low pressure (< 30 Pa) to a Gaussian profile, as

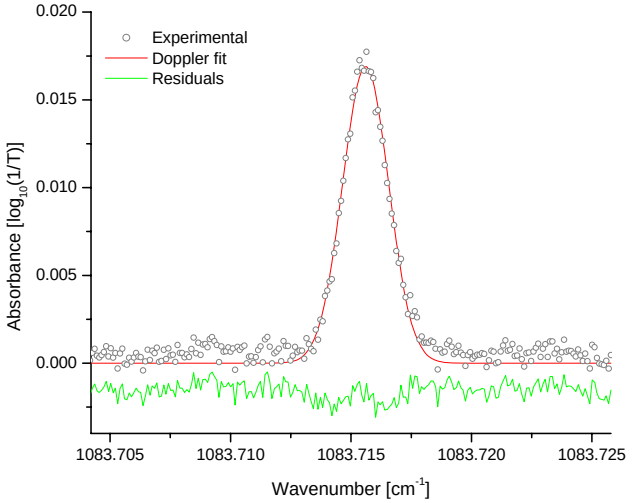

Figure 7.4. SO_2 spectral line recorded at low pressure (P = 29.5 Pa, T = 297 K, PLC = 92.3 cm). The experimental line shape is properly reproduced by the Doppler profile, thus suggesting that the instrumental function is nearly Gaussian.

shown in Figure 7.4. By setting the molecular Doppler half width to the value given by equation (3.19), γ_D^{TDL} resulted to range from to $3.6 \cdot 10^{-4}$ cm^{-1} to $1.6 \cdot 10^{-3}$ cm^{-1} and have an average value of $8.2 \cdot 10^{-4}$ cm^{-1}, for the employed 9.2 μm laser and the investigated micro-window.

7.2. Experimental Procedure for Sulphur Dioxide Vibrational Cross Section Measurements

The measurements of the absorption cross sections were carried out using the Bruker Vertex 70 FTIR instrument of Section 5.2 equipped with a 134.0 (± 0.5) mm path-length cell with KBr windows; the temperature in the cell was kept constant at 298 (± 1) K. A total of 128 interferograms for both the background and the spectra were co-added and transformed into the absorbance spectrum, using boxcar apodization and Mertz phase correction.

In analytical applications it is normal practice to employ a resolution greater than the full width at half height of the spectral absorption feature, in order to avoid non-linear behaviour at absorbances greater than 0.5. This is a good rule when solid or liquid samples are analyzed, but in the gas phase the situation is complicated by the fine rotational structure. Since for medium resolution gas phase measurements the rotational structure cannot be resolved, the optimum experimental conditions are those which include all the vibrational information and no rotational information. Therefore, the FTIR spectra were recorded at the resolution of 0.2 cm^{-1}, using SO_2 pressures in the range 100 – 1400 Pa, and the measurements were carried out on both pure sulphur dioxide and SO_2 mixed with 1000 kPa of nitrogen. While the employed resolution led to the maximum vibrational information, the effect of pressurization with nitrogen was to broaden the rotational spectral lines thus reducing the contribution of the fine rotational structure to the interferogram. Pressure measurements were performed employing three different capacitance vacuum gauges (Alcatel model ARD 1001, 1002 and 1003 with a full scale range of 1013, 101 and 10 hPa, respectively), each with a quoted manufacturer's full scale accuracy of 0.15%.

The same procedure described in the previous section for the evacuation and the filling of the cell was adopted and 20 minutes were waited before the entrance of the gas in the cell and the recording of the spectrum. Adsorption of the gas on the cell walls was checked both by direct measurement of pressure, and by monitoring the absorption spectrum: it was found to be negligible over a period of 2 hours, which is far longer than the time required to obtain a spectrum.

The vibrational absorbance cross section per molecule (cm^2 $molecule^{-1}$), $\sigma(\tilde{\nu})$, was calculated from the measured spectrum by using the following relationship

$$\sigma(\tilde{\nu}) = \frac{A(\tilde{\nu})\ln 10}{n\ell} \tag{7.3}$$

where $A(\tilde{\nu})$ is the absorbance at wavenumber $\tilde{\nu}$, n is the number density (molecules cm^{-3}) and ℓ is the optical path length (cm). Assuming the validity of the ideal gas law, the integrated cross section G_{int} (cm $molecule^{-1}$) is derived from the absorbance cross section by means of the following equation:

$$G_{int} = \int_{\tilde{\nu}_1}^{\tilde{\nu}_2} d\tilde{\nu}\ \sigma(\tilde{\nu}) = \frac{10^6 RT\ln 10}{N_A \ell P} \int_{\tilde{\nu}_1}^{\tilde{\nu}_2} d\tilde{\nu}\ A(\tilde{\nu}) \tag{7.4}$$

where P (Pa) and T (K) are the gas pressure and temperature, respectively, R is the molar gas constant (J K^{-1} mol^{-1}) and N_A is the Avogadro's number. The integration limits, $\tilde{\nu}_1$ and $\tilde{\nu}_2$, correspond to wavenumbers of negligible absorption.

The experimental uncertainty in the cross sections was estimated, as suggested by Nemtchinov and Varanasi [172], by taking into account the uncertainties of the pressure and temperature of the sample, of the optical path length, of the photometric accuracy of the FTIR spectrometer and of the evaluation of absorbance; in general, it resulted better than 7%.

7.3. SEMICLASSICAL CALCULATION OF SELF-BROADENING COEFFICIENTS

The sulphur dioxide self-broadening coefficients have been theoretically determined by using the semiclassical formalism presented in Section 3.8. The broadening coefficients γ_L^0 have been calculated for the lines of interest, obtaining values between 0.5 and 0.1 $cm^{-1}atm^{-1}$. This corresponds to collisional cross sections, $\sigma = \pi r^2$, between 880 and 175 $Å^2$ and radii r between 16.7 and 7.5 Å. For so large cross sections, the ATC approximation is reliable because collisional relaxation is well described by Eq. (3.37) up to large b values and what happens at short distances (deflection of the trajectory and velocity changes) is not important. Moreover, at large distances the relevant interaction is surely the dipole – dipole one. On the whole, the accuracy of theoretical calculations should be of the order of 10%, with the caution that an underestimation is possible for

the lines having a broadening coefficient smaller than 0.20 $cm^{-1}atm^{-1}$. In this case the contribution of interactions other than the dipole – dipole one could be not completely negligible.

Eq. (3.35) allows a straightforward interpretation of the dependence of γ_L on the rotational quantum numbers. Since the difference between upper and lower levels is not large, one usually considers the lower level l = J'', K_a'', K_c'': it is known that for SO_2 self-broadening is almost independent on J'', while it decreases for increasing values of K_a''. By Eq. (3.35) and (3.36) and Figure 3.3, it can be seen that an important role is played by energy transfer. The average absolute value of x_p depends on the rotational energy exchanged by the perturber:

$$\overline{|x_p|} = \frac{b}{v\hbar}\sum_p \rho_p \sum_{p'} \frac{1}{\mu_p^2}\left|\langle p|\mu_p|p'\rangle\right|^2 |E_{p'} - E_p|, \tag{7.5}$$

where two kinds of average are included: an average on ingoing states p, weighted by their population ρ_p, and an average on the dipole-allowed transitions $p \rightarrow p'$, weighted, according to Eq. (3.35), by the square of the dipole matrix moment $\left|\langle p|\mu_p|p'\rangle\right|^2$. By setting the relative velocity to its mean value $\bar{v}$ = 4.43×10^4 $cm\cdot s^{-1}$ and b to the typical value of 10 Å, $\overline{|x_p|}$ results to be 10.4. For a given lower state l of the absorbing molecule, the average absolute value of x_l is:

$$\overline{|x_l|} = \frac{b}{v\hbar}\sum_{l'} \frac{1}{\mu_l^2}\left|\langle l|\mu_p|l'\rangle\right|^2 |E_{l'} - E_l|. \tag{7.6}$$

From Figure 3.2 it can be argued that when $|x_l + x_p|$ $>\approx$ 5 the broadening contribution is strongly reduced. Hence, in order to get a large effect, x_l and x_p must either be both small or have opposite signs and similar absolute values. This is less probable when $\overline{|x_l|}$ becomes larger than $\overline{|x_p|}$. The dependence of $\overline{|x_l|}$ on J'' is plotted in Figure 7.5 for K_a'' = 0, 5, 10, 20, 30 and 40. For K_a'' = 0 and 5 $\overline{|x_l|}$ may become larger than $\overline{|x_p|}$ only when J'' > 40. On the contrary, for K_a'' = 10, 20, 30 and 40, $\overline{|x_l|}$ is almost independent on J'', while it increases with K_a'' and is always larger than $\overline{|x_p|}$.

On the whole, the absorption lines with higher K_a'' values have lower broadening coefficients because collisional relaxation is hampered by the larger energy amount involved in the dipole-allowed rotational transitions.

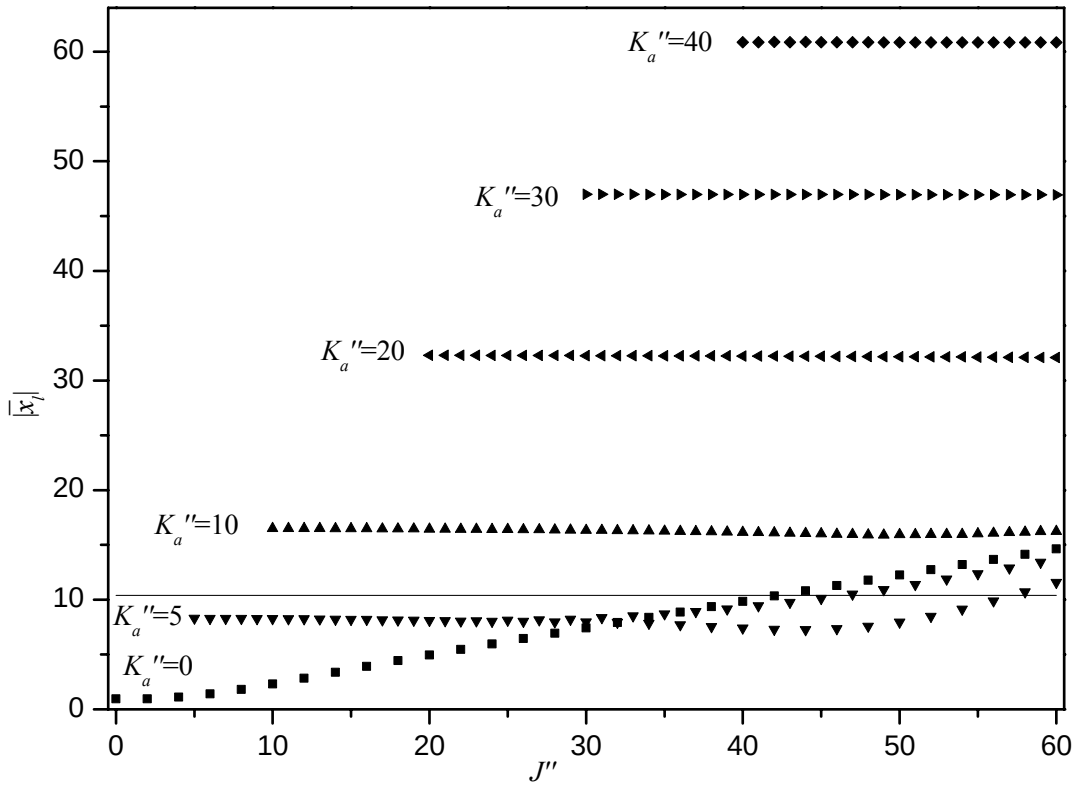

Figure 7.5. Dependence of the quantity $\overline{|x_l|}$, defined in Eq. 7.6, on the quantum number *J*". The cases K_a'' = 0 (■), 5 (▼), 10 (▲), 20 (◄), 30 (►) and 40 (◆) are considered. Solid line reports the average value $\overline{|x_p|}$ for the perturbing molecule.

7.4. EXPERIMENTAL RESULTS AND DISCUSSION

The self-broadening coefficients, γ_L^0, and the integrated absorption coefficients, S^0, have been obtained using a curve of growth technique. Since in the adopted experimental conditions the coefficients are linearly dependent on the pressure, the retrieved line parameters lie on straight lines of equations

$$\gamma_L = \gamma_L^{TDL} + \gamma_L^0 p_{SO_2} \tag{7.7}$$

$$S = S_0 + S^0 p_{SO_2} \tag{7.8}$$

where the intercepts should be zero within the experimental uncertainty. As a consequence, a linear regression of the line parameters plotted as a function of the gas pressure gives the involved coefficient, as shown in Figure 7.3 (b) and (c). Using this technique, it is possible to check the linearity of the line parameters and their physical consistency.

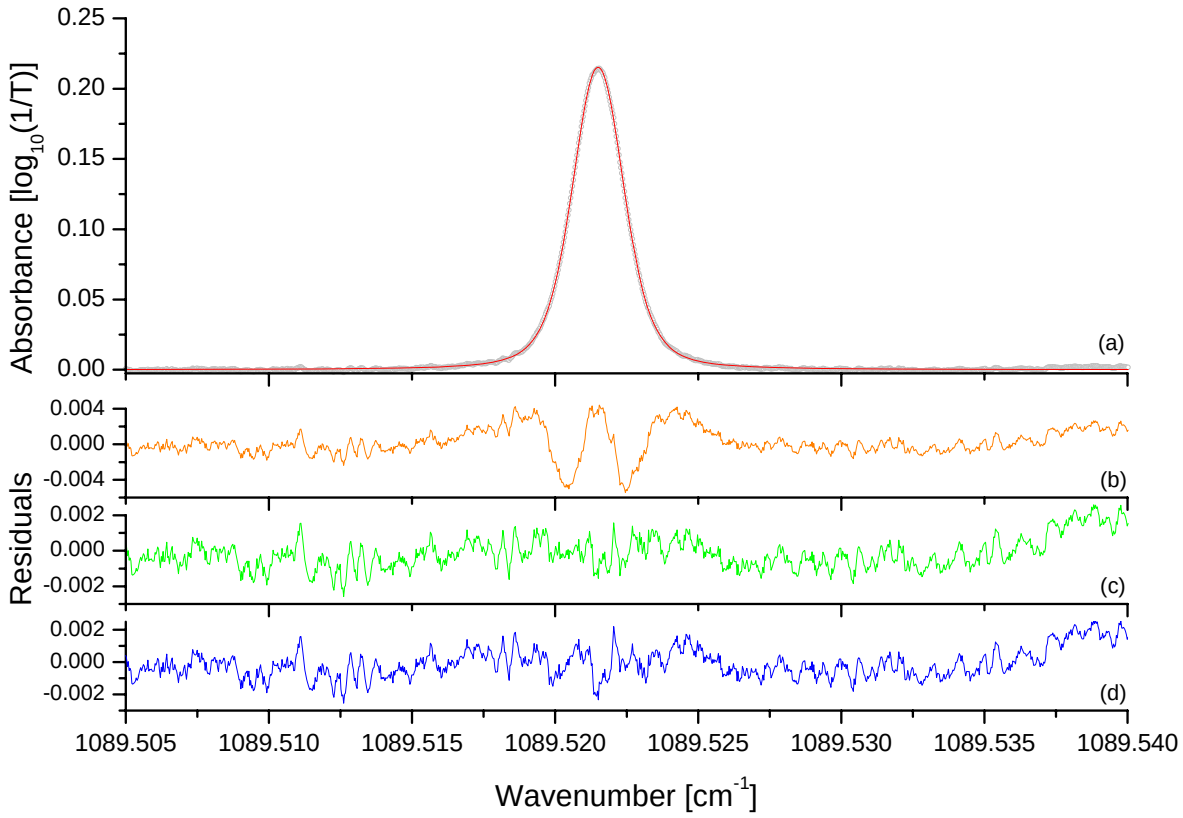

Figure 7.6. Isolated absorption line corresponding to the $20_{14,6} \leftarrow 21_{15,7}$ transition. Row (a) shows the experimental (○) and computed spectrum (—). Experimental details: SO_2 total pressure = 107.0 Pa, PLC = 92.3 cm, temperature = 297 K. The remaining rows show the residuals obtained from different models: (b, —) Voigt; (c, —) weak collision model (wcm); (d, —) strong collision model (scm). The standard deviations of the fits, σ (cm^{-1}), are: $\sigma_{Voigt} = 1.6 \times 10^{-3}$; $\sigma_{wcm} = 0.88 \times 10^{-3}$; $\sigma_{scm} = 0.90 \times 10^{-3}$. Note the deviations from the Voigt profile typical of Dicke narrowing and how they reduce when Galatry or Nelkin – Ghatak profiles are used.

Generally, the experimental features are well reproduced by the Voigt profile, even if in some circumstances the plot of the residuals shows some regular trends. These are not due to instrumental distortions, since the lines recorded at low pressure are well described by a Gaussian function. Rather, the shape of the residuals suggests that Dicke narrowing is acting, as shown in Figure 7.6 in the case of an isolated line corresponding to the ro-vibrational transition $20_{14,6} \leftarrow 21_{15,7}$. When the Dicke narrowing is taken into account, the line is properly reproduced by either the Nelkin – Ghatak or the Galatry profiles. However, in the majority of the circumstances and especially in dense spectral regions, neither the use of the weak and strong collision models is capable to completely account for the observed deviations. An example of such a situation is given in Figure 7.7 where the spectral region between 1089.69 and 1089.87 cm^{-1} is reproduced. The

possible explanation for this behaviour is the presence of weak absorptions underneath the stronger ones, as also suggested by the fact that the magnitude of some residuals increases with the pressure. These lines, being not resolved at all, cannot be taken into account during the fits but at the same time cause asymmetries in the observed absorptions. Further, the high density of lines in the region investigated is also due to the weak absorptions belonging to $\nu_1 + \nu_2 - \nu_2$ of $^{32}SO_2$ and ν_1 of $^{34}SO_2$. These, which at low pressure are below the detection threshold of the interferometer, become progressively more significant as the number density of the SO_2 sample increases thus explaining the increase in the magnitude of the residuals as the SO_2 pressure raises. For the same reasons, the Dicke narrowed profiles are not able to account for all the deviations. Anyway, it is remarkable that even in the presence of strongly overlapped lines, the physical meaning of the line parameters is preserved as confirmed by their linearity with respect to the pressure, see Figure 7.3 (b) and (c).

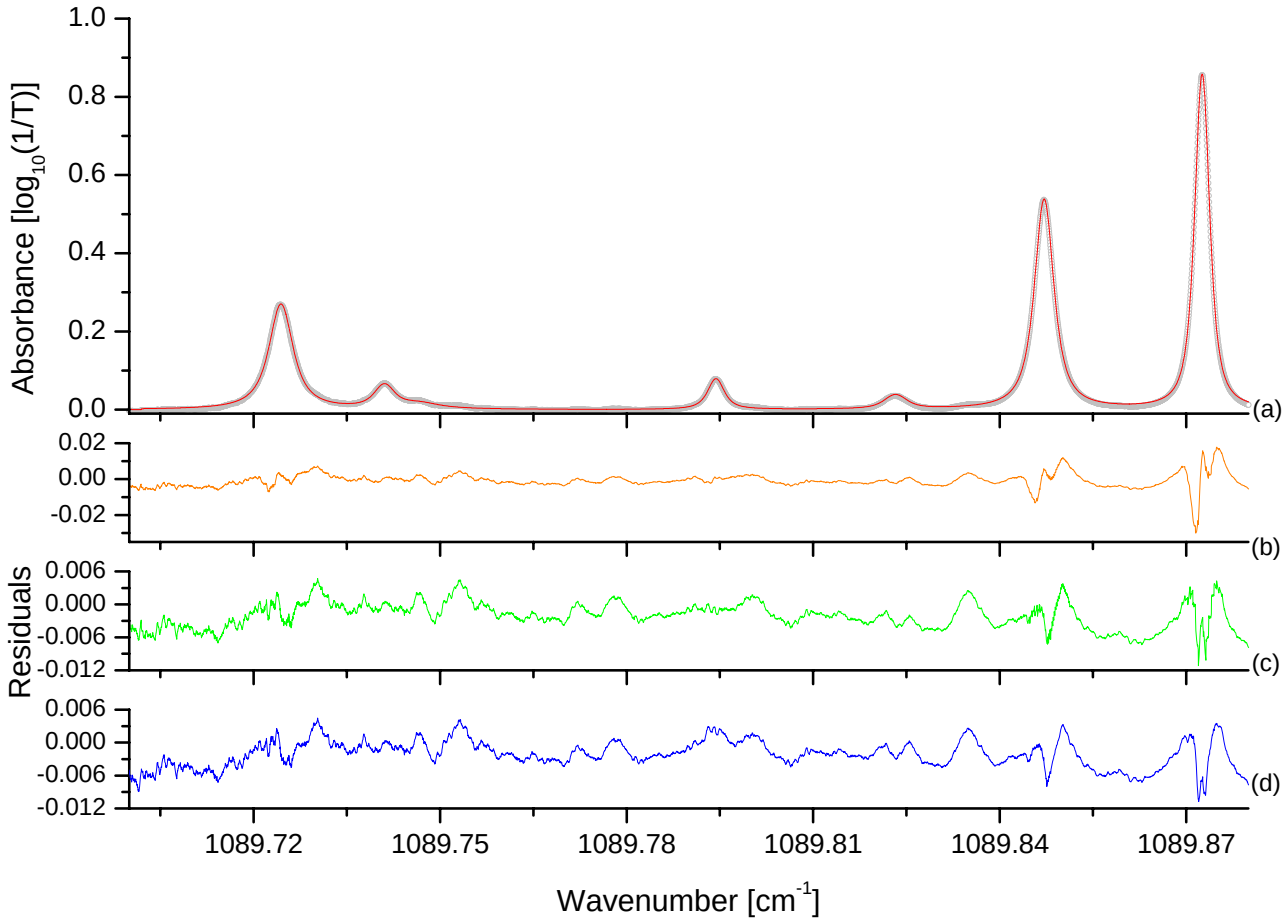

Figure 7.7. SO_2 spectrum between 1089.69 and 1089.87 cm^{-1}: row (a) shows the experimental (○) and computed spectrum (—). Experimental details: SO_2 total pressure = 511.4 Pa, PLC = 92.3 cm, temperature = 297 K. The remaining rows show the residuals obtained from different models: (b, —) Voigt; (c, —) weak collision model (wcm); (d, —) strong collision model (scm). The standard deviations of the fits, σ (cm^{-1}), are: $\sigma_{Voigt} = 4.0 \times 10^{-3}$; $\sigma_{wcm} = 3.1 \times 10^{-3}$; $\sigma_{scm} = 3.2 \times 10^{-3}$. The residuals persists even when the Dicke narrowed models are employed.

Table 7.1 (1 of 3). Line labelling, assignment and line parameters of ν_1 band of $^{32}SO_2$ [a]

Line N.	J'	K_a'	K_c'	J''	K_a''	K_c''	ν_0^{exp} [b]	$\gamma_L^{0,exp}$ [c]	$\gamma_L^{0,calc}$ [c]	S_{exp}^0 [d]	S_{lit}^0 [d, e]	S_{Hitran}^0 [d, f]
1	20	16	4	21	17	5	1083.25644(10)	0.262(11)	0.1496	6.32(11)	7.348	7.23
1	33	13	21	34	14	20			0.29288			
2	33	20	14	33	21	13	1083.3399(2)	0.24(3)	0.11372	0.315(8)	0.3669	0.296
5	55	8	48	56	9	47	1083.4370(4)	0.38(8)	0.43713	0.15(2)	0.2241	0.291
6	32	20	12	32	21	11	1083.4530(4)	0.23(6)	0.11040	0.26(3)	0.3802	0.306
7	37	12	26	38	13	25	1083.4796(2)	0.324(11)	0.33836	2.032(6)	2.080	2.27
10	24	15	9	25	16	10	1083.5169(2)	0.262(3)	0.19378	4.09(4)	4.237	2.27
11	31	20	12	31	21	11	1083.5635(2)	0.18(3)	0.10706	0.328(2)	0.3887	0.313
12	52	19	33	52	20	32	1083.5839(2)	0.261(12)	0.20093	0.12(2)	0.08710	0.0710
15	49	4	46	50	5	45	1083.61175(13)	0.52(5)	0.49231	0.095(12)	0.1267	0.153
16	50	9	41	51	10	42	1083.6283(3)	0.341(11)	0.38110	0.573(12)	0.5012	0.620
17	30	20	10	30	21	9	1083.6706(3)	0.191(14)	0.10374	0.318(7)	0.3943	0.317
18	41	11	31	42	12	30	1083.7149(2)	0.356(11)	0.36688	1.56(4)	1.475	1.48
19	28	14	14	29	15	15	1083.764(4)	0.270(5)	0.24000	3.70(5)	3.688	3.73
20	29	20	10	29	21	9	1083.7739(4)	0.199(7)	0.10036	0.365(4)	0.3953	0.318
21	20	14	6	21	15	7	1089.52139(7)	0.266(5)	0.20598	5.51(3)	6.790	7.15
22	33	11	23	34	12	22	1089.72440(9)	0.340(10)	0.35646	3.55(6)	3.698	4.01
24	29	18	12	29	19	11	1089.79423(13)	0.20(2)	0.13791	0.65(2)	0.8634	0.713
25	51	7	45	52	8	44	1089.8234(2)	0.40(6)	0.45981	0.51(5)	0.4501	0.580
26	24	13	11	25	14	12	1089.84713(3)	0.268(7)	0.25521	5.70(5)	6.071	6.09
27	15	15	1	16	16	0	1089.87257(4)	0.161(7)	0.1516	6.78(8)	7.679	7.15
28	28	18	10	28	19	9	1089.8912(7)	0.277(10)	0.13421	0.70(3)	0.870	0.719
30	27	18	10	27	19	9	1089.9877(3)	0.20(3)	0.13046	0.72(4)	0.8662	0.715
31	37	10	28	38	11	27	1090.03033(9)	0.35(2)	0.38531	2.71(10)	2.714	3.06
33	26	18	8	26	19	7	1090.0797(2)	0.21(3)	0.1267	0.90(3)	0.8500	0.702
34	46	8	38	47	9	39	1090.1414(2)	0.32(2)	0.41063	0.94(2)	0.9930	1.22
35	28	12	16	29	13	17	1090.1595(13)	0.31(2)	0.30616	5.1(2)	5.135	5.34
36	25	18	8	25	19	7	1090.1683(2)	0.21(3)	0.1229	1.01(4)	1.103	0.676
36 [g]	36	9	27	37	10	28			0.4022			
37	19	14	6	20	15	5	1090.22675(12)	0.22(2)	0.20141	6.2(2)	7.234	6.97
38	22	16	6	22	17	5	1096.5478(12)	0.195(14)	0.15667	1.16(8)	1.541	1.31

Table 7.1 continued (2 of 3)

Line N.	J'	K_a'	K_c'	J''	K_a''	K_c''	ν_0^{exp} [b]	$\gamma_L^{0,exp}$ [c]	$\gamma_L^{0,calc}$ [c]	S_{exp}^0 [d]	S_{lit}^0 [d, e]	S_{Hitran}^0 [d, f]
39	19	12	8	20	13	7	1096.60539(8)	0.30(2)	0.2674	8.1(2)	10.36	9.78
39	43	4	40	44	5	39			0.5053			
40	21	16	6	21	17	5	1096.6240(4)	0.25(2)	0.15233	1.16(5)	1.409	1.19
42	42	7	35	43	8	36	1096.6577(2)	0.48(7)	0.44232	1.84(11)	1.816	2.21
43	28	10	18	29	11	19	1096.66481(8)	0.335(14)	0.37415	6.70(14)	7.294	7.13
43 [h]	15	11	5	16	12	4			0.2927			
44	48	15	33	48	16	32	1096.6821(2)	0.12(8)	0.2892	0.35(7)	0.4880	0.419
45	20	16	4	20	17	3	1096.69442(12)	0.15(2)	0.14785	0.99(6)	1.229	1.04
47	37	8	30	38	9	29	1096.73588(13)	0.39(3)	0.4139	3.55(13)	3.253	3.78
49	19	16	4	19	17	3	1096.7617(3)	0.18(2)	0.14295	1.00(5)	1.002	0.847
50	26	14	12	26	15	11	1102.487(2)	0.21(2)	0.23003	2.34(10)	3.367	2.93
52	29	8	22	30	9	21	1102.5613(4)	0.39(4)	0.42856	6.5(3)	7.319	8.12
53	25	14	12	25	15	11	1102.5743(3)	0.26(2)	0.22577	2.93(10)	3.395	2.95
54	15	11	5	16	12	4	1102.61678(5)	0.33(2)	0.28482	13.1(3)	13.90	13.6
55	24	14	10	24	15	9	1102.6563(4)	0.37(3)	0.22154	3.18(14)	3.376	2.94
56	51	13	39	51	14	38	1102.6636(2)	0.32(6)	0.33643	0.86(3)	0.7669	0.483
56 [h]	30	12	18	30	13	17			0.3205			
58	23	14	10	23	15	9	1102.73521(12)	0.23(3)	0.21723	2.83(14)	3.329	2.89
59	22	14	8	22	15	7	1102.81016(7)	0.28(3)	0.21292	5.4(2)	4.937	4.92
59	41	5	37	42	6	36			0.4967			
60	24	9	15	25	10	16	1102.83387(10)	0.352(12)	0.39634	10.1(3)	10.02	10.7
61	21	14	8	21	15	7	1102.8830(2)	0.25(2)	0.20864	2.71(6)	3.073	2.67
64	20	14	6	20	15	5	1102.9522(3)	0.28(3)	0.20413	2.52(12)	2.865	2.49
65	49	13	37	49	14	36	1102.9616(2)	0.29(3)	0.3360	0.75(3)	0.7130	0.628
68	19	14	6	19	15	5	1103.0182(4)	0.21(2)	0.19951	2.46(11)	2.591	2.59
69	33	7	27	34	8	26	1103.0563(4)	0.402(13)	0.43908	5.37(10)	5.300	6.11
70	18	14	4	18	15	3	1103.0813(2)	0.27(4)	0.19472	2.09(11)	2.251	1.96
71	19	10	10	20	11	9	1103.08964(13)	0.35(3)	0.34122	12.4(6)	12.48	12.8
72	48	13	35	48	14	34	1103.1077(4)	0.29(6)	0.33539	0.57(6)	0.8085	0.713
74	17	14	4	17	15	3	1103.1408(3)	0.22(3)	0.18965	1.50(7)	1.835	1.59

Table 7.1 continued (3 of 3)

Line N.	J'	K_a'	K_c'	J''	K_a''	K_c''	ν_0^{exp} [b]	$\gamma_L^{0,exp}$ [c]	$\gamma_L^{0,calc}$ [c]	S_{exp}^0 [d]	S_{lit}^0 [d, e]	S_{Hitran}^0 [d, f]
76	16	14	2	16	15	1	1103.1972(3)	0.18(3)	0.18501	1.26(5)	1.324	1.15
79	38	6	32	39	7	33	1103.2432(3)	0.40(3)	0.47186	3.07(10)	3.064	3.70
80	47	13	35	47	14	34	1103.2505(3)	0.29(3)	0.33425	1.70(6)	1.629	1.43
80	15	14	2	15	15	1			0.1796			
81	28	8	20	29	9	21	1103.2824(3)	0.43(2)	0.42916	8.4(3)	7.972	8.79
82	14	11	3	15	12	4	1103.30473(9)	0.27(2)	0.27987	13.7(4)	14.56	14.2
83	46	13	33	46	14	32	1103.3921(5)	0.29(5)	0.33268	1.21(8)	1.031	0.909

[a] In case of overlapped transitions the literature value of the line intensity is obtained by summing the individual line intensities of each transition (where available). Figures in parentheses correspond to one standard deviation.
[b] Values expressed in cm^{-1}.
[c] Values expressed in cm^{-1} atm^{-1}.
[d] Values expressed in 10^{-22} cm molecule^{-1}.
[e] From Ref. [152].
[f] From Ref. [15].
[g] Transition belonging to $\nu_1 + \nu_2 - \nu_2$ of $^{32}SO_2$.
[h] Transition belonging to ν_1 of $^{34}SO_2$.

The retrieved parameters of the spectral lines belonging to the ν_1 band of the $^{32}SO_2$ isotopologue are listed in Table 7.1, together with the broadening coefficients calculated following the theory presented in Sections 3.8 and 7.3. The experimental and theoretical self-broadening parameters and their dependence on the $K_a^{"}$ pseudo-quantum number are shown in Figure 7.8 (a). Besides the good agreement between experimental and calculated pressure broadening coefficients, the plot also shows their decrease as $K_a^{"}$ increases. Considering the *b*-type character of the ν_1 band, this trend was expected, as outlined in the discussion at the end of Section 7.3. The retrieved line intensities of the ν_1 lines are compared with the literature values and the Hitran 2004 database [15] in Figure 7.8 (b). As can be seen the agreement is in general very satisfactory, indeed the ratios S^0_{exp} / S^0_{lit} and S^0_{exp} / S^0_{Hitran} are 0.92 and 1.00, respectively.

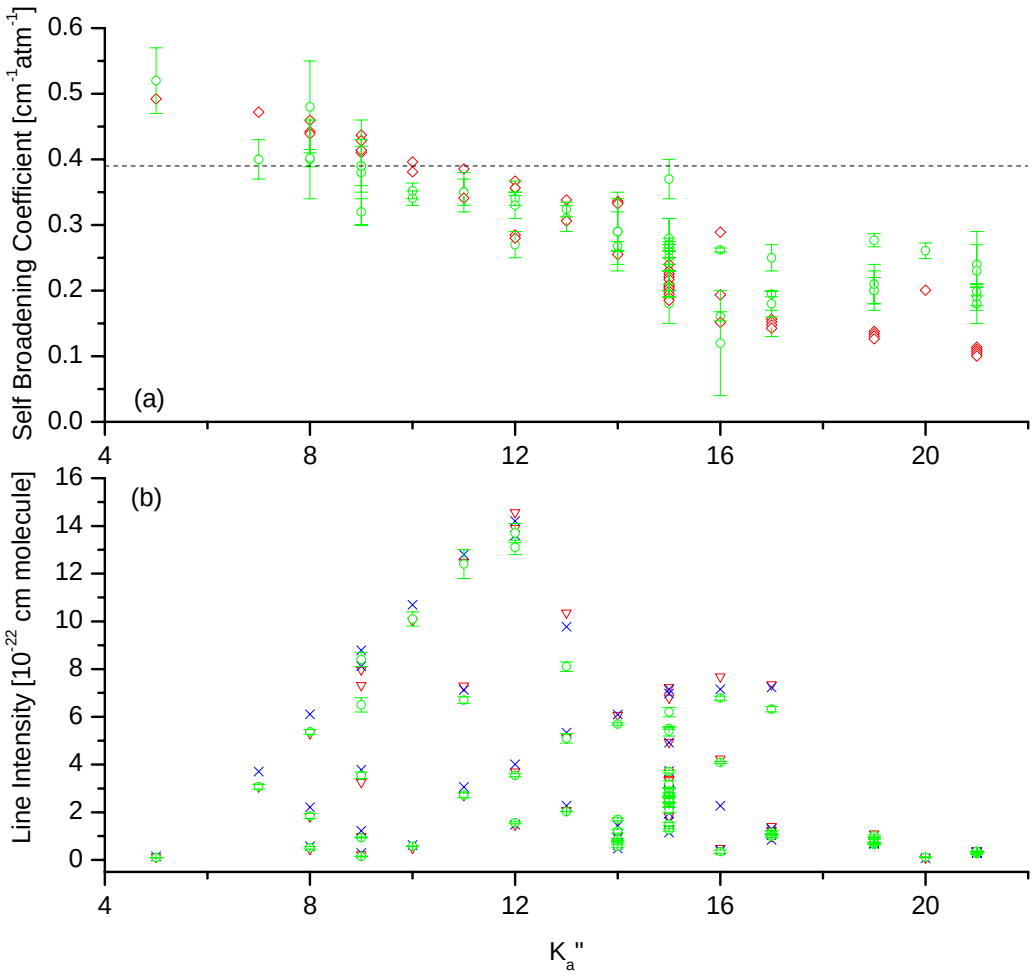

Figure 7.8. Self-broadening (panel a) and integrated absorption (panel b) coefficients of the ν_1 ro-vibrational transitions of $^{32}SO_2$. The upper diagram shows the comparison between the experimental (○) and calculated (◇) self-broadening coefficients and their decrease with increasing values of K_a"; the dotted line (--) is the self broadening coefficient given by Hitran 2004. In the lower panel the integrated intensities are compared with the literature values: (○) this work; (▽) from Ref. [152]; (×) from Ref.[15].

Besides the main absorptions coming from the ν_1 band of ^{32}S sulphur dioxide, 11 lines belonging to the $\nu_1 + \nu_2 - \nu_2$ hot band of the main isotopologue and 11 lines belonging to the ν_1 band of $^{34}SO_2$ were also identified and analyzed. The obtained line parameters are given in Tables 7.2 and 7.3, respectively. Theoretical values of the pressure broadening coefficients have been calculated for these transitions as well. In the case of $^{34}SO_2$, the calculations have been carried out considering the collisions with the main isotopic species. A graphical comparison between the experimental and the calculated broadening parameters is shown in Figure 7.9 (a) and 7.10 (a) for the $\nu_1 + \nu_2 - \nu_2$ of $^{32}SO_2$ and ν_1 of $^{34}SO_2$, respectively. The agreement is satisfactory but it is generally poorer than that obtained for the ν_1 band of the $^{32}SO_2$ isotopologue. This can be explained considering the larger uncertainties affecting the values obtained experimentally for the spectral lines of $\nu_1 + \nu_2 - \nu_2$ of $^{32}SO_2$ and ν_1 of $^{34}SO_2$, which are caused by their smaller intensity. As a consequence, these lines are more affected by the line shape distortions induced by either the neighbouring lines and the inversion procedure, particularly by the base line location. An analogous behaviour is observed when the integrated intensities here obtained are compared with the literature values; the graphical comparisons are given in Figures 7.9 (b) and 7.10 (b). Nevertheless, taking into account the weakness of the lines and the density of transitions in the spectra, the agreement between the data sets can be considered satisfactory.

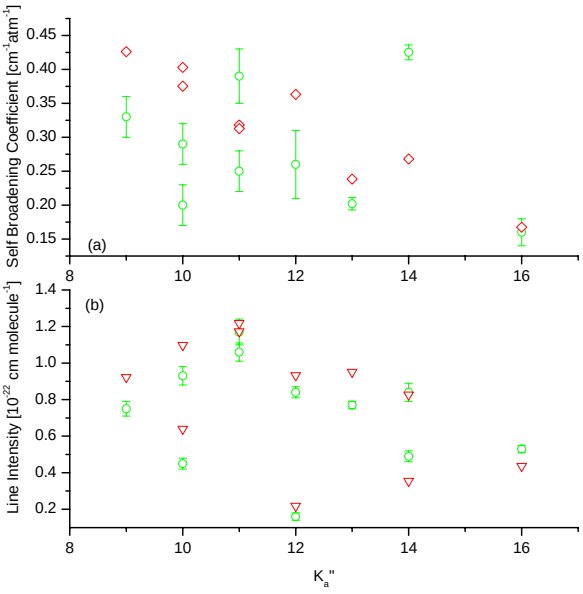

Figure 7.9. Self-broadening (panel a) and integrated absorption (panel b) coefficients of the $\nu_1 + \nu_2 - \nu_2$ ro-vibrational transitions of $^{32}SO_2$. The upper diagram shows the comparison between the experimental (○) and calculated (◇) self-broadening coefficients. In the lower panel the obtained integrated intensities (○) are compared with the values of Ref. [152] (▽).

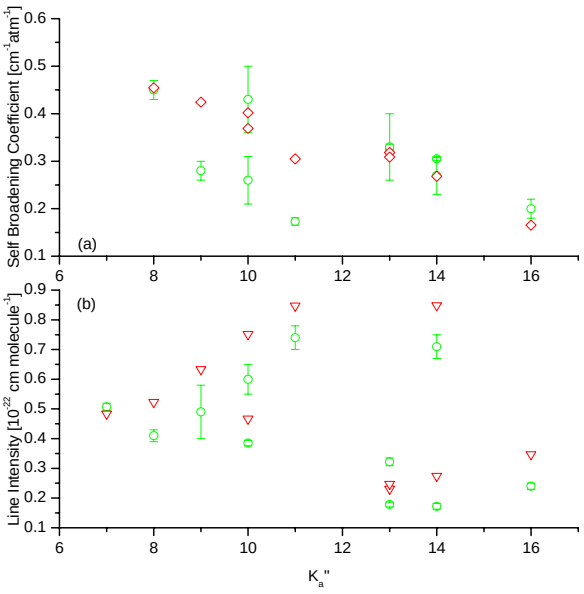

Figure 7.10. Self-broadening (panel a) and integrated absorption (panel b) coefficients of the ν_1 ro-vibrational transitions of $^{34}SO_2$. Panel (a) shows the comparison between the experimental (○) and calculated (◇) self-broadening coefficients. In panel (b) the obtained integrated intensities (○) are compared with the values of Ref. [167] (▽).

Table 7.2. Line labelling, assignment, and line parameters of the $\nu_1 + \nu_2 - \nu_2$ hot band of $^{32}SO_2$ [a]

Line N.	J'	K_a'	K_c'	J''	K_a''	K_c''	ν_0^{exp} [b]	$\gamma_L^{0,exp}$ [c]	$\gamma_L^{0,calc}$ [c]	S_{exp}^0 [d]	S_{lit}^0 [d, e]
4	36	11	25	37	12	16	1083.4293(4)	0.26(5)	0.36313	1.6(2)	2.175
8	18	15	3	19	16	4	1083.4845(2)	0.16(2)	0.16727	5.3(2)	4.364
9	27	13	15	28	14	14	1083.4935(2)	0.425(11)	0.26798	4.9(3)	3.544
29	18	13	5	19	14	6	1089.9139(4)	0.25(4)	0.22849	8.4(5)	8.265
29 [f]	51	17	35	51	18	34			0.2469		
32	27	11	17	28	12	16	1090.0597(3)	0.32(4)	0.33707	8.4(3)	9.327
32 [g]	20	12	8	21	13	9			0.2801		
41	13	12	2	14	13	1	1096.6290(3)	0.202(9)	0.23827	7.7(2)	9.513
48	27	9	19	28	10	18	1096.7446(9)	0.20(3)	0.40290	4.5(3)	6.389
51	14	10	4	15	11	5	1102.5453(5)	0.39(4)	0.31800	10.6(5)	11.73
66	23	8	16	24	9	15	1102.9831(3)	0.33(3)	0.42592	7.5(4)	9.218
73	18	9	9	19	10	10	1103.1241(3)	0.29(3)	0.37519	9.3(5)	10.98
78	13	10	4	14	11	3	1103.2290(3)	0.25(3)	0.31275	11.7(7)	12.18

[a] In case of overlapped transitions the literature value of the line intensity is obtained by summing the individual line intensities of each transition (where available). Figures in parentheses correspond to one standard deviation.
[b] Values expressed in cm^{-1}.
[c] Values expressed in cm^{-1} atm^{-1}.
[d] Values expressed in 10^{-23} cm $molecule^{-1}$.
[e] From Ref. [152].
[f] Transition belonging to ν_1 of $^{32}SO_2$.
[g] Transition belonging to ν_1 of $^{34}SO_2$.

Table 7.3. Line labelling, assignment and line parameters of the ν_1 band of $^{34}SO_2$ [a]

Line N.	J'	K_a'	K_c'	J''	K_a''	K_c''	ν_0^{exp} [b]	$\gamma_L^{0,exp}$ [c]	$\gamma_L^{0,calc}$ [c]	S_{exp}^0 [d]	S_{lit}^0 [d, e]
3	25	13	13	26	14	12	1083.3933(4)	0.305(3)	0.26801	1.72(10)	2.740
13	16	15	1	17	16	2	1083.6045(3)	0.20(2)	0.16544	2.40(11)	3.470
14	29	12	18	30	13	7	1083.6125(2)	0.325(11)	0.31836	1.78(8)	2.306
23	16	13	3	17	14	4	1089.7409(2)	0.27(4)	0.22763	7.1(4)	8.487
23[f]	32	10	22	33	11	23			0.3826		
46	24	9	15	25	10	16	1096.7061(2)	0.43(7)	0.40186	3.85(9)	4.669
57	20	8	12	21	9	13	1102.7295(2)	0.28(2)	0.42430	4.9(9)	6.334
62	29	6	24	30	7	23	1102.9206(3)	0.60(3)	0.46384	5.07(12)	4.838
62[f]	43	12	32	43	13	31			0.3493		
63	27	12	16	27	13	15	1102.9324(4)	0.33(7)	0.30852	3.22(13)	2.470
67	15	9	7	16	10	6	1102.9938(3)	0.26(5)	0.36911	6.0(5)	7.513
75	24	7	17	25	8	18	1103.1511(3)	0.45(2)	0.45457	4.1(2)	5.227
77	10	10	0	11	11	1	1103.2134(3)	0.173(8)	0.30495	7.4(4)	8.474

[a] In case of overlapped transitions the literature value of the line intensity is obtained by summing the individual line intensities of each transition (where available). Figures in parentheses correspond to one standard deviation.
[b] Values expressed in cm^{-1}.
[c] Values expressed in cm^{-1} atm^{-1}.
[d] Values expressed in 10^{-23} cm $molecule^{-1}$.
[e] From Ref. [167].
[f] Transition belonging to $\nu_1 + \nu_2 - \nu_2$ of $^{32}SO_2$.

The fits carried out using the profiles accounting for Dicke narrowing have led to the determination of the Dicke narrowing coefficients, which resulted to be $\beta = 0.11(2)$ $cm^{-1}atm^{-1}$ and $\Omega = 0.09(2)$ $cm^{-1}atm^{-1}$, within the weak and strong collision models, respectively. On the other hand, the self-broadening coefficients obtained by using these models agree within the statistical error with those obtained from the fits with the Voigt profile.

The integrated absorption coefficients obtained from the line parameter analysis have been used to derive the total band intensity of the ν_1 normal mode: it is resulted to be $3.32(12)\cdot10^{-18}$ $cm\cdot molecule^{-1}$. This value closely matches that obtained by Sumpf [153] from analogous high resolution measurements carried out by TDL spectroscopy.

The integrated band intensities of the ν_1, ν_2 and ν_3 fundamental bands derived from the medium resolution spectra, an example of which is given in Figure 7.11, are listed in Table 7.4 together with the most recent literature values. The resulting photo-absorption spectra are reproduced in Figures 7.12 (a) and (b) for the measurements carried out on pure sulphur dioxide and its mixture with nitrogen.

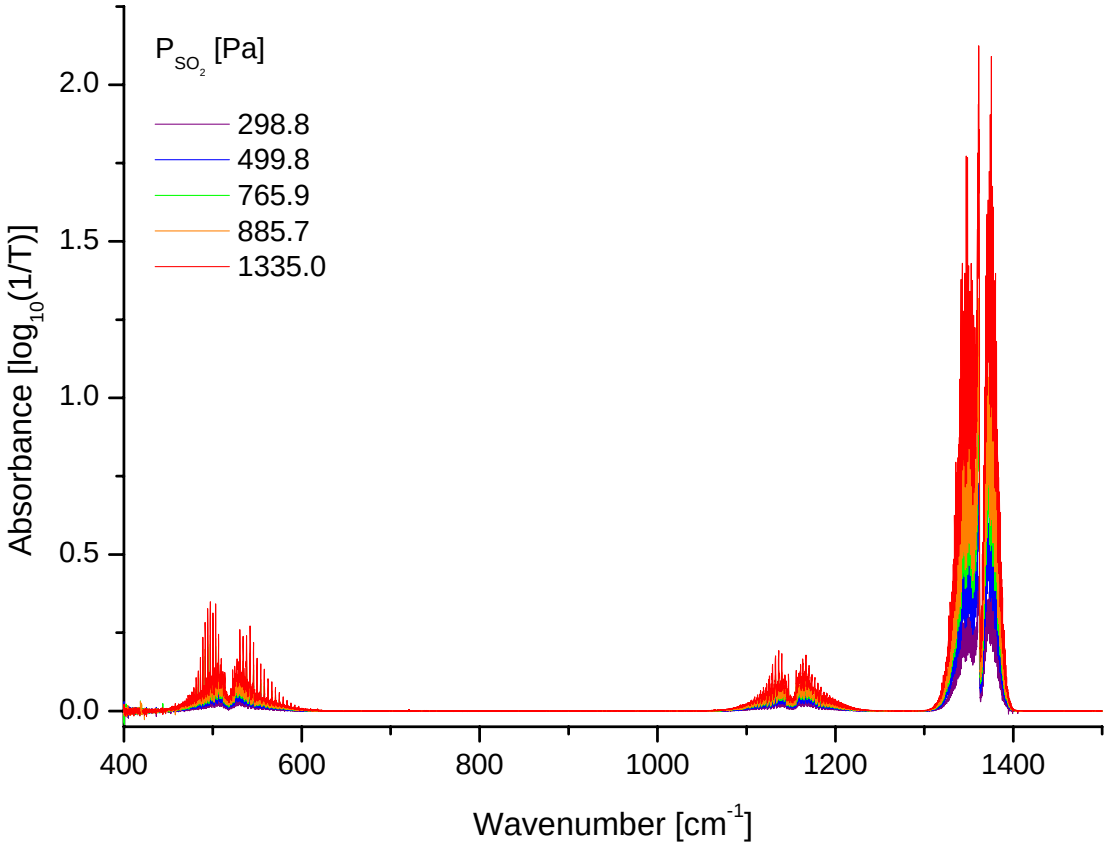

Figure 7.11. Example of the series of spectra recorded at different SO_2 pressure for the determination of the vibrational cross sections. The spectra were recorded using 1000 kPa of N_2 as buffer gas, the SO_2 partial pressures are indicated in figure. Experimental details: T = 298.0 K, PLC = 13.40 cm, 0.2 cm^{-1} resolution.

Table 7.4. Obtained integrated intensities of the ν_1, ν_2 and ν_3 fundamental bands of SO_2 and their comparison with the most recent literature values [a]

	$S^0_{\nu_1}$	$S^0_{\nu_2}$	$S^0_{\nu_3}$
This Work	0.359(3) [b] 0.353(3) [c] 0.332(12) [d]	0.424(8) [b] 0.417(13) [c]	2.78(2) [b] 1.730(13) [c]
Henningsen et al. [165]	-	-	2.61
Sumpf [153]	0.341(11) [d]	-	2.40(15) [d]
Chu et al. [152]	0.38286(90)	-	2.9657(43)
Kim and King [173]	0.342(12)	0.420(5)	3.19(3)
Kunimoto et al. [174]	0.439	-	3.50

[a] Values expressed as 10^{-17} cm molecule^{-1}. Figures in parentheses correspond to one standard deviation.
[b] From meausurements on pure SO_2.
[c] From measuremnents on SO_2 + 1000 kPa of N_2.
[d] Total band intensity, from high resolution measurements.

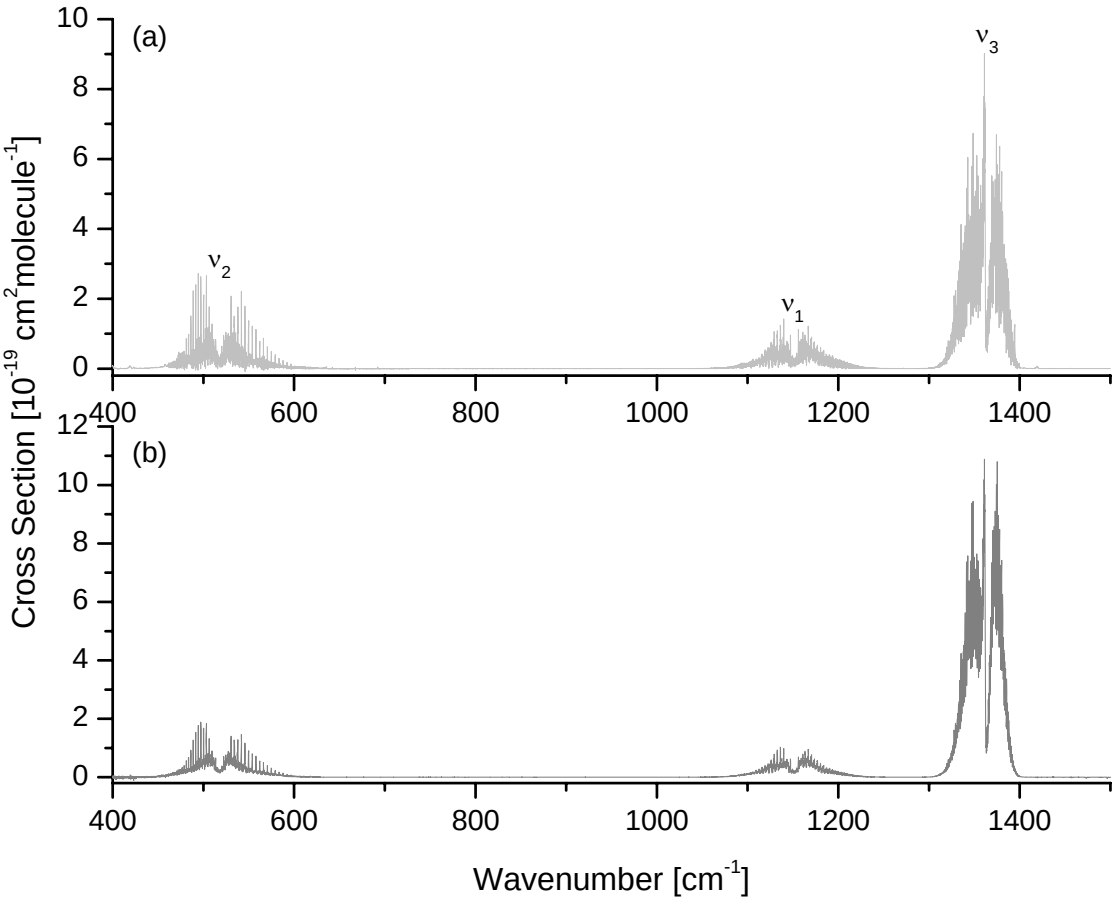

Figure 7.12. Photo absorption spectrum of the SO_2 fundamental bands: (a) from measurements on pure SO_2; (b) from measurements on SO_2 mixed with 1000 kPa of N_2. Experimental details: T = 297 K, PLC = 13.40 cm, 0.2 cm^{-1} resolution.

The experimental results show that, while the vibrational cross sections of ν_1 and ν_2 are essentially unaffected by the buffering with N_2, the ν_3 integrated band intensity obtained without N_2

is about 1.6 times smaller than that obtained upon pressurization with nitrogen. In order to understand this behaviour, a systematic study on the effects of interferogram truncation and finite resolution has been carried out following the treatment described by Ahro and Kauppinen [175]. They considered a simplified model, which is exemplified in Figure 7.13, of a rigid diatomic molecule having a Gaussian shaped vibrational band consisting of a series of Lorentzian rotational lines of separation $2B$. The corresponding interferogram consists of Gaussian wave-packets separated by $1/(2B)$. Therefore, the separation of the rotational wave-packets in the interferogram is inversely proportional to the distance between the rotational spectral lines and the width of the wave-packets is inversely proportional to the width of the vibrational band. Since there is very little information between the wave-packets, there is no advantage in collecting the interferogram in between the wave-packets, as shown in Figure 7.14.

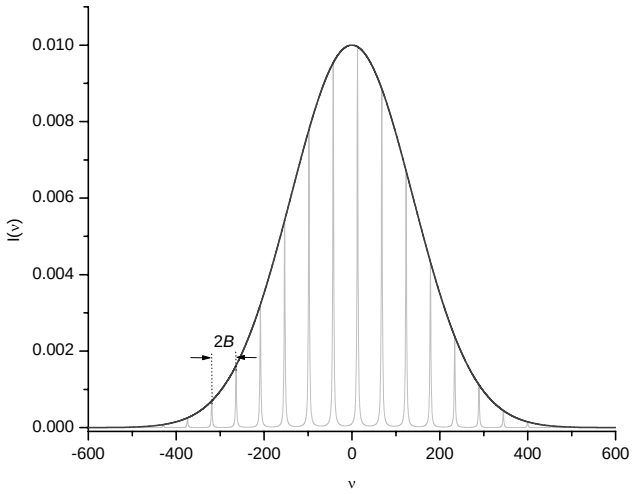

Figure 7.13. Example of Gaussian shaped vibrational band composed of a series of Lorentzian rotational lines having width Γ and separated by $2B$.

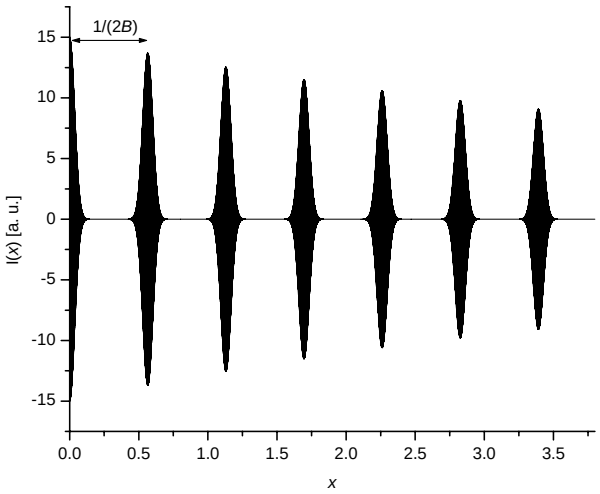

Figure 7.14. Part of the interferogram of a Gaussian shaped vibrational band composed of a series of Lorentzian rotational lines. The separation between the wave-packets is $1/(2B)$.

For the present purposes, a MatLab program, in which the vibrational bands are modelled as described above, has been written to simulate the effect of finite resolution. The routine calculates the interferogram of a given reference Gaussian shaped vibrational band at a resolution $R_{ref} = \left(2^N \Delta x\right)^{-1}$, where N is the number of points of the interferogram and $\Delta x = 1.38 \cdot 10^{-4}$ cm; this interferogram is then truncated in order to match the new resolution $R_{trunc} = \left(2^M \Delta x\right)^{-1}$, where $M < N$ is the number of points of the truncated interferogram. Finally, the new interferogram is Fourier transformed into the new spectrum, which results to have a lower resolution. Besides the number of points of the reference and truncated interferograms, the simulation parameters which can be varied

are the separation B between the rotational lines, their width Γ and the width σ of the Gaussian vibrational band.

Since the effect of pressurization with N_2 is to broaden the rotational lines, and given that the three fundamental bands of sulphur dioxide have similar rotational constants and similar broadening parameters, the simulations have been performed by considering a series of 6 reference vibrational bands with different peak absorbances (within the range 0.1 – 0.6) for each of which the reduced width, $\Gamma^* = \Gamma / R_{ref}$, of the rotational lines has been increased from 1.0 to 6.0. As reference spectrum, a Gaussian band with a nominal resolution of 0.05 cm^{-1} has been used and the resolution has been degraded to 0.22 cm^{-1}.

The results of the simulations are listed in Table 7.5 and illustrated in Figure 7.15. They show that as the rotational lines become broader, the distortions due to the finite resolution are reduced and the ratio between the area subtended by the vibrational band after and before the truncation, A_{trunc} / A_{ref} , increases and tends toward one. As can be seen in Figure 7.15, the present calculations also prove that the ratio A_{trunc} / A_{ref} reduces as the band peak absorbance increases. This result is in agreement with the investigations carried out by Parker and Tooke [176]. According to their work, two regimes need to be distinguished: in the first, the FWHM of the vibrational band is much smaller than the resolution; in the second one, the FWHM is comparable or larger than the resolution. In this regime, as truncation and apodization have a greater effect closer to the band centre, they have a major effect on bands having a larger absorbance. Therefore, the spectral distortions induced by the finite resolution are larger in vibrational bands which have higher peak absorbance and whose rotational lines are sharper. This is exactly the case of sulphur dioxide: since the ν_3 band has an higher peak absorbance than ν_1 and ν_2, it is much more distorted by the instrumental resolution. The effect of the buffer gas is to broaden the rotational lines, thus removing these distortion. On the other hand, the pressurization with nitrogen leaves the ν_1 and ν_2 bands almost unchanged due to their lower peak absorbance. In summary, since ν_3 has an higher peak absorbance than the ν_1 and ν_2 bands, it is more distorted than the other ones by the finite instrumental resolution. By using a buffer gas, the rotational lines are broadened such that these distortions are removed.

Table 7.5. Effect of the finite resolution on the area of a Gaussian shaped vibrational band as a function of peak absorbance, Abs^{Peak}, and reduced rotational line width, Γ^*, obtained from computer simulations

Abs^{Peak}	A_{trunc}/A_{ref}							
	Γ^*							
	1.0	*1.2*	*1.5*	*2.0*	*3.0*	*4.0*	*5.0*	*6.0*
0.10	0.94093	0.94099	0.94114	0.94171	0.94489	0.95205	0.96260	0.97357
0.15	0.91285	0.91294	0.91317	0.91400	0.91868	0.92922	0.94474	0.96087
0.25	0.85963	0.85997	0.86014	0.86148	0.86897	0.88584	0.91070	0.93654
0.40	0.78698	0.78719	0.78774	0.78976	0.80103	0.82641	0.86379	0.90266
0.50	0.74313	0.74338	0.74404	0.74646	0.75998	0.79039	0.83519	0.88178
0.60	0.70273	0.70300	0.70377	0.70655	0.72211	0.75709	0.80861	0.86220

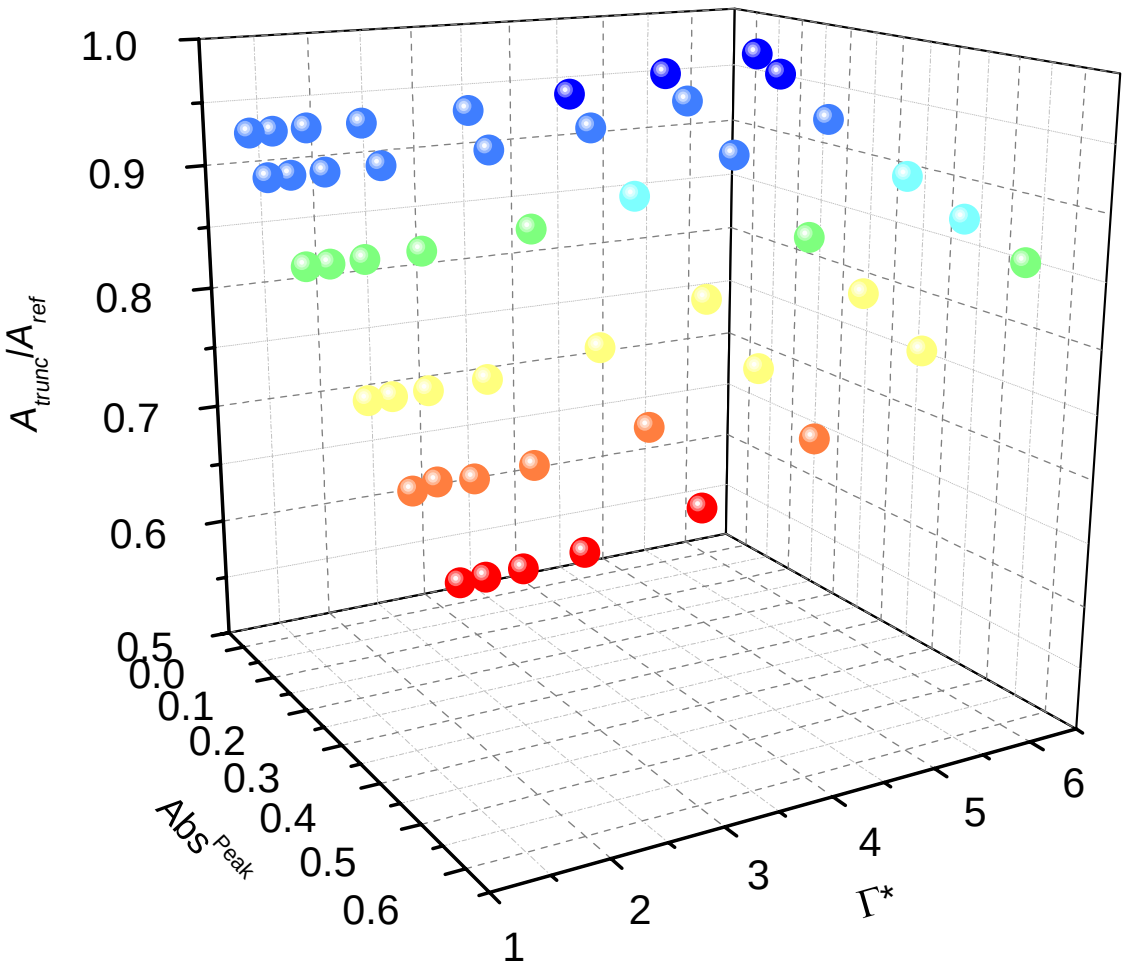

Figure 7.15. Simulated trend of the ratio between the areas of a Gaussian shaped vibrational bands at two different resolutions as a function of band peak absorbance and reduced rotational line width.

From Table 7.4 it can be seen that the fundamental bands ν_1 and ν_3 have received more attention than the ν_2 bending vibration, for which the most recent determination of the integrated band intensity seems that of Kim and King [173]. The agreement between their value and the present one is very good. Concerning the ν_1 band, all the cross sections of Table 7.4 match fairly well. Only the value given by Kunimoto et al. [174] is about 20% larger that the others. The integrated band intensities of the ν_3 band appear slightly more scattered. The value of 2.78×10^{-17} cm molecule^{-1} here measured lies in the middle between the two limiting literature values: 2.40×10^{-17} and 3.50×10^{-17} cm molecule^{-1}.

Finally, it should be pointed out that the total band intensities of the ν_1 fundamental band obtained from the high resolution measurements are slightly smaller than the integrated cross sections derived from low or medium resolution spectra. This is because the absorptions due to either the hot bands and the isotopic species contribute to the cross sections obtained from the latter measurements, whereas they can be excluded from the determinations based on the high resolution line intensities.

8. Vinyl Fluoride Spectroscopy: Vibrational analysis, Ab initio calculations and Line parameter determination

The last years have seen an increasing interest in spectroscopic studies of haloalkenes owing to their potential role as air pollutants and also to improve the theoretical studies of their reactivity toward hydroxyl radical and ozone (for example [177, 178] and references therein). Among these, vinyl fluoride, $H_2C=CHF$, has been studied extensively by spectroscopic methods, since it is widely used by industry mainly as a monomer for the production of synthetic resins, such as polyvinyl fluoride. Low resolution infrared investigations, mainly limited to the identification of the fundamental modes, have been carried out a long time ago [179 – 181] and an analysis of the partially resolved rotational structure has been performed around 900 cm^{-1} for the ν_8, ν_{10} and ν_{11} modes strongly interacting by Coriolis and anharmonic resonances [182]. Ground state parameters, obtained from the analysis of microwave spectra [183 – 185], have been more extensively determined combining the microwave data available in the literature together with infrared combination differences [186]. Many investigations have been also devoted to the determination of its structure ([187] and references therein) and a semi-experimental equilibrium structure has been derived from experimental ground state rotational constants and rovibrational interaction parameters calculated from an *ab initio* anharmonic force field [188].

The high resolution infrared spectra of vinyl fluoride have been deeply investigated in many spectral regions [189 – 193] and the obtained results have led to the determination of accurate molecular parameters for several fundamentals and overtone vibrations, and to a thorough understanding of the interaction mechanism for the observed perturbations.

Despite the industrial importance of vinyl fluoride, there exist no studies on the determination of the line parameters of the ro-vibrational absorption lines. The lack of literature

data is partly motivated by the complex structure of the room temperature high resolution spectrum, which presents a high density of lines with many overlapped transitions.

This chapter deals with the determination of the line parameters of vinyl fluoride in the ν_7 band atmospheric region around 8 μm. In addition, a complete vibrational study of the medium resolution gas phase spectrum in the 400 – 8000 cm^{-1} region is presented together with the measurements of the absolute infrared photo absorption cross sections. Accurate *ab initio* calculations of the harmonic and anharmonic force fields have been also performed: correlated harmonic force fields have been obtained from coupled cluster CCSD(T) calculations with the cc-pVQZ basis set, while anharmonic force constants have been computed employing the less resource demanding cc-pVTZ basis set.

8.1. EXPERIMENTAL DETAILS AND DATA INVERSION

The H_2C=CHF (purity ≈ 99%) gas samples were provided by Peninsular Chemical Research, Inc. and were used without further purification.

Medium and low resolution measurements

The low and medium resolution spectra of vinyl fluoride were recorded on the Bruker Vertex 70 FTIR spectrometer at a resolution between 0.2 and 1.0 cm^{-1} in the 400 – 5000 cm^{-1} region, and at 1.0 cm^{-1} in the 5000 – 8000 cm^{-1} range. The wavenumber accuracy in the investigated range (400 – 8000 cm^{-1}) was estimated to be around 0.2 cm^{-1}. A 134.0 (± 0.5) mm path-length, double walled, stainless steel gas cell equipped with KBr windows was employed in the range 400 – 5000 cm^{-1}, while a multipass cell (150 – 3750 cm) with CaF_2 windows was used in the NIR region. A total of 128 scans for both the sample and the background spectra were co-added and transformed into the corresponding absorbance or transmittance spectrum, using boxcar apodization function and Mertz phase correction.

For the vibrational analysis the sample pressures were varied in the range 0.37 – 40 kPa and the spectra were recorded at room temperature. For the absorption cross section measurements (400 – 3500 cm^{-1}), different pressures of vinyl fluoride were used, both for the pure compound and its mixture with N_2 (SIAD, purity > 99%) to a total pressure of 101 kPa. The temperature in the cell, continuously monitored by thermocouples, was kept constant at 298.0 K (± 0.5 K).

The absorbance cross-section per molecule (cm^2 $molecule^{-1}$), $\sigma(\tilde{\nu})$, was calculated from the measured infrared absorbance using the relationship given in Equation 7.3. The integrated cross section G_{int} (cm $molecule^{-1}$) was then derived from the absorbance cross section by means of equation 7.4. In the case of two or more overlapped bands without a clear separation a single integration was performed. The experimental uncertainty in the cross section measurements was estimated by taking into account the uncertainties of pressure and temperature of the sample, of the optical path length, of the photometric accuracy of the FTIR spectrometer and of the evaluation of the absorbance (26).

At the beginning of the experiments some spectra were recorded at two different resolutions (0.2 and 0.5 cm^{-1}) for different pressures of both pure vinyl fluoride and its mixture with N_2. A linear dependence of the absorbance with the sample pressure was observed over all the used concentration range. The calculated band intensities corresponding to the same concentration of the sample at different spectral resolutions was found to be equal within the error of the measurements; therefore the integrated cross sections were determined from the spectra of the pure gas (H_2C=CHF pressures in the range 4 – 33 hPa) recorded at the resolution of 0.5 cm^{-1} because they generally had a better signal-to-noise ratio, especially for the weaker absorption features.

High resolution measurements

The high resolution spectra of vinyl fluoride in the 8 μm atmospheric window were recorded on the TDL spectrometer of Università Ca' Foscari Venezia described in Chapter 5. It was used in the three beams configuration, in which the main part of the beam passed through the cell containing the sample, while the other two beams were sent through an empty reference cell and the Germanium etalon, respectively. The reference signals were used to obtain the transmission spectra using the procedure described following in the text. The measurements were carried out at 299 ± 1 K by adopting the same procedure described in Section 7.2 for sulphur dioxide. In the present experiments the elapsed time between filling of the cell and spectral acquisition was raised to 20 – 25 minutes due to the stickiness of vinyl fluoride. Further, a liquid nitrogen trap was used in order to facilitate the evacuation of the cell. Given the strong intensity of the absorptions, small concentrations of vinyl fluoride were used and each spectral microwindow was recorded up to nine different pressures within the range 5 – 200 Pa; no buffer gases were used. An example of the obtained spectra is given in Figure 8.1. Each experimental spectrum is the result of an average of 128 scans.

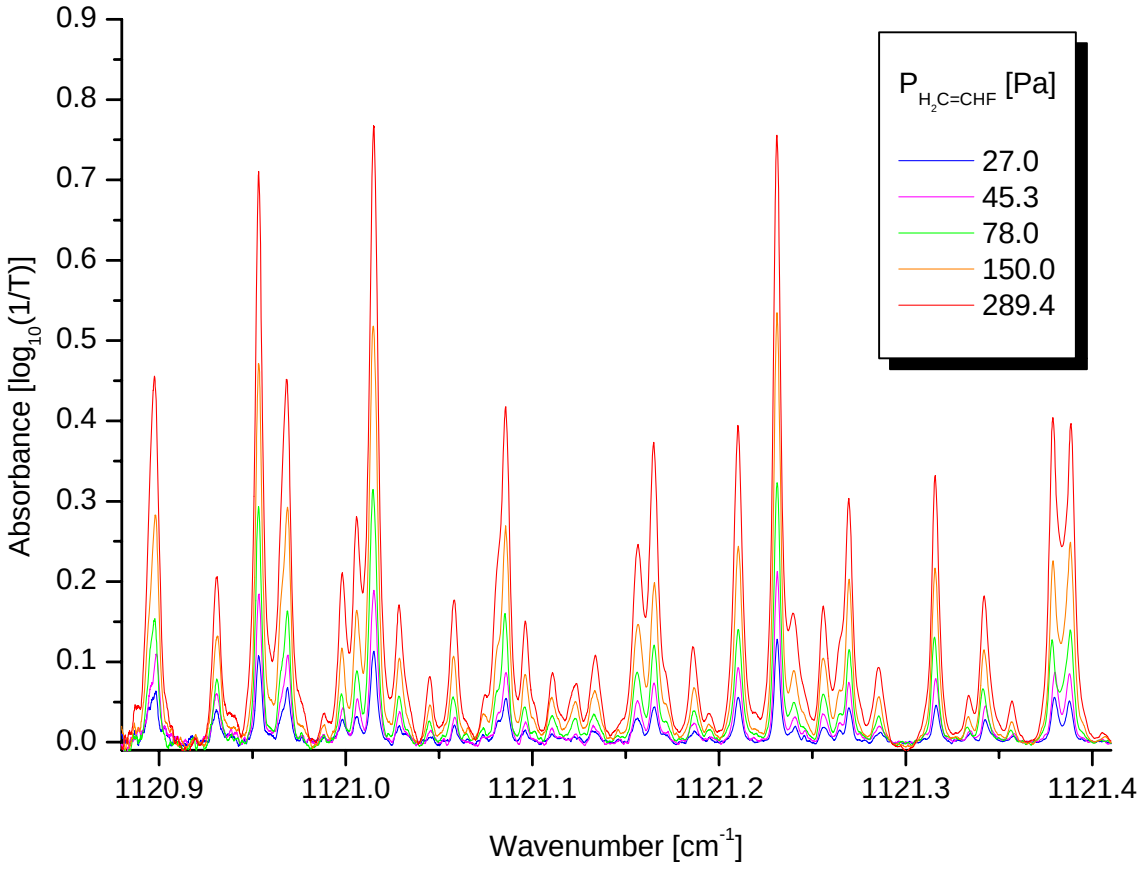

Figure 8.1. Example of the series of spectra recorded at different pressures of $H_2C{=}CHF$ in the region 1120.88 – 1121.41 cm^{-1}. Experimental details: PLC = 92.3 cm; T = 299.5 K; sample pressures are given in the figure.

Despite the adopted low pressures, the spectra appeared very crowded and therefore a data inversion based on a fit of the baseline was impracticable. Therefore, the transmission spectra were obtained by ratioing the sample and the reference spectra according to

$$T = \frac{T^{\star}_{sample}}{T^{\star}_{reference}} \tag{8.1}$$

where T^{*}_{sample} and $T^{*}_{reference}$ are in turn the sample and the reference signals normalized by the corresponding background. Denoting by I_{sample} and $I_{background}$ the spectra of the sample channel with filled and empty cell, respectively, and by $I^{sample}_{reference}$ and $I^{background}_{reference}$ the corresponding signals of the reference channel, $T^{\star}_{sample}$ and $T^{*}_{reference}$ are respectively given by:

$$T^{\star}_{sample} = \frac{I_{sample}}{I_{background}}; \qquad T^{\star}_{reference} = \frac{I^{sample}_{reference}}{I^{background}_{reference}}. \tag{8.2}$$

In this way, the drift of the laser and its power fluctuations equally affect the two channels and therefore their effects compensate by taking the ratio (8.1). A drawback of this approach is the degradation of the signal-to-noise ratio; nevertheless, it represents a good compromise when fitting the baseline is impossible or too imprecise.

After absorbance conversion, the spectra were wavenumber-calibrated by using the frequency of the H_2C=CHF lines obtained from the high resolution FTIR spectrum. The resulting wavenumber accuracy was, on average, $5.6 \cdot 10^{-4}$ cm^{-1}.

8.2. COMPUTATIONAL DETAILS

Quantum-chemical calculations were carried out at the correlated levels of coupled cluster theory with single and double excitations augmented by a perturbational estimate of the effects of connected triple excitations, CCSD(T). The Dunning's correlation consistent polarized valence basis sets cc-pVTZ and cc-pVQZ were employed. The frozen core approximation, where the carbon and fluorine 1*s*-like molecular orbitals are constrained to remain doubly occupied in the calculations, were adopted and spherical harmonics were used throughout.

At first, the molecular geometry of vinyl fluoride was optimized within the constraint of C_s symmetry point group at CCSD(T)/cc-pVTZ level of theory. At the computed equilibrium geometry, the harmonic force field was evaluated analytically employing the same level of theory. The CCSD(T)/cc-pVTZ cubic and quartic normal coordinates force constants (φ_{ijk}, φ_{ijkk}) were determined with the use of a finite difference procedure [194] involving displacements along the normal coordinates (step size 0.05 $amu^{½}$ bohr). All these calculations were performed with the Mainz-Austin-Budapest version of ACES II program package [195].

Since the semi-experimental structure of vinyl fluoride is in good agreement with the structure calculated at CCSD(T)/cc-pVQZ level of theory [188], an additional geometry optimization followed by the harmonic force field evaluation was performed at this level of theory. These calculations were carried out with the MOLPRO system of programs [196], where the hessian matrix is calculated numerically by finite differences [197].

8.3 DESCRIPTION OF THE SPECTRUM AND ASSIGNMENT

Vinyl fluoride is a planar near-prolate asymmetric top ($\kappa \cong -0.945$), belonging to the C_s symmetry point group. The *A* and *B* principal axes of inertia lie in the molecular symmetry plane, while the *C*-axis is perpendicular to it. The molecule has twelve fundamental vibrations of which nine of species *A*' ($\nu_1 - \nu_9$), that give rise to *A*/*B* hybrid bands, and three of species *A*" ($\nu_{10} - \nu_{12}$), that produce *C*-type absorptions. Survey spectra of vinyl fluoride in the region investigated, recorded at 1.0 cm^{-1} resolution, are shown in Figure 8.2. Few assignments are given below selected bands in order to facilitate the reading of the spectra, which provide a rich source of information on overtone and combination levels. The frequencies and the assignments for the observed bands are given in Table 8.1.

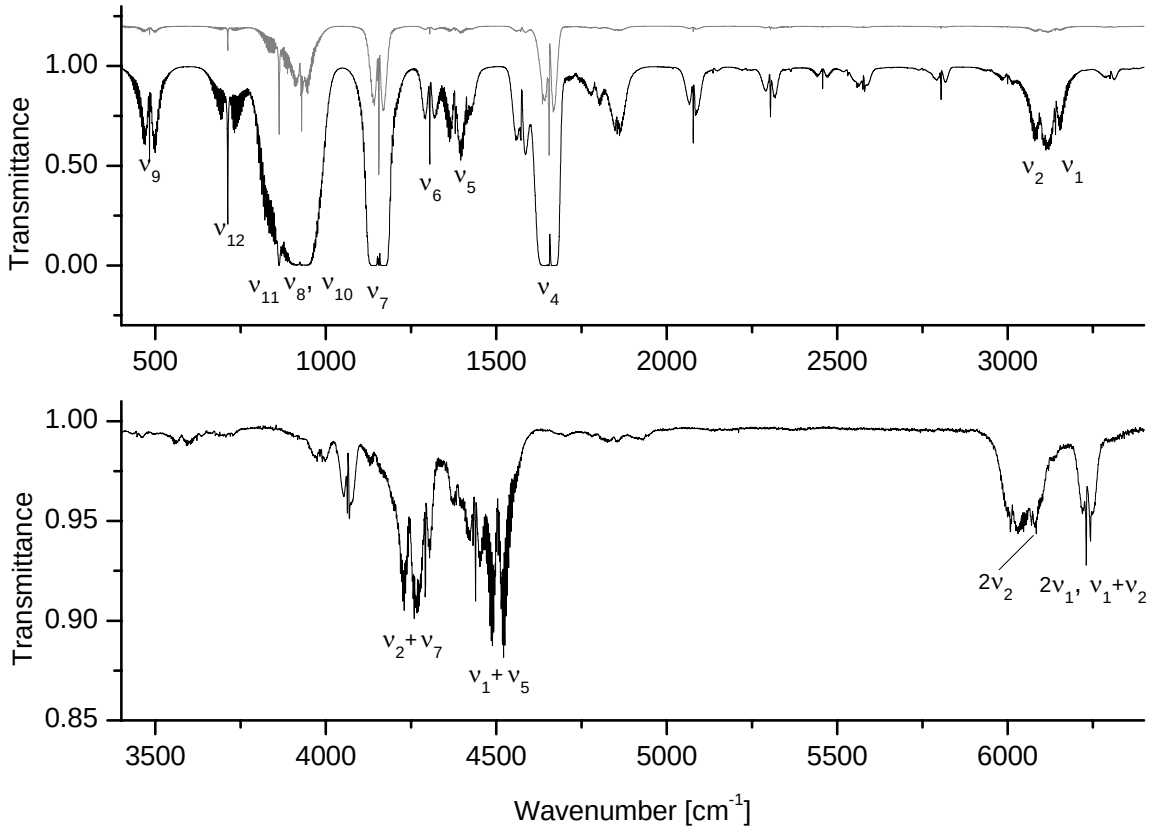

Figure 8.2. The gas-phase IR spectra of H_2C=CHF at 1.0 cm^{-1} resolution: (—) PLC = 13.4 cm, P = 613 Pa; and (—) PLC = 13.4 cm, P = 11.4 kPa. Only some representative bands are labelled. For a better reading, the (—) trace has been shifted upwards.

Table 8.1 (1 of 2). Observed band centres (cm^{-1}) of the gas-phase IR spectra of $H_2C{=}CHF$

Band	Observed envelope	Relative Intensity [a]	Wavenumber [b]
ν_9	A / B	m	482.9
$2\nu_9 - \nu_9$			485.5
ν_{12}	C	m	712.4 ± 0.2
$\nu_9 + \nu_{12} - \nu_9$			713.5
ν_{11}	C	s	863.1 ± 0.2
$\nu_9 + \nu_{11} - \nu_9$			864.3 ± 0.2
ν_8	A / B	s	927.8 ± 0.2
ν_{10}	C	s	929.1 ± 0.2
$\nu_7 + \nu_9 - \nu_9$			1152.7
ν_7	A	vs	1155.4
ν_6	A	w	1305.2
ν_5	A / B	m	1379.5
$2\nu_{12}$		vw	1424.4
$\nu_{11} + \nu_{12}$	A / B	w	1574.3 ± 0.5
$\nu_7 + \nu_9$		vw	1635.7
$\nu_4 + \nu_9 - \nu_9$			1652.8
ν_4	A	vs	1655.6
$\nu_{10} + \nu_{11}$	B / A	w	1790.3
$2\nu_8$	A / B	w	1854.6
$\nu_7 + \nu_9 + \nu_{11} - \nu_9$			2017.7
$\nu_7 + \nu_{11}$	C	vw	2018.6
$\nu_7 + \nu_8 + \nu_9 - \nu_9$			2075.6
$\nu_7 + \nu_8$	A	w	2077.7
$\nu_4 + \nu_9$	A	vw	2136.2
$2\nu_7$	A	vw	2304.1
$\nu_6 + \nu_7$	A	vw	2457.5
$\nu_5 + \nu_7$	A	vw	2530.7
$2\nu_6$		vw	2608.3
$2\nu_5$	A / B	vw	2751.8
$\nu_4 + \nu_7$	A	vw	2805.1
$\nu_4 + \nu_6$		vw	2949.6 ± 0.5

Table 8.1. (continued 2 of 2)

Band	Observed envelope	Relative Intensity [a]	Wavenumber [b]
$\nu_4 + \nu_5$	A	w	3000.3
ν_2	B / A	w	3094.5
ν_1	A / B	w	3140.7
$2\nu_4$	A	vw	3301.6 ± 0.5
$\nu_1 + \nu_8$	A / B	vw	4063.9
$\nu_2 + \nu_7$	B / A	vw	4246.0
$\nu_1 + \nu_7$	A / B	vw	4292.9
$\nu_1 + \nu_6$	A / B	vw	4439.7
$\nu_1 + \nu_5$	B / A	w	4505.6
$\nu_1 + 2\nu_5$	A / B	vw	5863.8 ± 0.5
$2\nu_2$	A / B	vw	6070.1 ± 0.5
$\nu_2 + \nu_3$	A / B	vw	6120.3 ± 0.5
$\nu_1 + \nu_2$	A / B	vw	6230.7 ± 0.5
$2\nu_1$	A / B	vw	6243.2 ± 0.5
$\nu_1 + \nu_2 + \nu_6$	A / B	vw	7531.1 ± 0.5
$2\nu_1 + \nu_5$	A / B	vw	7589.0 ± 0.5
$\nu_1 + \nu_2 + \nu_5$		vw	7603.0 ± 0.5

[a] Abbreviations as follow: vs = very strong, s = strong, m = medium, w = weak, vw = very weak.

[b] The experimental error is ± 0.1 cm^{-1} unless otherwise quoted.

The measured vibrational frequencies, and the corresponding calculated values, for the 12 normal modes of vibration are summarized in Table 8.2. The same table reports also the approximate description of the normal mode based on the total energy distribution. As it can be seen, there is an overall good agreement between calculated and observed frequencies. All the fundamentals, except the CH stretchings (ν_1, ν_2 and ν_3 normal modes), have been extensively analyzed at high resolution [189 – 193]. As shown in Figure 8.2, the ν_1 and ν_2 fundamentals, although partially overlapped, show a predominant *B*-type structure; the ν_3 band is very weak and overlapped by the stronger ν_2.

In the most favourable experimental conditions, a lot of overtones and combination bands could be observed and positively identified. The proposed assignments, which are listed in Table 8.1, have been made considering the calculated anharmonicity constants, the relative intensities and

the expected band contour of the combined normal vibrations. The assignments appear to be consistent throughout the entire spectral region investigated.

The presence of satellite peaks near the band origin of some fundamentals and combination bands provide further information on the vibrational energy levels of the hot bands of the ν_9 fundamental: $\nu_i + \nu_j - \nu_j$ and $\nu_i + \nu_j + \nu_k - \nu_j$, where ν_j is the vibrational level with $\nu_9 = 1$ located at about 483 cm^{-1}.

Table 8.2. Gas phase fundamental vibrations of H_2C=CHF

Symmetry species	Mode	Approximate description	Observed band center [cm^{-1}]	Calculated [a] band center [cm^{-1}]
A'	ν_1	CH_2 antisym. stretch	3140.7	3136.7
	ν_2	CH stretch	3094.5	3084.9
	ν_3	CH_2 sym. stretch	3062.1 [b]	3073.1 / 3040.8 [c]
	ν_4	C=C stretch	1655.6	1653.9 / 1657.1 [c]
	ν_5	CH_2 bend	1379.5	1375.5 / 1378.7 [c]
	ν_6	CH bend	1305.2	1304.0
	ν_7	CF stretch	1155.4	1155.7
	ν_8	CH_2 rock	927.8	927.5
	ν_9	C=CF bend	482.9	480.4
A"	ν_{10}	Torsion	929.1	930.2
	ν_{11}	CH_2 wag	863.1	854.6
	ν_{12}	CH out of plane bend	712.4	712.9

[a] From the hybrid anharmonic force field (see text).
[b] From Raman spectrum of the gas [181].
[c] Fermi perturbed / unperturbed values.

8.4 ROTATIONAL ANALYSIS

In the spectra recorded at the resolution of 0.2 cm^{-1}, a number of bands exhibit a resolved rotational structure which can be assigned and analyzed. From the rotational constants [186], the parameter $2(A - \overline{B})$, where $\overline{B} = (B + C)/2$, results to be 3.65 cm^{-1}. This value is large enough for the *B*- and *C*-type bands to show a resolved rotational structure, similar to the pattern observed in perpendicular bands of symmetric rotors. Therefore, since the separation between consecutive peaks is 3.6 ± 0.1 cm^{-1}, the observed rotational structure has to be attributed to the ${}^{P,R}Q_K$ clusters of *B*- or *C*-type bands: Figure 8.3 shows the rotational details of the ν_1 and ν_2 bands in the region around

3000 cm^{-1}. Some assignments of the ${}^{P}Q_K$ and ${}^{R}Q_K$ features of the ν_1 fundamental are also indicated. Note that the ${}^{R}Q_K$ heads of ν_2 are severely mingled with the ${}^{P}Q_K$ series of the ν_1 band.

The analysis has been carried out in the symmetric top approximation by a least squares fitting procedure to the following reduced equation:

$$\tilde{\nu}^{P,R} = \tilde{\nu}_0 + \left(A'-\overline{B}'\right) \mp 2\left(A'-\overline{B}'\right)K + \left[\left(A'-\overline{B}'\right) - \left(A''-\overline{B}''\right)\right]K^2 \qquad (8.3)$$

where the upper '–' and lower '+' signs refer to the *P*- and *R*-branch, respectively.

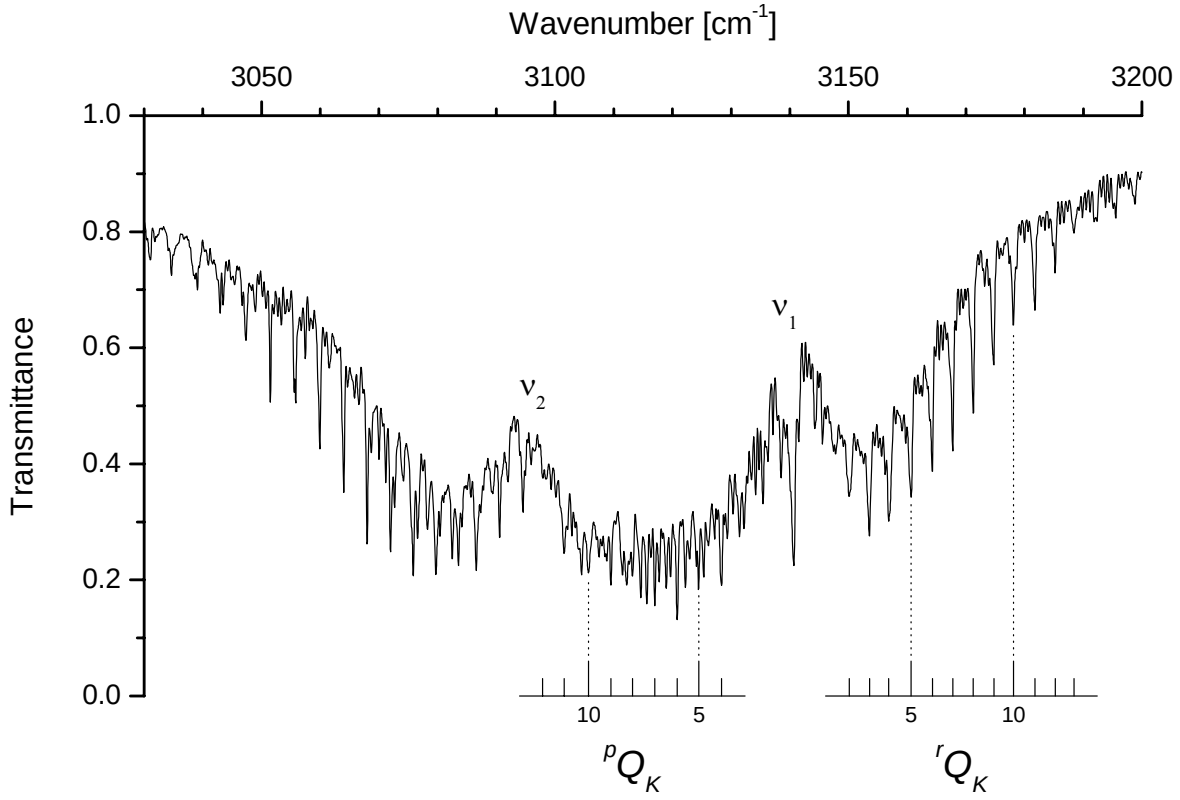

Figure 8.3. The gas-phase IR spectrum of the CH stretching region of H_2C=CHF at 0.2 cm^{-1} resolution (PLC = 13.4 cm, P = 3213 Pa, 298 K). The *B*-type rotational structure of the ν_1 band is labelled.

The rotational analysis has been performed only for the bands not yet investigated under high resolution. Then, the study has been carried out on the *B*-type component of the ν_1 and ν_2 fundamentals and $\nu_1 + \nu_5$, $\nu_4 + \nu_5$ and $\nu_6 + \nu_7$ combination bands. The band origins, $\tilde{\nu}_0$, the rotational parameters, the number of data used in the least squares fits, and the obtained standard deviations for all the considered five bands, are summarized in Table 8.3. The frequencies have been usually taken at the top of the sharp lines and the observed lines undergoing asymmetry splitting have not been used in the fitting procedure. In order to verify the consistency of the

assigned rotational structure, checks have been performed by using the ground state combination difference method in the symmetric top limit.

Table 8.3. Molecular parameters (cm^{-1}) of H_2C=CHF bands [a]

Band	$\tilde{\nu}_0$	$A'-\overline{B}'$	$A''-\overline{B}''$	N. of data	σ [b]
ν_1	3140.99(6)	1.8145(18) 1.8202 [c]	1.8235(19)	20	0.14
ν_2	3096.46(3)	1.7958(16) 1.8198 [c]	1.8200(17)	18	0.07
$\nu_1 + \nu_5$	4505.45(3)	1.8164(11) 1.8285 [c]	1.8145(11)	27	0.10
$\nu_4 + \nu_5$	2999.68(6)	1.824(3) 1.826 [c]	1.819(3)	14	0.12
$\nu_6 + \nu_7$	2457.57(3)	1.8119(10) 1.8270 [c]	1.8128(10)	24	0.09
		Average:	1.8180(17) 1.8261 [c]		

[a] The uncertainties given in parentheses are one standard deviation of the last significant digits.
[b] Standard deviation (cm^{-1}).
[c] Calculated values from the quadratic CCSD(T)/cc-pVQZ and cubic CCSD(T)/cc-pVTZ force constants.

8.5 INTEGRATED BAND INTENSITIES

The infrared spectra of vinyl fluoride has been divided into three main regions, by taking into account the different intensities of the absorption bands in the range 400 – 3500 cm^{-1}. The first, between 400 and 780 cm^{-1}, is reproduced in Figure 8.4 (a) and it is characterized by the weak absorptions originating from ν_9 (at 483 cm^{-1}) and ν_{12} (at 712 cm^{-1}). The second region, Figure 8.4 (b), is located between 780 and 1700 cm^{-1} and it shows several strong bands, i.e. the fundamentals ν_8, ν_{10}, ν_{11}, ν_7, ν_4, and the two weaker absorptions ν_5 and ν_6. Finally, as shown in Figure 8.4 (c), the spectrum between 1700 and 3500 cm^{-1} contains many very weak features, corresponding to the CH stretching fundamentals ν_1, ν_2 and ν_3, and various combination and overtone bands.

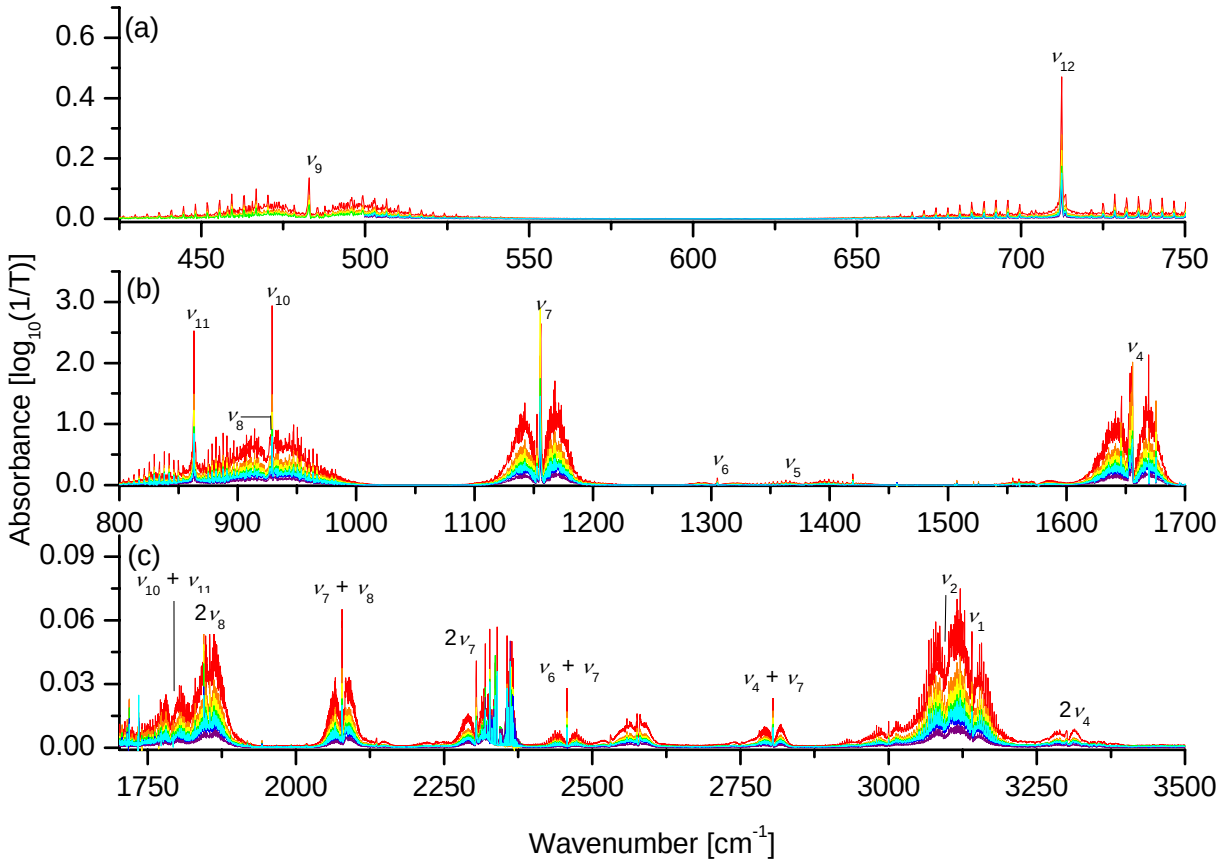

Figure 8.4. Regions of the gas phase IR spectrum of H_2C=CHF for the determination of the vibrational cross sections: (a) 400 – 780 cm^{-1}; (b) 780 – 1700 cm^{-1}; (c) 1700 – 3500 cm^{-1}. Experimental details: P = 438.0 Pa (—); 690.5 Pa (—); 817.5 Pa (—); 944.5 Pa (—); 1230 Pa (—); 1540 Pa (—); 2660 Pa (—); PLC = 13.4 cm; T = 298 K; 0.5 cm^{-1} resolution.

The retrieved integrated absorption cross sections together with their statistical errors are reported in Table 8.4; the estimated experimental uncertainty is better than 6.0%. For completeness, the same Table also includes the calculated intensity values. The agreement of the two sets of data is satisfactory; indeed the mean deviation between the experimental and calculated values is about 13%. The averaged photo-absorption spectrum for the region investigated in the present analysis is reproduced in Figure 8.5.

Table 8.4. Integrated cross sections of H_2C=CHF in the range 400 – 3500 cm^{-1}

Integration limits [cm^{-1}]	**Integrated absorption cross sections**		
	Experimental [a] [10^{-18} cm $molecule^{-1}$]	*Experimental* [a] [km mol^{-1}]	*Theoretical* [b] [km mol^{-1}]
420 – 580	0.714(12)	4.30(7)	4.24
610 – 1050	18.33(11)	110.4(7)	111.51
1050 – 1250	12.93(12)	77.9(7)	87.07
1250 – 1480	1.242(18)	7.48(11)	9.06
1520 – 1720	13.9(2)	83.7(12)	101.71
2000 – 2200	0.356(6)	2.14(4)	1.68
2900 – 3420	1.59(3)	9.57(18)	11.68

[a] Standard deviations in units of the last significant digits are given in parentheses. The estimated experimental uncertainties are better than 6.0% of the reported value.
[b] Sum of the computed intensities of the fundamentals comprised in the integration limits (see Table 8.6).

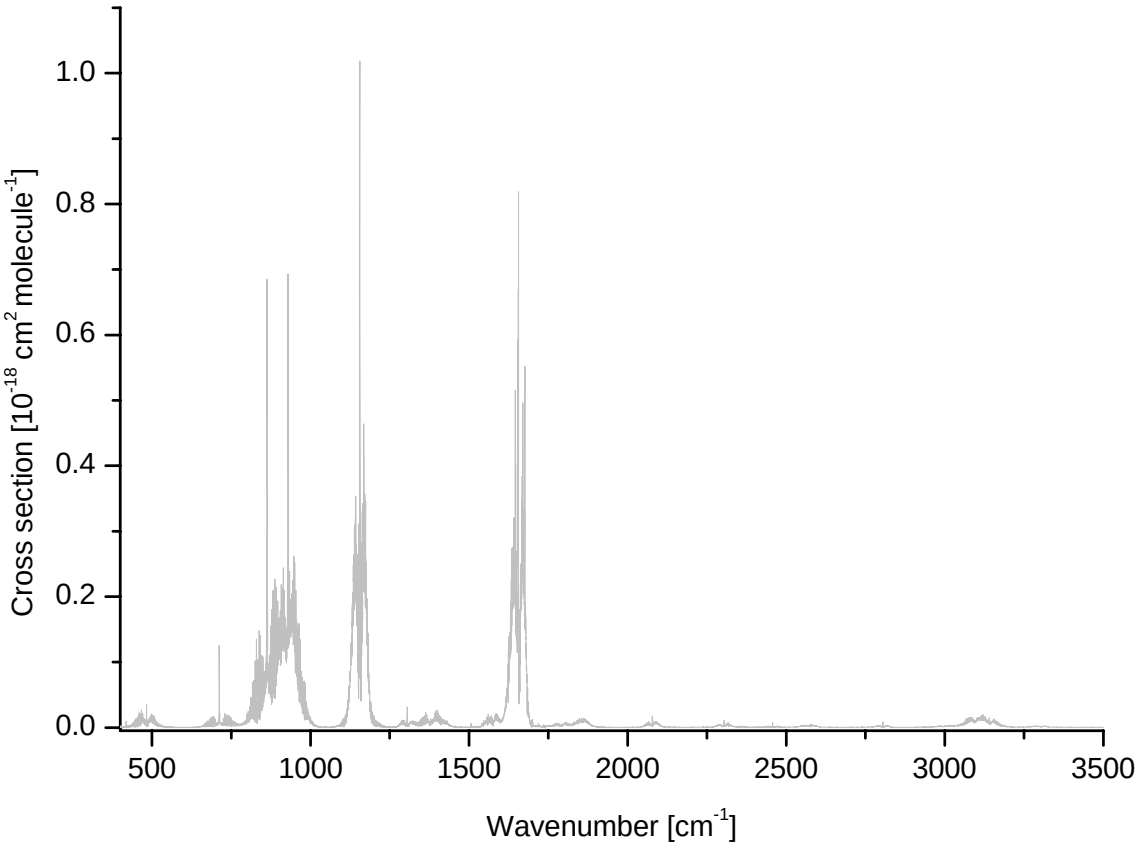

Figure 8.5. Averaged absorption cross section spectrum of H_2C=CHF in the region 400 – 3500 cm^{-1} (0.5 cm^{-1} resolution, T = 298 K).

8.6 EQUILIBRIUM GEOMETRY AND HARMONIC FORCE CONSTANTS

A detailed analysis of the equilibrium structure of vinyl fluoride with the determination of its semi-experimental structure has been reported recently by Demaison [188]. In general, CCSD(T) calculations give very reliable results in the determination of the equilibrium geometry. The systematic errors, on the basis of several structure optimizations, give an accuracy of 0.005 Å for bond lengths and 0.2° for bond angles [198]. From these considerations a geometry optimization has been carried out at CCSD(T)/cc-pVTZ level of theory, using the analytical gradients and the analytical derivatives of the dipole moment to compute the integrated infrared band intensities.

The harmonic force field has also been evaluated at the same level of theory from analytical second derivatives. On the basis of the structure calculations of Ref. [188] a CCSD(T)/cc-pVQZ geometry optimization has also been performed. Assuming the CCSD(T)/cc-pVQZ optimized equilibrium structure as the nearest to the true molecular geometry, the harmonic force field has been evaluated at the same level of theory in a Cartesian coordinates representation.

For the sake of completeness, Table 8.5 collects the set of 12 chemically intuitive internal coordinates R: of them, the planar $R_1 - R_9$ coordinates correspond to the nine determinable structural parameters which define the geometry of H_2C=CHF. Table 8.6 summarizes the fundamental frequencies computed with the harmonic force fields determined at the two levels of theory taken into account. The total energy distribution (TED %) values [199] in terms of the internal coordinates of Table 8.5 are also reported.

The integrated infrared band intensities, in units of km·mol^{-1}, have been computed employing the formula

$$A_i = 42.25472 \left| \frac{\partial \mu}{\partial Q_i} \right|^2 \tag{8.4}$$

where $\partial\mu/\partial Q_i$ are the dipole moment derivatives in $D\left(\text{Å amu}^{1/2}\right)^{-1}$, evaluated analytically at CCSD(T)/cc-pVTZ level of theory. These data are also included in Table 8.6.

Table 8.5. Internal coordinates of H_2C=CHF in the C_s symmetry point group and theoretical equilibrium geometries compared to the semi-experimental molecular structure (bond lengths in Å, bond angles in degrees)

		cc-pVTZ	cc-pVQZ	semi-experimental [a]
A'	C–F	1.3430	1.3428	1.3428
	C=C	1.3285	1.3253	1.3210
	$C–H_c$ [b]	1.0808	1.0801	1.0789
	$C–H_g$ [b]	1.0818	1.0809	1.0789
	$C–H_t$ [b]	1.0797	1.0790	1.0774
	$F\hat{C}C$	122.09	121.91	121.70
	$C\hat{C}H_c$	121.34	121.39	121.34
	$C\hat{C}H_g$	125.51	125.32	126.40
	$C\hat{C}H_t$	119.05	118.93	118.97
A"	$C–H_g$ out-of-plane bending			
	$C–H_c$ out-of-plane bending			
	Torsion			

[a] Ref. [188].
[b] c, *cis* to fluorine; g, geminal; t, *trans* to fluorine.

8.7 *AB INITIO ANHARMONIC FORCE FIELD*

The theoretical anharmonic force field has been calculated at the CCSD(T) level of theory using the ACES II program [195]. The cc-pVTZ basis set has been used in the frozen core approximation. Equilibrium molecular geometry has been calculated at first; then, the associated quadratic force constants have been evaluated analytically in Cartesian coordinates. The cubic and quartic force constants have been calculated in the reduced normal coordinates space with the use of a finite differences procedure, involving displacements along normal coordinates, through analytic calculation of the second derivatives at these displaced geometries.

As previously reported, the CCSD(T)/cc-pVQZ calculations of geometry and harmonic force field are assumed to better approach to the experimental values. However, in order to reduce the considerable amount of computer time required to obtain cubic and quartic force constants at this level of theory, a hybrid force field has been calculated. This has the geometry and second-order force constants at CCSD(T)/cc-pVQZ level of theory while the cubic and quartic force constants are evaluated at the CCSD(T)/cc-pVTZ level. The anharmonic spectroscopic constants have been derived from this hybrid force field, applying standard formulas based on second-order

rovibrational perturbation theory presented in Chapter 2.

Table 8.6. Harmonic wavenumbers ω_i, total energy distribution (TED %) and integrated band intensities obtained for H_2C=CHF at the CCSD(T) level of theory used in the calculations employing the cc-pVTZ and cc-pVQZ basis sets

			cc-pVTZ		cc-pVQZ
Mode		**TED %** [a]	*Wavenumber* [cm^{-1}]	*Intensity* [km mol^{-1}]	*Wavenumber* [cm^{-1}]
A'	ω_1	$R_5(55) + R_3(43)$	3280	1.96	3282
	ω_2	$R_4(92)$	3217	6.99	3221
	ω_3	$R_3(50) + R_5(44)$	3178	0.69	3178
	ω_4	$R_2(69)$	1703	93.08	1700
	ω_5	$R_9(48) + R_7(24) + R_8(23)$	1425	5.69	1418
	ω_6	$R_8(66) + R_7(20) + R_2(16)$	1335	2.50	1332
	ω_7	$R_1(51) + R_7(20) + R_6(20)$	1186	87.01	1179
	ω_8	$R_1(36) + R_9(32) + R_7(18)$	946	32.96	943
	ω_9	$R_6(78) + R_7(12)$	481	4.24	481
A''	ω_{10}	$R_{12}(100)$	956	35.58	954
	ω_{11}	$R_{11}(100)$	871	41.02	872
	ω_{12}	$R_{10}(96)$	725	1.95	725

[a] Terms ≥ 10%.

8.8 ANHARMONICITY CONSTANTS AND VIBRATIONAL RESONANCES

The anharmonicity constants x_{ij} of vinyl fluoride, calculated with the previously described force field, are reported in Table 8.7, together with the corresponding observed values (in parentheses). As stated in Chapters 2 and 4, these constants depend on the quadratic, cubic, and quartic force constants, and strong anharmonic interactions between fundamentals and overtones or combination bands may lead to a breakdown of the corresponding perturbation formulas. In these cases it is necessary to consider the x_{ij} effective constants (values indicated by an asterisk in Table 8.7), excluding such contributions from the perturbative summations (see Section 2.5). These effective anharmonicity constants have been introduced here to account for the following Fermi resonances: $(2\nu_{11} / \nu_4)$, $(2\nu_{12} / \nu_5)$, $(\nu_4 + \nu_5 / \nu_3)$, $(\nu_7 + \nu_9 / \nu_4)$, $(\nu_8 + \nu_9 / \nu_5)$, $(\nu_{10} + \nu_{12} / \nu_4)$.

Table 8.7. Anharmonicity constants x_{ij} (cm^{-1}) of $H_2C{=}CHF$ [a]

$i \setminus j$	1	2	3	4	5	6	7	8	9	10	11	12
1	– 30.7	– 10.1	– 102.5	0.2	– 17.1	– 4.9	– 3.4	– 5.4	– 1.5	– 3.5	– 15.9	– 4.1
2		– 50.9	– 20.2	–3.5	1.5	– 13.1	– 3.6	0.4	– 0.3	– 12.8	– 3.5	– 3.5
3			– 24.2	– 9.2 * (16.1)	– 14.7 * (10.6)	– 4.9	– 3.6	– 4.5	– 1.1	– 4.6	– 8.8	– 4.2
4				– 3.5	– 9.2 * (– 34.5)	– 12.5	– 7.3 * (– 6.8)	– 10.2	– 4.1 * (– 3.5)	– 6.2 * (– 5.6)	– 7.1 * (– 20.5)	– 3.9 * (– 3.3)
5					– 3.8	– 5.9	– 3.4	– 4.6 * (– 14.1)	– 0.6 * (– 10.1)	– 1.4	– 7.3	– 1.2 * (– 6.1)
6						– 2.3	– 2.9	– 0.2	1.0	– 1.8	– 0.8	– 1.4
7							– 3.2	– 5.3	– 2.1 * (– 2.7)	– 1.8	0.8	– 2.0
8								– 0.6	0.1 * (9.6)	– 0.7	2.0	0.3
9									1.3	– 0.1	0.9	1.1
10										– 3.4	– 1.2	– 0.7 * (– 1.3)
11											2.0 * (5.4)	– 1.2
12												– 0.6 * (0.6)

[a] The constants affected by Fermi resonances are marked by an asterisk, and the corresponding unperturbed values are given in parentheses.

In the wavenumber region from 5950 to 6250 cm^{-1} there is a resonant polyad involving 12 vibrational states detailed by the C—H overtones $2\nu_i$ (i = 1, 2, and 3), their combination bands $\nu_i + \nu_j$ (i = 1, 2; j = 2, 3), and three quanta combination bands $\nu_i + \nu_j + \nu_k$ (i =1, 2, 3; j = 4; k = 5, 6). This resonant polyad involves Darling-Dennison resonances defined from the following matrix elements (200):

$$\left\langle \mathrm{v}_i + 2 \quad \mathrm{v}_j \left| \hat{W} \right| \mathrm{v}_i \quad \mathrm{v}_j + 2 \right\rangle = \frac{k_{iijj}}{4} \left[(\mathrm{v}_i + 1)(\mathrm{v}_i + 2)(\mathrm{v}_j + 1)(\mathrm{v}_j + 2) \right]^{1/2} \tag{8.5}$$

and (201)

$$\left\langle \mathrm{v}_i + 1 \quad \mathrm{v}_j - 1 \left| \hat{W} \right| \mathrm{v}_i \quad \mathrm{v}_j \right\rangle = \frac{k_{iijj}}{4} \left[(\mathrm{v}_i + 1)(\mathrm{v}_j - 1)\mathrm{v}_j \right]^{1/2} \tag{8.6}$$

and the Fermi resonance matrix elements (37)

$$\left\langle \mathrm{v}_i \quad \mathrm{v}_j \quad \mathrm{v}_k \left| \hat{W} \right| \mathrm{v}_i - 1 \quad \mathrm{v}_j + 1 \quad \mathrm{v}_k + 1 \right\rangle = \phi_{ijk} \left[\frac{\mathrm{v}_i (\mathrm{v}_j + 1)(\mathrm{v}_k + 1)}{8} \right]^{1/2} \tag{8.7}$$

After diagonalization of the resonant matrix, three main wavenumber regions have been identified:

i. 5950 – 6000 cm^{-1} containing the $2\nu_3$ and other three quanta combination bands;
ii. 6000 – 6150 cm^{-1} with $\nu_1 + \nu_3$, $2\nu_2$, $\nu_2 + \nu_3$ and many other three quanta bands;
iii. 6200 – 6250 cm^{-1} with $\nu_1 + \nu_2$ and $2\nu_1$.

From inspection of the eigenvectors, it has been found that many transitions involving the combination bands are strongly mixed and, in some instances, the assignment becomes matter of taste.

The experimental and *ab initio* rotational constants are compared in Table 8.8. The calculated values have been computed with the hybrid anharmonic force field previously described. The agreement between calculated and experimental values is good and all the constants exhibit comparable small discrepancies.

Table 8.8. Theoretical rotational constants (cm^{-1}) of H_2C=CHF: comparison with experimental data

Vibrational state	Parameter	Calculated [a]	Observed	(O. – C.) % [b]
Ground	*A*	2.1539779	2.1543131 [c]	0.02
	B	0.3530043	0.35480820 [c]	0.51
	C	0.3028079	0.30414491 [c]	0.44
$v_1 = 1$	*A*	2.1476373	–	–
	B	0.3525442	–	–
	C	0.3023963	–	–
$v_2 = 1$	*A*	2.1473513	–	–
	B	0.3526590	–	–
	C	0.3024622	–	–
$v_3 = 1$	*A*	2.1459824	–	–
	B	0.3527206	–	–
	C	0.3024300	–	–
$v_4 = 1$	*A*	2.1447260	2.143574 [d]	–0.05
	B	0.3518468	0.3534695 [d]	0.46
	C	0.3016102	0.3029452 [d]	0.44
$v_5 = 1$	*A*	2.1624859	2.16768 [e]	0.24
	B	0.3536094	0.355282 [e]	0.47
	C	0.3025695	0.303892 [e]	0.44
$v_6 = 1$	*A*	2.1466726	2.147330 [e]	0.03
	B	0.3539970	0.355780 [e]	0.50
	C	0.3029657	0.304274 [e]	0.43
$v_7 = 1$	*A*	2.1617585	2.1607684 [c]	–0.05
	B	0.3524318	0.35428992 [c]	0.52
	C	0.3013644	0.30270804 [c]	0.44
$v_8 = 1$	*A*	2.1793511	2.190790 [f]	0.52
	B	0.3447842	0.3539404 [f]	2.59
	C	0.3020702	0.30334301 [f]	0.42
$v_9 = 1$	*A*	2.1520283	2.15120869 [g]	–0.04
	B	0.3529377	0.354653821 [g]	0.48
	C	0.3024772	0.303760709 [g]	0.42
$v_{10} = 1$	*A*	2.1492821	2.1371708 [f]	–0.57
	B	0.3601694	0.35446577 [f]	–1.61
	C	0.3030510	0.30437546 [f]	0.03
$v_{11} = 1$	*A*	2.1148872	2.115590 [f]	0.03
	B	0.3523780	0.3540522 [f]	0.47
	C	0.3030240	0.30435560 [f]	0.44
$v_{12} = 1$	*A*	2.1534229	2.1533486 [h]	0.00
	B	0.3525343	0.35435860 [h]	0.51
	C	0.3029195	0.30427227 [h]	0.44

[a] From the hybrid anharmonic force field (see text).
[b] (O. – C.) % = (Obs. – Calc.) × 100 / Obs.
[c] Ref. [186]. [d] Ref. [190]. [e] Ref. [192]. [f] Ref. [193]. [g] Ref. [191]. [h] Ref. [189].

Table 8.9 contains the equilibrium quartic centrifugal distortion constants (A-reduction), calculated from the quadratic force field (CCSD(T)/cc-pVQZ), and compares them with their experimental counterparts. The equilibrium sextic centrifugal distortion constants (A-reduction) calculated from CCSD(T)/cc-pVTZ cubic force field are reported in Table 8.9 as well. Comparisons with the available experimental ground state constants for quartic and sextic terms reveal a good agreement between theory and experiment.

Table 8.9. Experimental and calculated quartic and sextic centrifugal distortion constants (cm^{-1}) for H_2C=CHF

		Observed [a]	**Calculated**	**(O. – C.) %** [b]
Δ_J	$\times 10^6$	0.28126	0.27850	0.98
Δ_{JK}	$\times 10^5$	–0.2537	–0.26563	–4.70
Δ_K	$\times 10^4$	0.44367	0.45255	–2.00
δ_J	$\times 10^7$	0.5891	0.58000	1.54
δ_K	$\times 10^5$	0.1186	0.11028	7.02
Φ_J	$\times 10^{12}$	0.47	0.49756	–5.86
Φ_{JK}	$\times 10^{12}$	–	–0.14783	–
Φ_{KJ}	$\times 10^9$	–0.223	–0.24040	–7.80
Φ_K	$\times 10^8$	0.259	0.27861	–7.57
ϕ_J	$\times 10^{12}$	0.217	0.21150	2.53
ϕ_{JK}	$\times 10^{11}$	–	0.26819	–
ϕ_K	$\times 10^9$	0.46	0.44460	3.35

[a] Ref. [186].
[b] (O. – C.) % = (Observed – Calculated) × 100 / Observed.

8.9 LINE SHAPE PARAMETERS

The high resolution spectrum of vinyl fluoride in the 8.7 μm atmospheric region is characterized by the ro-vibrational transitions belonging to the ν_7 band, which corresponds to the C—F stretching. As pointed out at the beginning of the chapter, this spectral region is rather crowded: the high density of lines, about 90 lines per cm^{-1}, can be appreciated in Figure 8.6 (a). Besides the stronger absorptions of the ν_7 normal mode, the majority of the weakest lines is due to

the ro-vibrational transitions of the $\nu_7 + \nu_9 - \nu_9$ hot band. Indeed, according to the Boltzmann distribution, at 299 K the population of the $\nu_9 = 1$ vibrational level is about 10% relative to that of the ground state. Hence, the ro-vibrational transitions of $\nu_7 + \nu_9 - \nu_9$ are about one order of magnitude weaker than those of the ν_7 band. Due to their intensity the hot band lines strongly affect the main features and therefore they must be considered during the fitting procedure.

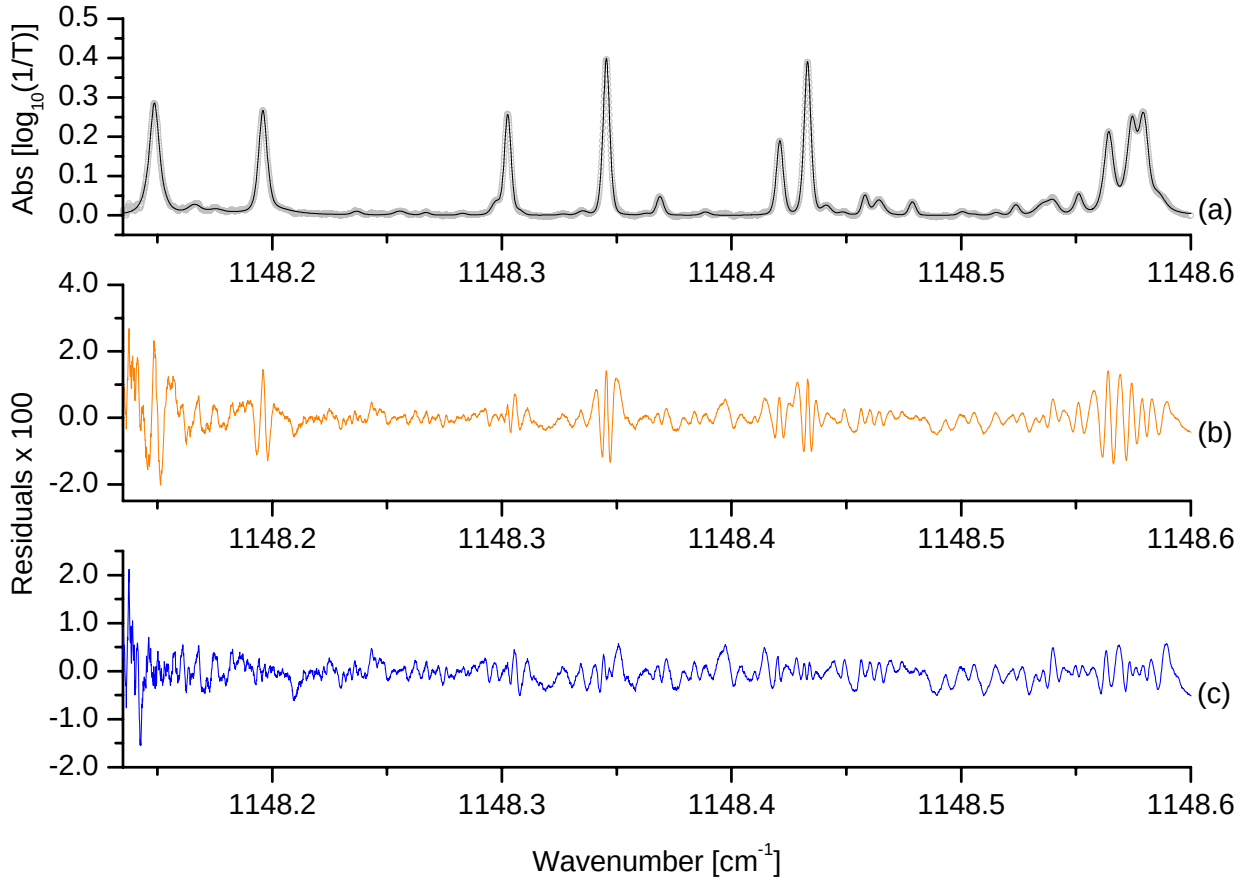

Figure 8.6. Vinyl fluoride spectrum between 1148.14 and 1148.60 cm^{-1}: (a) experimental (○) and computed (—) spectra. Experimental details: H_2C=CHF total pressure = 30.6 Pa, PLC = 92.3 cm, temperature = 299 K. The remaining rows show the residuals obtained from different models: (b) Voigt; (c) strong collision model (scm). The standard deviations of the fits, σ (cm^{-1}), are: $\sigma_{Voigt} = 4.5 \times 10^{-3}$; $\sigma_{scm} = 2.6 \times 10^{-3}$.

As first, the spectral lines have been fitted to the Voigt profile. However, the residuals show significant deviations from this model, as illustrated in Figure 8.6 (b). Besides, the majority of self-broadening coefficients cannot be properly determined. This is because, due to the low H_2C=CHF pressures employed, the Doppler ($\gamma_D \cong 1.0 \cdot 10^{-3}$ cm^{-1}) and the instrumental ($\gamma_D^{TDL} \cong 1.7 \cdot 10^{-3}$ cm^{-1}) line widths dominate over the Lorentzian component, and the pressure broadening is not enough pronounced to give well determined values of the collisional half widths. It has been observed that, in order to obtain the self-broadening coefficients from the fits with the Voigt profile, the vinyl fluoride pressure has to be raised up to about 200 Pa.

Table 8.10. (1 of 4). Line labelling, assignment and line parameters of ν_7 ro-vibrational transitions of $H_2C{=}CHF$ [a]

Line N.	J'	K_a'	K_c'	J''	K_a''	K_c''	$\tilde{\nu}_0$ [cm^{-1}]	γ_L^0 [cm^{-1} atm^{-1}] *Voigt*	*Nelkin - Ghatak*	Ω^0 [cm^{-1} atm^{-1}]	S^0 [10^{-21} cm $molecule^{-1}$]
1	10	7	4	11	8	3	1120.8982(5)	-	0.42(7)	0.74(19)	0.84(12)
2	18	9	9	18	10	8	1120.9310(2)	-	0.52(6)	0.15(3)	0.515(6)
3	49	1	48	50	1	49	1120.95340(8)	0.32(5)	0.348(14)	0.14(6)	1.558(11)
	49	2	48	50	2	49					
4	47	5	42	48	5	43	1120.9688(2)	-	0.39(4)	0.89(11)	0.74(3)
5	16	9	7	16	10	6	1120.9980(2)	-	0.20(7)	-	0.340(12)
6	48	8	40	49	8	41	1121.0060(2)	-	0.39(5)	0.30(5)	0.52(2)
7	48	3	45	49	3	46	1121.0149(2)	-	0.429(11)	0.24(5)	2.140(13)
	48	8	41	49	8	42					
8	15	9	6	15	10	5	1121.02867(10)	-	0.34(6)	-	0.287(8)
12	48	4	45	49	4	46	1121.0858(2)	0.31(2)	0.27(2)	0.34(11)	0.86(2)
18	48	9	39	49	9	40	1121.16520(11)	0.22(4)	0.36(3)	0.22(7)	0.83(2)
21	47	4	43	48	4	44	1121.2103(2)	0.301(12)	0.32(3)	0.32(11)	0.981(6)
22	49	0	49	50	0	50	1121.2313(2)	0.304(8)	0.311(9)	0.33(14)	1.73(2)
	49	1	49	50	1	50					
26	47	6	41	48	6	42	1121.2698(2)	0.44(8)	0.42(7)	1.07(7)	0.76(2)
28	48	10	38	49	10	39	1121.3161(5)	0.20(2)	0.47(5)	0.57(15)	0.713(5)
31	48	2	46	49	2	47	1121.3795(6)	0.29(2)	0.27(3)	-	0.912(8)
32	48	3	46	49	3	47	1121.3878(2)	0.39(2)	0.39(4)	-	1.189(9)
33	41	7	35	42	7	36	1126.0878(4)	-	0.68(4)	0.67(9)	1.30(2)
34	41	4	38	42	4	39	1126.0907(5)	-	0.53(9)	0.51(22)	2.10(2)
35	41	7	34	42	7	35	1126.1165(5)	-	0.94(5)	0.37(11)	1.90(2)
36	18	4	15	19	5	14	1126.1207(3)	-	0.82(40)	-	0.94(7)
37	40	4	36	41	4	37	1126.1545(7)	0.37(5)	0.32(2)	0.76(17)	3.4(3)
38	18	4	14	19	5	15	1126.1723(6)	-	0.60(20)	0.98(12)	0.66(7)
41	41	8	33	42	8	34	1126.24550(7)	-	0.27(10)	0.15(5)	1.6(2)
44	40	5	35	41	5	36	1126.2800(2)	-	0.316(11)	0.37(9)	1.67(2)
45	42	13	29	43	13	30	1126.2966(3)	-	0.53(14)	0.31(10)	0.74(2)
46	42	0	42	43	0	43	1126.35166(14)	0.58(2)	0.72(10)	0.56(11)	3.62(2)
	42	1	42	43	1	43					

Table 8.10 (continued 2 of 4)

Line N.	J'	K_a'	K_c'	J''	K_a''	K_c''	$\tilde{\nu}_0$ [cm^{-1}]	γ_L^0 [cm^{-1} atm^{-1}] *Voigt*	*Nelkin - Ghatak*	Ω^0 [cm^{-1} atm^{-1}]	S^0 [10^{-21} cm molecule^{-1}]
47	41	2	39	42	2	40	1126.3608(2)	-	0.23(4)	0.38(4)	2.19(2)
48	41	9	32	42	9	33	1126.3880(2)	-	0.36(11)	0.53(9)	1.48(2)
49	41	3	39	42	3	40	1126.3947(2)	0.60(8)	0.87(22)	1.0(2)	2.35(2)
50	41	13	28	42	13	29	1127.0336(11)	-	0.34(10)	1.6(7)	0.72(2)
51	39	5	34	40	5	35	1127.05060(7)	0.35(12)	0.49(9)	0.52(12)	1.63(3)
52	40	2	38	41	2	39	1127.0586(3)	-	-	0.29(8)	1.61(3)
53	41	0	41	42	0	42	1127.0721(5)	-	0.85(2)	-	3.5(4)
	41	1	41	42	1	42					
54	40	3	38	41	3	39	1127.1007(2)	-	0.19(6)	0.56(13)	1.68(2)
55	40	9	31	41	9	32	1127.1264(9)	-	0.51(20)	0.33(15)	1.86(4)
58	41	14	27	41	14	28	1127.1974(9)	-	-	-	0.65(7)
60	39	3	36	40	3	37	1127.2245(10)	-	0.59(10)	0.51(9)	2.27(4)
62	40	10	30	41	10	31	1127.2693(6)	-	0.60(20)	0.86(10)	1.80(4)
66	41	15	26	42	15	27	1127.3690(3)	-	0.50(11)	-	0.78(3)
67	39	6	33	40	6	34	1127.3764(4)	-	0.50(11)	0.87(20)	2.17(4)
68	39	5	35	40	5	36	1127.3929(5)	-	0.70(6)	0.17(2)	2.63(3)
69	40	11	29	41	11	30	1127.4073(5)	-	0.75(25)	0.37(9)	2.11(3)
71	40	1	39	41	1	40	1127.4473(7)	-	0.47(3)	0.78(5)	7.88(4)
72	33	5	28	34	5	29	1131.6307(5)	-	0.45(6)	0.63(3)	2.64(2)
73	34	1	33	35	1	34	1131.6497(3)	-	0.59(2)	0.23(3)	4.27(3)
74	34	2	33	35	2	34	1131.6620(2)	-	0.61(6)	-	6.61(3)
	34	10	24	35	10	25					
79	33	5	29	34	5	30	1131.73595(9)	0.51(9)	0.43(5)	0.76(15)	3.77(2)
	35	15	20	36	15	21					
80	33	4	30	34	4	31	1131.77691(13)	-	0.33(8)	0.31(9)	3.01(3)
82	34	11	23	35	11	24	1131.79872(8)	-	0.82(7)	0.69(6)	2.11(2)
84	33	2	31	34	2	32	1131.84041(11)	0.35(2)	0.87(4)	0.66(6)	3.26(2)
85	33	6	27	34	6	28	1131.84719(9)	-	0.65(9)	1.5(3)	3.08(2)
86	33	6	28	34	6	29	1131.86042(12)	-	0.31(8)	1.2(3)	2.74(3)
89	35	16	19	36	16	20	1131.9421(3)	0.85(9)	0.88(8)	0.46(2)	0.75(2)

Table 8.10 (continued 3 of 4)

Line N.	J'	K_a'	K_c'	J''	K_a''	K_c''	$\tilde{\nu}_0$ [cm^{-1}]	γ_L^0 [cm^{-1} atm^{-1}] *Voigt*	*Nelkin - Ghatak*	Ω^0 [cm^{-1} atm^{-1}]	S^0 [10^{-21} cm molecule^{-1}]
92	33	3	31	34	3	32	1131.9971(3)	-	0.84(6)	0.37(14)	7.58(2)
	33	7	26	34	7	27					
93	33	7	27	34	7	28	1132.0010(2)	-	-	0.43(3)	2.47(4)
94	34	12	22	35	12	23	1132.0107(4)	-	0.70(8)	0.60(16)	2.09(3)
96	32	3	29	33	3	30	1132.0408(3)	-	0.29(7)	1.5(3)	4.13(4)
97	34	0	34	35	0	35	1132.0455(3)	-	0.89(9)	0.96(14)	7.23(4)
	34	1	34	35	1	35					
99	32	4	28	33	4	29	1132.06298(10)	-	0.88(5)	0.655(8)	3.94(2)
100	27	12	15	28	12	16	1137.0217(6)	-	0.96(21)	0.40(7)	2.07(2)
101	27	6	19	27	7	20	1137.04048(13)	-	0.88(10)	0.75(11)	3.50(3)
102	25	3	22	26	3	23	1137.0520(3)	0.35(4)	-	0.71(14)	2.84(5)
103	26	1	25	27	1	26	1137.0768(4)	-	0.253(5)	0.191(12)	4.9(3)
106	26	2	25	27	2	26	1137.15207(14)	-	-	1.1(4)	2.23(2)
107	26	8	18	27	8	19	1137.1564(2)	0.74(4)	0.54(5)	0.22(9)	5.93(2)
108	27	13	14	28	13	15	1137.1707(2)	-	0.36(7)	0.61(15)	3.626(14)
	28	17	11	29	17	12					
109	25	2	23	26	2	24	1137.18880(8)	0.77(9)	0.76(2)	0.87(15)	6.552(13)
113	26	9	17	27	9	18	1137.28139(12)	-	0.78(5)	0.68(18)	4.455(12)
114	25	4	21	26	4	22	1137.32001(10)	0.33(3)	0.88(8)	0.312(7)	3.876(13)
115	27	14	13	28	14	14	1137.33787(6)	-	0.68(15)	-	2.52(2)
117	28	18	10	29	18	11	1137.36254(12)	-	1.1(2)	0.95(30)	0.36(3)
119	26	10	16	27	10	17	1137.41444(8)	-	0.39(4)	1.3(4)	3.585(14)
120	25	4	22	26	4	23	1137.46439(9)	-	0.56(20)	0.39(8)	4.4(3)
121	10	1	10	11	1	11	1148.1499(8)	0.80(20)	0.70(2)	0.15(5)	2.8(2)
123	10	7	3	11	7	4	1148.1963(4)	-	0.69(6)	0.34(2)	3.05(4)
125	10	8	2	11	8	3	1148.30268(13)	0.48(4)	0.68(4)	0.32(8)	2.88(2)
126	9	1	8	10	1	9	1148.3454(3)	0.74(2)	0.80(2)	0.41(5)	4.253(13)
127	8	0	8	9	1	9	1148.3689(2)	-	0.85(8)	-	0.73(7)
128	10	9	1	11	9	2	1148.42090(10)	0.31(4)	0.54(6)	0.51(14)	2.59(2)
129	9	2	7	10	2	8	1148.4328(2)	0.75(2)	0.39(3)	0.87(20)	4.29(2)

Table 8.10 (continued 4 of 4)

Line N.	J'	K_a'	K_c'	J''	K_a''	K_c''	$\tilde{\nu}_0$ [cm^{-1}]	γ_L^0 [cm^{-1} atm^{-1}] *Voigt*	*Nelkin - Ghatak*	Ω^0 [cm^{-1} atm^{-1}]	S^0 [10^{-21} cm molecule^{-1}]
131	9	1	8	9	2	7	1148.4574(4)	0.51(10)	0.87(8)	-	0.63(3)
136	20	1	19	20	2	18	1148.5397(4)	-	1.1(4)	-	0.75(7)
137	10	10	0	11	10	1	1148.5511(3)	-	1.1(4)	0.70(20)	0.98(3)
138	9	3	6	10	3	7	1148.5643(2)	0.47(12)	0.45(5)	-	3.30(5)
139	9	3	7	10	3	8	1148.5741(2)	0.65(21)	0.91(15)	0.94(20)	4.6(4)
140	9	2	8	10	2	9	1148.5792(3)	-	0.85(8)	-	5.3(3)

[a] Figures in parentheses refer to one standard deviation.

Table 8.11 (1 of 2). Line parameters of $\nu_7 + \nu_9 - \nu_9$ ro-vibrational transitions of $H_2C{=}CHF$ [a]

Line N.	$\widetilde{\nu}_0$ [cm^{-1}]	γ_L^0 [cm^{-1} atm^{-1}]		Ω^0 [cm^{-1} atm^{-1}]	S^0 [10^{-22} cm $molecule^{-1}$]
		Voigt	*Nelkin - Ghatak*		
9	1121.0453(6)	-	-	-	1.03(4)
10	1121.0579(3)	-	0.19(9)	0.36(9)	4.62(6)
11	1121.0812(6)	-	0.390(9)	-	3.8(3)
13	1121.0962(2)	0.38(4)	0.29(6)	0.18(7)	3.87(13)
14	1121.1107(3)	-	-	-	2.91(10)
15	1121.1226(2)	-	0.56(13)	-	2.8(2)
16	1121.1336(2)	-	0.46(8)	-	3.72(14)
17	1121.15649(11)	0.43(3)	0.29(5)	0.36(11)	7.44(13)
19	1121.1717(2)	-	0.50(17)	0.17(3)	1.7(2)
20	1121.1865(2)	-	0.14(6)	0.30(4)	2.58(8)
23	1121.2403(2)	-	0.41(6)	0.68(4)	4.8(3)
24	1121.2563(2)	-	-	-	3.86(11)
25	1121.2643(2)	-	0.77(6)	0.34(2)	1.7(3)
27	1121.2858(3)	-	0.38(8)	-	2.23(6)
29	1121.3426(6)	0.41(4)	0.40(9)	0.57(20)	4.87(11)
30	1121.3573(7)	-	0.47(10)	-	0.72(7)
39	1126.1799(7)		1.3(4)	0.66(20)	4.8(4)
40	1126.1974(4)	-	-	-	9.62(12)
42	1126.2622(2)	-	1.0(4)	-	4.1(6)
43	1126.2696(2)	-	1.2(5)	-	2.0(5)
56	1127.1343(10)	-	0.90(40)	-	17.2(12)
57	1127.1890(12)	-	0.66(15)	0.95(27)	5.4(4)
59	1127.2199(9)	-	0.74(20)	-	9.6(9)
63	1127.2822(9)	-	-	-	2.3(3)
64	1127.3031(6)	-	1.2(5)	0.69(20)	10.4(3)
65	1127.3533(6)	-	0.86(28)	1.1(5)	2.9(6)
70	1127.4313(9)	-	-	1.2(6)	1.2(4)
75	1131.6877(2)	-	-	-	8.62(8)
76	1131.70390(10)	-	-	-	3.81(2)
77	1131.7231(2)	0.53(9)	0.77(18)	0.54(14)	7.4(2)

Table 8.11 (continued 2 of 2)

Line N.	$\widetilde{\nu}_0$ [cm^{-1}]	γ_L^0 [cm^{-1} atm^{-1}]		Ω^0 [cm^{-1} atm^{-1}]	S^0 [10^{-22} cm molecule^{-1}]
		Voigt	*Nelkin - Ghatak*		
78	1131.7321(3)	-	1.4(4)	0.35(11)	3.9(3)
81	1131.7833(2)	-	1.2(3)	1.1(4)	5.7(3)
83	1131.8243(2)	-	0.29(8)	0.64(18)	7.03(13)
87	1131.8745(2)	-	0.34(2)	-	5.2(3)
88	1131.8819(2)	-	0.26(2)	0.51(24)	6.2(2)
90	1131.9711(2)	-	-	-	6.2(3)
91	1131.9806(2)	-	0.39(7)	-	4.5(2)
95	1132.0262(3)	-	0.93(10)	0.69(18)	11.2(5)
98	1132.0558(2)	-	0.28(3)	0.32(9)	2.0(2)
104	1137.0955(2)	-	0.98(13)	0.62(20)	6.53(11)
105	1137.1034(3)	-	0.95(20)	0.49(9)	8.29(11)
110	1137.2241(3)	-	1.2(3)	0.66(13)	2.9(3)
111	1137.2578(2)	-	1.4(4)	0.28(11)	6.7(5)
112	1137.26507(13)	-	0.76(23)	0.80(3)	1.11(3)
116	1137.3515(2)	-	0.60(10)	0.13(3)	2.7(2)
118	1137.37004(11)	-	0.65(20)	1.1(5)	7.1(6)
122	1148.1675(11)	-	-	-	3.8(9)
124	1148.2978(5)	0.78(25)	0.78(25)	-	7.6(3)
130	1148.4406(5)	0.63(5)	0.63(5)	-	5.6(8)
132	1148.4636(4)	-	1.1(2)	1.2(3)	12.1(3)
133	1148.4782(3)	-	0.56(15)	-	5.3(5)
134	1148.5235(2)	-	0.79(25)	-	4.0(9)
135	1148.5349(5)	-	0.58(13)	-	6.7(7)

[a] Figures in parentheses refer to one standard deviation.

On the other hand, the 'w' shape of the residuals suggests a narrowing of the spectral lines due to Dicke effect. Therefore, the lines have also been fitted employing the Nelkin – Ghatak profile. When this strong collision model is used, there is a dramatic reduction of the residuals, as shown in Figure 8.6 (c), and the standard deviation of the fit decreases by about a factor of two. In addition, this leads to a determination of many of the broadening coefficients that have not been obtained using the Voigt profile.

The results indicate that in the investigated pressure range the self-broadened vinyl fluoride sample appears as a system strongly affected by the motional narrowing effect, in which both the velocity changing collisions and the internal state changing-, dephasing-collisions play an almost equal role in determining the shape of the spectral lines. Consequently, the line profiles accounting for the Dicke narrowing effect must be employed to model the experimental features.

The retrieved line parameters for the ν_7 lines are listed in Table 8.10, where both the self-broadening coefficients given by the fits with the Voigt profile and those obtained employing the Nelkin – Ghatak profile have been reported. The line parameters of the hot band have been determined as well, and they are reproduced in Table 8.11. Nevertheless, the quantum numbers of the transitions are not given because of the lack of a reliable assignment of the ro-vibrational transitions at present. Again, the self-broadening and narrowing coefficients of few lines (usually weak or blended) have not been reported because their accuracy is too low. As stressed before, this is due to the small range of vinyl fluoride pressures adopted in the experiments, which limits the accuracy of the measurements for some lines. On the other hand, the use of low pressures is strongly recommended, in order to avoid saturation effects, and hence working in the experimental conditions of applicability of the Beer – Lambert law.

Since the ν_7 normal mode belongs to the *A*' symmetry species, it gives rise to a *A*/*B* hybrid band which presents both *A*- and *B*-type ro-vibrational transitions. The ν_7 *B*-type transitions are much weaker then the *A*-type ones, and hence only few *B*-type lines have been observed. These transitions have self-broadening coefficients, which seem to decrease with increasing pseudo quantum number K_a'', as illustrated in Figure 8.7. This dependence agrees with the trend obtained for the ν_1 band of sulphur dioxide (which is a *B*-type band as well) in Chapter 7, and with the

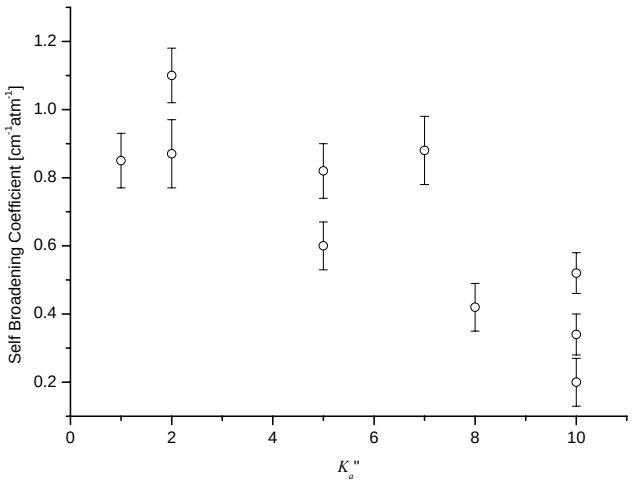

Figure 8.7. K_a'' dependence of the self-broadening coefficients for the *B*-type transitions of vinyl fluoride.

theoretical predictions of Tejwani [168] for *B*-type transitions. On the other hand, the calculations carried out by Tejwani for *A*-type transitions predicted a decrease of the pressure broadening coefficients with increasing K_a'' as well as a significant *J* dependence. The results obtained here for the *A*-type transitions suggest that, for a given value of K_a'', there is a decrease of the self-broadening coefficients as *J*" increases. This trend, which is illustrated in Figure 8.8 for K_a'' = 0, 1, tends to persist up to K_a'' = 6. Then for K_a'' ≥ 7, no regular trend of the broadening parameters has been observed. Nevertheless, this can be caused by the smaller number of transitions observed with K_a'' ≥ 9, which gives poorer statistics, and their smaller intensity. Indeed, the strong overlapping among some spectral lines, which often cannot be resolved, is one of the unavoidable factors limiting the accuracy of the retrieved parameters, in particular for the weakest lines, such as the *B*-type transitions or the transitions having K_a'' > 9.

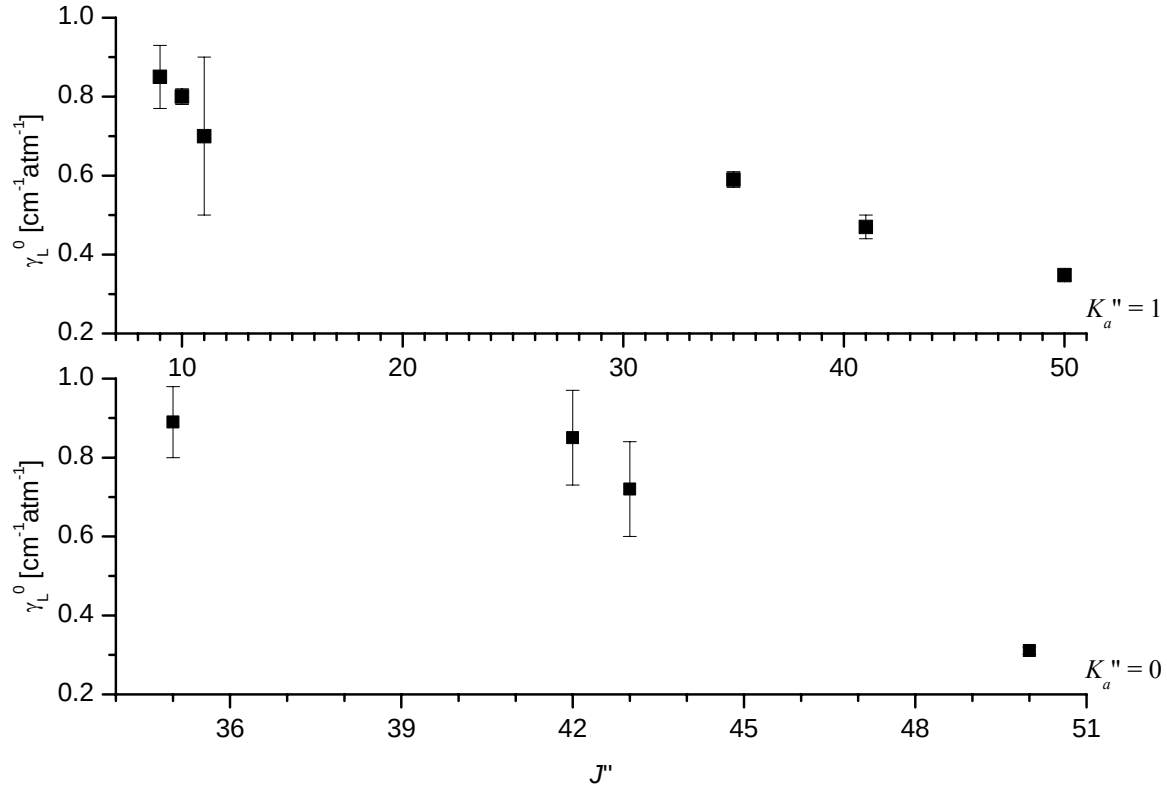

Figure 8.8. *J*" dependence of the self broadening coefficients for *A*-type transitions of vinyl fluoride with K_a'' = 0, 1.

The fits employing the Nelkin – Ghatak profile led to the determination of the narrowing parameter, which resulted to be 0.51 (± 0.20) cm^{-1} atm^{-1}. As can be seen, the magnitude of the self-broadening and self-narrowing have a similar extent.

Concerning the individual narrowing coefficients, they do not show any clear dependence upon the quantum numbers, except for $K_a^{''} = 0$, 2 transitions, where the narrowing coefficients seem to decrease smoothly with *J*", as shown in Figure 8.9.

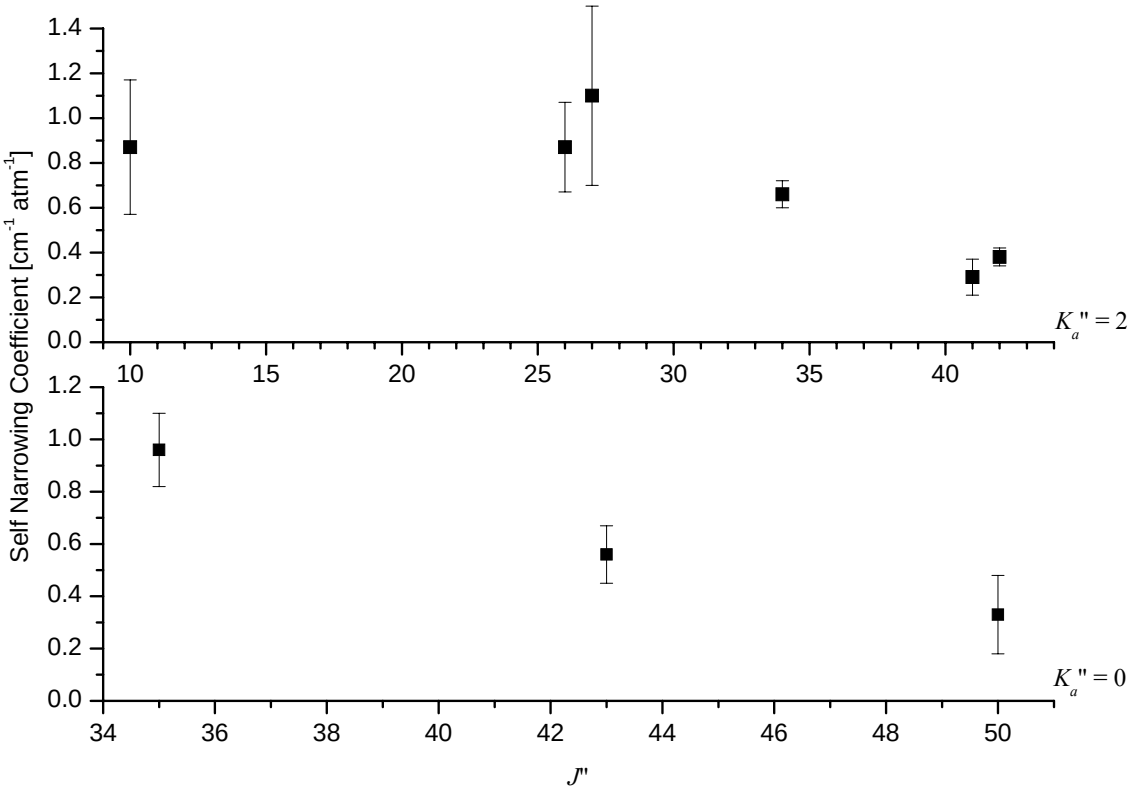

Figure 8.9. *J*" dependence of the self-narrowing coefficients of vinyl fluoride. For $K_a^{''}$ = 0 and 2 transitions, Ω^0 decrease with increasing *J*" values.

This observation, together with the unusually large narrowing coefficient obtained for some of the analysed lines, may suggest that, despite the low H_2C=CHF pressure, line mixing effects could occur. Another effects which can be responsible for the large narrowing coefficients is the speed-dependence of the line widths. Nevertheless, further investigations are required to say whether or not line mixing or speed dependencies arise.

9. Jet-Cooled Diode Laser Spectrum and FTIR Integrated Band Intensities of CF_3Br

Fully halogenated compounds, such as chlorofluorocarbons and halons, are largely employed by industry due to their versatility. For example, they are used as refrigerants, fire-extinguishers, solvents and foam-blowing agents.

On the other hand, these chemicals actively take part to the photochemistry of the Earth's atmosphere and are sources of a number of radicals which may destroy ozone catalytically. Once in the stratosphere, chlorinated and brominated organic compounds undergo photochemical oxidation, thus releasing chlorine and bromine atoms that critically affect the Earth's protective ozone layer. Among the bromine sources there are the long-lived anthropogenic halons and methyl bromide: between 1980 and the late 1990s emissions of these compounds have resulted in more than a doubling of the atmospheric bromine loading [202]. Bromotrifluoromethane (CF_3Br, Halon 1301, Freon 13B1), which is characterized by a long stratospheric lifetime of about 65 years, has the highest Ozone Depletion Potential among the sources of bromine (12 referred to CFC 11, as reported in Ref. [203]), and therefore it has been banned by the Montreal Protocol since 2003. Its averaged global tropospheric mixing ratio has been estimated equal to 2.6 ppt [204]: this value may seem rather low, but it must be underlined that bromine is considered up to 45 – 70 times more efficient than chlorine as a catalyst of stratospheric ozone depletion [205].

The vibrational infrared spectrum of bromotrifluoromethane shows two strong absorption bands, ν_1 and ν_4 located at 1085 and 1210 cm^{-1}, respectively, and a number of weaker fundamental, overtone and combination features. Hence, this compound can heavily contribute to the greenhouse effect. In addition to its importance in the atmospheric chemistry, CF_3Br has been proposed as a prototype molecule for infrared laser chemistry and isotopically selective multiphoton induced dissociation (Refs. [206 – 209] and references therein).

Owing to the severe environmental effects and the suggested variety of applications, CF_3Br has been the subject of many spectroscopic studies in the last decades. Concerning the microwave

and the millimetre regions, the ^{12}C species has been extensively analyzed in the past [210 – 215] thus leading to the determination of the dipole moment and to an accurate set of ground state constants for both the $^{79/81}Br$ isotopologues; the bromine nuclear quadrupole constants have been theoretically investigated, employing several DFT and hybrid HF/DFT methods [216]. Recently, also the ^{13}C species have been studied [217] employing both radiofrequency-microwave double resonance (RFMWDR) and conventional microwave spectroscopic techniques.

The infrared spectrum of CF_3Br has been originally assigned by Plyler and Acquista [218] and subsequently by Polo and Kent Wilson [219]; the structure of many fundamental, overtone and combination bands has been analysed at low and medium resolution employing grating [220, 221] and Fourier transform spectrometers [222]. Successively, the advent of tunable diode laser and FTIR spectrometers with a greater resolving power has allowed a more accurate ro-vibrational analysis of the fine structure of the infrared spectrum (see for example Refs. [223 – 225]).

The last years have seen a renewed interest in spectroscopic studies of similar halogenated pollutants (for example Ref. [226 – 228] and references therein), since an accurate ro-vibrational analysis of the bands falling in the mid infrared region can support the quantitative detection and the temperature profiles modelling of these compounds. Furthermore, since a better understanding of their radiative forcing needs accurate information about absorption strengths, the integrated cross section measurements in a wavenumber range as wide as possible can be useful.

The present Chapter deals with the jet-cooled high-resolution study of the CF_3Br spectrum in the ν_1 band region around 1085 cm^{-1}. The high resolution analysis of the ν_1 fundamental has been carried recently [229]; here the study is extended to the weaker absorptions coming from $2\nu_5$ and $\nu_2 + \nu_3$ for both the bromine isotopologues.

The previous ro-vibrational investigations of these bands, which were carried out several years ago [230, 231] with a diode laser spectrometer, were lacking of some important spectral regions: for example, the *P* branch of $2\nu_5$ at 200 K was completely overlapped by the stronger *R* branch of the ν_1 fundamental, so the analysis was restricted to the *R* branch transitions. In addition, the *K*-structure of both these bands appeared not completely resolved even at a resolution of about 0.002 cm^{-1} and the accuracy of the measurements, limited by the secondary standards employed, was estimated around 0.003 cm^{-1}. In the present work the use of a slit-jet expansion has permitted for the first time to access the resolved *P* branch transitions, thus recording the high-resolution spectrum of $2\nu_5$ between 1090 and 1102 cm^{-1}. In the region of $\nu_2 + \nu_3$, a new and more complete data set has been obtained from the analysis of either the cold (about 50 K) free-jet spectrum and that recorded at the stratospheric temperature of 200 K. The measurements cover about 85% of the range 1110 – 1130 cm^{-1}, thus furnishing *P* and *R* transitions at higher *J* values than the previous

data. As a consequence, a more reliable and accurate set of spectroscopic parameters has been obtained for $2\nu_5$ and $\nu_2 + \nu_3$ of both bromine isotopologues. Furthermore, many features belonging to various hot bands have been identified, and the corresponding molecular constants have been determined. In addition, the vibrational cross sections have been measured for all the absorptions in the spectral range between 450 and 2500 cm^{-1}, thus obtaining the integrated band intensities for many fundamental and combination bands and extending the analysis to spectral regions not previously investigated [232 – 235].

9.1. EXPERIMENTAL DETAILS

Details of the home built supersonic free-jet system have been given previously in Chapter 5. In these measurements, the pulsed supersonic planar expansion of the gas sample composed by 15% of CF_3Br in helium was regulated by a modified solenoid valve (General Valves, Series 9) driven by a controller (Iota One, General Valve Corporation). Laser scans (about 0.3 cm^{-1} wide, duration of about 1 ms) and gas pulses (about 2 ms) were properly synchronized by using an electronic delay generator: a four channel digital oscilloscope (Tektronix TDS 3014) was used to acquire simultaneously the jet spectrum and the signals employed for reference purpose. Up to 128 scans were averaged together without appreciably increasing the observed linewidths. The stagnation pressure was varied between 150 and 180 kPa, while the pump system kept the background pressure below 0.3 Pa, thus minimizing absorptions coming from the rotationally warm background gas. Linewidths up to $7 \cdot 10^{-4}$ cm^{-1} (FWHM) were measured in the free-jet spectrum, mainly limited by residual Doppler broadening and laser jitter noise. From spectral simulations a rotational temperature of about 50 K was estimated. For the spectra recorded at 200 K, a 92.3 cm path-length cell was employed; the observed line-widths were generally better than $1.2 \cdot 10^{-3}$ cm^{-1}. The wavenumber calibration was based on SO_2 line positions measured in a room temperature reference cell.

The infrared absorption cross sections were obtained from experiments carried out in a 134.0 (± 0.5) mm path-length stainless steel cell, equipped with KBr windows; the temperature in the cell, continuously monitored, has been kept constant at 298.0 K (± 0.5 K). The infrared spectra were recorded on the Bruker Vertex 70 FTIR instrument presented in Section 5.2; a total of 128 interferograms for both the sample and the background spectra were co-added and transformed into the corresponding absorbance spectrum using boxcar apodization and Mertz phase correction. The spectra were recorded at resolutions of 0.2 and 0.5 cm^{-1}: different pressures of CF_3Br (Matheson,

purity > 99%) were used, both pure and mixed with nitrogen (SIAD, purity > 99%) to a total pressure of 101 kPa. The pressures were measured employing different capacitance vacuum gauges (Alcatel model ARD 1001, 1002 and 1003 with a full scale range of 1000, 100 and 10 mbar, respectively), each with a quoted manufacturer's full scale accuracy of 0.15%. A 15 minute delay between filling of the cell and recording of the spectrum was adopted. The same experimental procedure for sample handling outlined in Section 8.2 for vinyl fluoride was adopted.

9.2. HIGH RESOLUTION SPECTRA: DESCRIPTION OF THE 2 ν_5 AND $\nu_2 + \nu_3$ BAND REGIONS

The CF_3Br molecule is a prolate symmetric rotor belonging to the C_{3V} symmetry point group. Therefore it has nine infrared active normal modes of vibration which are of either A_1 ($\nu_1 - \nu_3$) or E ($\nu_4 - \nu_6$) symmetry. A survey spectrum recorded at 0.5 cm^{-1} resolution is presented in Figure 9.1.

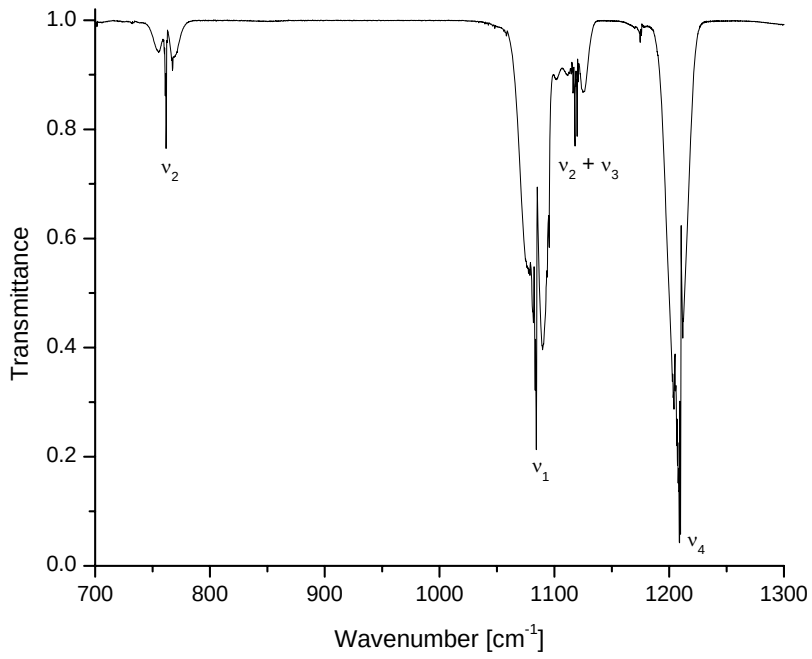

Figure 9.1. Survey spectrum of CF_3Br between 700 and 1300 cm^{-1}. The strongest bands fall in this spectral region. Experimental conditions: P = 90.4 Pa; T = 298 K; PLC = 13.4 cm; 0.5 cm^{-1} resolution.

The vibrations of A_1 symmetry species are non-degenerate, whereas the modes having E symmetry are doubly degenerate. Since the relative abundances of the ^{79}Br and ^{81}Br isotopes is 50.7% and 49.3%, respectively, the two bromine isotopologues, $CF_3{}^{79}Br$ and $CF_3{}^{81}Br$, are present in almost equal amounts. Therefore, the diode laser spectrum of natural CF_3Br appears rather crowded, being also present features coming from several hot bands. Concerning the vibrations here investigated, the $2\nu_5$ band is a hybrid band and it is composed of two components: $2\nu_5^0$ which is the parallel component, and $2\nu_5^{\pm 2}$ which is the perpendicular component. Strictly speaking, the two components behave as two different bands which are coupled

together by vibration-rotation interactions. On the other hand, being the combination of two parallel bands, the $\nu_2 + \nu_3$ vibration is in turn a parallel band.

The region between 1090 and 1102 cm^{-1} is characterized by the ν_1 band *R* branch and the parallel component of the $2\nu_5$ overtone, centred at about 1095 cm^{-1}. The proximity of the bromine isotopologue band origins (about 0.12 cm^{-1}) causes a considerable overlapping of the *K*-structure. Furthermore, even at 200 K, the *P* branch transitions appear completely buried under the stronger absorption features of the near ν_1 fundamental (band origins at 1084.76902 and 1084.52168 cm^{-1} for $CF_3{}^{79}Br$ and $CF_3{}^{81}Br$, respectively). Only the spectrum recorded in a free-jet expansion has permitted the access to this spectral region, leading to the assignment of some *P*(*J*) multiplets, which otherwise are completely masked by the *R*(*J*) features of ν_1 . Figure 9.2 reproduces the spectrum around 1093.6 cm^{-1}, where the multiplets *P*(14 – 15) and *P*(13 – 14) of $CF_3{}^{79}Br$ and $CF_3{}^{81}Br$, respectively, are located.

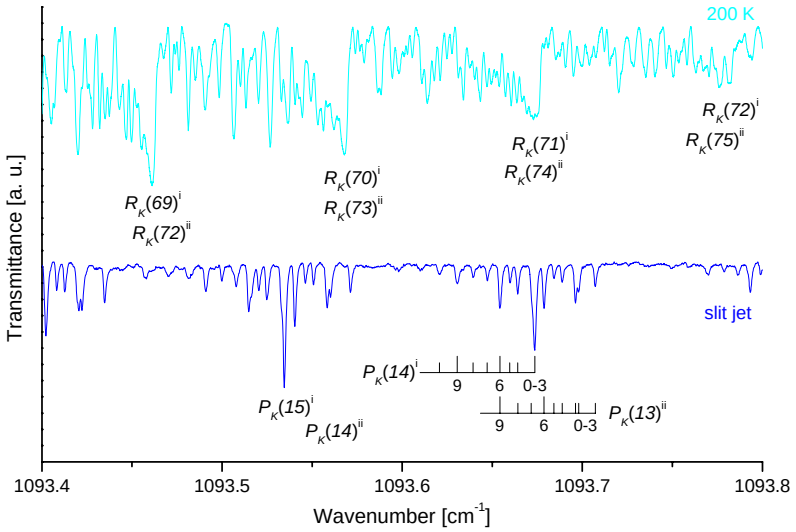

Figure 9.2. CF_3Br spectrum around 1093.6 cm^{-1}. Upper trace: spectrum recorded at 200 K showing the $R_K(J)$ multiplets of the ν_1 fundamental. Lower trace: slit-jet spectrum illustrating the $P_K(J)$ lines of $2\nu_5{}^0$ overtone. i refers to $CF_3{}^{79}Br$, ii refers to $CF_3{}^{81}Br$.

The upper trace, referring to the 200 K spectrum, clearly shows how the absorptions of the ν_1 fundamental completely cover the weaker $2\nu_5$ transitions which, conversely, are evident in the colder (50 K) slit-jet spectrum. A similar spectral simplification is achieved in the *Q*-branch region, where transitions with high and low (*J*, *K*) values occur together. This effect can be observed in Figure

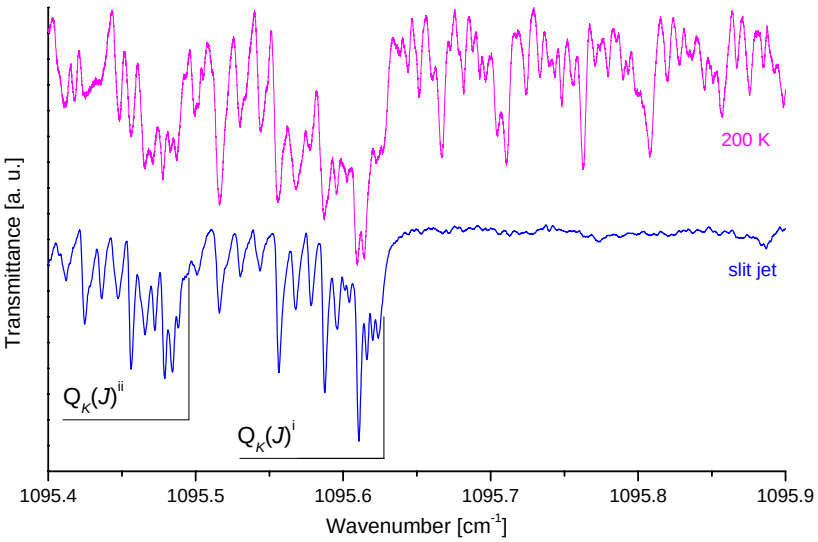

Figure 9.3. Portion of the $2\nu_5{}^0$ *Q* branch around 1095.6 cm^{-1}. Upper trace: spectrum recorded at 200 K. Lower trace: slit-jet spectrum; $Q_K(J)$ bandheads labelled by i and ii refer to $CF_3{}^{79}Br$ and $CF_3{}^{81}Br$, respectively.

9.3: at 200 K (upper trace) the structure appears congested and partially masked by the *R*-branch transitions belonging to the ν_1 fundamental, while in the supersonic expansion (lower trace) the two bandheads of $CF_3{}^{79/81}Br$ $2\nu_5$ overtone are well separated.

Figure 9.4 reports a wide portion of the free-jet spectrum: owing to the noticeable cooling, it closely resembles that of a parallel band, with a rather dense *Q* branch extending to lower wavenumbers and well-defined clusters separated by about 2*B* that constitute the *P* and *R* branches.

In the same figure it is also shown the computed spectrum calculated employing the spectroscopic Hamiltonian parameters obtained in the present investigation: as it can be seen, there is a good agreement between the computed and experimental spectra. No transitions belonging to the perpendicular component of this overtone band (i.e. $2\nu_5^{\pm 2}$) have been observed in the range 1090 – 1102 cm^{-1}.

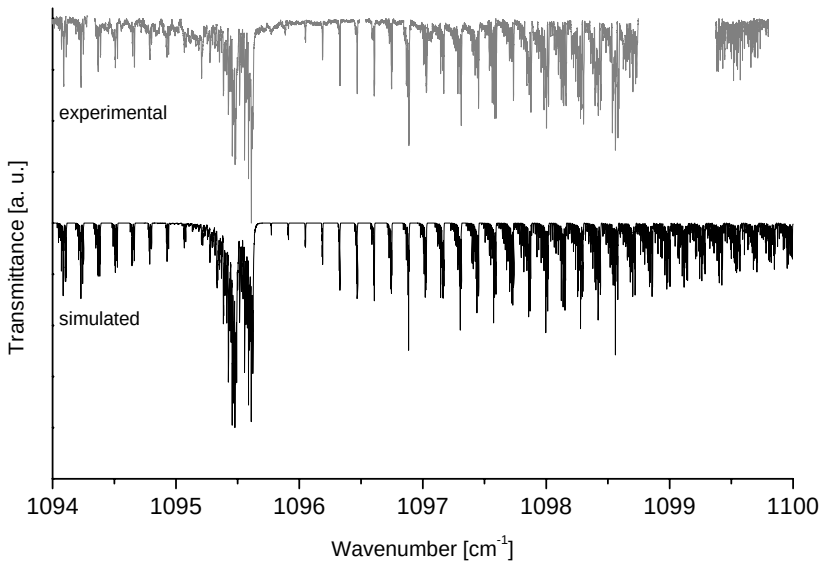

Figure 9.4. Portion of the survey free-jet spectrum of the $2\nu_5{}^0$ overtone. Upper trace: experimental spectrum. Lower trace: simulated spectrum (*T* = 50 K, FWHM = 0.0007 cm^{-1}).

The $\nu_2 + \nu_3$ combination band shows the typical parallel-type structure: compared to the $2\nu_5$ overtone the density of lines is greater, because the term $\Delta(A - B)$, mainly ruling the *K*-component positions within a given multiplet, is much smaller. Another difference is the presence of many hot bands, whose intensities are considerable even at low temperature: the strongest identified features belong to the $\nu_2 + 2\nu_3 - \nu_3$ and $\nu_2 + \nu_3 + \nu_6 - \nu_6$ hot bands of both the isotopologues. As shown in Figure 9.5 the absorptions due to $\nu_2 + \nu_3 + \nu_6 - \nu_6$ are still clearly observable in the spectrum recorded at 200 K. Indeed, the lower vibrational states of both the $\nu_2 + 2\nu_3 - \nu_3$ and $\nu_2 + \nu_3 + \nu_6 - \nu_6$ hot bands have at 200 K a relative Boltzmann population with respect to the ground state of about 16% and 22%, respectively. In Figure 9.5 it is also demonstrated how the absorptions due to hot bands are no longer observable in the slit-jet spectrum. Another example of the rotational cooling, achieved thanks to the supersonic expansion, is highlighted in Figure 9.6 by comparing the width of the *Q* branch of the $\nu_2 + \nu_3$ of $CF_3{}^{79}Br$ at 200 K with that obtained in the supersonic jet.

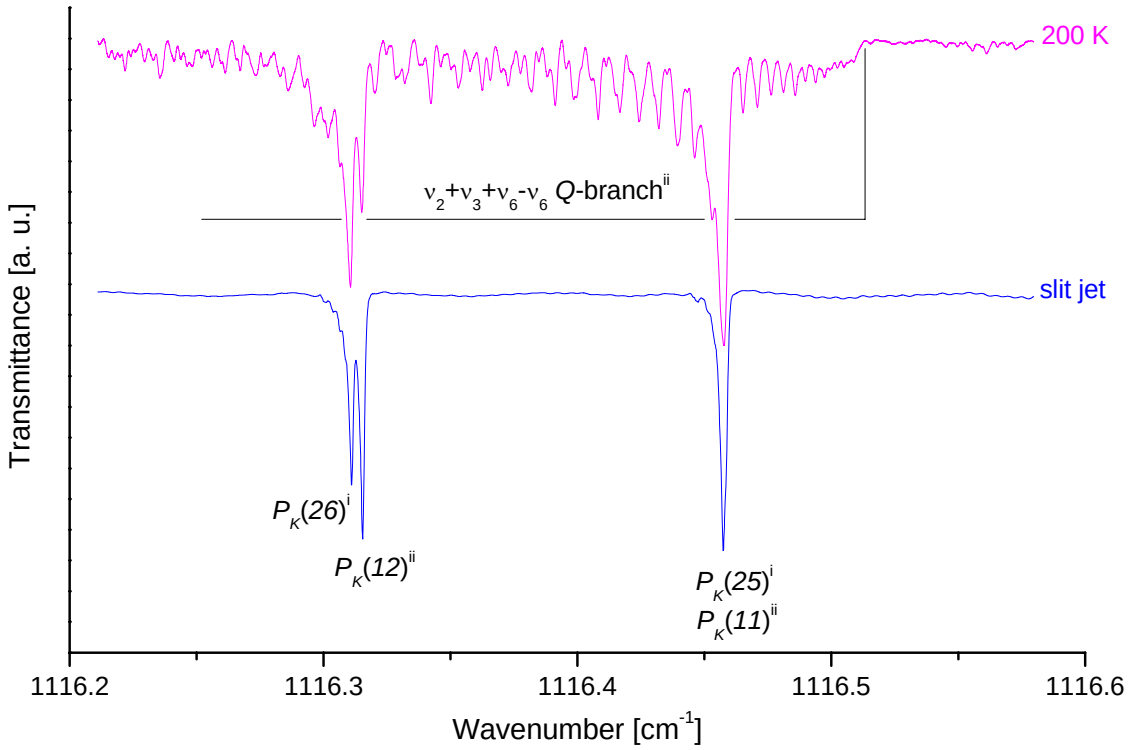

Figure 9.5. A portion of CF_3Br $\nu_2 + \nu_3$ band region near 1116 cm^{-1}. Upper trace: 200 K spectrum. Lower trace: slit jet spectrum. Note how in the free jet spectrum the Q-branch of the $\nu_2 + \nu_3 + \nu_6 - \nu_6$ hot band completely disappears. i refers to $CF_3{}^{79}Br$, ii refers to $CF_3{}^{81}Br$.

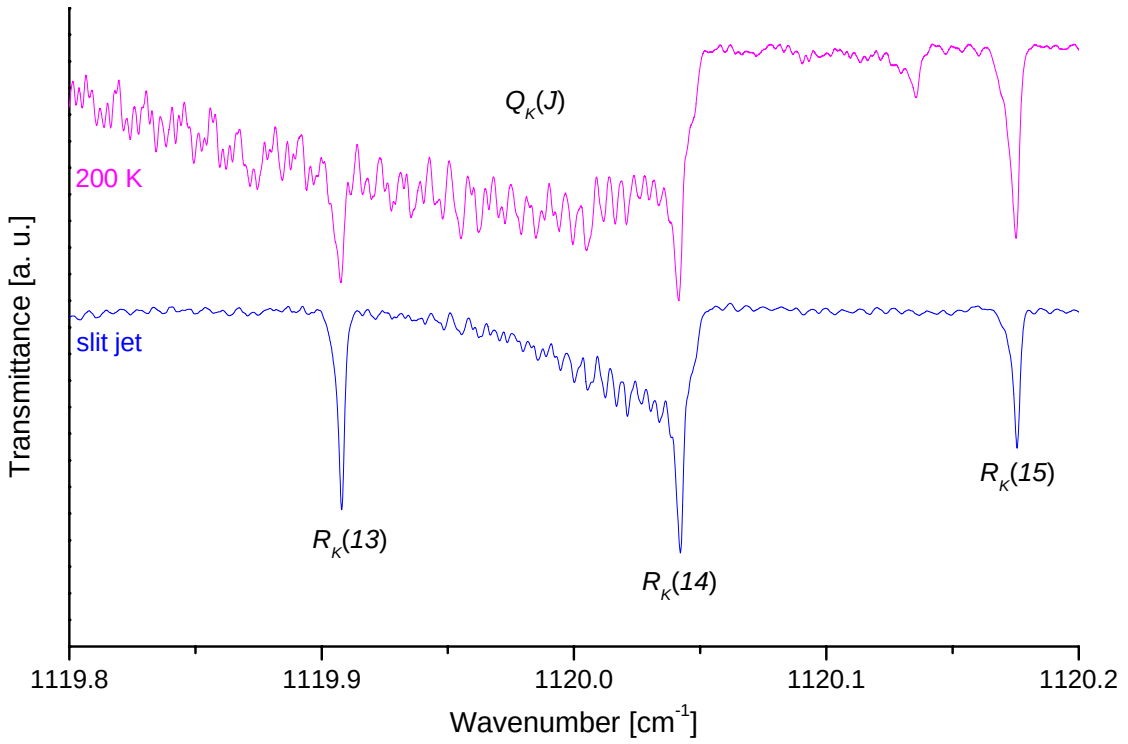

Figure 9.6. Portion of the $\nu_2 + \nu_3$ band of CF_3Br around 1120.0 cm^{-1}. Upper trace: spectrum recorded at 200 K, the $Q_K(J)$ branch of $CF_3{}^{79}Br$ is indicated. Lower trace: slit-jet spectrum, $R_K(J)$ multiplets of $CF_3{}^{81}Br$ $\nu_2 + \nu_3$ are labelled.

9.3 ROVIBRATIONAL ANALYSIS OF $2\nu_5$ AND $\nu_2 + \nu_3$

The ro-vibrational analysis, which has led to the spectroscopic constants of both the $2\nu_5^0$ and the $\nu_2 + \nu_3$ parallel bands, has been carried out by fitting the assigned transitions to the theoretical model represented by the Hamiltonian of equation 3.42. As fitting-prediction software, the Picket's CALPGM package has been employed [236]: an uncertainty of 0.0007 cm^{-1} has been attributed to well resolved single lines, whereas for blended or scarcely resolved features, an uncertainty of 0.002 cm^{-1} has been assumed.

The spectroscopic constants of the $2\nu_5^0$ band for the both the $^{79/81}Br$ isotopologues obtained from the free-jet spectrum together with the molecular constants obtained by the whole set of data (i.e. slit jet and 200 K spectra) are presented in Table 9.1. The complete analysis has led to the identification of 375 and 353 lines for $CF_3{}^{79}Br$ and $CF_3{}^{81}Br$, respectively.

Table 9.1. Spectroscopic constants (cm^{-1}) for the $2\nu_5{}^0$ band of CF_3Br [a]

	$CF_3{}^{79}Br$		$CF_3{}^{81}Br$	
	Slit jet	*Slit jet and 200 K*	*Slit Jet*	*Slit Jet and 200 K*
$\tilde{\nu}_0$	1095.6276(2)	1095.62746(11)	1095.4955(2)	1095.49544(11)
B'	0.0700141(9)	0.0700150(2)	0.0693629(8)	0.0693639(2)
B''	0.069985970 [b]	0.069985970 [b]	0.069333439 [b]	0.069333439 [b]
$\Delta(A-B)\times10^3$	–0.532(2)	–0.5314(12)	–0.530(3)	–0.5341(13)
$D_J'\times10^8$	0.75(8)	0.794(9)	0.69(7)	0.788(9)
$D_J''\times10^8$	0.8989 [b]	0.8989 [b]	0.8868 [b]	0.8868 [b]
$D_{JK}'\times10^7$	0.41(3)	0.440(5)	0.42(3)	0.375(6)
$D_{JK}''\times10^7$	0.43393 [b]	0.43393 [b]	0.42720 [b]	0.42720 [b]
$\Delta D_K\times10^8$	-	-	-	0.22(7)
N. of data	188	375	179	353
$\sigma\times10^3$	0.35	0.46	0.59	0.55
J_{max}	32	53	33	53
K_{max}	15	33	15	36

[a] Quoted errors refer to one standard deviation.
[b] From Ref. [215].

Although the overall agreement between experimental and computed spectra is good, concerning the $K \leq 3$ transitions small discrepancies from the computed line positions have been observed in some of the multiplets analyzed of both the isotopologues. Because no irregularities have been found in the near ν_1 and $\nu_2 + \nu_3$ bands, as possible perturber the $2\nu_5^{\pm 2}$ vibration, with different rotational interactions, has been considered; however, the inclusion of the corresponding terms in the Hamiltonian did not improve the overall results. The lack of directly observed transitions of $2\nu_5^{\pm 2}$, as well as of other bands in the investigated region, has made a better characterization impossible: furthermore, this interacting scheme may be complicated by the interaction of $2\nu_5^{\pm 2}$ with other dark states represented by the $\nu_5 + 2\nu_6$ combination band.

Regarding the $\nu_2 + \nu_3$ band, different spectral sections in the *P*, *Q* and *R* branches have been investigated and the *K*-structure in the *P*(*J*) and *R*(*J*) multiplets has been resolved and unambiguously assigned. Table 9.2 reports the spectroscopic parameters for the $^{79/81}$Br isotopologues obtained from the free-jet spectrum and those obtained by the whole set of data (slit jet together with 200 K spectra). The complete analysis has led to the identification of 347 and 635 lines for $CF_3{}^{79}Br$ and $CF_3{}^{81}Br$, respectively.

As stated in the previous Section and shown in Figure 9.5, in the region between 1100 and 1130 cm^{-1} the spectrum recorded at 200 K reveals several absorptions coming from different hot bands. The strongest identified absorptions belong to $\nu_2 + 2\nu_3 - \nu_3$ and $\nu_2 + \nu_3 + \nu_6 - \nu_6$: for the hot band of ν_6, the perpendicular component is too weak to be observed and therefore the analysis has dealt only with the parallel component. Since the observed features are very weak and generally the *K*-structure is unresolved, the rotational analysis has been limited to the *J* peaks. The analysis has been carried out using the polynomial method, and the *J* peaks have been fitted to the following equation:

$$\tilde{\nu}(m) = A + B \cdot m + C \cdot m^2 + D \cdot m^3 \qquad (9.1)$$

with

$$A = \tilde{\nu}_0$$

$$B = B' + B''$$

$$C = B' - B''$$

$$D = -2\,(D_J' + D_J'')$$

and $m = -J$ for the P branch and $J + 1$ for the R branch. The set of spectroscopic parameters obtained for $CF_3{}^{79}Br$ and $CF_3{}^{81}Br$ is reported in Table 9.3.

Table 9.2. Spectroscopic constants (cm^{-1}) for the $\nu_2 + \nu_3$ band of CF_3Br [a]

	$CF_3{}^{79}Br$		**$CF_3{}^{81}Br$**	
	Slit jet	*Slit jet and 200 K*	*Slit Jet*	*Slit Jet and 200 K*
$\tilde{\nu}_0$	1120.0511(2)	1120.05110(10)	1118.0000(2)	1117.99994(10)
B'	0.0698300(7)	0.06983037(10)	0.0691789(5)	0.06917932(8)
B''	0.069985970 [b]	0.069985970 [b]	0.069333439 [b]	0.069333439 [b]
$\Delta(A - B) \times 10^4$	–0.35(3)	–0.383(4)	–0.42(2)	–0.444(2)
$D_J' \times 10^8$	0.87(5)	0.900(2)	0.87(3)	0.8890(12)
$D_J'' \times 10^8$	0.8989 [b]	0.8989 [b]	0.8868 [b]	0.8868 [b]
$D_{JK}' \times 10^7$	0.44(4)	0.4070(9)	0.41(2)	0.3989(6)
$D_{JK}'' \times 10^7$	0.43393 [b]	0.43393 [b]	0.42720 [b]	0.42720 [b]
$\Delta D_K \times 10^8$	0.24 [c]	0.25(3)	0.24 [c]	0.257(12)
N. of data	86	347	99	635
$\sigma \times 10^3$	0.49	0.49	0.39	0.49
J_{max}	37	85	43	88
K_{max}	21	42	24	48

[a] Quoted errors refer to one standard deviation.
[b] From Ref. [215]. [c] From Ref. [231].

Table 9.3. Spectroscopic constants (cm^{-1}) for the $\nu_2 + 2\nu_3 - \nu_3$ and $\nu_2 + \nu_3 + \nu_6 - \nu_6$ hot bands of CF_3Br [a]

	$CF_3{}^{79}Br$		$CF_3{}^{81}Br$	
	$\nu_2 + 2\nu_3 - \nu_3$	$\nu_2 + \nu_3 + \nu_6 - \nu_6$	$\nu_2 + 2\nu_3 - \nu_3$	$\nu_2 + \nu_3 + \nu_6 - \nu_6$
$\tilde{\nu}_0$	1120.9422(5)	1118.5611(4)	1119.1300(4)	1116.5180(4)
B'	0.069767(6)	0.069703(6)	0.069131(6)	0.069047(7)
B''	0.069934(6)	0.069861(6)	0.069298(6)	0.069204(7)
$(D_J' + D_J'') \times 10^8$	1.84(14)	2.4(2)	2.44(15)	1.9(2)
N. of data	63	50	52	48
$\sigma \times 10^3$	0.51	0.27	0.39	0.33
J_{max}	64	85	52	71

[a] Quoted errors refer to three standard deviations.

9.4. CROSS SECTION MEASUREMENTS BY MEDIUM RESOLUTION FTIR SPECTRA

The absorbance cross-section per molecule (cm^2 $molecule^{-1}$) of the sample, $\sigma(\tilde{\nu})$, has been calculated from the measured infrared absorbance using the relationship given in Equation 7.3. The integrated cross section G_{int} (cm^2 $molecule^{-1}$ cm^{-1}) is then derived from the absorbance cross section by means of equation 7.4. If two or more strongly overlapped bands without a clear separation are present in a given spectral interval, a single integration has been performed.

At the beginning of the experiments some spectra have been recorded at two different resolutions (0.2 and 0.5 cm^{-1}) for different pressures of both the pure CF_3Br and its mixture with N_2. A portion of the recorded spectra is given in Figure 9.7, where it is shown the ν_2 band at different pressures of CF_3Br. The validity of the Beer – Lambert's law has been checked by plotting the integrated absorbance as a function of the sample pressure. A linear dependence has been observed over the whole concentration range used in the present investigation, as shown in Figure 9.8. The calculated band intensities, corresponding to the same concentration of the sample and different spectral resolution, have been found to be equal within the error of the measurements. Therefore the cross sections have been determined from the spectra of the pure gas measured at the resolution of 0.5 cm^{-1}, because they generally have a better signal-to-noise ratio, especially for the weaker absorption features.

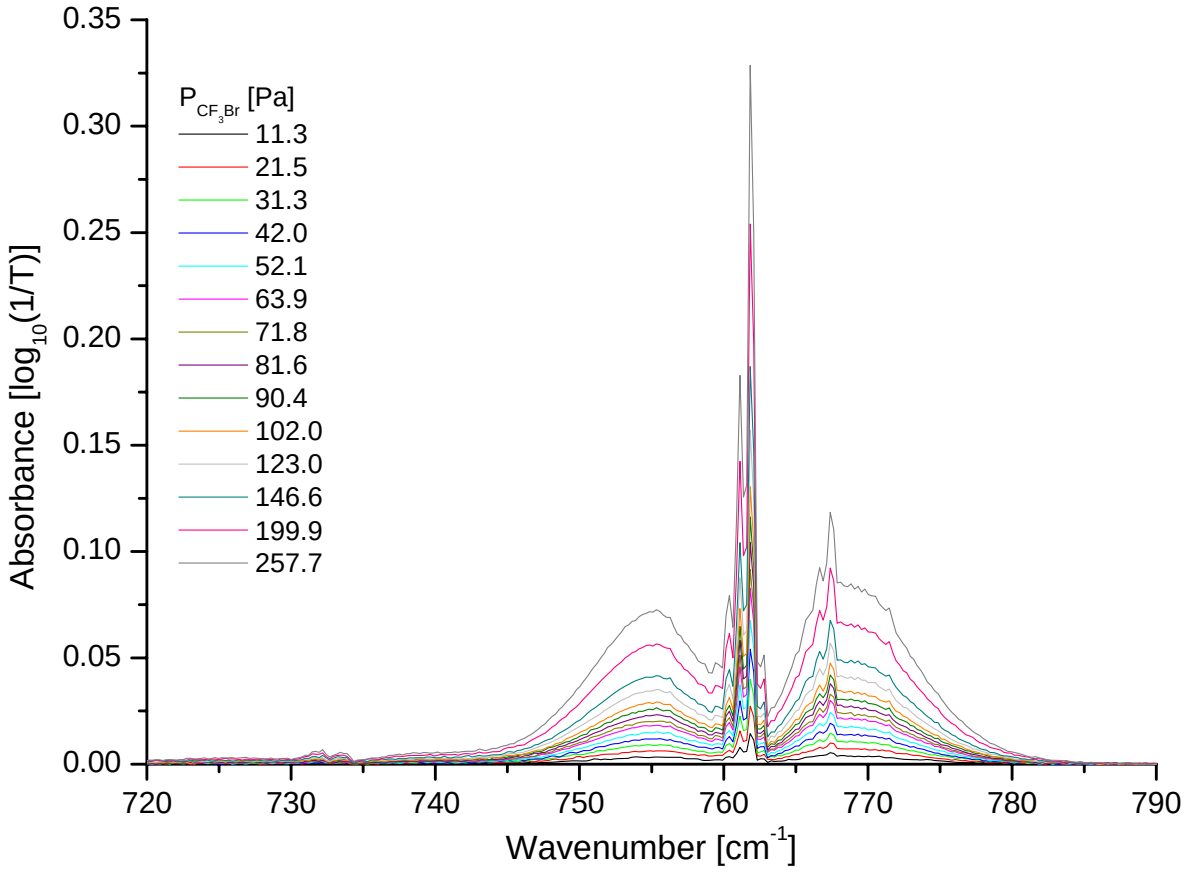

Figure 9.7. Example of the series of spectra recorded at different CF_3Br pressures for the determination of the vibrational cross sections. The reported band is the ν_2 normal mode. Experimental details: T = 298 K, PLC = 13.4 cm, 0.5 cm^{-1} resolution, CF_3Br pressures are given in figure.

The survey spectrum of bromotrifluoromethane in the range 450 – 2500 cm^{-1} reveals several absorption bands: by taking into account their different intensities, the infrared spectrum has been divided into three main regions. The first one is located between 450 and 715 cm^{-1} and it is characterized by the weak absorptions originating from the ν_5 fundamental (at 548 cm^{-1}) and the $2\nu_3$ overtone (at 700 cm^{-1}): here the pressure of the sample has been kept in the range 10 – 80 hPa. The second range, located between 720 and 1250, shows two strong fundamentals (ν_1 and ν_4), a medium one (ν_2) and some weak combination ($\nu_1 + \nu_3$, $\nu_5 + \nu_6$, $\nu_2 + \nu_3$) and overtone bands ($2\nu_5$): here

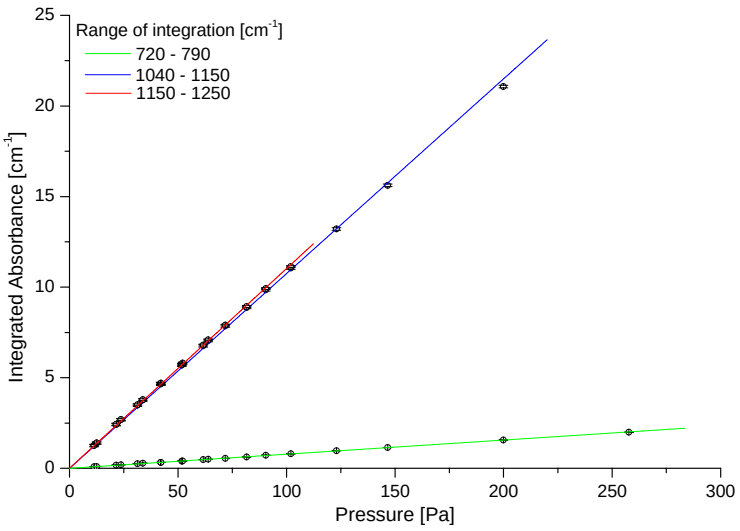

Figure 9.8. Linear dependence of the integrated absorbance on the pressure within the three integration regions corresponding to the strongest absorption.

the intensities have been measured with the pressure in the range 10 – 300 Pa. Finally, between 1250 and 2500 cm^{-1} the spectrum contains many very weak features, corresponding to various combination and overtone bands: here the pressure has been varied in the range 10 – 80 hPa.

The retrieved integrated absorption cross sections together with their statistical errors are reported in Table 9.4. The estimated experimental uncertainty is around 5.5%. For comparison, in Table 9.4 the most recent literature data [234, 235] are listed as well. In the range 720 – 1250 cm^{-1} the integration limits have been chosen to facilitate the comparison among the different sets of data. In the other regions many bands appear not completely resolved and so the data refer to several bands grouped together: in the range 1360 – 1800 cm^{-1} the absorptions appear so strongly overlapped that the integration limit has been extended to measure their overall intensities. Figure 9.9 shows the resulting averaged photo-absorption spectrum for some regions investigated in the present analysis.

Table 9.4. Integrated absorption cross sections (10^{-18} cm molecule^{-1} cm) of CF_3Br in the range 450 – 2500 cm^{-1}

INTEGRATION LIMITS	***INTEGRATED ABSORPTION CROSS SECTION***		
[cm^{-1}]	*This work* [a]	*Drage et al.* [b]	*Orkin et al.* [c]
720 – 790	5.6(2)	5.5 (8%)	5.45 (4%)
1040 – 1150	77.8(1.4)	74 (7%)	79.7 (2%)
1150 – 1250	78.7(9)	74 (7%)	78.3 (2%)
500 – 600	0.380(4)		
670 – 715	0.379(2)		
810 – 880	0.150(2)		
1250 – 1360	1.249(5)		
1360 – 1800	0.624(17)		
1800 – 1910	0.177(8)		
1940 – 2000	0.131(3)		
2120 – 2240	0.125(7)		
2240 – 2340	0.717(10)		
2340 – 2480	0.65(2)		

[a] In parentheses standard deviations in units of the last significant digits are given. The estimated experimental uncertainties are 5.5% the reported value.

[b] From Ref. [235]. The estimated uncertainty includes the statistical as well as the systematic uncertainty.

[c] From Ref. [234]. Uncertainties are the 95% confidence intervals and do not include the systematic uncertainty.

9.5 EVALUATION OF RADIATIVE FORCING AND GLOBAL WARMING POTENTIAL

The overlap between the infrared spectrum of a greenhouse gas (GHG) and the portion of the blackbody spectrum emitted by the Earth's surface that is not absorbed by naturally occurring atmospheric gases is referred to as the radiative forcing capacity of the greenhouse gas. The radiative forcing is therefore the amount of energy per unity area per unit time absorbed by a greenhouse gas. In the absence of the greenhouse species, this energy would be lost into space. However, the greenhouse impact of a gas also depends on its atmospheric lifetime. For these reason, the global warming potential index, GWP, has been introduced to quantify the greenhouse capacity of a gaseous compound and therefore its ability to contribute to the global warming. The GWP is the radiative forcing weighted by the residence time of the gas in the atmosphere.

Since halocarbons strongly absorb infrared radiation between 500 and 1500 cm^{-1}, they are potentially strong greenhouse gases. Their greenhouse capacity is magnified by at least two factors. First, many of their absorption bands lie in the atmospheric window region between 8 and 12 μm (800 – 1200 cm^{-1}) where there is a minimum in the atmospheric absorption. Second, the majority of halocarbons are molecules which contain C—F bonds. The vibrational transitions involving this chromofore generally have large absorption cross sections. In addition, the C—F bond is relatively unreactive in the oxidizing environment of the atmosphere and therefore fluorinated halocarbons have long atmospheric residence lifetimes.

Several models for the determination of the radiative forcing have been developed. These models are used to evaluate the upward, downward and net irradiances at each level in a model atmosphere which is assumed as a standard. This atmosphere is parameterized by the vertical profiles of pressure, temperature, atmospheric-constituents-mixing-ratio and amounts of clouds at different positions comprised between the sea level and about 10 mbar. These models are usually computationally expensive and a radiative transfer model has to be defined.

Pinnock et al. [237] have proposed a simple method for the evaluation of the instantaneous radiative forcing: they used a narrow band radiative forcing model to calculate the instantaneous, cloudy sky, radiative forcing per unit cross section as a function of wavenumber for the global annual mean Earth sky. The radiative forcing per unit cross section for the average Earth sky, F, is simulated by subdividing the spectral interval 0 – 2500 cm^{-1} in 250 bands each of width 10 cm^{-1} and then considering the effects for an increase of a 1-ppbv in the concentration of a GHG. The resultant radiative forcing, F, is shown in Figure 9.10.

By using this narrow-band radiative forcing model it is possible to estimated the radiative forcing of a GHG from the integrated absorption cross sections measured from the infrared

spectrum of the involved GHG. The radiative forcing, *RF*, in Watts per square meter for a 1-ppbv increase is given by

$$RF = \sum_{i=1}^{N} \sigma_i F_i^{\sigma_i} \tag{9.2}$$

where $F_i^{\sigma_i}$, expressed in W m^{-2} $(cm^{-1})^{-1}$ $(cm^2$ $molecule^{-1})^{-1}$, is the radiative forcing per unit cross section per wavenumber in the spectral interval *i* and σ_i is the absorption cross section in cm^2 $molecule^{-1}$, averaged over the spectral interval *i*.

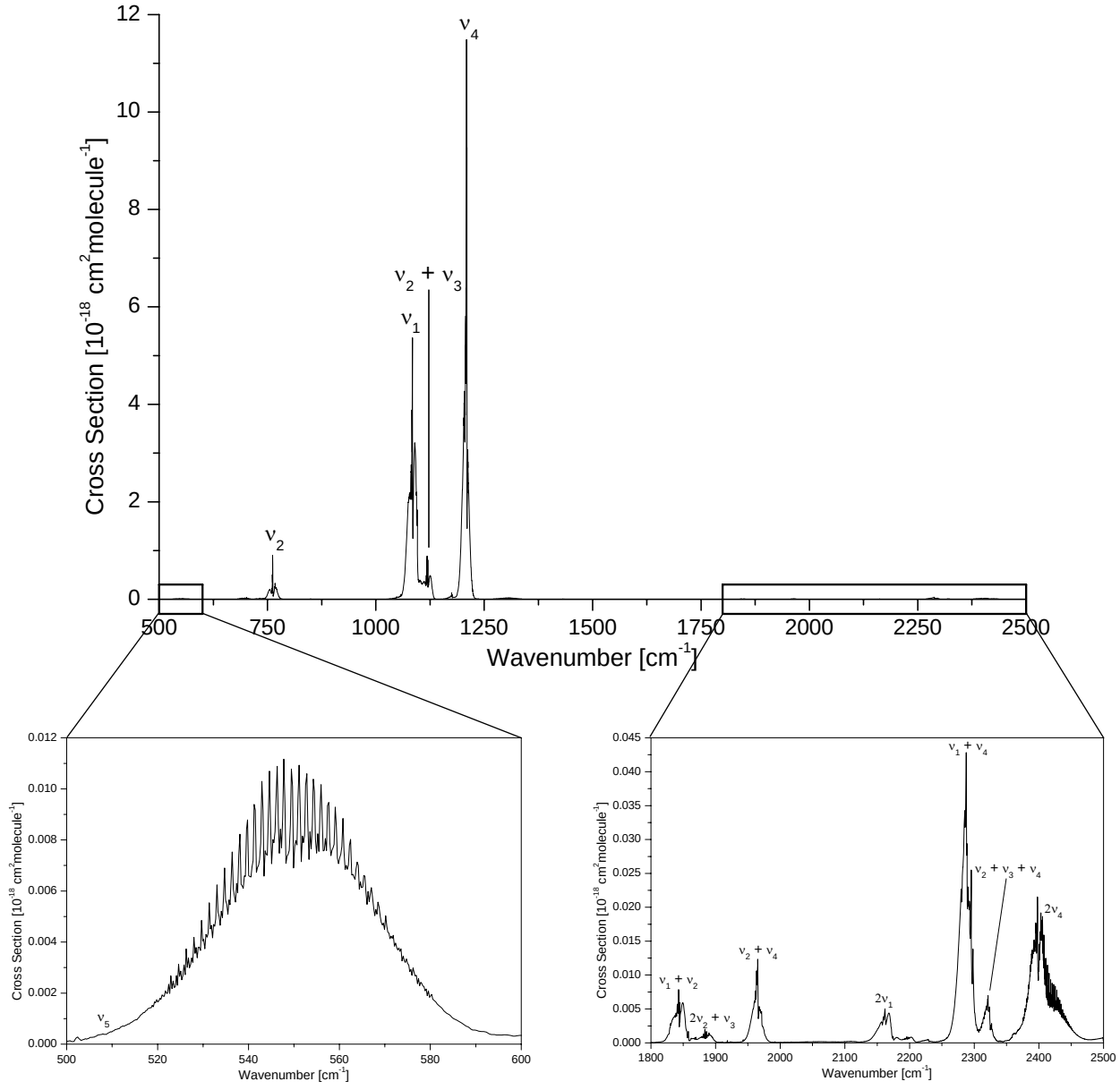

Figure 9.9. Averaged absorption cross sections (0.5 cm^{-1} resolution, T = 298 K) of CF_3Br in the region 500 – 2500 cm^{-1}.

The assumption for this model is that the concentration of a GHG in the atmosphere is small, so that its absorption can be considered optically thin. Since halocarbons do satisfy this requirement, their radiative forcing can be calculated by using equation (9.2).

It has been pointed out that the contribution of a GHG to the global warming is expressed by the GWP and the latter depends on both the radiative forcing and the atmospheric lifetime of the GHG. More precisely, the Global Warming Potential parameter is defined as the potential of 1 kg of a compound to contribute to radiative forcing relative to that of 1 kg of a reference compound [235, 238]:

$$GWP = \frac{RF_{GHG}\dfrac{1000}{m_{GHG}}\displaystyle\int_0^{TH} e^{-t/\tau_{GHG}}\,dt}{RF_{ref}\dfrac{1000}{m_{ref}}\displaystyle\int_0^{TH} e^{-t/\tau_{ref}}\,dt} \tag{9.3}$$

where RF is the radiative forcing, m is the molecular mass in g mol^{-1}, τ is the atmospheric lifetime in years, and TH is the time horizon. As reference gas, either CO_2 or CFC-11 (Freon-11, $CFCl_3$) are used.

A mean value of 0.300 W m^{-2} ppbv^{-1} (with an estimated accuracy of 5.5% and a standard deviation of 2%) for the radiative forcing of CF_3Br has been obtained by adopting the above described narrowband model and considering all the data in the range 450 – 2500 cm^{-1}. This result is in very good agreement with the value of 0.31 W m^{-2} ppbv^{-1} given by Drage et al. who took into account only the absorptions between 720 and 1250 cm^{-1}. This occurs since this region is characterized by the strongest bands of CF_3Br, as it can be seen from Figure 9.9. Consequently, the maximum radiative forcing of CF_3Br is within this spectral interval. This is shown in Figure 9.10 where the photo-absorption cross section spectrum is superimposed to the narrow band radiative forcing: the strongest CF_3Br absorptions fall in the regions of maximum radiative forcing.

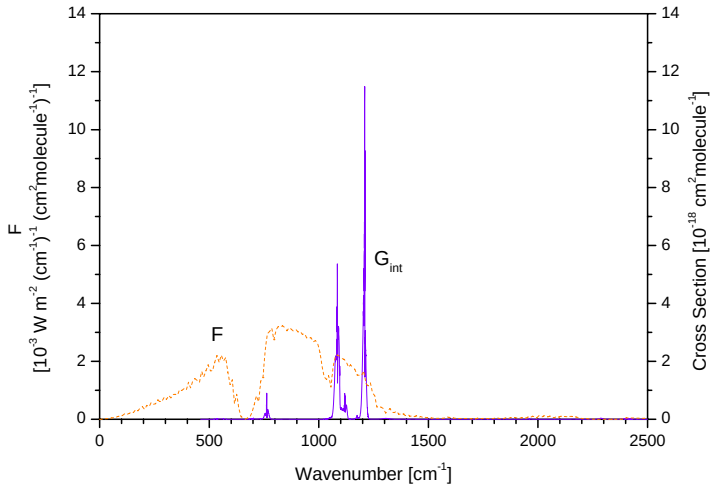

Figure 9.10. Narrow band radiative forcing F (orange dashed line) for average Earth sky and averaged absorption cross section G_{int} (violet solid line) of CF_3Br (0.5 cm^{-1} resolution, T = 298 K).

The GWP of CF_3Br has been calculated by taking carbon dioxide as reference gas for time horizons of 20, 100 and 500 years. The reason for calculating the GWP at different time horizons is twofold [234]: (i) for some environmental feedbacks it is important to evaluate both the short and long term effects of a GHG; (ii) the degradation process of CO_2 on a global scale is complicated by the exchange among different reservoirs and hence it cannot be described correctly by a single atmospheric lifetime. The lifetime and the radiative forcing for CO_2 have been taken from Ref. [235] and are 150 years and $1.1 \cdot 10^{-5}$ W m^{-2} ppb^{-1}, respectively. A period of 65 years has been taken for the atmospheric lifetime of CF_3Br [235]. The obtained GWPs are listed in Table 9.5, where they are compared with the most recent literature values. The agreement between the GWP here obtained with those of Drage et al. [235] is very satisfactory, whereas there are large discrepancies with respect to those published by Orkin et al. [234]. These results reflect the strong influence of the applied radiative transfer models on the evaluation of the radiative forcing. Indeed, while the present determinations as well as those of Drage et al. are based on the narrow band model, Orkin et al. used the experimentally measured spectrum of the outgoing Earth's radiation obtained from the NIMBUS-4 satellite at a latitude of 15° N [236].

Table 9.5. Global warming potentials ($\times 10^{18}$) of CF_3Br for time horizon of 20, 100 and 500 years.

Time Horizon [years]	This work	Drage et al. [235]	Orkin et al. [234]
20	7.2	7.7	5.5
100	5.5	5.8	5.0
500	3.5	3.7	1.9

Finally, some considerations about the accuracy are probably needed. The narrow band model relies on some approximations which limit its accuracy when compared with line-by-line calculation of the radiative forcing. On the other hand, the line-by-line approaches are computationally expensive and require accurate spectroscopic line parameters which are not always available. In their work, Pinnock et al. stated that the radiative forcing obtained with the narrow band model agree within ±0.3% with the radiative forcing computed by a more complex formulation of the radiative transfer model. One of the biggest source of uncertainty is probably represented by the atmospheric lifetimes. Indeed, not only the decays of the gas concentrations are modelled as a first order kinetic which may be inappropriate for some gases, but the available values have a wide variability: the lifetime of CF_3Br varies from 65 years to 110 years [235]. By considering the estimated accuracy of the radiative forcing here determined and its deviations from

the values given by Drage et al., it can be stated than the accuracy of the measurements can be taken in the range 6 – 10%.

10. Frequency Down-Chirped QCL Spectroscopy: Time Dependent Measurements of Collisional Processes in a Dicke Narrowed Spectral Line of Water Vapour

One of the most widespread and useful applications of conventional high resolution infrared spectroscopy, trace gas detection, relies on the use of line shape functions derived from measurements of molecular absorption spectra [19]. An accurate knowledge of the line parameters is not only essential for reliable atmospheric retrievals of gas concentrations, but may also be employed to infer information about the intermolecular interactions driving the inelastic collisional relaxation processes. Within this approach the absorption lines are fitted in the frequency, or inverse wavelength, domain to theoretical line shape functions, which account for different physical processes that occur during the scattering event. The model that best reproduces the experimental measurements is then assumed to offer the most likely explanation of the collision dynamics. In this way, phenomena such as confinement narrowing [55], speed dependent cross sections [51, 240 – 243] and line mixing [53, 244] have been studied. Information about intermolecular potentials is gained by comparing the retrieved pressure broadening coefficients with those computed by semi-classical [65, 66, 68, 69] or quantum mechanical calculations [246 – 247].

On the other hand, time dependent spectroscopic techniques have been demonstrated to be more appropriate tools for studying molecular relaxation rates. With the advent of the laser, transient phenomena analogous to those observed in magnetic resonance experiments [76] were observed in the medium infrared and near-infrared regions. These coherent transient effects not only depend upon the dynamics of the radiation – matter interaction, but can also be used to study collisional decay processes [20]. By using microwave and infrared – microwave double resonance

spectroscopy, Oka and collaborators [21] studied energy transfer and derived selection rules for the collision induced transitions. The effects of M_J changing collisions [247] and of velocity changing collisions [248] were also studied. More recently, Rohart et al. [60] investigated the velocity dependence of the collisional cross sections of methyl fluoride perturbed by foreign gas collisions. They proposed that the most suitable approach was the use of a time domain speed-dependent Voigt profile, based on a phenomenological description of the speed dependence.

The present chapter is intended to demonstrate that the frequency down-chirped radiation emitted by a Quantum Cascade laser, used in the intra-pulse method, is capable of giving complementary information about collisional processes in gases to that obtained by the methods outlined above. This builds upon the way in which such a spectrometer may be used to create and study saturation [80], molecular alignment [81] and transient gain [121]. One of the problems which may be studied in this way is the collisional narrowing of some of the absorption lines of water vapour.

Understanding the mechanism of the collisional narrowing of the few water lines which exhibit oblate top behaviour has been a longstanding challenge in water spectroscopy, since the earliest experiments at Lincoln Laboratory of MIT [249 – 252]. These unusual absorption lines show a significant narrowing of the pressure broadened half width. This narrowing has been mainly attributed to confinement narrowing, which can be accompanied by the speed dependence of the line parameters [253 – 255]. The Dicke narrowing of the absorption lines of the ν_2 band of water is observed to mostly affect ro-vibrational transitions having high J and K_c values, i.e. when the rotation is mainly about the C axis, which lies perpendicular to the molecular plane, as sketched in Figure 10.1.

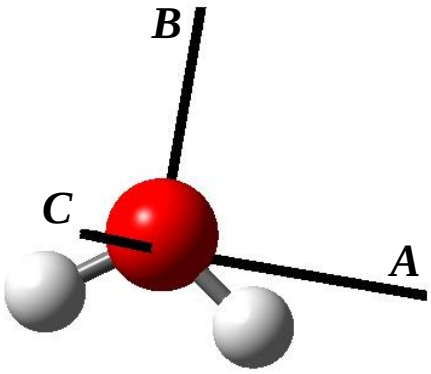

Figure 10.1. Water molecule and orientation of the principal axes of inertia.

The first intra-pulse observation of the unusual behaviour of the line broadening of $15_{0,15} \leftarrow 16_{1,16}$ and $15_{1,15} \leftarrow 16_{0,16}$ doublet of water vapour ν_2 fundamental band was made by McCulloch et al. [80]. This doublet is centred at 1276.6262 cm^{-1} and appears unresolved at the instrumental resolution, since the separation between the K components is about $1.8 \cdot 10^{-3}$ cm^{-1}. In the present Chapter the time dependence of the collisional broadening of this unresolved doublet is investigated, by making use of the change in the chirp rate which occurs in a QCL excited with a long duration current pulse. The aim is twofold: (i) demonstrating the chirp rate dependence of the collisional cross sections; (ii)

showing the type of information which can be gained by using this experimental technique when applied to the study of molecular relaxation processes.

10.1. Experimental Method and Data Inversion

The Quantum Cascade laser spectrometer used for the measurements has been described in Section 5.4. The distributed feedback laser, operating around 7.8 μm, was excited by a rectangular current pulse of 1.5 μs duration, and at a repetition rate of 2.5 kHz. The substrate temperature of the QCL was maintained at a constant value by a Peltier thermoelectric cooler.

The operation of the spectrometer relies on the rapid local heating induced in the QCL by the current pulse, which changes the refractive index and the spacing of the built-in distributed feedback grating, and generates an optical pulse with a frequency down-chirped spectrum. The tuning range and chirp rate $(d\nu/dt)$ of the frequency swept output from the laser were determined by the use of a solid Ge etalon with a free spectral range of 0.0195 cm^{-1}. The rate of the frequency down-chirp decreases along the temporal profile of the pulse, it varies in a non-uniform fashion and depends on the amplitude of the current pulse, its repetition frequency, and the substrate temperature. Figure 10.2 shows the wavenumber tuning and the chirp rate of the employed QCL, for an initial temperature of –25 °C and a drive voltage of 14.5 V.

By changing the base temperature of the QCL, it is possible to change the position of the centre of the unresolved $15_{0,15} \leftarrow 16_{1,16}$ and $15_{1,15} \leftarrow 16_{0,16}$ doublet within the tuning range of the laser. Since the laser down-chirp rate decreases throughout the duration of the pulse (as exemplified in Figure 10.2), with the fastest chirp rate occurring at the beginning of the pulse and the slowest one at the end, this allows the absorption line to be interrogated at different chirp rates. Three different chirp rates were chosen by changing the injection current and the initial temperature of the QCL. These chirp rates, corresponding to 20, 35 and 75 MHz ns^{-1}, will be referred to as slow, medium and fast, respectively.

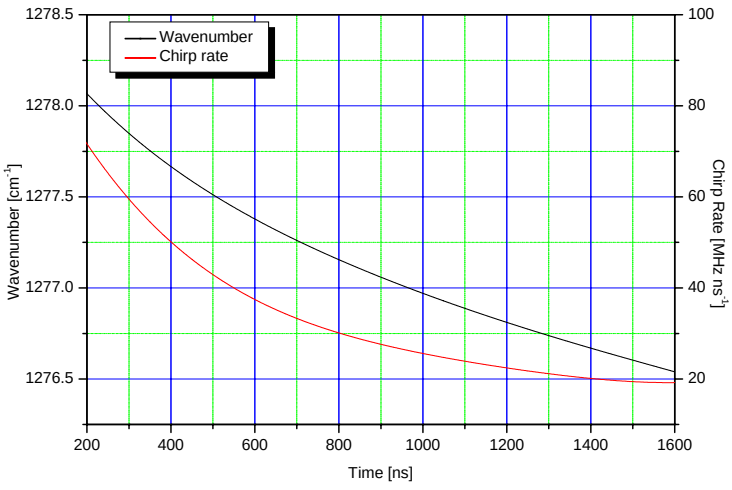

Figure 10.2. Wavenumber tuning and chirp rate of the 7.8 μm QCL employed in the experiments operating at -25 °C and 14.5 V (see Table 10.1).

The experimental conditions adopted to obtain the different chirp rates are summarized in Table 10.1. The unresolved $15_{0,15} \leftarrow 16_{1,16}$ and $15_{1,15} \leftarrow 16_{0,16}$ *K* doublet at the three chirp rates is shown .in Figure 10.3. As the chirp rate is varied, the time taken by the electromagnetic radiation to sweep through the inhomogeneously broadened spectral line varies from about 6 ns at slow chirp rate to about 1.5 ns at fast chirp rate, thus changing the time scale of the experimental observations.

For each chirp rate, spectra of the Dicke narrowed absorption line perturbed by helium, neon, argon, nitrogen and carbon dioxide were acquired. In all the experiments, the water vapour partial pressure were set to 2.5 ± 0.2 Torr, and the foreign gas pressures were increased from 2 up to a maximum of 600 Torr. The path length adopted for the experiment was 37 m, corresponding to 76 passes through the cell. Each of the observed spectra was the result of an average of 8000 intra-pulse spectra recorded in consecutive pulses.

Table 10.1. Experimental conditions adopted to record the water absorption line at slow, medium and fast chirp rates

	dν/dt [MHz ns^{-1}]	**Laser Temperature [°C]**	**Drive Voltage [V]**
Slow chirp	20	–25.0	13.0
Medium chirp	35	–25.0	14.5
Fast chirp	75	–15.0	15.5
Pulse duration: 1.5 μs;		Repetition rate: 2.5 kHz	

The experimental absorption features were fitted to a Voigt profile, by employing the Visual Line-Shape Fitting Program presented in Chapter 6. During the fits, the Doppler half width was fixed to a value determined from the low pressure spectrum of pure water. According to equation 7.1, this effective Doppler half width actually represents the molecular Doppler half width convolved with the instrumental function, which was assumed Gaussian. From the effective Doppler half widths, γ_D^{eff}, the instrumental line widths, γ_D^{QCL}, were derived. They are listed in Table 10.2, together with the theoretical values predicted by means of the uncertainty relation, equation 5.10. The agreement among the two sets of data is very good, thus indicating that the instrumental function is really a Gaussian (or nearly) distribution.

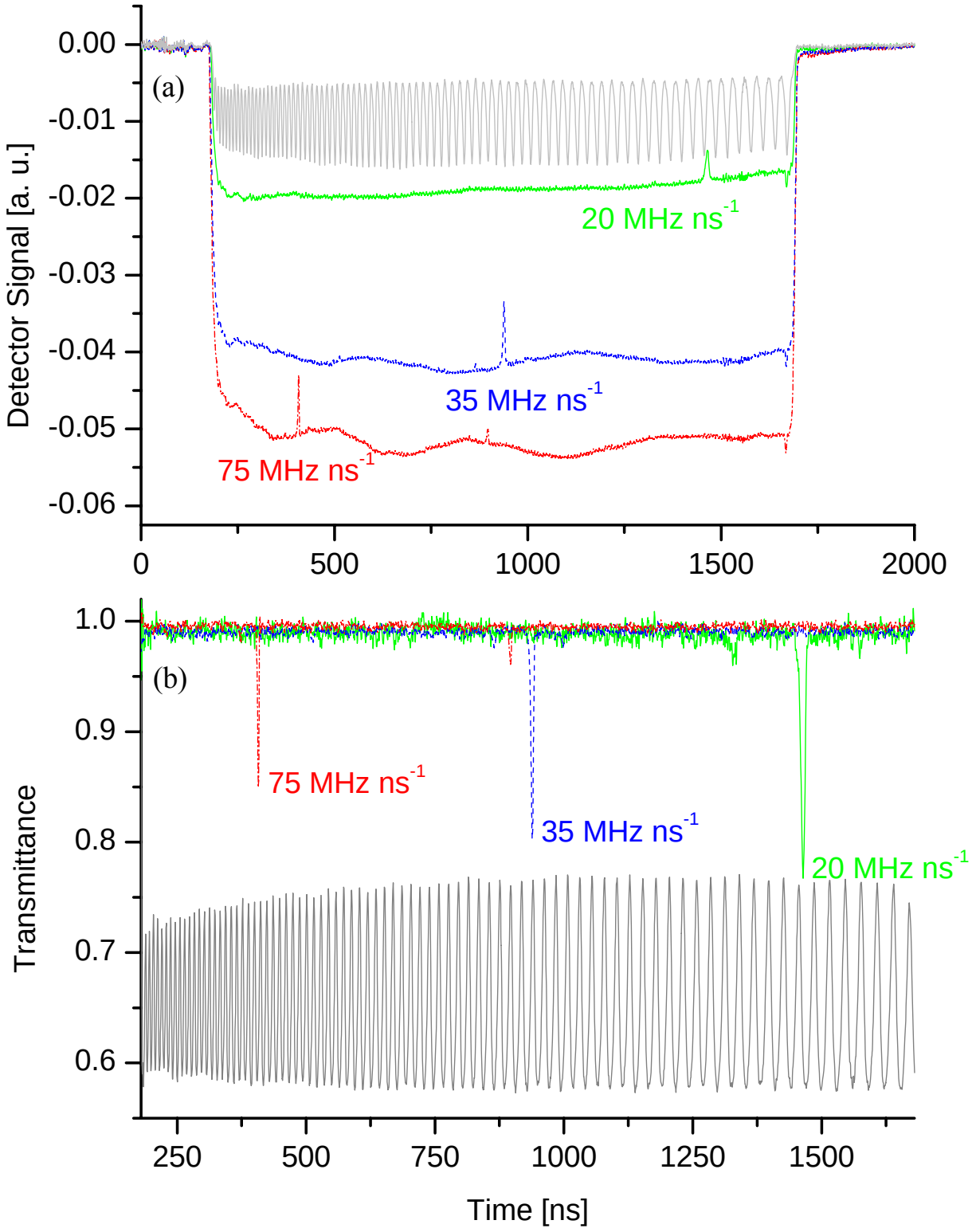

Figure 10.3. Dicke narrowed water line recorded at different chirp rates: (—) 20 MHz ns^{-1}, (--) 35 MHz ns^{-1} and (-·-) 75 MHz ns^{-1}. Panel (a) shows the spectra recorded by the detector, and panel (b) shows the corresponding transmission spectra. In order to illustrate the frequency down-chirp during the pulse, the etalon fringe pattern is also shown.

Table 10.2. Effective Doppler half widths obtained at the different chirp rates, and comparison of the corresponding QCL instrumental line widths with the theoretical predictions of the uncertainty relation.

Chirp Rate	γ_D^{eff} [10^{-3} cm^{-1}]	$\gamma_D^{QCL,\,fit}$ [10^{-3} cm^{-1}]	$\gamma_D^{QCL,theory}$ [10^{-3} cm^{-1}]
Slow	2.6(2)	1.8(2)	1.6
Medium	2.8(3)	2.0(3)	2.1
Fast	3.7(3)	3.2(3)	3.1

The water vapour self-broadening contribution to the line width was obtained from the spectrum of pure water vapour, and was taken into account in the retrievals of the foreign gas pressure broadening coefficients. Even if the Voigt profile is not fully suited to fit the absorption spectral lines, which are partially asymmetric especially at lower pressures, it is important to note that the aim of the experiment is not a classical determination of spectroscopic line parameters, as that carried out for sulphur dioxide and vinyl fluoride. Rather, the interest is focused in the relative value of the pressure broadening coefficients at different chirp rates. Under these circumstances the deviations from the Voigt profile appear to be similar at the various chirp rates, and hence the resulting retrieved coefficients are consistent with each other. Further, this approach also leads to a direct comparison with existing literature values.

The pressure broadening coefficients were determined as slope of the straight lines which result when the best-fit half widths are plotted against the gas buffer pressure. When narrowing occurred, only the higher pressures points corresponding to a linear relation between the half width and the buffer gas pressure were employed for deriving the pressure broadening coefficients. During these fits the data points were weighted on the basis of their error.

10.2 Rapid Passage Signals and Chirp Rate Dependence of Collisional Processes: Water Vapour

Collisions with Neon and Argon

The pressure broadening coefficients, retrieved for all the buffer gases at the investigated chirp rates, are listed in Table 10.3. It should be pointed out that, although the asymmetric absorption lines were fitted using a symmetrical function, the present data are close to those determined by Eng et al. [250, 252] by tunable lead salt diode laser spectroscopy. Indeed, for the transitions $16_{0,16} \leftarrow 15_{1,15}$ and $16_{1,16} \leftarrow 15_{0,15}$ (which are the *R*-branch equivalent of the *P*-branch

transitions here investigated) they give a pressure broadening parameter (full width half maximum) of 0.56(6) MHz Torr^{-1} [252] and 0.26(2) MHz Torr^{-1} [250] for nitrogen and argon, respectively. This partly justifies the approach of fitting the lines on the basis of the simple and computationally inexpensive Voigt profile.

Within the group of investigated collision partners, collisions of water with the noble gases argon and neon induced similar behaviour. The main feature of their interaction with water is a strong narrowing of the absorption line, which is mainly due to the effect of the velocity changing collisions. The narrowing is shown in Figure 10.4 for collisions with Ar, at slow and fast chirp rates. Similar behaviour is observed for Ne. As can be seen, a very pronounced decrease of the half width, with respect to that of pure water vapour, occurs as a consequence of the addition of the rare gases. The narrowing persists up to a pressure of about 270 Torr. The resultant line width has a minimum between 75 and 200 Torr, which is in a good agreement with the pioneering observations of Eng and co-workers [250]. Indeed, they stated that a minimum is reached in the pressure range between 50 and 200 Torr. In particular, from Figures 2 and 3 of Ref. [250], it can be deduced that for Ar the minimum occurs at about 140 Torr. In this case, at slow chirp rate the minimum is observed at 133 Torr. The good agreement between the present experimental observations and the measurements made at MIT confirms the reliability of the retrieved data, thus excluding the effects of strong instrumental artefacts.

Table 10.3. Obtained pressure broadening coefficients, HWHM, of the Dicke narrowed water line, at the investigated chirp rates for the various collisional partners

Chirp Rate	**Broadening Coefficient [MHz Torr^{-1}]**				
[MHz ns^{-1}]	**He**	**Ne**	**Ar**	**N_2**	**CO_2**
20	0.241(9)	0.071(11)	0.114(5)	0.206(7)	1.01(3)
35	0.143(4)	0.047(5)	0.088(2)	0.204(7)	1.14(3)
75	0.174(4)	0.043(5)	0.086(4)	0.301(7)	1.15(4)

This suggests that it is possible to use this instrumental method to explore the role played by the chirp rate on the interaction between a molecular gas and the chirped laser radiation, and to determine how this interaction is affected by collisional processes and transport effects. Figure 10.4 clearly displays the dependence of the collisional cross sections and the dynamics of the intermolecular interactions upon the chirp rate, and hence on the time taken to sweep through the absorption line. It is evident that the effect of the velocity changing collisions is more pronounced at slow chirp rate and in the low pressure regime. On the other hand, in the high pressure regime, where the normal pressure broadening behaviour is recovered, the slow chirp measurements also

show efficient line broadening. This is due to the larger number of collisions between water and buffer gas which take place at slow chirp rate, i.e. when the observation time is longer.

From Table 10.3 it can be seen that the neon broadening coefficients are smaller than those of argon, i.e. Ar exhibit less narrowing than Ne. Nevertheless, the effectiveness of the narrowing is expected to increase as the ratio m_a/m_b decreases, where m_a and m_b indicate the masses of the absorber and the buffer gas, respectively. In other words, it is more likely that heavier collisional partners cause a change in the velocity of the target molecule. A possible explanation for the observed behaviour is the greater polarizability of the argon atom compared to that of neon, as also pointed out by Pine in HF broadening measurements [55]. As a result, the dipole – induced dipole interaction, which is mainly responsible for the H_2O – rare gas atom collisions [21], is stronger for Ar than for Ne.

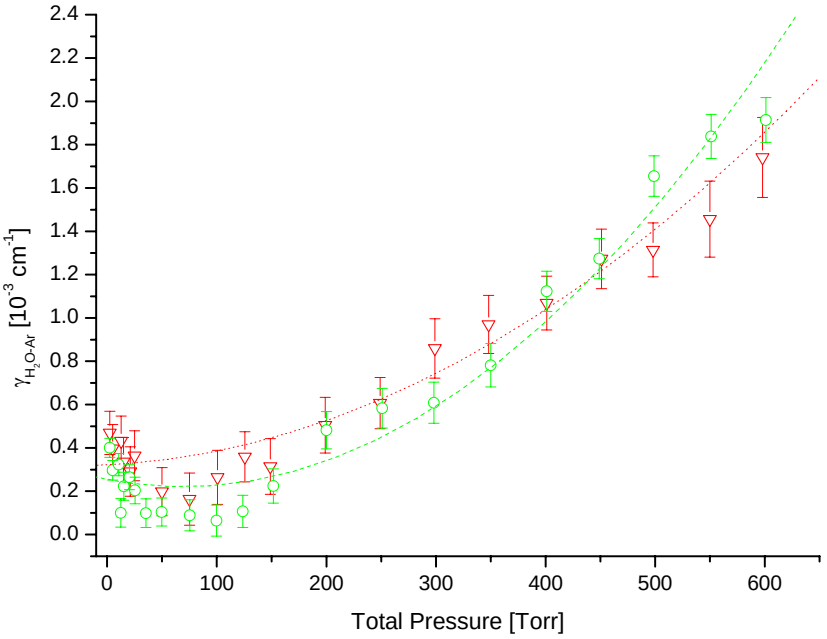

Figure 10.4. Plot of the water line half width with increasing Ar partial pressures. Notice the strong narrowing affecting the line for pressures smaller than 250 Torr. (○) Slow chirp rate; (▽) Fast chirp rate. The dashed second order polynomial fits are displayed to help the recognition of the data trend. The medium chirp results are not displayed for clarity.

A narrowing of the inhomogeneous broadening due to collisions can be related to the macroscopic polarization, as demonstrated by Rohart et al. [60] and Köhler and Mäder [256]. In particular, Rohart et al. showed that, when the Doppler broadening is reduced, molecules remain polarized for a longer time. In the present frequency down-chirped experiments, the rapid sweep through an absorption line induces a polarization, which interferes constructively with the laser field to generate a delayed pulse of amplified emission. In the experiments on water – neon broadening it has been observed that the magnitude of this pulse is directly related to the degree of narrowing, as shown in Figure 10.5. A similar effect occurs when argon is used as a collision partner. The amplitude of the emission peak progressively increases as the pressure of rare gas is raised. This gain signal reaches a maximum at a total pressure of about 50 Torr, then it starts to decrease owing to collisional damping. This represents a clear experimental observation of how the reduction of the inhomogeneous broadening is linked to the macroscopic polarization of the gas. Moreover, since

the gas pressure at which the maximum gain occurs does not correspond exactly to the pressure at which the minimum width is reached, it is clear that the collision processes do not affect the constructive polarization interference leading to gain, and the line width of the absorptive part of the signal, identically.

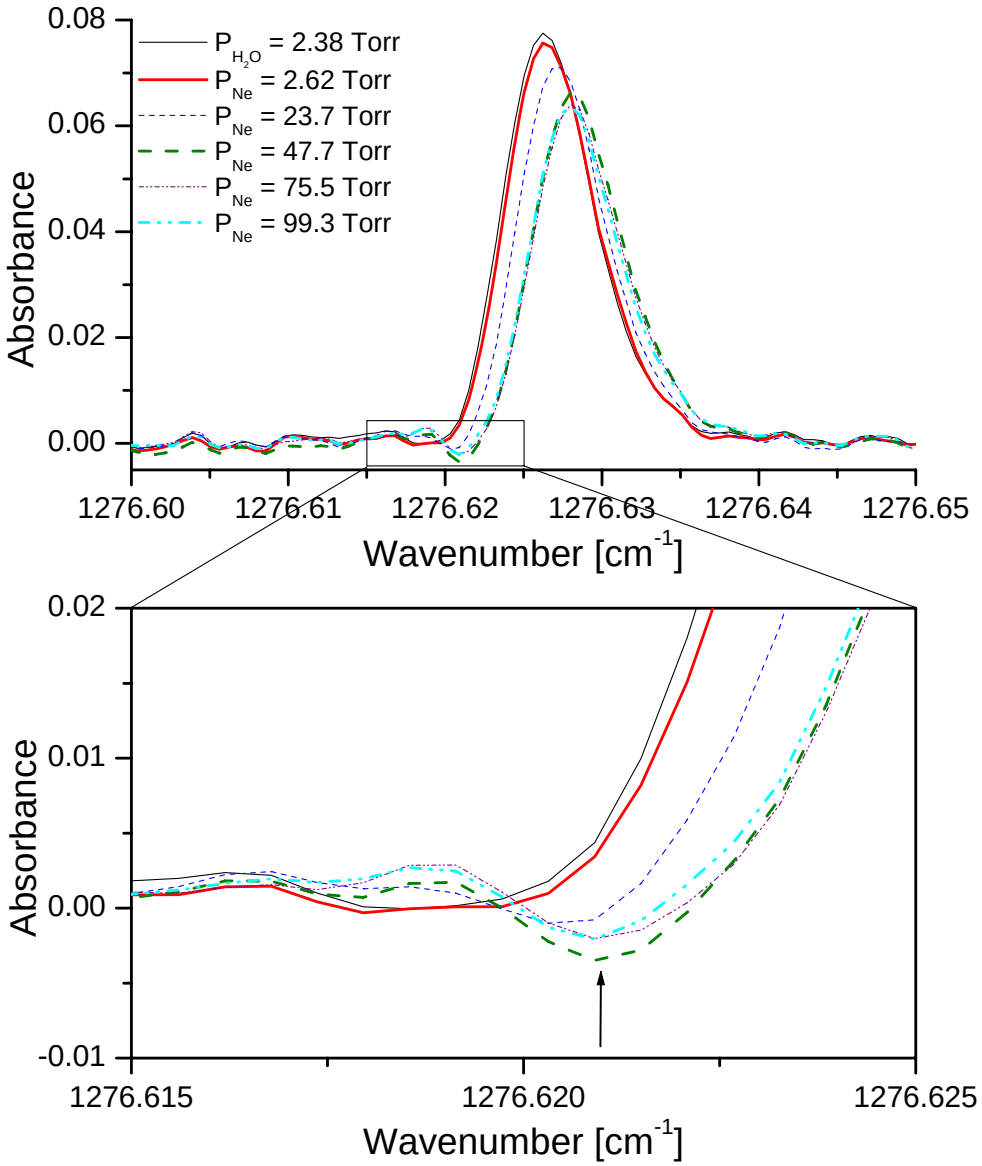

Figure 10.5. Increase of the transient emission as the Ne pressure is increased up to 47.7 Torr. The emission signal then starts to decrease as the Ne pressure is increased further. The magnitude of the emission peak is strictly related to the macroscopic polarization of the gas sample.

Collisions with Helium and Nitrogen

The collisional effects of neither the lightest rare gas helium, nor molecular nitrogen, resemble those produced by collisions of water with argon or neon. The collisions of either helium

or nitrogen with water produce very little narrowing, whereas their primary effect is to broaden the absorption line. The trend of the pressure broadened collisional half width is reproduced in Figure 10.6 (a) and (b) for helium and nitrogen, respectively. When nitrogen is used, a very small line narrowing is produced by velocity changing collisions, but at nitrogen pressures greater than 52 Torr the line width increases linearly with the pressure of N_2. With helium, the pressure broadening coefficient of water decreases when moving from a slow to a medium chirp rate. This effect has been attributed to the reduction in the observation time. The cause for this greater decrease in the pressure broadening for helium than for nitrogen has been ascribed primarily to the difference in the intermolecular interaction potentials: that between helium and water may be described as a dipole – hard sphere interaction, whereas that between water and nitrogen is a stronger dipole – quadrupole interaction. In a very simplified picture, the helium atoms move with Brownian-like motion, while nitrogen molecules follow a diffusive motion, whose driving force is the attraction by water molecules. As a result, when the time of observation is shortened, the number of collisions between water and helium is far more reduced than those between water and nitrogen, as the electrostatic interaction between nitrogen and water molecules drive their motion, whereas helium atoms move almost randomly. For both He and N_2 collisions with water, the pressure broadening coefficients increase on changing from medium to fast chirp rate. This may be due to the short sampling time, resulting in a selection of the higher velocity atoms or molecules, with resultant more energetic collisions which produce faster relaxation rates.

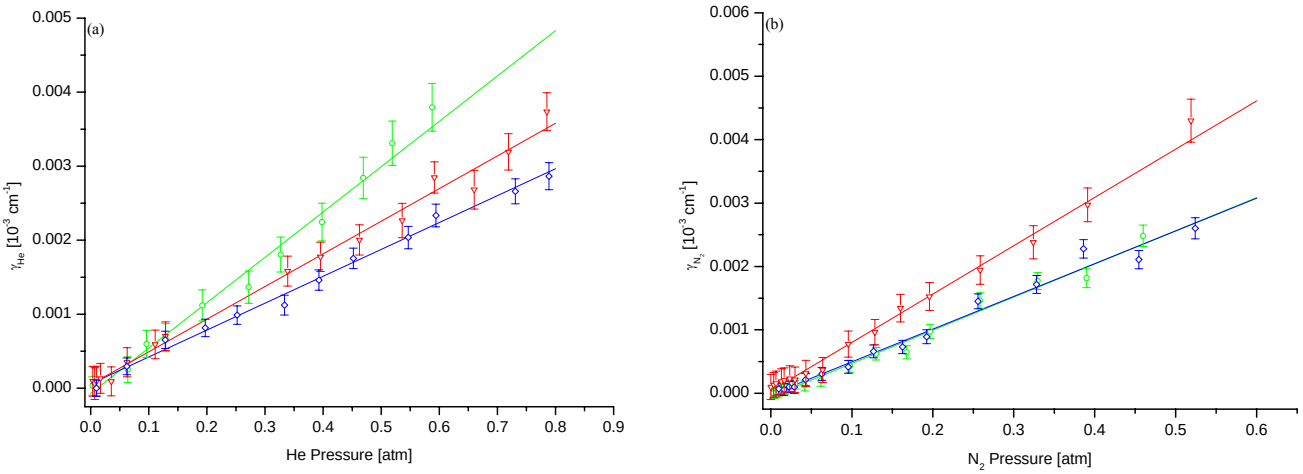

Figure 10.6. Collisional half-width as a function of the buffer gas pressure: (a) helium – water collisions; (b) nitrogen – water collisions. (○) slow chirp rate; (◇) medium chirp rate; (▽) fast chirp rate.

The difference between the intermolecular interaction potentials of water with nitrogen and helium may also help to explain why, at slow chirp rate, collisions between water and helium are

more effective in broadening the absorption line of water than those with nitrogen. At slower chirp rate the number of collisions increases, but the scattering process between water and helium is of shorter range than that between water and nitrogen. Oka [21] pointed out that, when such short range collisions occur, the electric dipole-like propensity rules for collision induced transitions are no longer valid, and a wider range of collision-induced transitions may occur. As a result, a greater number of internal states, into which the absorber molecule can be scattered, becomes available. It should also be pointed out that for these collisions the short-range repulsive force may play a significant role [21].

Collisions with Carbon Dioxide

Collisions between water and carbon dioxide produce a very different effect on the shape of the absorption line of water. Besides being the most efficient collisional partner of those broadening the spectral line of water, it is also the only one able to cause sufficient broadening that a symmetrical line shape is measured when relatively low pressures of CO_2 are used. An example of this effect is shown in Figure 10.7. Further, when CO_2 is used as buffer gas, the absorption line shows no collisional narrowing, and the pressure broadened half width increases linearly with pressure, as shown by Figure 10.8.

The CO_2 pressure broadening coefficients are on average four times greater than those obtained for N_2. In addition, CO_2 is very efficient in killing the rapid passage effects with a small amount of added gas, i.e. in the pressure region from 35 – 50 Torr. Above this pressure range, the rapid passage distortion of the line shape is completely suppressed, and the line shape can be well

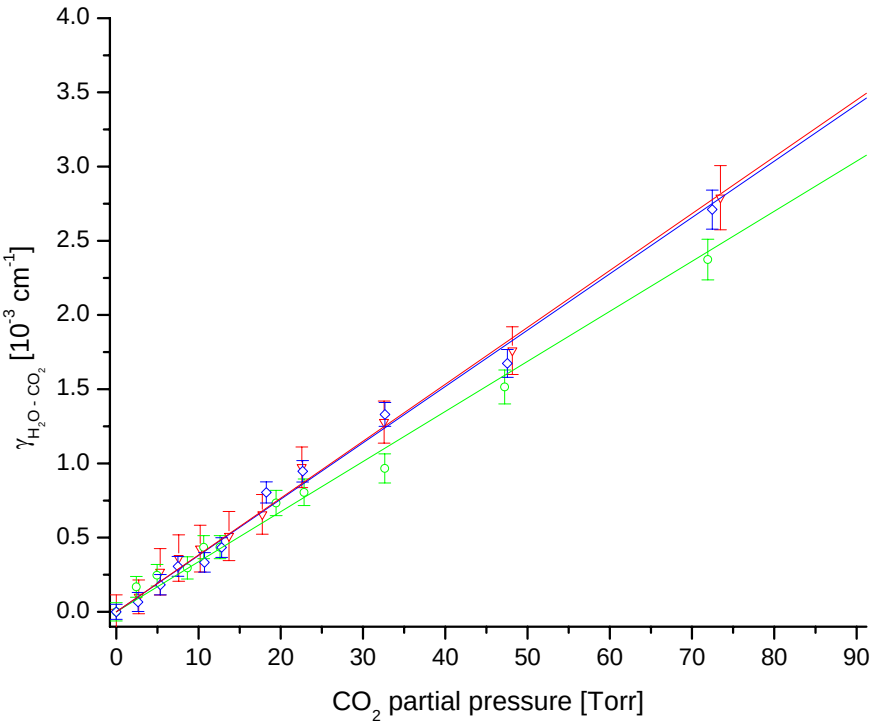

Figure 10.8. Linear increase of the line width of the water line in the CO_2 broadening experiments. (○) Slow, (◇) medium, (▽) fast chirp rate.

described by the Voigt function, as illustrated in Figure 10.7.

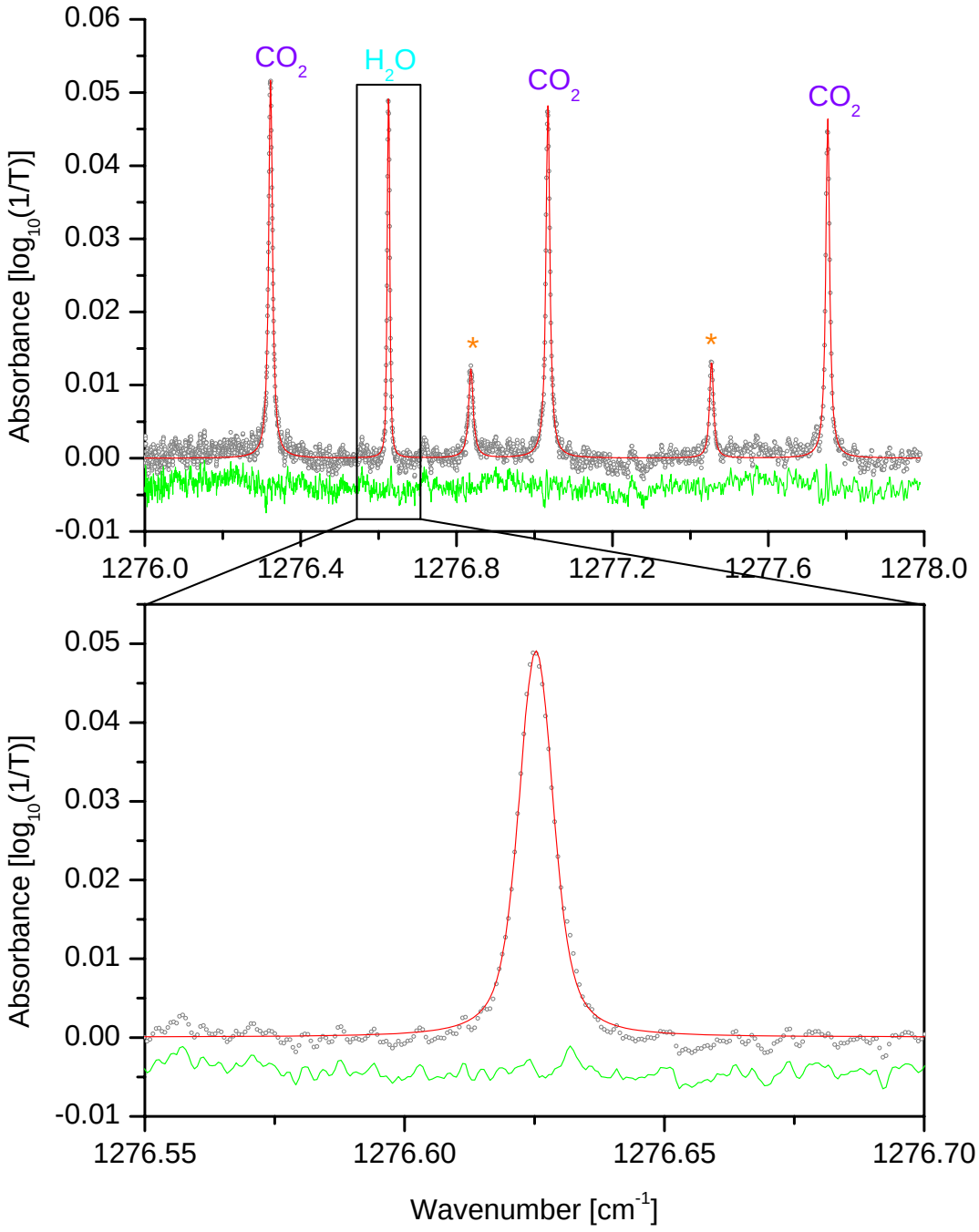

Figure 10.7. Symmetric line shapes recovered when CO_2 is used as buffer gas. (◦) Experimental spectrum: P_{H_2O} = 2.54 Torr, P_{CO_2} = 32.7 Torr, dv/dt = 35 MHz ns^{-1}, path length = 37 m; (—) Voigt fit; (—) residuals. The residuals have been displaced for clarity. The water line and the carbon dioxide transitions are indicated, the lines marked by an asterisk are due to CH_4 impurities contained in the CO_2 sample. A zoom of the water vapour absorption line is shown in the lower trace.

This behaviour is very unusual for the spectra obtained with a QCL spectrometer using the intra-pulse method [117]. Since the absorption spectrum of the $^{18}O^{12}C^{16}O$ isotopomer was measured as well [122] (see Figure 10.7), it has been possible study the effects of the collision interaction on

both the perturber and the perturbed molecules. The unusual effects of CO_2 as collisional partner were also detected in nitrous oxide broadening experiments, whose detailed analysis is the subject of the next chapter.

A comparison of the effect of about 22.5 Torr of a buffer gas on the shape of the water absorption line is given in Figure 10.9, for each of the collisional partners.

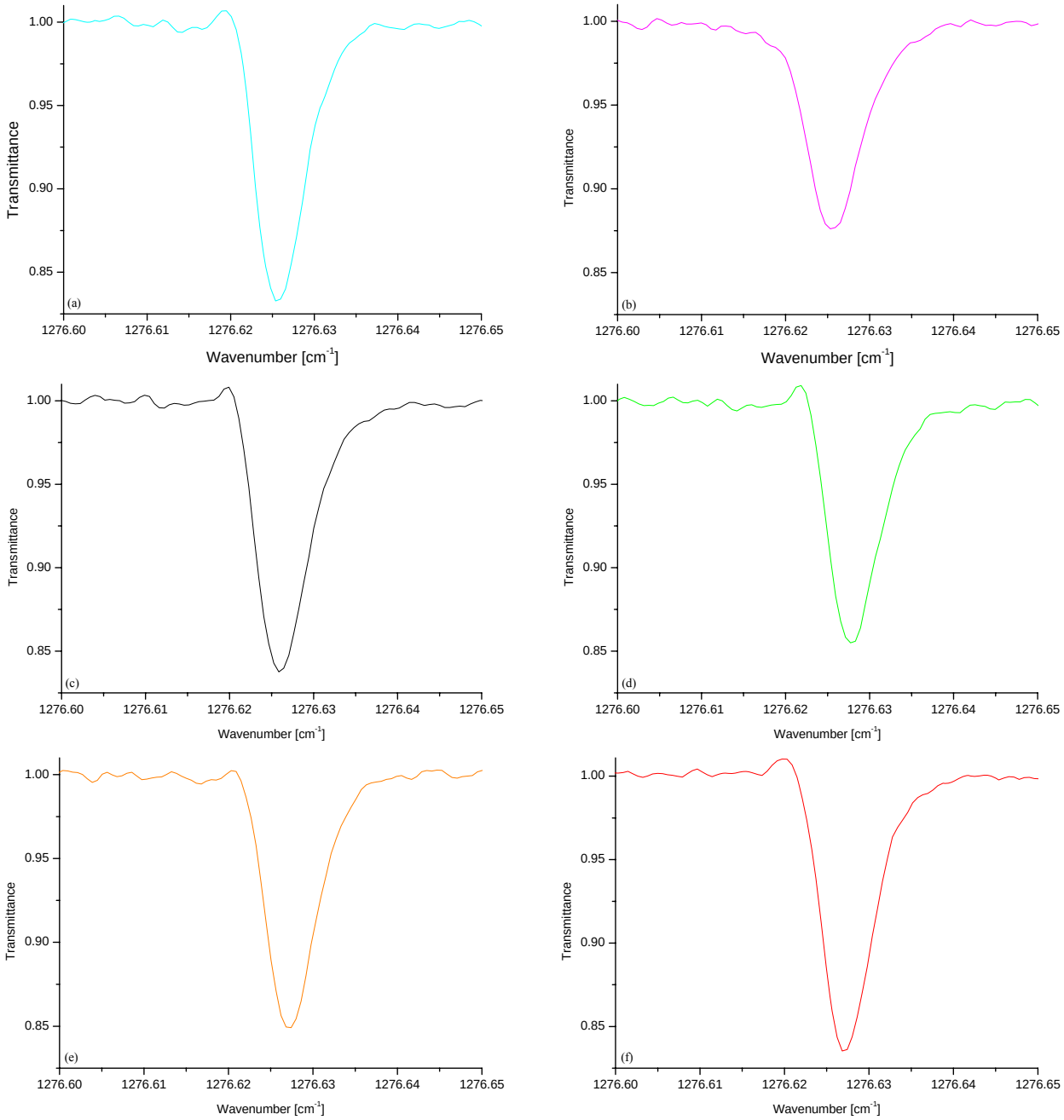

Figure 10.9. Effect of about 22.5 Torr of the different foreign gases on the water absorption line. While N_2 (c), He (d), Ne (e) and Ar (f) play a similar role on the shape of the absorption, which remains unchanged respect to that of pure water (a), CO_2 (b) is very effective in quenching the rapid passage effects and recovering of a symmetrical pressure broadened line shape.

As can be seen, despite their different pressure broadening coefficients, collisions with N_2, He, Ne and Ar (panels c – f) produce very similar effects on the overall line shape, which remains almost unchanged from that of pure water (panel a). In contrast, carbon dioxide (panel b) produces a very efficient quenching of the asymmetries caused by rapid passage.

The very strong differences observed between carbon dioxide and all other investigated gases, in particular nitrogen, cannot be simply explained in terms of the effects normally included in the description of their intermolecular interactions. Indeed, in the standard treatment of pressure broadening, both CO_2 and N_2 interact with water mainly through dipole – quadrupole interaction [257], and hence they are expected to play similar collisional effects on the absorption line shape and on the relaxation rates of water. Based on these results, given the analogies among the collisional effects of nitrogen and rare gases, the unusually effective interactions between water and carbon dioxide cannot be purely related to an increase of the quadrupole moment of the foreign gas, when nitrogen is replaced by carbon dioxide.

Such an explanation may be satisfactory when static techniques, such as TDL or FTIR spectroscopy, are used, but not when the effects of the time dependent processes are measured directly. In the present case, the time dependence of the relaxation processes, measured by using different chirp rates, has allowed the measurements of intermolecular collision effects which cannot be understood from the standard interaction potentials. A more plausible explanation may involve a very efficient energy transfer between colliding molecules, which can be caused by scattering into a large number of ro-vibrational levels of carbon-dioxide.

In summary, it has been not only demonstrated the time dependence of the collisional cross sections and the related relaxation processes, but also information on the intermolecular and transport processes, responsible for some unusual collisional effects shown by the Dicke narrowed absorption lines, has been gained.

11. Frequency Down-chirped QCL Spectroscopy: Time Dependent Measurements of Nitrous Oxide and Carbon Dioxide Collisional Relaxations

In the previous chapter, the results obtained for the $15_{0,15} \leftarrow 16_{1,16}$ and $15_{1,15} \leftarrow 16_{0,16}$ Dicke-narrowed doublet of the ν_2 band of water vapour have shown that the time dependence of the collisional processes may be investigated by the use of the frequency down-chirped electromagnetic radiation emitted by a long pulse duration QCL.

In the present Chapter the frequency down-chirped measurements are extended to the ro-vibrational lines of the ν_1 band of nitrous oxide perturbed by a range of collision partners. The investigation involves a demonstration of the chirp rate dependence of the collisional cross sections, and also the study of the molecular relaxation processes which affect nitrous oxide. The ν_1 band of nitrous oxide is a simpler system than water, as the complications arising from the motional narrowing are not present, and the *l*-doubling, equivalent to the *K* doubling in water, only occurs in the states in which the ν_2 bending vibration is excited.

Another difference between transitions studied in nitrous oxide and water is that the transition dipole moments of the ν_1 ro-vibrational transitions of nitrous oxide are much larger than those of the Dicke narrowed lines of water. As a result, the N_2O molecules interact strongly with the radiation field produced by the QCL. The resulting rapid passage signals observed in pure nitrous oxide, and with nitrogen as collision partner, have previously been described and analyzed [81]. In the present measurements, one of the most interesting collision partners among those that have been used, carbon dioxide, is a linear molecule of nearly the same mass and similar rotational constants as nitrous oxide. As observed in water vapour broadening experiments, it shows a completely different behaviour from the other collision partners, inducing very efficient broadening of the absorption lines of nitrous oxide and causing symmetrical line shapes to be observed at low partial

pressures of CO_2. The effects of carbon dioxide may be inferred by studying the weakly allowed transitions [258] of the unsymmetrical isotopomer $^{18}O^{12}C^{16}O$, which interleave the absorption lines of N_2O. In order to demonstrate the difference in overall intensity between the absorption lines in the ν_1 band of nitrous oxide and those of the 10002-00001[17] band of $^{18}O^{12}C^{16}O$, and their ability to couple to the radiation field, total band intensities and transition dipole moments of both Fermi resonance pairs of carbon dioxide and nitrous oxide are given in Table 11.1. For sake of completeness and comparison purposes, the corresponding properties of ν_2 band of water are also given. The carbon dioxide bands denoted as 10001 and 10002 form a dyad of levels, which are mixtures of the ν_1 fundamental and $2\nu_2^0$ overtone[18] [2]. These are strongly coupled through Fermi resonance.

Table 11.1. Total band intensities and transition dipole moments for the absorption bands of nitrous oxide, carbon dioxide and water vapour in the 8 μm region

Molecule	**Isotope** [a]	**Band** [b]	**Band centre** [cm^{-1}]	S_v [cm^{-2} atm^{-1}]	$\|R\|$ [D][c]
N_2O [d]	446	$02^00\text{-}00^00$	1168.1323	7.00	2.57×10^{-2}
		$10^00\text{-}00^00$	1284.9033	2.080×10^{2}	1.336×10^{-1}
CO_2 [e]	628	10002-00001 f. l. ($02^00\text{-}00^00$)	1259.425	7.93×10^{-4}	4.06×10^{-3}
		10001-00001 f. u. ($10^00\text{-}00^00$)	1365.843	8.91×10^{-4}	4.13×10^{-3}
H_2O [f]	161	010-000	1634.967	9.74×10^{-2}	1.224×10^{-1}

[a] Isotopic notation : 446 = $^{14}N^{14}N^{16}O$, 628 = $^{16}O^{12}C^{18}O$, 161 = $^{1}H^{16}O^{1}H$.
[b] In carbon dioxide the two bands are treated as a Fermi resonance doublet, 1 and 2, denoted as lower, f. l. ≡ 2. and upper, f. u. ≡ 1. The equivalent vibrational levels in nitrous oxide are indicated in brackets.
[c] $|R|$, the matrix element of the rotationless electric dipole moment, in Debye.
[d] from Ref. [259]; [e] from Ref. [258]; [f] from Ref. [15].

11.1. EXPERIMENTAL PROCEDURE AND DATA INVERSION

As the Quantum Cascade laser spectrometer, and the experimental and data analysis procedures have been described in Sections 5.4 and 10.1, respectively, only a brief outline of the experimental approach will be given.

[17] The notation used to denote the CO_2 bands is the following: $v_1v_2lv_3s$, where *s* denotes *e* (1) or *f* (2) and pertains to the vibrational angular momentum *l*.
[18] The ν_2 fundamental band is located at about 672.2 cm^{-1}.

The frequency down-chirped radiation emitted by the QCL is caused by the heating of the laser during a current pulse. With a pulse duration of about 1.5 μs the tunability range is usually about 3 cm^{-1}. By changing the injection current and the initial temperature of the QCL it is possible to change the spectral window covered by the spectrometer, and hence move the relative positions of the absorption lines within the tuning window. In particular, by operating at lower temperature and higher current, the spectral window is displaced toward higher wavenumbers. As the tuning range within a window may be larger than the shift of the centre of a tuning window, there is a considerable overlap between successive windows. The total spread of the spectral region covered may be extended to about 5 – 6 cm^{-1}, by superimposing the spectra acquired under different initial temperature – injection current conditions. Three different combinations of temperature – current were adopted: they will be referred to as slow, medium and fast chirp rates, and they correspond to a progressive shift of the acquired spectral region toward lower wavenumbers. The QCL operating conditions employed to achieve the different chirp rates are given in Table 11.2.

Table 11.2. QCLs operating conditions for the adopted chirp rates

	He, Xe, N_2 Broadening		**CO_2 Broadening**	
	Temperature [°C]	Voltage [V]	Temperature [°C]	Voltage [V]
Slow chirp rate	–24.0	10.5	–25.0	13.0
Medium chirp rate	–20.0	10.5	–25.0	14.5
Fast chirp rate	–2.0	10.5	–15.0	15.5
Pulse duration [μs]	1.5		1.5	
Repetition rate [kHz]	20		2.5	

The experimental absorption features were fitted to the Voigt employing VLSFP. As pointed out in the previous Chapter, although the lines are asymmetric, the asymmetries at different chirp rates affect the absorption lines in a similar way, thus ensuring the mutual consistency of the pressure broadening coefficients retrieved at different chirp rates. On the other hand, given their chirp rate dependence, the retrieved broadening coefficients are not strictly connected to those obtained from time independent spectroscopic techniques, and therefore they will be referred to as effective, or apparent, broadening parameters.

The perturbing gases helium, xenon, nitrogen and carbon dioxide were chosen on the basis of their masses and type of intermolecular interactions involved in the collisions with nitrous oxide. Unfortunately, as the xenon cylinder contained only a small amount of gas, a limited data set has

been obtained for this perturber. The obtained xenon broadening coefficients are reported for completeness. The N_2O partial pressures were varied between 0.013 and 0.125 Torr, depending on the chosen optical path (usually 37 m or about 70 m), and were kept fixed within a broadening experiment. The buffer gas pressures were progressively increased up to a total pressure of 400 Torr and the measurements were carried out at room temperature.

11.2. Theory: Modelling the Rapid Passage Signals

The structure of the rapid passage signals may be modelled by solving the coupled Maxwell-Bloch equations. According to the theory presented in Section 3.9, in these equations each transition is treated as a two level system, whose resonance frequency is ω_0. The electromagnetic radiation emitted by the QCL induces the formation of a dipole that dephases from the driving field at a rate γ_2; the rate of the population decay from the upper level is γ_1.

In the modelling of the fast passage signals observed in NMR [76] and microwave [78] spectroscopy, the spectral lines are generally assumed to be homogeneously broadened. However, owing to the Doppler effect, in the MIR region the absorption spectral lines are inhomogeneously broadened to a significant amount. Following the approach of Stoner et al. [77], who took into account the broadening due to inhomogeneity of the magnetic field in ESR experiments, the inhomogeneous Doppler broadening was introduced into the Maxwell – Bloch equations by treating each velocity component as an individual emitter, as schematically shown in Figure 11.1. Indeed, during the frequency sweep of the laser, each homogeneously broadened velocity component of the Maxwell – Boltzmann velocity distribution is swept through sequentially, so that the velocity packets are excited as a phased array [80]. The total response over the inhomogeneously broadened line was then obtained by summing over the different contributions from the emitters. The phased array behaviour causes a stronger damping of the oscillatory structure and leads to a better agreement between theoretical predictions and experimental observations.

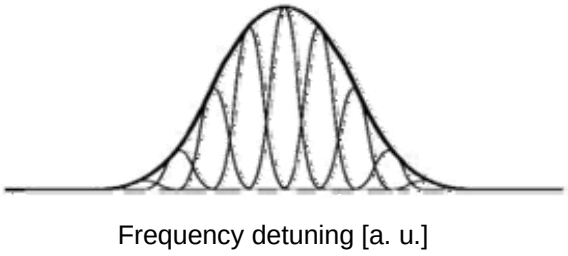

Figure 11.1. Schematic diagram of the contributions of the different homogeneously broadened components in a inhomogeneously broadened spectral line.

Besides, as the QCL radiation is linearly polarized, it gives rise to molecular alignment and optical pumping [81, 121]. Duxbury et al. showed that, in order to account for these effects, allowance should be made for the projection of molecule-fixed transition dipole moment on the

space fixed direction of the laser field [81]. When no magnetic fields are present, there are M_J degenerate transitions and one non-degenerate transition with $M_J = 0$. Given the selection rule $\Delta M_J = 0$, this lead to $M_J + 1$ effective transition components for each ro-vibrational transition. The effective transition dipole moment for a particular M_J component value depends on the corresponding direction cosines. From Table 3.2 it follows that for a linear molecule, the transition dipole moment corresponding to the quantum number M_J is given by

$$\langle \mu_v \rangle_{M_J} = \langle v' | \mu_v | v'' \rangle \frac{\left(J^2 - M_J^2\right)^{1/2}}{[(2J-1)(2J+1)]^{1/2}} \tag{11.1}$$

where $\langle v' | \mu_v | v'' \rangle$ is the vibrational transition dipole moment.

In the calculations the so-called "bundled" approach of Ref. [81] was used. Accordingly, each ro-vibrational transition was assumed to comprise a limited number of two level systems, each of which interacts independently with the laser field. Each of these two level systems has an effective transition dipole moment, derived by multiplying the vibrational transition moment by an average direction cosine. The latter results from a weighted average of the direction cosines of the M_J components which are grouped in the same two level system. The resulting effective transition dipole moments have to meet the requirement that the sum of the squares of the effective direction cosines must be equal to the sum of the squares of the complete set of direction cosines for the same ro-vibrational transition.

An alternative way of looking at the behaviour of frequency swept optical pulses was developed by Rothenberg and Grischowsky in 1986 [260]. By sending a frequency swept optical pulse through a sodium cell, they were able to record oscillatory signals similar to those measured in the mid-infrared region by using a QCL spectrometer in the intra-pulse method. In his theoretical treatment Rothenberg [261] derived an analytic solution for the output field emitted from the cell as the sum of the input field and that radiated by the medium. The resultant oscillatory structure may therefore be though of as a self-induced heterodyne between the input radiation and the field radiated by the resonant system. The QCL therefore proves to be a very efficient way of inducing this type of behaviour in the nanosecond time regime. A combination of the approach here adopted with that of Rothenberg may prove to be an effective way of improving the modelling the resultant line shapes.

11.3 Rapid Passage Signals and Chirp Rate Dependence of Collisional Processes: Nitrous Oxide and Carbon Dioxide

Nitrous Oxide Effective Broadening Parameters and Relaxation Processes

A typical spectrum recorded using the QCL spectrometer is presented in Figure 11.2 (a). The time dependent increase in the spacing of fringes, obtained by using a solid Germanium etalon, clearly shows the degree of frequency chirping. The delayed emission signals, which follow the absorption features, are also visible. These occur owing to the constructive interference between the laser and the induced polarization in the gas, as described in the previous Section. They are a consequence of the lack of collisional damping of this interaction since, at low concentrations of nitrous oxide, the mean time between successive collisions is longer than or comparable to the time required by the radiation to sweep through the absorption line, a necessary condition for the observation of a self-induced heterodyne signal.

A part of the spectral region studied, together with the labelling of the absorption lines, is displayed in Figure 11.2 (b). This Figure is the result of the superposition of two spectral windows covered by varying the initial temperatures and injection currents of the laser, as described in the experimental Section. The assignments of the observed absorption lines of N_2O, their line strengths and their pressure broadening coefficients are listed in Table 11.3. The various chirp rates, at which the spectral lines were acquired, are given in Table 11.4. It is evident that the lines observed in the carbon dioxide broadening experiments do not quite match those acquired in the spectra perturbed by helium, xenon and nitrogen. This is due to the slightly different chirp characteristics of the laser used for the CO_2 broadening measurements, as the earlier laser failed between the two sets of experiments.

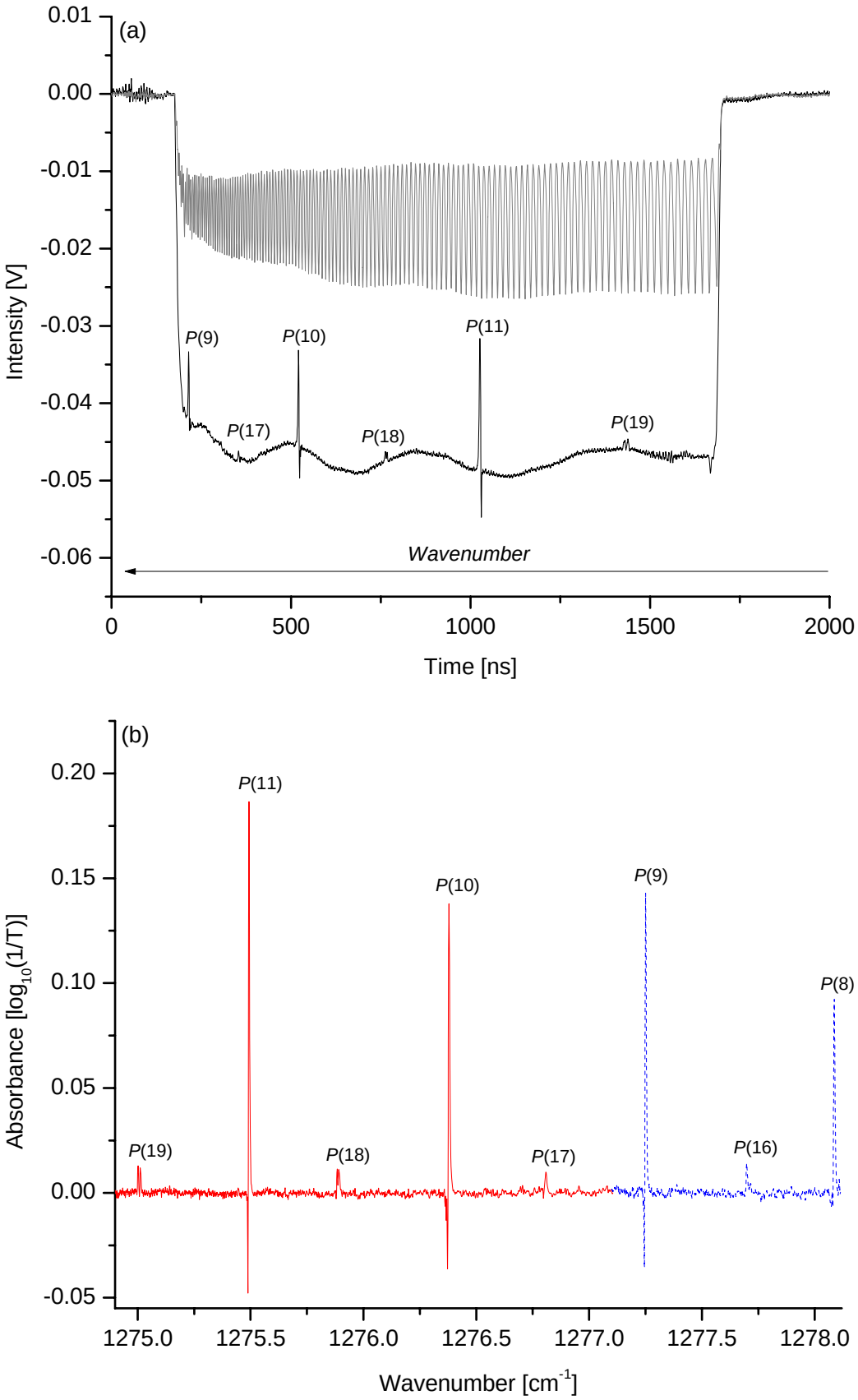

Figure 11.2. Upper panel. A typical spectrum recorded by the intra-pulsed QCL spectrometer: (—) etalon fringe pattern, 0.0195 cm^{-1} free spectral range; (—) N_2O spectrum: P_{N_2O} = 0.12 Torr, PLC = 37 m. Lower panel: Expanded spectral regions of the spectrum of nitrous oxide selected by changing the laser starting temperature and driving voltage: (—) -15 °C, 15.5 V; (--) -25°C, 14.5 V. Both the spectra were acquired using 1.5 μs pulse amplitude, 2.5 kHz repetition rate. Nitrous oxide line labelling as given in Table 11.3.

Table 11.3. Observed N_2O transitions, assignment, line strength and N_2-broadening coefficient

Line	$\tilde{\nu}_0$ [cm^{-1}] [a]	Vib. State	J'	J''	S^0 [10^{-20} cm molecule^{-1}] [a]	$\gamma^0_{N_2}$ [MHz Torr^{-1}] [b]
P(20)	1274.0859	$2_1^1\,1_0^1$ (e)	19	20	0.8593	
	1274.0991	$2_1^1\,1_0^1$ (f)			0.8588	
P(12)	1274.6166	1_0^1	11	12	14.76	3.29(2)
P(19)	1274.9885	$2_1^1\,1_0^1$ (e)	18	19	0.8790	
	1274.9987	$2_1^1\,1_0^1$ (f)			0.8870	
P(11)	1275.4929	1_0^1	10	11	14.23	3.32(2)
P(18)	1275.8877	$2_1^1\,1_0^1$ (e)	17	18	0.9032	
	1275.8952	$2_1^1\,1_0^1$ (f)			0.9072	
P(10)	1276.3658	1_0^1	9	10	13.55	3.37(4)
P(17)	1276.7836	$2_1^1\,1_0^1$ (e)	16	17	0.9193	
	1276.7886	$2_1^1\,1_0^1$ (f)			0.9233	
P(9)	1277.2353	1_0^1	8	9	12.70	3.39(2)
P(16)	1277.6761	$2_1^1\,1_0^1$ (e)	15	16	0.9274	
	1277.6790	$2_1^1\,1_0^1$ (f)			0.9314	
P(8)	1278.1012	1_0^1	7	8	11.73	3.45(2)
P(15)	1278.5653	$2_1^1\,1_0^1$ (e)	14	15	0.9274	
	1278.5662	$2_1^1\,1_0^1$ (f)			0.9314	
P(7)	1278.9637	1_0^1	6	7	10.60	3.48(4)

[a] from Ref. [15].
[b] from Ref. [259].

Table 11.4. Different chirp rates at which the nitrous oxide absorptions have been studied

Line	Chirp Rates [MHz ns^{-1}]					
	He, Xe, N_2 broadening			**CO_2 broadening**		
	Slow	*Medium*	*Fast*	*Slow*	*Medium*	*Fast*
P(20)	-	-	34.7	-	-	-
P(12)	-	-	41.4	-	-	-
P(19)	-	36.2	49.4	-	-	34.6
P(11)	-	45.8	62.4	-	-	39.9
P(18)	-	55.9	75.6	-	-	52.2
P(10)	32.8	70.1	94.8	-	31.8	69.8
P(17)	39.7	87.8	114.4	21.3	39.5	85.5
P(9)	49.7	107.9	-	33.0	55.9	100.5
P(16)	62.0	-	-	51.7	76.3	-
P(8)	77.5	-	-	64.4	94.9	-
P(15)	98.4	-	-	-	-	-
P(7)	118.7	-	-	-	-	-

The effective foreign gas broadening coefficients of nitrous oxide, retrieved from the analysis of the spectra, are listed in Table 11.5. The variation of these coefficients with chirp rate, and hence with the time of observation, is plotted in Figure 11.3. As can be seen, there is a general tendency for the effective pressure broadening coefficients to increase from slow (~ 30 MHz ns^{-1}) to medium (~ 70 MHz ns^{-1}) chirp rates. There is then little change when the chirp rate is increased further. By increasing the chirp rate, the time taken by the radiation to sweep through the spectral line decreases, and this is equivalent to a decrease in the time of observation. A reduced observation time will reduce the average number of collisions which occur during the passage of the radiation through the absorption line, and hence it is expected to lead to a smaller effective pressure broadening coefficient. This clearly contrasts with the experimental observations. A possible explanation is that, when the observation time is reduced, the collisions between fast moving molecules give the major contribution to the observed spectrum. Since the slowest molecules relax less rapidly [19, 262], their contributions at longer observation times are enhanced. The reduction in the observation time (i.e. faster chirp rate) thus induces an increasing role of the collisions between fast moving molecules leading concomitantly to a more efficient apparent decay rate. The effect is then very similar to selecting a limited number of high velocity components from a Maxwellian molecular velocity distribution. The observed pressure broadening coefficient is the average effect

of these high velocity collisions which, involving a higher energy, are more effective in scattering the N_2O molecules into other internal states. In other words, molecules moving faster also relax faster, as pointed out by Mattick et al. [262], Rohart et al. [60], and Köhler and Mäder [256]. The increase of the effective pressure broadening coefficients with the chirp rate is more noticeable for xenon and carbon dioxide, while it is less pronounced for helium, whose retrieved coefficients seem to be less affected by the chirp rate. This is in good agreement with the theoretical predictions. Indeed, the speed dependence of the relaxation rates is expected to be more evident as the ratio m_a/m_b decreases, where m_a and m_b are respectively the masses of the active and buffer species.

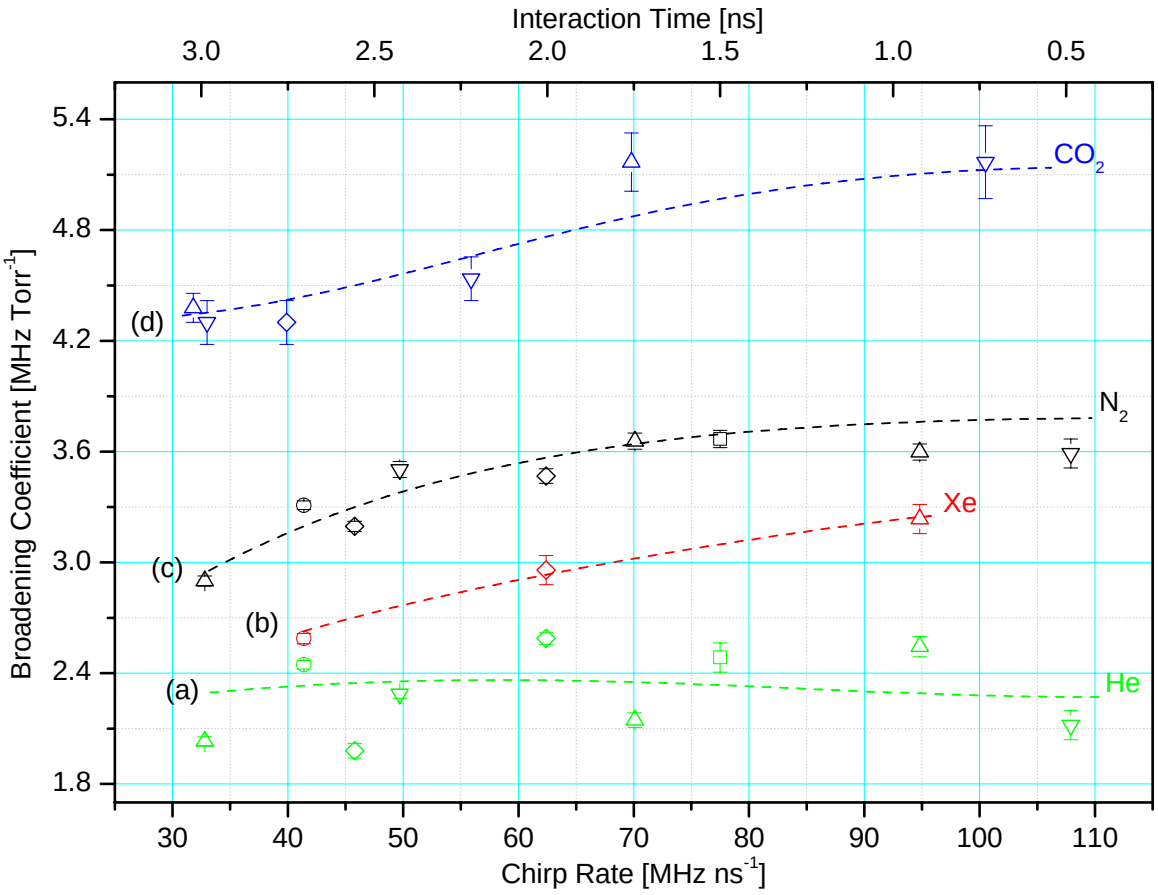

Figure 11.3. Chirp rate dependence of the retrieved effective nitrous oxide – foreign gas broadening coefficients: (a) $\gamma^0_{N_2O-He}$; (b) $\gamma^0_{N_2O-Xe}$; (c) $\gamma^0_{N_2O-N_2}$; (d) $\gamma^0_{N_2O-CO_2}$. Transitions: ○ $P(12)$; ◇ $P(11)$; △ $P(10)$; ▽ $P(9)$; □ $P(8)$. The dotted lines are added to allow the trends to be easily visualised.

Table 11.5. Obtained helium, xenon, nitrogen and carbon dioxide effective broadening coefficients in MHz Torr^{-1}, HWHM, for the investigated nitrous oxide ν_1 transitions

Line	Slow Chirp Measurements			Medium Chirp Measurements			Fast Chirp Measurements			
	γ^0_{He}	$\gamma^0_{N_2}$	$\gamma^0_{CO_2}$	γ^0_{He}	$\gamma^0_{N_2}$	$\gamma^0_{CO_2}$	γ^0_{He}	γ^0_{Xe}	$\gamma^0_{N_2}$	$\gamma^0_{CO_2}$
P(12)	-	-	-	-	-	-	2.45(2)	2.59(3)	3.31(2)	-
P(11)	-	-	-	1.98(4)	3.20(3)	-	2.59(3)	2.96(8)	3.47(4)	4.30(11)
P(10)	2.03(2)	2.90(3)	-	2.15(4)	3.67(6)	4.38(7)	2.54(6)	3.23(8)	3.60(6)	5.2(2)
P(9)	2.29(2)	3.50(4)	4.30(11)	2.13(8)	3.59(8)	4.54(11)	-	-	-	5.2(2)
P(8)	2.49(8)	3.67(7)	4.06(11) [a]	-	-	4.1(2) [a]	-	-	-	-

[a] The value is affected by instrumental distortions of the absorption line shape due to the vicinity of the beginning of the laser pulse.

Since the interaction time with the laser radiation plays a key role in determining the observed line shape, the effective pressure broadening coefficients are more closely correlated with the relaxation rates derived from time dependent measurements than with those obtained using time independent absorption spectroscopy. Further, the results show how a partial understanding of the speed dependence of the collisional cross sections, arising from their time dependence, could be gained by using frequency down-chirped QCL spectroscopy.

As it was observed for water vapour, carbon dioxide is not only the most efficient gas for broadening the absorption lines of the radiating species, but it is also unusually effective in changing the shape of the absorption lines. This is illustrated in Figure 11.4, where a comparison is made among the effects of nearly equal amounts of different buffer gases on the shape of the spectral lines of nitrous oxide. As demonstrated in this Figure, when carbon dioxide is used as a collision partner, the resultant broadening may exhibit features which are characteristic of either nitrogen or helium collisions. Indeed, as far as their effect on the rapid passage induced emission spike is concerned, CO_2 and N_2 act in a similar way. The first additions of CO_2 greatly reduce the amplitude of the gain peak, and normal pressure broadening behaviour is observed for $P_{buffer} > 30$ Torr. On the other hand, at low pressures of buffer gas (up to about 30 Torr), both CO_2 and He play an important role in reducing the peak absorbance of the signal. In contrast, collisions with nitrogen have little effect over this pressure range.

From these results it may be concluded that the intermolecular collisions are quite selective, since the ability of different collision partners to modify either the magnitude of the transient gain spike or the absorptive part of the spectral line are very distinctive, particularly that of carbon dioxide. Secondly, in the conventional studies of pressure broadening, it is common to explain the effects in terms of scattering events calculated using an electrostatic model, with a progressive increase of the quadrupole moment along the series of collision partners, helium, nitrogen and carbon dioxide. The results here obtained demonstrate that all of the experimental observations cannot reconcile with predictions made purely on the basis of such a model.

One of the effects omitted in the electrostatic model is the possibility of resonant energy transfer between collision partners. It appears to be highly possible that an intermolecular energy transfer may take place between nitrous oxide and carbon dioxide molecules during molecular collisions. In particular, the scattering efficiency of carbon dioxide could be explained by an interaction which involves a ro-vibrational energy exchange. This kind of relaxation process has been taken into account in earlier studies on molecular amplifiers [263] and optically pumped gas lasers [264]. Vibrational relaxations involves collisions which induce intra-molecular forces along the normal modes of a molecule. Such forces may not be directly related to either the interaction

potential, or to the distance of closest approach between the colliding species. Within this framework, the formation of weakly bound van der Waals complexes may promote intermolecular energy transfer. The structure of the $(CO_2)_2$, $(N_2O)_2$, $(CO_2–N_2O)$ and $(CO_2–H_2O)$ dimers have been widely studied by molecular beam spectroscopy [265 – 269]. The $(CO_2)_2$, $(N_2O)_2$, $(CO_2–N_2O)$ dimers have slipped parallel structures and their alignments are modelled using a distributed quadrupole moment [270 – 273].

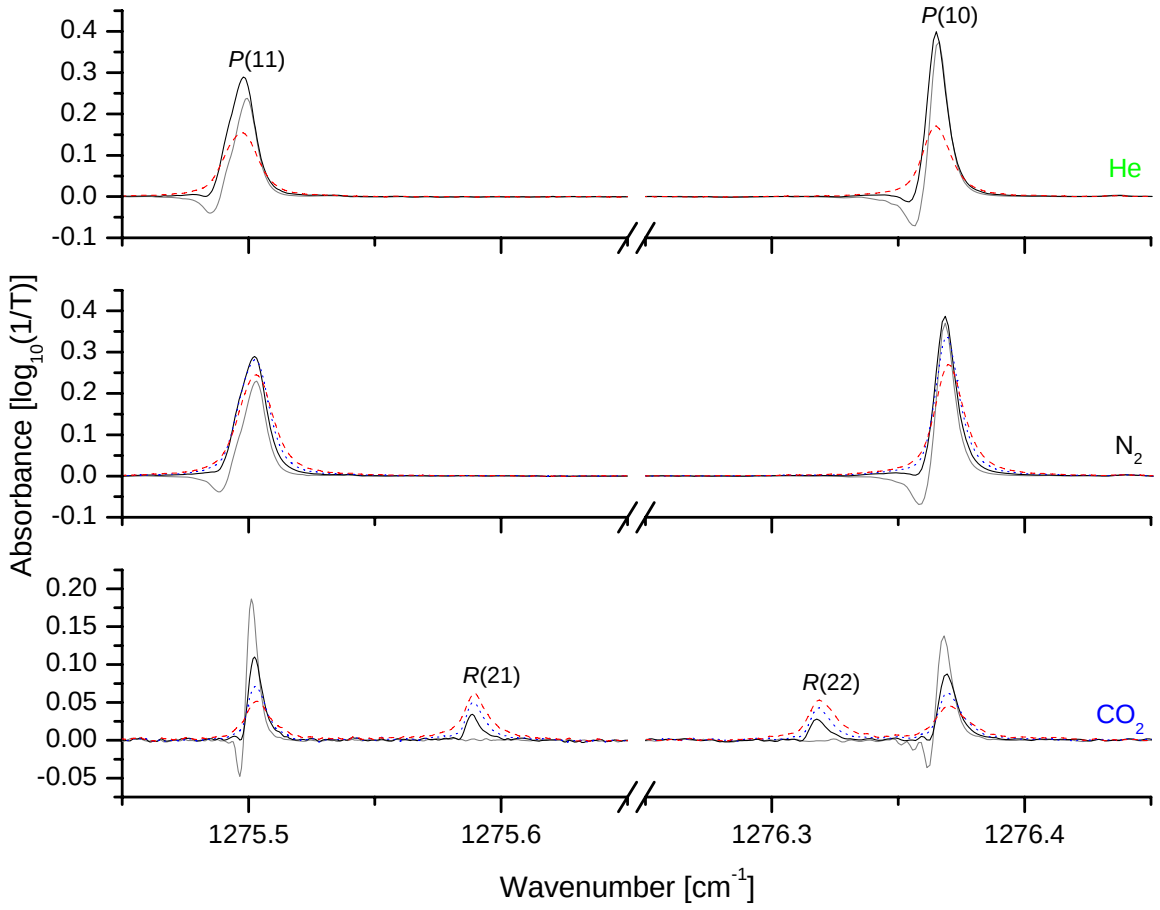

Figure 11.4. Comparison of the different effects on the N_2O absorption line shapes caused by collisions with helium, nitrogen and carbon dioxide. He broadening: P_{N_2O} = 0.013 Torr; PLC = 66 m; (—) P_{He} = 0 Torr; (—) P_{He} = 9.2 Torr; (--) P_{He} = 29.7 Torr. N_2 broadening: P_{N_2O} = 0.013 Torr; PLC ≈ 66 m; (—) P_{N_2} = 0 Torr; (—) P_{N_2} = 10.7 Torr; (···) P_{N_2} = 21.1 Torr; (--) P_{N_2} = 34.2 Torr. CO_2 broadening: P_{N_2O} = 0.12 Torr; PLC = 37 m; (—) P_{CO_2} = 0 Torr; (—) P_{CO_2} = 9.8 Torr; (···) P_{CO_2} = 20.4 Torr; (--) P_{CO_2} = 35.2 Torr.

It is also interesting to note the saturation of the absorption lines, which arises when very low pressures of nitrous oxide are used. Saturation effects using intra-pulsed QCL were first described by McCulloch et al. [80], who observed the variation with the pressure of the peak absorbance of some representative transitions of ethylene. In the analysis of the current experiments the saturation is derived from the integrated line intensities. As can be seen in Table 11.3, under

stationary conditions, the relative integrated line intensity of the $P(12)$, $P(11)$ and $P(10)$ N_2O transitions is expected to follow the order $S^0_{P(12)} > S^0_{P(11)} > S^0_{P(10)}$, where S^0 denotes the integrated line strength, or integrated absorption coefficient. Nevertheless, when a low pressure sample is interrogated by the down-chirped radiation, the integrated intensities of the three lines follow a completely reversed order.

This is illustrated in Figure 11.5 in the case of helium broadening. It can be seen that the magnitudes of the integrated intensities appear to follow the order $S^0_{P(10)} > S^0_{P(11)} > S^0_{P(12)}$ at $P < 15$ Torr. When $P \cong 18$ Torr, the three lines have nearly the same integrated absorption coefficient, and after that the usual ratios for the magnitudes of the relative intensity is recovered. Further, an increase of the integrated intensities follows the first addition of He. Such behaviour can be understood by considering the increase of the total number density as helium is added. The effect of the increased density is to increase the number of collisions able to "quench" the saturation, by removing molecules from the upper state and hence allowing more radiation to be absorbed. The anomalous decrease in the integrated line intensities does not seem an artefact due to data inversion, because it appears to follow a regular trend and it is reproducible at different chirp rates and for different collisional partners. A possible explanation may be the adsorption of the nitrous oxide molecules on the cell walls. Nevertheless, the adsorption does not affect the foreign pressure broadening coefficient. Indeed, due to the small N_2O pressures employed, the self-broadening contribution to the collisional half widths is negligible in comparison to both the broadening induced by the buffer gas and the Doppler one. This is confirmed by the observation of the linear dependence of the collisional half width upon the gas buffer pressure.

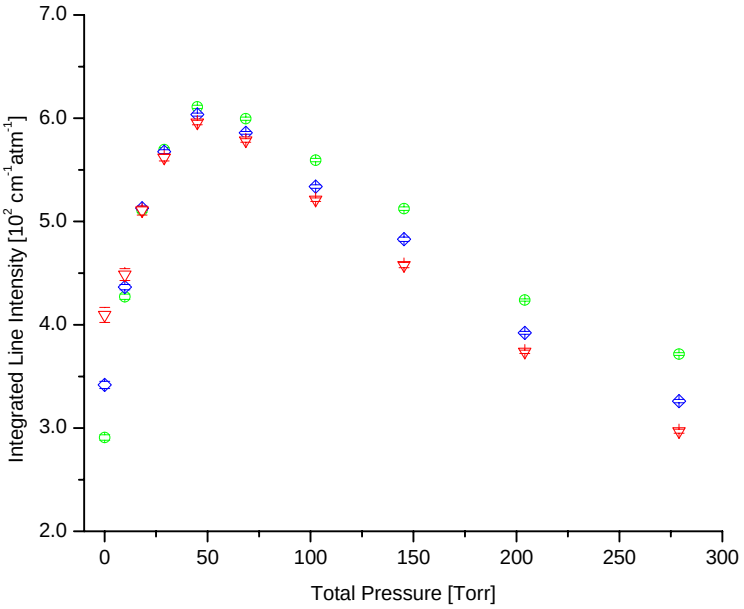

Figure 11.5. Saturation of the absorption lines observed when a low pressure sample of nitrogen is interrogated by the down-chirped radiation emitted by the intra-pulsed QCL. At $P_{Total} < 18$ Torr the lines appear to have a relative integrated intensity which is the reverse of that predicted by the integrated absorption coefficient. As the collisional damping increases the usual behaviour is recovered. ○ $P(12)$; ◇ $P(11)$; ▽ $P(10)$.

Finally, it is instructive to compare the present results with those obtained from the water-vapour broadening experiments. It is expected that the broadening parameters retrieved from water and nitrous oxide experiments exhibit a different behaviour, since they represent two very different

types of system. Nitrous oxide is characterized by very strong transition dipole moments, and hence a very strong coupling to the radiation field. The strength of the transitions allows the use of very low absorber pressures within the gas cell. A combination of these effects is responsible for the observed strong rapid passage signals. On the other hand, water represents a more complicated system. The complications arise from different factors which include: (i) the effect of the velocity changing collisions, causing the narrowing of the spectral line; (ii) the participation of speed dependencies of the collisional cross sections; (iii) the relatively weakness of the absorption line, and hence the need for higher sample pressures to be employed; (iv) the M_J changing collisions, which can play an important role; (v) the unresolved K doublet which constitutes the absorption line. Nevertheless, the investigations on the behaviour of water and nitrous oxide have two common features. The first one is the chirp rate dependence of the effective broadening parameters, which is strictly related to the time dependence of the collisional processes. The second is the unusual effect of carbon dioxide as collision partner, which suggests that in both cases the method of intermolecular energy transfer differs from that expected to be caused by dipolar or quadrupolar interactions.

Carbon Dioxide Rapid Passage Signals

During the carbon dioxide broadening measurements, some absorptions due to the $^{18}O=^{12}C=^{16}O$ unsymmetrical isotopomer were observed. In the main isotopomer, these transitions are infrared inactive because of its $D_{\infty h}$ symmetry. Nevertheless, in the reduced $C_{\infty v}$ symmetry of the $^{18}O^{12}C^{16}O$ isotopic species, the ^{18}O atom slightly shifts the molecular centre of mass from the centre of charge, allowing the IR non-active vibrational modes to become observable. The observed ro-vibrational transitions, listed in Table 11.6, belong to the lower 10002 – 00001 component of the Fermi coupled bands, which have been analyzed by Toth in a very complete study of the CO_2 high resolution spectrum between 1200 and 1430 cm^{-1} [258].

Besides the carbon dioxide transitions, weak lines due to minor methane impurities contained in the CO_2 cylinder were detected [121]. Such impurities were also noted by Toth, in the gas cylinders which he used for his measurements [258]. His estimate was a level of 2 to 5 ppm by volume, which is similar to the concentrations found in the present measurements.

The large effects of carbon dioxide in broadening the absorption lines and suppressing the rapid passage signals in nitrous oxide, when it acts as buffer gas, find their correspondence in the rapid quenching of the $^{18}O^{12}C^{16}O$ rapid passage signals, when the isotopomer acts as an active

species perturbed by collisions with the major isotopic species. This property is shown in Figure 11.6, where a comparison is made between the spectrum of fully mono-substituted ^{18}O carbon dioxide (trace a) and the carbon dioxide spectrum perturbed by 0.12 Torr of nitrous oxide (trace b) or 2.5 Torr of water vapour (trace c).

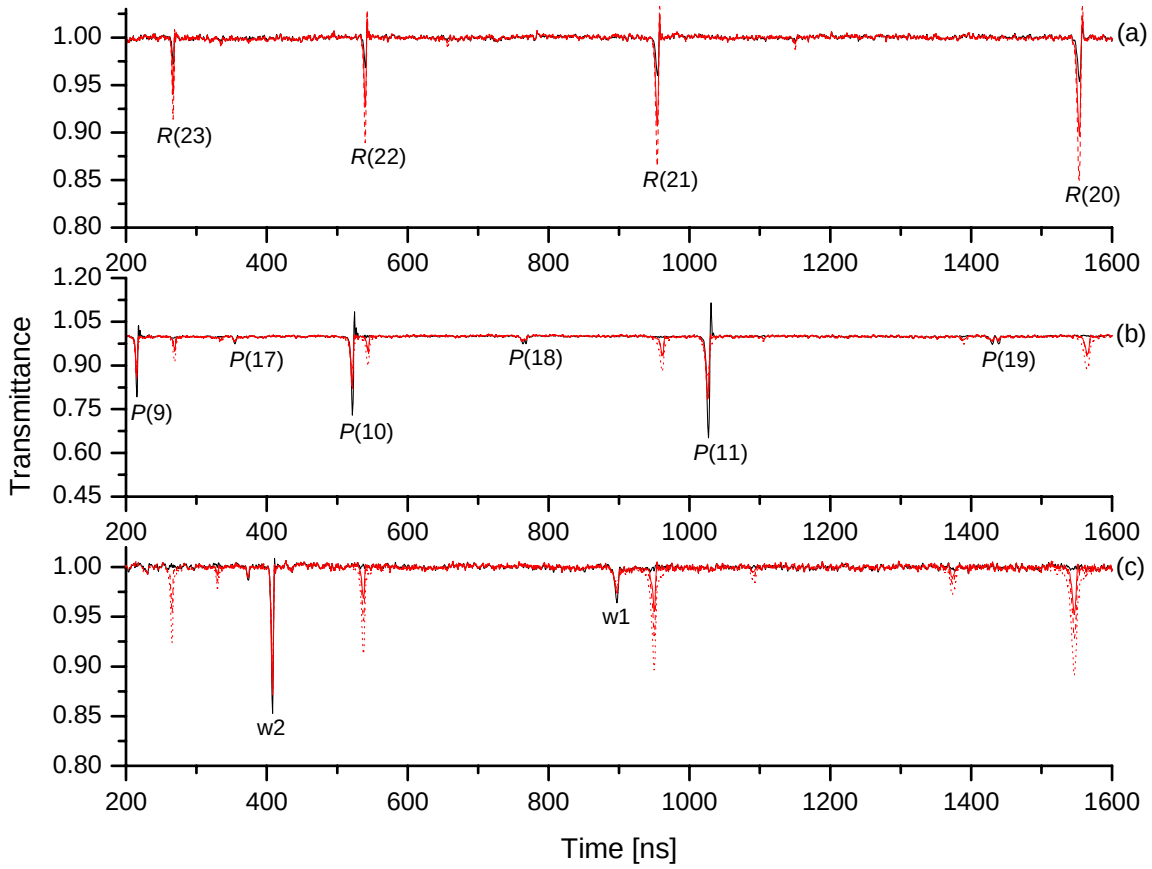

Figure 11.6. Effect of collisional damping on the rapid passage signals of carbon dioxide. Trace a: spectrum of an enhanced concentration of $^{18}O^{12}C^{16}O$. (—) 0.51 Torr; (—) 0.71 Torr; (--)1.12 Torr. Trace b: CO_2 in natural isotopic abundance perturbed by a fixed amount of nitrous oxide (P_{N_2O} = 0.12 Torr): (—) pure N_2O; (—) P_{CO_2} = 8.17 Torr; (--) P_{CO_2} = 9.98 Torr; (···) P_{CO_2} = 25.4 Torr. Trace c: CO_2 in natural isotopic abundance perturbed by a fixed amount of water vapour (P_{H_2O} = 2.54 Torr): (—) pure H_2O; (—) P_{CO_2} = 5.35 Torr; (--) P_{CO_2} = 10.02 Torr; (···) P_{CO_2} = 22.6 Torr. Line labelled w1 refer to the ν_2 $15_{1,15} \leftarrow 16_{0,16}$, $15_{0,15} \leftarrow 16_{1,16}$ unresolved *K* doublet of H_2O; line labelled w2 refer to the $8_{3,5} \leftarrow 9_{3,6}$ transition of the ν_2 band of HDO.

Table 11.6. Assignment, line strength and self-broadening coefficient of the observed ro-vibrational transitions belonging to the 10002 – 00001 band of $^{18}O^{12}C^{16}O$

Line	ν_0 [cm^{-1}] [a]	J'	J''	S^0 [10^{-25} cm molecule^{-1}] [a]	γ^0_{self} [MHz Torr^{-1}] [a]
$R(20)$	1274.85161	21	20	5.735	3.81
$R(21)$	1275.58379	22	21	5.582	3.77
$R(22)$	1276.31567	23	22	5.402	3.73
$R(23)$	1277.04724	24	23	5.199	3.69
$R(24)$	1277.77849	25	24	4.977	3.65

[a] From Ref. [258].

Table 11.7. Parameters used for numerical integration of Maxwell – Bloch equations

Parameter	Value	
	Line $R(20)$	Line $R(23)$
Number of time steps	10^5	
Number of velocity component	400	
Transition dipole moment [D]	4.13×10^{-3}	4.06×10^{-3}
CO_2 self broadening, full width half maximum [MHz Torr^{-1}]	7.6	7.4
CO_2 - N_2O broadening, full width half maximum [MHz Torr^{-1}]	7.2	7.2
Chirp rate [MHz ns^{-1}]	34	95
Laser power [mW]	40	
Path length [m]	20	

In order to understand this behaviour, the experimental observations have been compared with theoretical predictions obtained by solving the coupled Maxwell – Bloch equations for the carbon dioxide absorber. The equations have been integrated numerically by using an home made program written in C. The initial polarization $P_{t\to-\infty}$ and the initial population difference $w_{t\to-\infty}$ have been set to 0 and –1, respectively, which mean absence of polarization and all the molecules in the ground state. In the program code, the QCL has been assumed to show a linear chirp rate, a constant peak power and a constant mode waist in the absorption cell through the absorption transition. The effect of reorienting, M_J changing- collisions has not been taken into account. The calculations have been carried out by considering both carbon dioxide self- and foreign broadening

for transitions lying at chirp rates of about 30 and 100 MHz ns^{-1}. The input parameters for the Maxwell – Bloch simulation program are given in Table 11.7.

The experimental features are shown in Figure 11.7, while the shapes resulting from the Maxwell – Bloch calculations are illustrated in Figure 11.8. By comparing these two Figures it can be seen that, despite the larger oscillatory structure predicted by the calculations at low pressures, the simulated signals are in satisfactory agreement with the experimental spectra. Therefore, it is reasonable to conclude that the rapid quenching of the rapid passage signals is mainly due to the small transition dipole moment of carbon dioxide, and the damping is mainly caused by the CO_2 self-broadening, i.e. by collisions of the active $^{18}O^{12}C^{16}O$ molecules with those of the main isotopic species.

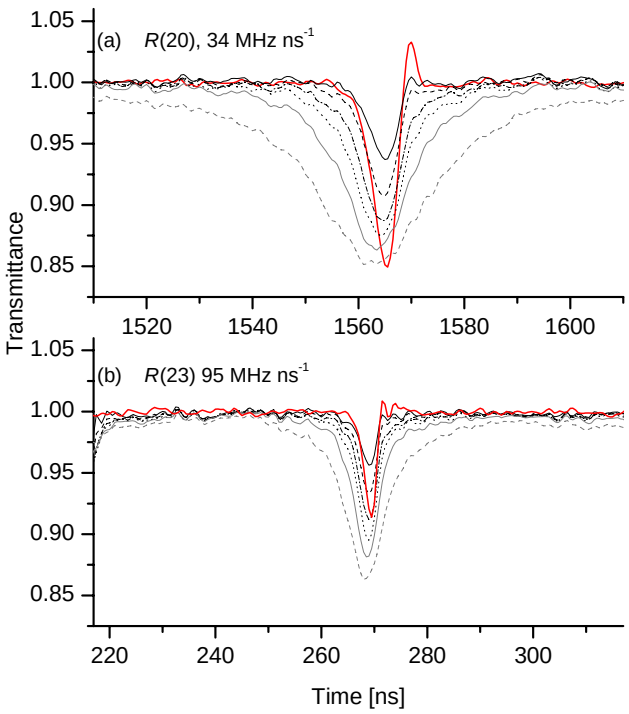

Figure 11.7. Effects of the collisional damping on the shape of two CO_2 absorption lines. Trace a: $R(20)$ transition recorded at a chirp rate of 34 MHz ns^{-1}. Trace b: $R(23)$ transition recorded at a chirp rate of 95 MHz ns^{-1}. (—) $^{18}O^{12}C^{16}O$, P = 1.1 Torr. Natural isotopic abundant CO_2 perturbed by 0.12 Torr of nitrous oxide: P_{total} = (—) 8.28, (--) 15.12, (-·-) 25.5, (···) 35.4, (—) 53.1, (--) 99.5 Torr.

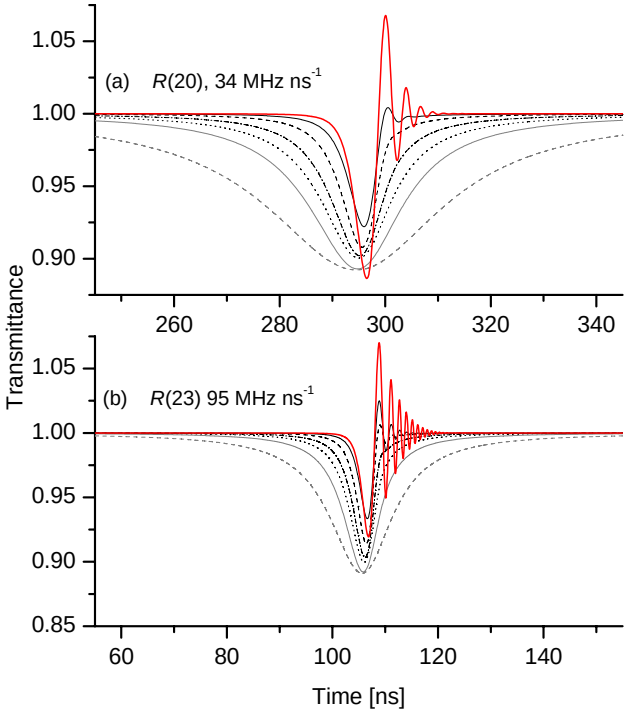

Figure 11.8. Theoretical effects of the collisional damping on the shape of two CO_2 absorption lines centred at chirp rates of 34 and 95 MHz ns^{-1}, respectively, obtained by solving the Maxwell – Bloch equations. Trace a: $R(20)$ transition, 34 MHz ns^{-1}. Trace b: $R(23)$ transition, 95 MHz ns^{-1}. (—) $^{18}O^{12}C^{16}O$, P = 1.1 Torr. Natural isotopic abundant CO_2 perturbed by 0.12 Torr of nitrous oxide: P_{total} = (—) 8.3, (--) 15, (-·-) 25.5, (···) 35, (—) 53, (--) 99.5 Torr.

Besides the larger oscillatory structures predicted at low pressure, the signal calculated at slower chirp rate show a more pronounced broadening than the observed spectra. Recently, there has been more experimental and theoretical work on the structure of the rapid passage signals of the $5s$ – $5p$ transitions in another of the alkali atoms, rubidium [274, 275]. In their first paper Zamith et al. considered the two level system excited by the linearly chirped pulse as being undamped [274].

Using a model similar to that developed by Rothenberg [261], they obtained a good representation of the rapid passage structure, but their calculations predicted a less rapid decay of the amplitude of the oscillatory signals with respect to that observed experimentally. In a subsequent paper, Delagnes et al. [275] included the effect of interference between the electric field radiated on and off resonance, in addition to the self-heterodyne effect [261, 274], and obtained better agreement between experimental and calculated signals. It is possible that a similar correction, involving interference between the on and off resonant fields, may be necessary to model the decay of molecular rapid passage signals of the type here described.

Conclusions and Outlook

Summary

The ever increasing need for improvements in the accuracy of remote sensing measurements of Earth's and planetary atmospheres, has led to numerous recent efforts to obtain improved spectroscopic parameters for molecules of atmospheric and astrophysical interest. In particular, line shapes are crucial elements for remote sounding techniques and for understanding of the Earth's atmospheric properties. Further, their detailed knowledge sheds light on the physics of the interaction between molecular gases and electromagnetic radiation and on the involved collisional processes.

With this background, the main target of this PhD thesis was to set up the procedure to perform laboratory measurements of the line parameters for molecules having an environmental and astrophysical relevance. This task represented both an experimental and an analytical problem.

Experimentally, the study of the line shape absorption profiles required a precise knowledge of the instrumental function, in order to account for the spectrometer contribution to the shape of the spectral lines. Hence, investigations were made to characterize the instrumental function of the tunable diode laser spectrometer employed in the experiments: the instrumental response resulted to be Gaussian (or nearly) shaped. Further, the distortions caused by spectrometer components and optics were identified, and then avoided or minimized as much as possible. Also the sample handling procedure and the experimental conditions were carefully controlled.

Analytically, the line parameter determination requires an efficient data analysis software and accurate line shape models, which account for the different chemical-physical processes taking place in a gas phase sample. These processes go from inhomogeneous Doppler and homogeneous collisional broadening, passing through collisional narrowing and speed dependence effects, arriving to the complex line mixing processes and the very refined models which consider the combined effects of the different phenomena and their correlations.

The programming efforts led to the development of a line-shape analysis software, called Visual Line-Shape Fitting Program (VLSFP), which was implemented to fit the experimentally recorded spectral lines. VLSFP performs the fit of the spectral features on the basis of different theoretical line shape functions which include Gaussian, Lorentz and Voigt profiles, as well as the Galatry and

Nelkin – Ghatak ones, which respectively represent the weak- and strong-collision models accounting for Dicke narrowing effect. The fitting routine, which is executed as a background task, is based on a box constrained Levenberg – Marquardt algorithm; the experimental lines can be fitted singularly or simultaneously. The program, written combining C# and Visual Basic programming languages, can be fully controlled from its graphical interface. Besides displaying the experimental and the computed spectrum together with their residuals, the interface lets the user to run and stop the fitting procedure. At the end of the fit, the obtained parameters are displayed together with their errors. A number of additional tools and options are further accessible from menu and tool bars: they let the user to control the details of the fit and to input the experimental conditions, such as temperature, pressure and optical path. The application has been implemented following an *Object Oriented Programming* approach, which permits an easier maintenance and future developments.

The experimental procedure and VLSFP were first applied to the determination of the line parameters of sulphur dioxide. These measurements also furnished a test for the fitting code and led to further improvements of the experimental method and data processing.

Sulphur dioxide is a very important molecule of proved atmospheric and astrophysical importance. It actively enters into the sulphur cycle and its main sources arise from human activities. Further, it is present in the Venus atmosphere and in the interstellar medium, particularly in star forming regions. The self-broadening coefficients and integrated absorption coefficients were determined experimentally in the atmospheric region around 9.2 μm. The self-broadening coefficients were also calculated theoretically, employing a semi-classical formalism based on the Anderson – Tsao – Curnutte approximation. In addition, the vibrational absorption cross sections of the three fundamental bands were measured from medium resolution spectra recorded with a FTIR interferometer. The determination of the self-broadening and integrated absorption coefficients was made through the analysis of the spectra recorded with a tunable diode laser spectrometer. The majority of ro-vibrational transitions belonged to the ν_1 fundamental band of the $^{32}SO_2$ isotopologue, but also absorptions belonging to both the $\nu_1 + \nu_2 - \nu_2$ hot band of $^{32}SO_2$ and to the ν_1 band of $^{34}SO_2$ were observed, and the corresponding line parameters were obtained. The self-broadening coefficients obtained theoretically were in good agreement with the experimental ones, thus indicating that SO_2 interacts mainly through dipole – dipole interaction, with only a small contribution coming from the quadrupole electrostatic potential. The good agreement between obtained parameters and literature values ensured that the experimental procedure and the data inversion were not affected by strong artefacts and it also demonstrated the reliability of VLSFP.

The retrieval of the line shape parameters was then extended to vinyl fluoride, for which no literature values were available. Vinyl fluoride is a compound widely used by industry, and once in the atmosphere it can react with hydroxyl radicals and ozone. The high resolution spectra were measured in the ν_7 band region around 8.9 μm by TDL spectroscopy. The analysis was complicated by the high density of lines, many of which were strongly overlapped or even not resolved. Anyway, the self-broadening coefficients and integrated absorption coefficients of a large number of lines, belonging to either the ν_7 fundamental or the $\nu_7 + \nu_9 - \nu_9$ hot band, were determined. The line shapes showed deviations from the Voigt profile, which were satisfactorily modelled by using the strong collision model represented by the Nelkin – Ghatak profile. These fits, which led to the determination of the self-narrowing coefficients, suggested that the collisional broadening and narrowing had similar magnitudes.

Besides line parameter determinations, either high resolution ro-vibrational analysis and low-medium resolution investigations were performed. A detailed study of the gas phase vibrational spectrum of vinyl fluoride was carried out both experimentally and theoretically. The vibrational analysis was performed on spectra recorded at low and medium resolution by employing a FTIR spectrometer. The observed absorption features were identified as fundamentals, overtones and up to three quanta combination bands, leading to an almost complete understanding of the infrared spectrum within the range 400 – 8000 cm^{-1}. Some of the partially resolved rotational structures were also analyzed, and preliminary rotational parameters for the ν_1 and ν_2 fundamentals and a number of combination bands were determined. Finally, the integrated absorption cross sections in the 400 – 3500 cm^{-1} region were measured for the first time. The obtained values well agreed with those retrieved by *ab initio* calculations, carried out at the CCSD(T)/cc-pVTZ level of theory. The quantum mechanics calculations at the CCSD(T)/cc-pVQZ level led to the determination of an hybrid force field, from which accurate values of anharmonicity constants and rotational and centrifugal distortion parameters were obtained. The comparison of the theoretical rotational constants with the experimentally available ones showed a very remarkable agreement, suggesting that the determined hybrid force field represented a very realistic description.

The obtained results provided basic information, which can be used for high–resolution infrared studies as well as to improve theoretical investigations about the reactivity of vinyl fluoride toward hydroxyl radical and ozone.

The ro-vibrational investigations concerned the analysis of the high resolution diode laser spectrum of CF_3Br in the region between 1090 and 1130 cm^{-1}. In order to simplify the spectral structure which was rather crowded, the spectra were recorded in a supersonic planar expansion and at the reduced temperature of 200 K. The rotational temperature reached in the supersonic

expansion was about 50 K. The combination of supersonic slit-jet expansion data with those recorded at 200 K was successfully employed to obtain a set of parameters for the $2\nu_5^0$ and $\nu_2 + \nu_3$ bands of both $CF_3{}^{79}Br$ and $CF_3{}^{81}Br$ isotopologues, with a resulting improved accuracy with respect to the previous studies. Together with the data of the near ν_1 fundamental previously reported, the obtained Hamiltonian parameters provided a nearly complete understanding of the ro-vibrational fine structure of CF_3Br in the region around 9 μm. In addition, from medium resolution FTIR spectra, the vibrational cross sections were measured over the spectral region between 500 and 2500 cm^{-1}. From these, the radiative forcing and Global Warming Potentials of this environmental hazardous compound were derived, thus furnishing useful data for radiative transfer models and global climate calculations.

Finally, as the last topic treated in this thesis, investigations on collisional processes and relaxation rates were carried out. In particular the time dependence of the collisional cross sections was explored, by using the frequency down-chirped radiation emitted by a Quantum Cascade Laser spectrometer employed in the intra-pulse method.

Frequency domain investigations of the spectral absorption line shapes are widely employed to explore the physics behind molecular collisions and to infer the intermolecular interactions which drive them. On the other hand, time domain spectroscopic techniques have always been effectively used to provide a deeper understanding of intermolecular interactions. Since they are more directly related to the effects of molecular collisions on the polarization of a gas, the time domain measurements provide a rich source of information about molecular relaxation rates.

Intra-pulse Quantum Cascade laser spectroscopy lies at the interface between frequency and time domain techniques. Indeed, besides giving a spectrum which can be conveniently analyzed in the frequency domain, it presents features typical of a coherent transient experiment.

Two series of experiments were designed to investigate the physics of the interaction of chirped infrared laser radiation with low pressure gases. In the first series, the collisional and transport processes responsible for the observed line shape of the ν_2 water vapour unresolved transition pair, $15_{0,15} \leftarrow 16_{1,16}$ and $15_{1,15} \leftarrow 16_{0,16}$, were investigated. The study was carried out by analyzing the behaviour of this line using three different chirp rates, while collisionally perturbing the water molecules by means of a range of atomic and molecular collision partners. In particular, the effects of collisions between water and helium, neon, argon, nitrogen and carbon dioxide, at chirp rates of 20, 35 and 75 MHz ns^{-1}, were studied.

Among the rare gases used, neon and argon caused a significant narrowing of the water absorption, with Ne giving the larger narrowing. A demonstration was made that a narrowing of the absorption line may be related to an increase of the macroscopic polarization of the gas sample. He and N_2

showed a fairly similar effect on the water absorption line, with nitrogen giving a small narrowing of the spectral half width. The observed differences between the broadening effects of He and N_2, and their variation with the chirp rate, were interpreted in terms of different motion properties of the two buffer gases within the time scale investigated. Finally, CO_2 played an unusually effective role in broadening the water absorption feature, and quenching the rapid passage signals. It was also the only gas, among the studied ones, able to perturb the water sufficiently strongly that a symmetrical line shape was recovered.

A second series of experiments was directed to extend to nitrous oxide the studies on the time dependence of the collisional processes. In particular, the chirp rate dependence of the collisional cross sections of nitrous oxide perturbed by helium, xenon, nitrogen and carbon dioxide was studied for a number of ν_1 ro-vibrational transitions. A general result was that the retrieved pressure broadening parameters tend to increase with increasing chirp rates. The increase was more pronounced for xenon, carbon dioxide and nitrogen. The trend was interpreted as resulting from a sort of speed dependence of the relaxation rates, since at faster chirp rates only the high velocity components of the molecular speed distribution were mainly involved in the collision processes.
Given its peculiar behaviour, carbon dioxide was investigated both as a buffer gas and as an absorbing molecule. As observed for water vapour, when it played the role of collisional partner it was very effective in broadening the absorption lines of nitrous oxide and quenching their rapid passage signals. These effects were mirrored when carbon dioxide played the role of active species. In fact, the rapid passage signals of the $^{18}O^{12}C^{16}O$ absorption lines were readily suppressed by addition of a small amount of gas, which could be either a foreign gas or the main isotopic species $^{12}C^{16}O_2$. These experimental observations were compared with the signals obtained from the solution of the optical Bloch (or Maxwell – Bloch) equations. The results suggested that the small transition dipole moment was mainly responsible for the rapid quenching of the rapid passage signals in CO_2. The very different behaviour demonstrated by carbon dioxide with respect to the remaining damping gases, particularly nitrogen, seemed difficult to reconcile with a theoretical model which takes into account only an electrostatic potential and attributes the differences only to an increase of quadrupole moment along the series helium, neon, argon, nitrogen, carbon dioxide. Rather, a resonant intermolecular energy transfer, related to ro-vibrational relaxation, was proposed.
Summarizing, not only the chirp rate dependence of the collisional cross sections was demonstrated, but it was shown that the experimental absorption line shapes and the related parameters are affected by a great number of factors. Some of these factors, such as the transition dipole moment, are intrinsically associated with the nature of the absorbing species. Other factors, such as the

motional narrowing and the speed dependence of the relaxation rates, are directly connected to the physics of the collisional processes and their time dependence.

Possible Developments

The possibilities of development of the issues tackled in this thesis are probably limited only by personal imagination. Spectroscopic line parameters depend on the molecular species, its temperature and concentration, and the presence of other gases. These conditions are very inhomogeneous in the atmospheres and hence, even for a given molecule, the shape of a spectral line varies depending on its surroundings. Therefore, it is clear the importance of making spectroscopic measurements of both line-by-line parameters and absorption cross sections under a variety of conditions, which span over a large range of pressures (from dPa to MPa) at different temperatures and for a variety of buffer gases. Among these, the measurements at different temperatures, which allow the study of temperature dependence of the broadening parameters, would only require the presence of a temperature controlled cell.

As far as the measurements in the presence of buffer gases are concerned, it would be interesting to retrieve the pressure broadening coefficients of sulphur dioxide and vinyl fluoride perturbed by nitrogen and oxygen. These would provide useful data for remote sounding of the Earth's atmosphere. In addition, given the astrophysical importance of SO_2, hydrogen and helium foreign broadening measurements may be carried out.

On the other hand, in the determination of vinyl fluoride line parameters some questions still need to be addressed. One is the assignment of the $\nu_7 + \nu_9 - \nu_9$ hot band transitions. A second involves further investigations about the causes for the observed deviations from the Voigt profile. This issue would also require further developments on VLSFP, in order to include line shape functions which take into account the effects of the speed dependence, line mixing and the correlation between internal state changing-, dephasing-collisions and velocity changing collisions. The implementation of correlated, soft or hard, collision models will be the most straightforward, since the majority of the program code does already exist. A further improvement of VLSFP would be the addition of a so-called multispectrum fitting routine, in which spectra recorded under different conditions can be fitted simultaneously. Although this is not strictly necessary for the study of spectra recorded with laser spectrometers, it would speed up the analysis procedure and, at least in principle, it would yield to an improved precision of the retrieved parameters. The implementation of the multifitting procedure can be achieved with a rather small programming

effort, since the major modifications involve the graphical interface and the routines used to load the data input.

Developments and improvements may involve the instrumentation, as well. Besides the above mentioned temperature-controlled cell, a multipass cell would be useful. A longer optical path would yield the possibility of obtaining stronger signals and hence higher signal-to-noise ratio. Further, lower sample pressures can be used and this would give the opportunity of a better modelling of the instrumental function. The spectral acquisition would benefit of a computer controlled digitizer with higher vertical resolution: this would improve the signal-to-noise ratio further, and would permit to correct for the laser drift, thus reducing the contribution of the instrumental function to the spectral line shapes.

Among the other topics, some words need to be spent about the potential of QCL spectrometers used in the intra-pulse method in exploring the physics of the interaction of the chirped infrared radiation with gas phase samples. The QCL-based approach for chirped spectroscopy is still at the beginning, and researches in this area appear to be unique. In this thesis, it has been shown that the frequency down-chirped technique may be conveniently employed to infer information about the physics of the absorption process itself, as well as that of intermolecular collisions. In the absorption process the way in which different collisional partners affect the absorptive part of the signal can be studied. Besides, the delayed rapid passage emission, which is directly related to the macroscopic polarization of the gas, can be studied as well. Therefore it is possible to gain useful information on the processes which occur during the molecular collisions and the related energy transfers. Hence, the studies on the line shapes observed in the frequency down-chirped spectra should be encouraged. In particular the development of appropriate theoretical line shape functions taking into account the chirp rate dependence would be important, since there is wealthy of information about relaxation rates, collisional processes and intermolecular energy transfers that can be obtained by employing this kind of spectroscopy.

Bibliographic Information & Appendices

References

[1] Buijs, H., Infrared spectroscopy, Springer handbook of atomic, molecular and optical physics, Drake, G. W. F., ed., Springer, Würzburg, 2006, pp. 607 – 613.

[2] Herzberg, G. H., Molecular spectra and molecular structure, vol. II Infrared and Raman spectra of polyatomic molecules, Krieger publishing company, Malabar, 1991.

[3] Duxbury, G., Infrared vibration-rotation spectroscopy. From free radicals to the infrared sky, John Wiley & Sons, Chichester, 2000.

[4] Flaud, J.-M., Infrared quantitative spectroscopy and atmospheric satellite measurements, **A1**, 21st Colloquium on high resolution molecular spectroscopy, Castellammare di Stabia, Italy, 2009.

[5] Flaud, J.-M., Infrared spectroscopy in the atmosphere, Spectroscopy from space, Demaison, J.; Sarka, K.; Cohen, E. A. eds., NATO science series, Kluwer Academic Publisher, London, 2001, pp. 187 – 200.

[6] Tinetti, G., Spectral retrieval of exoplanet atmospheres, **C3**, 21st Colloquium on high resolution molecular spectroscopy, Castellammare di Stabia, Italy, 2009.

[7] Swain, M. R., Probing exoplanet atmospheres with infrared molecular spectroscopy, **C1**, 21st Colloquium on high resolution molecular spectroscopy, Castellammare di Stabia, Italy, 2009.

[8] Kaltenegger, L., Spectral evolution of a rocky planet - How the right spectral lines can change a planet, **C2**, 21st Colloquium on high resolution molecular spectroscopy, Castellammare di Stabia, Italy, 2009.

[9] Goicoechea, J. R.; Swinyard, B.; Tinetti, G.; Nakagawa, T.; Enya, K.; Tamura, M.; Ferlet, M.; Isaak, K. G.; Wyatt, M.; Aylward, A. D.; Barlow, M.; Beaulieu, J.-P.; Boccaletti, A.; Cernicharo, J.; Cho, J.; Claudi, R.; Jones, H.; Lammer, H.; Leger, A.; Martin-Pintado, J.; Miller, S.; Najarro, F.; Pinfield, D.; Schneider, J.; Selsis, F.; Stam, D. M.; Tennyson, J.; Viti, S.; White, G., Using SPICA space telescope to characterize exoplanets, SPICA EP-RAT, 2008.

[10] Swain, M. R.; Vasisht, G.; Tinetti, G., The presence of methane in the atmosphere of an extrasolar planet, Nature, **452**, 2008, pp. 329 – 331.

[11] Tinetti, G.; Vidal-Madjar, A.; Liang, M.-C.; Beaulieu, J.-P.; Yung, Y.; Carey, S.; Barber, R. J.; Tennyson, J.; Ribas, I.; Allard, N.; Bellester, G. E.; Sing, D. K.; Selsis, F., Water vapour in the atmosphere of a transit extrasolar planet, Nature, **448**, 2007, pp. 169 – 171.

[12] Birk, M.; Hausamann, D.; Schreier, F.; Wagner, G., High resolution infrared laboratory spectroscopy of atmospheric constituents at DLR, Spectroscopy from space, Demaison, J.; Sarka, K.; Cohen, E. A., Eds., NATO science series, Kluwer Academic Publisher, London, 2001 pp. 219 – 233.

[13] Herman, M.; Hurtmans, D.; Vander Auwera, J., High resolution molecular spectroscopy, Spectroscopy from space, Demaison, J.; Sarka, K.; Cohen, E. A., Eds., NATO science series, Kluwer Academic Publisher, London, 2001 pp. 201 – 218.

[14] Perrin, A., Review on the existing spectroscopic databases for atmospheric applications, Spectroscopy from space, Demaison, J.; Sarka, K.; Cohen, E. A., Eds., NATO science series, Kluwer Academic Publisher, London, 2001 pp. 235 – 258.

[15] Rothman, L. S.; Jacquemart, D.; Barbe, A.; Benner, D. C.; Birk, M.; Brown, L. R.; Carleer, M. R.; Chackerian, C., Jr.; Chance, K.; Coudert, L. H.; Dana, V.; Devi, V. M.; Flaud, J.-M.; Gamache, R. R.; Goldman, A.; Hartmann, J.-M.; Jucks, K. W.; Maki, A. G.; Mandin, J.-Y.; Massie, S. T.; Orphal, J.; Perrin, A.; Rinsland, C. P.; Smith, M. A. H.; Tennyson, J.; Tolchenov, R. N.; Toth, R. A.; Vander Auwera, J.; Varanasi, P.; Wagner, G., The *HITRAN* 2004 molecular spectroscopic database, Journal of Quantitative Spectroscopy and Radiative Transfer **96**, 2005, pp. 139 – 204.

[16] Jacquinet-Husson,N.; Scott, N. A.; Chédin, A.; Garceran, K.; Armante, R.; Chursin, A. A.; Barbe, A.; Birk, M.; Brown, L. R.; Camy-Peyret, C.; Claveau, C.; Clerbaux, C.; Coheur, P. F.; Dana, V.; Daumont, L.; Debacker-Barilly, M. R.; Flaud, J.-M.; Goldamn, A.; Hamdouni, A.; Hess, M.; Jacquemart, D.; Köpke, P.; Mandin, J. Y.; Massie, S.; Mikhailenko, S.; Nemtchinov, V.; Nikitin, A.; Newnham, D.; Perrin, A.; Perevalov, V. I.; Régalia-Jarlot, L.; Rublev, A.; Schreier, F.; Schult, I.; Smith, K. M.; Tashkun, S. A.; Teffo, J. L.; Toth, R. A.; Tyuterev, Vl. G.; Vander Auwera, J.; Varanasi, P.; Wagner, G., The 2003 edition of the GEISA/IASI spectroscopic database, Journal of Quantitative Spectroscopy and Radiative Transfer **95**, 2005, pp. 429 – 467.

[17] Pickett, H. M.; Poynter, R. L.; Cohen, E. A.; Delitsky, M. L.; Perason, J. C.; Muller, H. S. P., Submillimeter, millimeter, and microwave spectral line catalogue, Journal of Quantitative Spectroscopy and Radiative Transfer, **60**, 1998, pp. 883 – 890.

[18] Vander Auwera, J., Vibration-rotation line intensities for constituents of planetary atmospheres, **A2**, 21st Colloquium on high resolution molecular spectroscopy, Castellammare di Stabia, Italy, 2009.

[19] Hartmann, J.-M.; Boulet, C.; Robert, D., Collisional effects on molecular spectra. Laboratory experiments and models, consequences for applications, Elsevier, New York 2008.

[20] Schoemaeker, R. L., Coherent transient infrared spectroscopy, Laser and coherence spectroscopy, Steinfeld, J. I. ed., Plenum Press., 1978, pp. 197 – 371.

[21] Oka, T., Collision-induced transitions between rotational levels, Advances in atomic and molecular physics, **9**, 1973, 127 – 206.

[22] Pilar, F. L., Elementary quantum chemistry, 2nd edition, Dover edition, New York, 1991.

[23] Messiah, A., Quantum mechanics, Dover edition, New York, 1999.

[24] Hollas, J. M., Modern spectroscopy, 2nd edition, John Wiley & Sons, Chichester, 1987.

[25] Kroto, H. W., Molecular rotation spectra, John Wiley & Sons, London, 1975.

[26] Levine, I. N., Quantum chemistry, 4th edition, Prentice-Hall, Inc., Englewood Cliffs, 1991.

[27] Atkins, P. W.; Friedman, R. S., Molecular quantum mechanics, 3rd edition, Oxford University Press, Oxford, 1997.

[28] Gordy, W.; Cook, R. L., Microwave molecular spectra, 3rd edition, John Wiley & Sons, New York, 1984.

[29] Zare, R. N., Angular momentum. Understanding spatial aspects in chemistry and physics, John Wiley & Sons, New York, 1988.

[30] McHale, J. L., Molecular spectroscopy, 1st edition, Prentice Hall, London, 1999.

[31] Wilson, E. B., Jr.; Howard, J. B., The vibration-rotation energy levels of polyatomic molecules. 1. Mathematical theory of semirigid asymmetrical top molecules, The Journal of Chemical Physics, **4**, 1936, pp. 260 – 267.

[32] Nielsen, H. H., The vibration-rotation energies of molecules, Reviews of Modern Physics, **23**, 1951, pp. 90 – 136.

[33] Mills, I. M., Vibration-rotation structure in asymmetric- and symmetric-top molecules, Molecular spectroscopy: modern research, vol. I, Rao, K. N.; Mathews, C. W., Eds, Academic Press Inc., New York, 1972, pp. 115 – 140.

[34] King, G. W.; Hainer, R. M.; Cross, C. P., The asymmetric rotor. I. Calculation and symmetry classification of energy levels, The Journal of Chemical Physics, **11**, 1943, pp. 27 – 42.

[35] Wang, S. C.; On the asymmetrical top in quantum mechanic, Physical Review, **34**, 1929, pp. 243 – 252.

[36] Aliev, M. R.; Watson, J. K. G., Higher-order effects in the vibration-rotation spectra of semirigid molecules, Molecular spectroscopy: modern research, vol. III, Rao, K. N., Ed. Academic Press, Inc., London, 1985, pp. 1 – 67.

[37] Papoušek, D.; Aliev, M. R.; Molecular vibrational/rotational spectra, Elsevier, Amsterdam, 1982.

[38] Sarka, K.; Demaison, J., Perturbation theory, effective Hamiltonians and force constants, Computational molecular spectroscopy, P. Jensen, R. Bunker Eds., John Wiley & Sons, Chichester, 2000.

[39] Watson, J. K. G., Determination of centrifugal-distortion coefficients of asymmetric-top molecules. II. Dreizler, Dendl, and Rudolph's sesults, The Journal of Chemical Physics, **48**, 1968, pp. 181 – 185.

[40] Watson, J. K. G., Vibration spectra and structure, J. R. During; Elsevier, Amsterdam, 1977.

[41] Townes, C. H.; Shawlow, A. L., Microwave spectroscopy, Dover Publications, Inc., New York, 1975.

[42] King, G. W.; Hainer, R. M.; Cross, P. C., The asymmetric rotor. I. Calculation and symmetry classification of energy levels, The Journal of Chemical Physics, **11**, 1943, pp. 27 – 42.

[43] Badger, R. M.; Zumwat, L. R., The band envelopes of unsymmetrical rotator molecules. I. Calculation of the theoretical envelopes, The Journal of Chemical Physics, **6**, 1938, pp. 711 – 717.

[44] McDowell, R. S., QQ separations in type B band envelopes of asymmetric top molecules, Spectrochimica Acta, **30A**, 1974, pp. 1271 – 1274.

[45] Smith, M. A. H.; Rinsland, C. P.; Fridovich, B.; Rao, K. N., Intensities and collision broadening parameters from infrared spectra, Molecular spectroscopy: Modern research, vol. III, Rao, K. N., Ed., Academic Press, Inc., London, 1985, pp. 111 – 248.

[46] Rautian, S. G.; Sobel'man, I. I., The effect of collisions on the Doppler broadening of spectral lines, Soviet Physics Uspekhi (English translation), **9**, 1967, pp. 701 – 716.

[47] Varghese, P. L.; Hanson, R. K., Collisional narrowing effects on spectral line shapes measured at high resolution, Applied Optics, **23**, 1984, pp. 2376 – 2385.

[48] Dicke, R. H., The effect of collisions upon the Doppler width of spectral lines, Physical Review, **89**, 1953, pp. 472 – 473.

[49] Pine, A. S., Line shape asymmetries in Ar-broadened HF (v = 1–0) in the Dicke-narrowing regime, The Journal of Chemical Physics, **101**, 1994, pp. 3444 – 3452.

[50] Robert D.; Thuet, J. M.; Bonamy, J.; Temkin, S., Effect of speed-changing collisions on the spectral line shape, Physical Review A, **47**, 1993, R771 – R773.

[51] Duggan, P.; Sinclair, P. M.; Berman, R; May, A. D.; Drummond, J. R., Testing lineshape models: measurements for v = 1–0 CO broadened by He and Ar, Journal of molecular spectroscopy, **186**, 1997, pp. 90 – 98.

[52] Hartmann, J.-M.; Bouanich, J.-P.; Jucks, K. W.; Blanquet, Gh.; Walrand, J.; Bermejo, D.; Domenech, J.-L.; Lacome, N., Line-mixing effect in N_2O *Q* branches: model, laboratory and atmospheric spectra, The Journal of Chemical Physics, **110**, 1999, 1959 – 1968.

[53] Pieroni, D.; Nguyen, V. T.; Brodbeck, C.; Claveau, C.; Valentin, A.; Hartmann, J.-M.; Gabard, T.; Champion, J.-P.; Bermejo, D.; Domenech, J.-L., Experimental and theoretical study of line mixing in methane spectra. I. The N_2-broadened ν_3 band at room temperature, The Journal of Chemical Physics, **110**, 1999, 7717 – 7732.

[54] Rao, D. R.; Oka, T., Dicke narrowing and pressure broadening in the infrared fundamental band of HCl perturbed by Ar, Journal of molecular spectroscopy, **122**, 1987, pp. 16 – 27.

[55] Pine A. S., Collisional narrowing of HF fundamental band spectral lines by neon and argon, Journal of molecular spectroscopy, **82**, 1980, 435 – 448.

[56] Galatry, L. Simultaneous effect of Doppler and foreign gas broadening on spectral lines, Physical Review, **122**, 1961, pp. 1218 – 1223.

[57] Nelkin, M.; Ghatak, A., Simple binary collision model for Van Hove's $G_s(r, t)$, Physical Review, **135**, 1964, A4 – A9.

[58] Lepère, M., Line profile study with tunable diode laser spectrometers, Spectrochimica Acta Part A, **60**, 2004, pp. 3249 – 3258.

[59] Coy, S. L., Speed dependence of microwave rotational relaxation rates, The Journal of Chemical Physics, **73**, 1980, pp. 5531 – 5555. Erratum, **76**, 1982, p. 2112.

[60] Rohart, F.; Mäder, H.; Nicolaisen, H.-W., Speed dependence of rotational relaxation indiced by foreign gas collisions: studies on CH_3F by millimeter wave coherent transients, The Journal of Chemical Physics, **101**, 1994, 6475 – 6486.

[61] Baranger, M., Simplified quantum-mechanical theory of pressure broadening, Physical Review, **111**, 1958, pp. 481 – 493; Baranger, M., Problem of overlapping lines in theory of pressure broadening, Physical Review, **111**, 1958, pp. 494 – 504; Baranger, M., General impact theory of pressure broadening, Physical Review, **112**, 1958, pp. 855 – 865.

[62] Kolb, A. C.; Griem, H., Theory of line broadening in multiplet spectra, Physical Review, 111, 1958, pp. 514 – 521.

[63] Fano, U., Pressure broadening as a prototype of relaxation, Physical Review, **131**, 1963, pp. 259 – 268.

[64] Ben-Reuven, A., Spectral line shapes in gases the binary-collision approximation, Advances in Chemical Physics, **33**, 1976, pp. 235 – 293.

[65] Anderson, P. W., Pressure broadening in the microwave and infra-red regions, Physical Review, 76, 1949, pp. 647 – 661.

[66] Tsao, C. J.; Curnutte, B., Line-widths of pressure-broadened spectral lines, Journal of Quantitative Spectroscopy and Radiative Transfer, **2**, 1962, pp. 41 – 91.

[67] Baldacchini, G.; Marchetti, S.; Montelatici, G; Buffa, G.; Tarrini, O; Experimental and theoretical investigation of self-broadening and self-shifting of ammonia transition lines in the ν_2 band, The Journal of Chemical Physics, **76**, 1982, pp. 5271 – 5277.

[68] Murphy, J. S.; Boggs, J. E., Collision broadening of rotational absorption lines. I. Theoretical formulation, The Journal of Chemical Physics, **47**, 1967, pp. 691 – 702; Murphy, J. S.; Boggs, J. E., Collision broadening of rotational absorption lines. II. Self-broadening of symmetric-top molecules, The Journal of Chemical Physics, **47**, 1967, pp. 4152 – 4158; Murphy, J. S.; Boggs, J. E., Collision broadening of rotational absorption lines. III. Broadening by linear molecules and inert gases and determination of molecular quadrupole moment, The Journal of Physical Chemistry, **49**, 1968, pp. 3333 – 3343; Murphy, J. S.; Boggs, J. E., Collision broadening of rotational absorption lines. IV. Pressure broadening of the ammonia inversion spectrum, The Journal of Physical Chemistry, **50**, 1969, pp. 3320 – 3329; Murphy, J. S.; Boggs, J. E., Collision broadening of rotational absorption lines. V. Pressure broadening of microwave spectra involving asymmetric-top molecules, The Journal of Chemical Physics, **51**, 1969, pp. 3891 – 3901.

[69] Robert, D.; Bonamy, J., Short range force effects in semiclassical line broadening calculations, Le Journal de Physique, **40**, 1973, pp. 923 – 943.

[70] Khodos, V. V.; Ryndynk, D. A.; Vaks, V. L., Fast-passage microwave molecular spectroscopy with frequency sweeping, The European Physical Journal. Applied Physics, **25**, 2004, pp. 203 – 208.

[71] Abragam, A., The principles of nuclear magnetism, Oxford University Press., Oxford, 1983.

[72] Brewer, R. G.; Shoemaker, R. L., Photo echo and optical nutation in molecules, Physical Review Letters, **27**, 1971, 631 – 634. Brewer, R. G.; Shoemaker, R. L., Optical free induction decay, Physical Review A, **6**, 1972, pp. 2001 – 2007.

[73] Allen, L.; Eberly, J. H., Optical resonance and two-level atoms, Dover Publications, Inc., New York, 1987.

[74] Melinger, J. S.; Gandhi, S. R.; Hariharan, A.; Goswami, D.; Warren, W. S., Adiabatic population transfer with frequency-swept laser pulses, The Journal of Chemical Physics, **101**, 1994, pp. 6439 – 6454.

[75] Li, Y.-Q.; Xiao, M., Transient spectroscopy with a current-switched semiconductor diode laser, Journal of Optics B: Quantum and Semiclassical Optics, **1**, 1999, 541 – 545.

[76] Ernst, R. R., Advances in magnetic resonance, vol. II, Academic Press., New York, 1966, pp. 1 – 135.

[77] Stoner, J. W.; Szymanski, D.; Eaton, S. S.; Quine, R. W.; Rinard, G. A.; Eaton, G. R., Direct-detected rapid-scan EPR at 250 MHz, Journal of Magnetic Resonance, **170**, 2004, 127 – 135.

[78] McGurk, J. C.; Schmalz, T. G.; Flygare, W. H., Fast passage in rotation spectroscopy: theory and experiment, The Journal of Chamical Physics, **60**, 1974, 4181 – 4188.

[79] Loudon, R., The quantum theory of light, 3rd edition, Oxford University Press., Oxford, 2000.

[80] McCulloch, M. T.; Duxbury, G.; Langford, N., Observation of saturation and rapid passage signals in the 10.25 micron spectrum of ethylene using frequency chirped quantum cascade laser, Molecular Physics, **104**, 2006, pp. 2767 – 2779.

[81] Duxbury, G.; Langford, N.; McCulloch, M. T.; Wright, S., Rapid passage induced population transfer and coherences in the 8 micron spectrum of nitrous oxide, Molecular Physics, **105**, 2007, pp. 741 – 754.

[82] Császár, A. G.; Allen, W. D.; Yamaguchi, Y.; Schaefer, III, H. F., *Ab initio* dermination of accurate ground electronic state potential energy hypersurfaces for small molecules, Computational molecular spectroscopy, Jensen, P.; Bunker, R., Eds., John Wiley & Sons, Chichester, 2000.

[83] Leach, A. R., Molecular modelling. Principles and applications, 2nd edition, Pearson Prentice Hall, Dorchester, 2001.

[84] Dunning, T. H. Jr., Gaussian basis sets for use in correlated molecular calculations. I. The atoms boron through neon and hydrogen, The Journal of Chemical Physics, **90**, 1989, pp. 1007 – 1023.

[85] Bartlett, R. J., Coupled-cluster approach to molecular structure and spectra: a step toward predictive quantum chemistry, Journal of Physical Chemistry, **93**, 1989, pp. 1697 – 1708.

[86] Simons, J.; Nichols, J., Quantum mechanics in chemistry, Oxford University Press, Oxford, 1997.

[87] Pulay, P., Analytical derivative techniques and the calculation of vibrational spectra, Modern Electronic structure theory, Part II, Yarkony, D. R., Ed., World Scientific Publishing Company, 1995, pp. 1191 – 1240.

[88] Pulay, P., Ab initio calculation of force constants and equilibrium geometries in polyatomic molecules. I. Theory, Molecular Physics, **17**, 1969, pp. 197 – 204.

[89] Kosterev, A. A.; Tittel, F. K.; Gmachl, C.; Capasso, F.; Sivco, D. L.; Baillargeon, J. N.; Hutchinson, A. L.; Cho, A. Y., Trace-gas detection in ambient air with a thermoelectrically cooled, pulsed quantum-cascade distributed feedback laser, Applied Optics, **39**, 2000, pp. 6866 – 6872; Kosterev, A. A.; Tittel, F. K.; Köhler, R.; Gmachl, C.; Capasso, F.; Sivco, D. L.; Cho, A. Y.; Wehe, S.; Allen, M. G., Thermoelectrically cooled quantum-cascade-laser-based sensor for the continuous monitoring of ambient atmospheric carbon monoxide, Applied Optics, **41**, 2002, pp. 1169 – 1173.

[90] Beyer, T.; Braun, M.; Lambrecht, A., Fast gas spectroscopy using pulsed quantum cascade lasers, Journal of Applied Physics, **93**, 2003, pp. 3158 – 3160.

[91] Nelson, D. D.; Shorter, J. H.; McManus, J. B.; Zahniser, M. S., Sub-part-per-billion detection of nitric oxide in air using a thermoelectrically cooled mid-infrared quantum cascade laser spectrometer, Applied Physics B. Lasers and Optics, **75**, 2002, pp. 343 – 350; Baren, R. E.; Parrish, M. E.; Shafer, K. H.; Howard, C. N.; Shi, Q.; Nelson, D. D.; McManus, J. B.; Zahniser, M. S., Quad quantum cascade laser spectrometer with dual gas cells for the simultaneous analysis of mainstream and sidestream cigarette smoke, Spectrochimica Acta Part A, **60**, 2004, pp. 3437 – 3447.

[92] McCulloch, M. T.; Langford, N.; Duxbury, G., Real-time trace-level detection of carbon dioxide and ethylene in car exhaust gases, Applied Optics, **44**, 2005, pp. 2887 – 2894.

[93] Cheesman, A.; Smith, J. A.; Ashfold N. R.; Langford, N.; Wright, S.; Duxbury, G., Application of a quantum cascade laser for time-resolved, in situ probing of CH_4/H_2 and C_2H_2/H_2 gas mixtures during microwave plasma enhanced chemical vapor deposition of diamond, The Journal of Physical Chemistry A, **110**, 2006, pp. 2821 – 2828.

[94] Joly, L.; Robert, C.; Parvitte, B.; Catoire, V.; Durry, G. ; Richard, G. ; Nicoullaud, B.; Zéninari, V., Develpment of a spectrometer using continuous wave distributed feedback quantum cascade laser operating at room temperature for the simultaneous analysis of N_2O and CH_4 in the Earth's atmosphere, Applied Optics, **47**, 2008, pp. 1206 – 1214.

[95] Waechter, H.; Mohn, J.; Tuzson, B.; Emmenegger, L; Sigrist, M. W., Determination of N_2O isotopomers with quantum cascade laser based absorption spectroscopy, Optics Express, **16**, 2008, pp. 9239 – 9244; Tuzson, B.; Zeeman, M. J.; Zahniser, M. S.; Emmenegger, L., Quantum cascade laser based spectrometer for in situ stable carbon dioxide isotope measurements, Infrared Physics & Technology, **51**, 2008, pp. 198 – 206.

[96] Webster, C. R.; Flesch, G. J.; Scott, D. C.; Swanson, J. E.; May, R. D.; Woodward, W. S.; Gmachl, C.; Capasso, F.; Sivco, D. L.; Baillargeon, J. N.; Hutchinson, A. L.; Cho, A. Y., Quantum-cascade laser measurements of stratospheric methane and nitrous oxide, **40**, 2001, pp. 321 – 326.

[97] Nelson, D. D.; McManus, B.; Urbanski, S. ; Herndon, S.; Zahniser, M. S., High precision measurements of atmospheric nitrous oxide and methane using thermoelectrically cooled mid-infrared quantum cascade lasers and detectors, Spectrochimica Acta Part A, **60**, 2004, pp. 3325 – 3335.

[98] McCulloch, M. T.; Normand, E. L.; Langford, N.; Duxbury G.; Newnham, D. A., Highly sensitive detection of trace gases using the time-resolved frequency downchirp from pulsed quantum-cascade lasers, Journal of the Optical Society of America B: Optical Physics, **20**, 2003, pp. 1761 – 1768.

[99] Wright, S.; Duxbury, G.; Langford, N., A compact quantum-cascade laser based spectrometer for monitoring the concentrations of methane and nitrous oxide in the troposphere, Applied Physics B. Laser and Optics, **85**, 2006, pp. 243 – 249.

[100] Hay, K. G.; Wright, S.; Duxbury, G.; Langford, N., In-flight measurements of ambient methane, nitrous oxide and water using a quantum cascade based spectrometer, Applied Physics B. Laser and Optics, **90**, 2008, pp. 329 – 337.

[101] Cascade Technologies, http://www.cascade-technologies.com/.

[102] Demtröder, W., Laser Spectroscopy, Vol. 1: Basic principles, 4th edition, Springer, Berlin, 2008.

[103] Powell, R. C., Types of lasers, Springer handbook of atomic, molecular and optical physics, Drake, G. W. F., ed., Springer, Würzburg, 2006, pp. 1035 – 1049.

[104] Perkins, W. D., Fourier transform-infrared spectroscopy. Part I. Instrumentation, Topics in Chemical Instrumentation, **63**, 1986, pp. A5 – A10.

[105] Griffiths, P. R.; de Haseth, J. A., Fourier transform infrared spectroscopy, John Wiley & Sons, Chichester, 1986.

[106] Kauppinen, J.; Heinonen, J.; Kauppinen, I., Interferometers based on the rotational motion, Applied spectroscopy reviews, **39**, 2004, pp. 99 – 129.

[107] Smalley, R. E.; Wharton, L; Levy, D. H., Molecular optical spectroscopy with supersonic beams and jets, Accounts of chemical research, **10**, 1977, pp. 139 – 145.

[108] Arnó, J.; Bevan, J. W., Infrared spectroscopy in supersonic free jets and molecular beams, Jet spectroscopy and molecular dynamics, Hollas, J. M.; Phillips, D., Eds., Blackie Academic & Professional, Glasgow, 1995, pp. 29 – 73.

[109] Skinner, A. R.; Chandler, D. W., Spectroscopy with supersonic jets, American Journal of Physics, **48**, 1980, pp. 8 – 13.

[110] Amrein, A.; Quack, M.; Schmitt, High-resolution interferometric Fourier transform infrared absorption spectroscopy in the supersonic free jet expansions: carbon monoxide, nitric oxide, methane, ethyne, propyne, and trifluoromethane, The Journal of Physical Chemistry, **92**, 1988, pp. 5455 – 5466.

[111] Pietropolli Charmet, A.; Stoppa, P.; Toninello, P.; Giorgianni, S.; Ghersetti, S., Rovibrational analysis of the ν_1 fundamental of CF_3Cl from diode laser spectra in a supersonic slit-jet expansion, Physical Chemistry Chemical Physics, **5**, 2003, pp. 3595 – 3599.

[112] Pietropolli Charmet, A.; Spettroscopia a diodo laser di derivati dell'etilene e del metano e realizzazione di un getto libero supersonico impulsato, PhD Tesis, Dottorato di ricerca in Scienze Chimiche XIV ciclo, 2001.

[113] Silfvast, W. T., Laser fundamentals, 2nd edition, Cambridge University Press, Cambridge, 2004.

[114] Faist, J.; Capasso, F.; Sivco, D. L.; Sirtori, C.; Hutchinson, A. L.; Cho, A. Y., Quantum cascade laser, Science, **264**, pp. 553 – 556, 1994.

[115] Kazarinov, R. F.; Suris, R. A., Amplification of electromagnetic waves in a semiconductor superlattice, Soviet Physics – Semiconductors, **5**, 1971, pp. 707 – 709.

[116] Köhler, R.; Tredicucci, A.; Beltram, F.; Beere, H. E.; Linfield, E. H.; Davies, A. G.; Ritchie, D. A.; Iotti, R. C.; Rossi, F., Terahertz semiconductor-heterostructure laser, Nature, **417**, 2002, pp. 156 – 159.

[117] Duxbury, G.; Langford, N.; McCulloch, M. T.; Wright, S., Quantum cascade semiconductor infrared and far-infrared lasers: from trace gas sensing to non-linear optics, Chemical Society Reviews, **34**, 2005, pp. 921 – 934.

[118] Namjou, K.; Cai, S.; Whittaker, E. A.; Faist, J.; Gmachl, C.; Capasso, F.; Sivco, D. L.; Cho, A. Y., Sensitive absorption spectroscopy with a room-temperature distributed-feedback quantum-cascade laser, Optics Letters, **23**, 1998, pp. 219 – 221.

[119] Normand, E.; McCulloch, M.; Duxbury, G.; Langford, N., Fast, real-time spectrometer based on a pulsed quantum-cascade laser, Optics Letters, **28**, 2003, pp. 16 – 18.

[120] Bracewell, R. N., The Fourier transform and its applications, 2nd edition, McGraw-Hill, New York, 1986.

[121] Duxbury, G.; Langford, N.; Hay, K., Delayed rapid passage and transient gain signals generated using a chirped 8 μm quantum cascade laser, Journal of Modern Optics, **55**, 2008, pp. 3293 – 3303.

[122] Duxbury, G.; Langford, N.; Hay. K.; Tasinato, N., Quantum cascade laser spectroscopy: diagnostics to non-linear optics, Journal of Modern Optics, **56**, 2009, pp. 2034 – 2048.

[123] Kisiel, Z., PROSPE – Programs for Rotational SPEctroscopy, http://info.ifpan.edu.pl/~kisiel/prospe.htm/.

[124] Benner, D. C.; Rinsland, C. P.; Devi, V. M.; Smith, M. A. H.; Atkins, D., A multispectrum nonlinear least squares fitting technique, Journal of Quantitative Spectroscopy and Radiative Transfer, **53**, 1995, pp. 705 – 721.

[125] Pine, A. S.; Gabard, T., Speed-dependent broadening and line mixing in CH_4 perturbed by Ar and N_2 from multispectrum fits, Journal of Quantitative Spectroscopy and Radiative Transfer, **66**, 2000, pp. 69 – 92.

[126] Plateaux, J.-J.; Regalia, L.; Boussin, C.; Barbe, A., Multispectrum fitting technique for data recorded by Fourier transform spectrometer : application to N_2O and CH_3D, Journal of Quantitative Spectroscopy and Radiative Transfer, **68**, 2001, pp. 507 – 520.

[127] Jacquemart, D.; Mandin, J.-Y.; Dana, V.; Picqué, N.; Guelachvili, G., A multispectrum fitting procedure to deduce molecular line parameters : application to the 3-0 band of $^{12}C^{16}O$, The European Physical Journal D, **14**, 2001, pp. 55 – 69.

[128] Zou, Q.; Nemtchinov, V.; Varanasi, P., An instrumental function and non-linear least-squares multi-spectral-line-fitting algorithm applicable to FTS studies, Journal of Quantitative Spectroscopy and Radiative Transfer, **75**, 2002, pp. 53 – 61.

[129] Carlotti, M., Global-fit approach to the analysis of limb-scanning atmospheric measurements, Applied Optics, **27**, 1988, pp. 3250 – 3254.

[130] Wavemetrics Inc., http://www.wavemetrics.com.

[131] Microcal, http://www.originlab.com/.

[132] Levenberg, K., A method for the solution of certain non-linear problems in least squares, The Quartely of Applied Mathematics, **2**, 1944, pp. 164 – 168.

[133] Marqhardt, D. V., An algorithm for the least squares estimation of non-linear parameters, SIAM Journal on Applied Mathematics, **11**, 1963, pp. 431 – 441.

[134] Madsen, K.; Nielsen, H. B.; Tingleff, O., Methods for non-linear least squares problems, 2nd edition, Informatics and mathematical modelling, Technical University of Danemark, Lyngby, 2004.

[135] Press, W. H.; Teukolsky, S. A.; Vetterling, W. T.; Flannery, B. P., Numerical recipes in C. The art of scientific computing, Cambridge University Press, Cambridge, 1992.

[136] Kanzow, C.; Yamashita, N.; Fukushima, M., Levernberg – Marquardt methods with strong local convergence properties for solving nonlinear equations with convex constraints, Journal of Computational and Applied Mathematics, **172**, 2004, pp. 375 – 397.

[137] Stroustrup, B., The C++ programming language, 3rd edition, Addison – Wesley, Reading, 1997.

[138] Wells, R. J., Rapid approximation to the Voigt/Faddeeva function and its derivatives, Journal of Quantitative Spectroscopy and Radiative Transfer, **62**, 1999, pp. 29 – 48.

[139] Ouyang, X.; Varghese, P. L., Reliable and efficient program for fitting Galatry and Voigt profiles to spectral data on multiple lines, Applied Optics, **28**, 1989, pp. 1538 – 1545.

[140] Thompson, W. J., Numerous neat algorithms for the Voigt profile function, Computers in Physics, **7**, 1993, pp. 627 – 631.

[141] Schreier, F., The Voigt and complex error function: a comparison of computational methods, Journal of Quantitative Spectroscopy and Radiative Transfer, **48**, 1992, pp. 743 – 762.

[142] Drayson, S. R., Rapid computation of the Voigt profile, Journal of Quantitative Spectroscopy and Radiative Transfer, **16**, 1976, pp. 611 – 614.

[143] Hui, A. K.; Armstrong, B. H.; Wray, A. A., Rapid computation of the Voigt and complex error functions, Journal of Quantitative Spectroscopy and Radiative Transfer, **19**, 1978, pp. 509 – 516.

[144] Kuntz, M., A new implementation of the Humlíček algorithm for the calculation of the Voigt profile function, Journal of Quantitative Spectroscopy and Radiative Transfer, **57**, 1997, pp. 819 – 824.

[145] Humlíček, J., An efficient method for evaluation of the complex probability function: the Voigt function and its derivatives, Journal of Quantitative Spectroscopy and Radiative Transfer, **21**, 1979, pp. 309 – 131.

[146] Humlíček, J., Optimized computation of the Voigt and complex probability functions, Journal of Quantitative Spectroscopy and Radiative Transfer, **27**, 1982, pp. 437 – 444.

[147] Letchworth, K. L.; Benner, D. C., Rapid and accurate calculation of the Voigt function, Journal of Quantitative Spectroscopy and Radiative Transfer, **107**, 2007, pp. 173 – 192.

[148] Mankin, G. W.; Coffey, M. T.; Goldman, A., Airborne observation of SO_2, HCl, and O_3 in the stratospheric plume of the Pinatubo volcano in July 1991, Geophysical Research Letters, **19**, 1992, pp. 179 – 182; Goldman, A.; Murcray, F. J.; Rinsland, C. P.; Blatherwick, R. D.; David, S. J.; Murcray, F. H.; Murcray, D. G., Mt. Pinatubo SO_2 column measurements from Mauna Loa, Geophysical Research Letters, **19**, 1992, pp. 183 – 186.

[149] Nummelin, A.; Bergman, P; Hjalmarson, Å.; Friberg, P.; Irvine, W. M.; Millar, T. J.; Ohishi, M.; Saito, S., A three-position spectral line survey of Sagittarus B2 between 218 and 263 GHz. II. Data analysis, The Astrophysical Journal Supplement Series, **128**, 2000, pp. 213 – 243; Schilke, P.; Benford, D. J.; Hunter, T. R.; Lis, D. C.; Phillips, T. G., A line survey of Orion-KL from 607 to 725 GHz, The Astrophysical Journal Supplement Series, **132**, 2001, pp. 281 – 364.

[150] Nelson, R. M.; Lane, A. L.; Matson, D. L.; Fanale, F. P.; Nash, D. B.; Johnson, T. V., Io: longitudinal distribution of sulfur dioxide frost, Science, **210**, 784 – 786, 1980.

[151] Bruno, B.; de Bergh, C.; Fegley, B.; Maillard, J.-P.; Crisp, D.; Owen, T.; Pollak, J. B.; Grinspoon, D., The abundance of sulfur dioxide below the clouds of Venus, Geophysical Research Letters, **20**, 1993, 1587 – 1590.

[152] Chu, P. M.; Wetzel, S. J.; Lafferty, W. J.; Perrin, A.; Flaud, J.-M.; Arcas, Ph.; Guelachvili, G., Line intensities for the 8-μm bands of SO_2, Journal of Molecular Spectroscopy, **189**, 1998, pp. 55 – 63.

[153] Sumpf, B., Line intensity and self-broadening investigations in the ν_1 and ν_3 bands of SO_2, Journal of Molecular Structure, **599**, 2001, pp. 39 – 49.

[154] Müller, H. S. P.; Brünker, S., Accurate rotational spectroscopy of sulphur dioxide, SO_2, in ist ground vibrational state and first excited bending states, $v = 0, 1$, up to 2 THz, Journal of Molecular Spectroscopy, **232**, 2005, pp. 213 – 222.

[155] Guelachvili, G.; Ulenikov, O. N.; Ushakova, G. A., Analysis of the ν_1 and ν_3 absorption bands of $^{32}S^{16}O_2$, Journal of Molecular Spectroscopy, **188**, 1984, pp. 1 – 5; Guelachvili, G.; Naumenko, O. V.; Ulenikov, O. N., Analysis of the SO_2 absorption Fourier spectrum in the regions 1055 to 2000 and 2200 to 2550 cm^{-1}, Journal of Molecular Spectroscopy, **125**, 1987, pp. 128 – 139.

[156] Flaud, J.-M.; Perrin, A.; Salah, L. M.; Lafferty, W. J.; Guelachvili, G., A reanalysis of the (010), (020), (100), and (001) rotational levels of $^{32}S^{16}O_2$, Journal of Molecular Spectroscopy, **160**, 1993, pp. 272 – 278.

[157] Kühnemann, F; Heiner, Y.; Sumpf, B.; Herrmann, Ka., Line broadening in the ν_3 band of SO_2: studied with diode laser spectroscopy, Journal of Molecular Spectroscopy, **152**, 1992, pp. 1 – 12.

[158] Sumpf, B.; Fleischmann, O.; Kronfeldt, H.-D., Self-, air-, and nitrogen-broadening in the ν_1 band of SO_2, Journal of Molecular Spectroscopy, **176**, 1996, pp. 127 – 132.

[159] Sumpf, B.; Schöne, M.; Kronfeldt, H.-D., Self- and air-broadening in the ν_3 band of SO_2, Journal of Molecular Spectroscopy, **179**, 1996, pp. 137 – 141.

[160] Sumpf, B.; Schöne, M.; Fleischmann, O.; Heiner, Y.; Kronfeldt, H.-D., Quantum number and temperature dependence of foreign gas-broadening coefficients in the ν_1 and ν_3 bands of SO_2: collisions with H_2, air, He, Ne, Ar, Kr, and Xe, Journal of Molecular Spectroscopy, **183**, 1997, pp. 61 – 71.

[161] Lazarev, V. V.; Ponomarev, Yu. N.; Sumpf, B.; Fleischmann, O.; Waschull, J.; Kronfeldt, H.-D.; Stroinova, V. N., Noble gas pressure-induced broadening and shift of H_2O and SO_2 absorption lines, Journal of Molecular Spectroscopy, **173**, 1995, pp. 177 – 193.

[162] Joly, L.; Zéninari, V.; Parvitte, B.; Weidmann, D.; Courtois, D.; Bonetti, Y.; Aellen, T.; Beck, M.; Faist, J.; Hofstetter, D., Spectroscopic study of ν_1 band of SO_2 using a continuous-wave DFB QCL at 9.1 μm, Applied Physics B. Laser and Optics, 77, 2003, pp. 703 – 706.

[163] Zéninari, V.; Joly, L.; Grouiez, B.; Parvitte, B.; Barbe, A., Study of SO_2 line parameters with a quantum cascade laser spectrometer around 1090 cm^{-1}: comparison with calculations of the ν_1 and $\nu_1 + \nu_2 - \nu_2$ bands of $^{32}SO_2$ and the ν_1 band of $^{34}SO_2$, Journal of Quantitative Spectroscopy and Radiative Transfer, **105**, 2007, pp. 312 – 325.

[164] Grouiez, B.; Parvitte, B.; Joly, L.; Courtois, D.; Zéninari, V., Comparison of a quantum cascade laser used in both cw and pulsed modes. Application to the study of SO_2 lines around 9 μm, Applied Physics B. Laser and Optics, **90**, 2008, pp. 177 – 186.

[165] Henningsen, J.; Barbe, A.; De Backer-Barilly, M.-R., Revised molecular parameters for $^{32}SO_2$ and $^{34}SO_2$ from high resolution study of the infrared spectrum in the 7–8 μm wavelength region, Journal of Quantitative Spectroscopy and Radiative Transfer, **109**, 2008, pp. 2491 – 2510.

[166] Lafferty, W. J.; Fluad, J.-M.; Sams, R. L.; Abib Ngom, E. H., High resolution analysis of the rotational levels of the (000), (010), (100), (001), (020), (110), and (011) vibrational states of $^{34}S^{16}O_2$, Journal of Molecular Spectroscopy, **252**, 2008, pp. 72 – 76.

[167] Flaud, J.-M.; Lafferty, W. J.; Sams, R. L., Line intensities for ν_1, ν_3 and $\nu_1 + \nu_3$ bands of $^{34}SO_2$, Journal of Quantitative Spectroscopy and Radiative Transfer, **110**, 2009, pp. 669 – 674.

[168] Tejwani, G. D. T., Calculation of pressure-broadened linewidths of SO_2 and NO_2, The Journal of Chemical Physics, **57**, 1972, pp. 4676 – 4681.

[169] Sauke, T. B.; Becker, J. F., Modelling, measuring, and minimizing the instrument response function of a tunable diode laser spectrometer, Journal of Quantitative Spectroscopy and Radiative Transfer, **91**, 2005, pp. 453 – 484.

[170] Nadezhdinskii, A. I., Diode laser spectroscopy: precise spectral line shape measurements, Spectrochimica Acta Part A, **52**, 1996, pp. 1041 – 1060.

[171] MatLab & Simulink, http://www.mathworks.com/.

[172] Nemtchinov, V.; Varanasi, P, Absorption cross-sections of HFC-134a in the spectral region between 7 and 12 μm, Journal of Quantitative Spectroscopy and Radiative Transfer, **83**, 2004, pp. 285 – 294.

[173] Kim, K.; King, W. T., Integrated infrared intensities and the atomic polar tensors in SO_2, The Journal of Chemical Physics, **80**, 1984, pp. 969 – 973.

[174] Kunimoto, T.; Masuzaki, H.; Ueoka, S., Experimental studies of the radiative properties of sulfur dioxide, Journal of Quantitative Spectroscopy and Radiative Transfer, **25**, 1981, pp. 345 – 349.

[175] Ahro, M.; Kauppinen, J., Nonlinearity of Beer's law in gas-phase FT-IR spectroscopy, Applied Spectroscopy, **55**, 2001, pp. 50 – 54.

[176] Parker, S. F.; Tooke, P. B., The effect of apodisation and finite resolution on Fourier transform infrared and Raman spectra, Spectrochimica Acta Part A, **53**, 1997, pp. 2245 – 2252.

[177] Sekušak, S.; Liedl, K. R.; Sabljić, A**.,** Reactivity and regioselectivity of hydroxyl radical addition to halogenated ethenes, The Journal of Physical Chemistry A, **102**, 1998, pp. 1583 – 1594.

[178] Ljubić, I.; Sabljić, A., Theoretical study of the mechanism and kinetics of gas-phase ozone additions to ethene, fluoroethene, and chloroethene: a multireference approach, The Journal of Physical Chemistry A, **106**, 2002, pp. 4745 – 4757; Ljubić, I.; Sabljić, A., Ozonolysis of fluoroethene: theoretical study of unimolecular decomposition paths of primary and secondary fluorozonide, The Journal of Physical Chemistry A, **109**, 2005, pp. 2381 – 2393.

[179] Torkington, P.; Thompson, H. W., The infra-red spectra of fluorinated hydrocarbons. I, Transactions Faraday Society, **41**, 1945, pp. 236 – 245.

[180] Scherer, J. R.; Potts, W. J., Assignment of the vinyl fluoride waggings modes, The Journal of Chemical Physics, **31**, 1959, pp. 1691 – 1692.

[181] McKean, D. C., CH stretching frequencies, bond length and strengths in halogenated ethylenes, Spectrochimica Acta, **31A**, 1975, pp. 1167 – 1186.

[182] Elst, R.; Oskam, A., Coriolis interaction between ν_8, ν_{10}, and ν_{11}, in the infrared spectrum of vinyl fluoride, Journal of Molecular Spectroscopy, **39**, 1971, pp. 357 – 363.

[183] Morgan, H. W.; Goldstein, J. H., Microwave spectrum and molecular structure of vinyl fluoride, The Journal of Chemical Physics, **30**, 1959, pp. 1025 – 1028.

[184] Gerry, M. C. L., The microwave spectrum and centrifugal distortion constants of vinyl fluoride, Journal of Molecular Spectroscopy, **45**, 1973, pp. 71 – 78.

[185] Hayashi, M.; Inagusa, T., Microwave spectrum, structure, and dipole moment of vinyl fluoride, Journal of Molecular Spectroscopy, **138**, 1989, pp. 135 – 140.

[186] Stoppa, P.; Giorgianni, S.; Gambi, A.; De Lorenzi, A.; Ghersetti, S., High resolution FTIR spectrum of vinyl fluoride near 9 μm: rovibrational analysis of the ν_7 band, Molecular Physics, **84**, 1995, pp. 281 – 290.

[187] Smith, B. J.; Coffey, D. Jr.; Radom, L., Theoretical and experimental structures of vinyl fluoride and vinyl alcohol, The Journal of Chemical Physics, **97**, 1992, pp. 6113 – 6120.

[188] Demaison, J., Ab initio anharmonic force field and equilibrium structure of vinyl fluoride and vinyl iodide, Journal of Molecular Spectroscopy, **239**, 2006, pp. 201 – 207.

[189] Gambi, A.; De Lorenzi, A.; Giorgianni, S.; Stoppa, P., High-resolution FTIR spectrum of vinyl fluoride: rovibrational analysis of the torsion mode at 712 cm^{-1}, Journal of Molecular Spectroscopy, **171**, 1995, pp. 504 – 512.

[190] De Lorenzi, A.; Giorgianni, S.; Stoppa, P.; Gambi, A., A Fourier transform infrared study of CH_2=CHF in the ν_4 band region near 1650 cm^{-1}, Molecular Physics, **87**, 1996, pp. 581 – 591.

[191] Gambi, A.; De Lorenzi, A.; Giorgianni, S., High-Resolution Infrared Spectrum of Vinyl Fluoride at 500 cm^{-1}, Journal of Molecular Spectroscopy, **182**, 1997, pp. 378 – 384.

[192] Stoppa, P.; Pietropolli Charmet, A.; Visinoni, R.; Giorgianni, S., Laser infrared spectroscopy of vinyl fluoride in the 1280-1400 cm^{-1} region, Molecular Physics, **103**, 2005, pp. 657 – 666.

[193] Tasinato, N.; Stoppa, P.; Pietropolli Charmet, A.; Giorgianni, S.; Gambi, A., High-resolution infrared study of vinyl fluoride in the 750-1050 cm^{-1} region: rovibrational analysis and resonances involving the ν_8, ν_{10}, and ν_{11} fundamentals, The Journal of Physical Chemistry A, **110**, 2006, pp. 13412 – 13418.

[194] Schneider, W.; Thiel, W., Anharmonic force fields from analytic second derivatives: method and application to methyl bromide, Chemical Physics Letters, **157**, 1989, pp. 367 – 373.

[195] Stanton, J. F.; Gauss, J.; Watts, J. D.; Szalay, P. G.; Bartlett, R. J., with contributions from Auer, A. A.; Bernholdt, D. E.; Christiansen, O.; Harding, M. E.; Heckert, M.; Heun, O.; Huber, C.; Jonsson, D.; Jusélius, J.; Lauderdale, W. J.; Metzroth, T.; Michauk, C.; O'Neill, D. P.; Price, D. R.; Ruud, K.; Schiffmann, F.; Varner, M. E.; Vázquez, J., and the integral packages *MOLECULE* (Almlöf J.; Taylor, P. R.), PROPS (Taylor, P. R.), and *ABACUS* (Helgaker, T.; Jensen, H. J. Aa.; Jørgensen, P; Olsen, J.). The Mainz-Austin-Budapest version of *ACES* II. For the current version, see http://www.aces2.de.

[196] Werner, H. –J.; Knowles, P. J. with contributions of Amos, R. D.; Bernhardsson, A.; Celani, P.; Cooper, D. L.; Deegan, M. J. O.; Dobbyn, A. J.; Eckert, F.; Hampel, C.; Hetzer, G.; Korona, T.; Lindh, R.; Lloyd, A. W.; McNicholas, S. J.; Manby, F. R.; Meyer, W.; Mura, M. E.; Nicklass, A.; Palmieri, P.; Pitzer, R.; Rauhut, G.; Schütz, M.; Stoll, H.; Stone, A. J.; Tarroni, R.; Thorsteinsson, T., MOLPRO (version 2002.6) package of *ab initio* programs.

[197] Eckert, F.; Pulay, P.; Werner, H.-J., *Ab initio* geometry optimization for large molecules, Journal of Computational Chemistry, **18**, 1997, pp. 1473 – 1483.

[198] Bak, K. L.; Gauss, J.; Jørgensen, P.; Olsen, J.; Helgaker, T.; Stanton, J. F., The accurate determination of molecular equilibrium structures, The Journal of Chemical Physics, **114**, 2001, pp. 6548 – 6556.

[199] Allen, W. D.; Császár, A. G.; Horner, D. A., The puckering inversion barrier and vibrational spectrum of cyclopentene. A scaled quantum mechanical force field algorithm, Journal of American Chemical Society, **114**, 1992, pp. 6834 – 6849.

[200] Mills, I. M.; Robiette, A. G., On the relationship of normal modes to local modes in molecular vibrations, Molecular Physics, **56**, 1985, pp. 743 – 765.

[201] Lehmann, K. K., Beyond the *x-K* relations. Calculations of 1-1 and 2-2 resonance constants with application to HCN and DCN, Molecular Physics, **66**, 1989, pp. 1129 – 1137.

[202] Montzka, S. A.; Butler, J. H.; Hall, B. D.; Mondeel, D. J.; Elkins, J. W., A decline in tropospheric organic bromine, Geophysical Research Letters, **30**, 2003, pp. 1826 – 1829.

[203] Scientific Assessment of Ozone Depletion 2006, Report 50 of the World Meteorological Association's Global Ozone Research and Monitoring Project, National Oceanic and Atmospheric Administration, National Aeronautics and Space Administration, United Nations Environment Programme, World Meteorological Organization, European Commission.

[204] National Oceanic and Atmospheric Administration (NOAA); the data can be found on the web site: http://www.cmdl.noaa.gov/infodata/ftpdata.html.

[205] Sinnhuber, B.-M.; Sheode, N.; Sinnhuber, M.; Chipperfield, M. P.; Feng, W., The contribution of anthropogenic bromine emissions to past stratospheric ozone trends: a modelling study, Atmospheric Chemistry and Physics Discussions, **6**, 2006, pp. 6497 – 6524,

[206] Lupo, D. W.; Quack, M., IR-laser photochemistry, Chemical Reviews, **87**, 1987, pp. 181 – 216.

[207] Fawzy, W.; Schwendeman, R. H., Infrared radiofrequency double resonance in the ν_1 band region of CF_3Br, Journal of Molecular Spectroscopy, **130**, 1988, pp. 193 – 203.

[208] Parthasarathy, V.; Sarkar, S. K.; Iyer, N. V.; Rama Rao, K. V. S.; Mittal, J. P., Laser isotope separation of ^{13}C: a comparative study, Applied Physics B. Laser and Optics, **56**, 1993, pp. 321 – 325;

[209] del Barrio, J. I.; Fernández Cézar, F.; Martin, E.; Tablas, F. M. G.; Fuss, W., Pulsed infrared selective dissociation of CF_3Br as a function of pressure, temperature, fluence and wavelength, Applied Physics B. Laser and Optics, 63, 1996, pp. 51 – 56; del Barrio, J. I.; Fernández Cézar, F.; Tablas, F. M. G., Pulsed infrared carbon selective dissociation of CF_3Br with N_2 and D_2 as buffers, Chemical Physics Letters, **270**, 1997, pp. 71 – 76.

[210] Sheridan, J.; Gordy, W., The microwave spectra and molecular structures of trifluoromethyl bromide, iodide and cyanide, The Journal of Chemical Physics, **20**, 1952, pp. 591 – 595.

[211] Sheridan, J.; Gordy, W., Interatomic distances in CF_3Br, CF_3I, and CF_3CN, Physical Review, **77**, 1950, pp. 292L – 293L.

[212] Sharbaugh, A. H.; Pritchard, B. S.; Madison, T. C., Microwave spectrum of CF_3Br, Physical Review, **77**, 1950, p. 302L.

[213] Cox, A. P.; Duxbury, G.; Hardy, J. A.; Kawashima, Y., Microwave spectra of CF_3Br and CF_3I. Structures and dipole moments, Journal of Chemical Society, Faraday Transactions 2: Molecular and Chemical Physics, **76**, 1980, pp. 339 – 350.

[214] Harder, H.; Nicolaisen, H. W.; Dreizler, H.; Mader, H., Quadrupole transitions in CF_3Br investigated by two-dimensional Fourier transform spectroscopy in the microwave-radiofrequency range, Journal of Molecular Spectroscopy, **160**, 1993, pp. 244 – 252.

[215] Carpenter, J. H.; Muse, J. D.; Smith, J. G., Millimetre-wave spectrum of CF_3Br, Journal of Chemical Society, Faraday Transactions 2: Molecular and Chemical Physics, **78**, 1982, pp. 139 – 146.

[216] Bailey, W. C.; Gonzalez, F. M., Calculation of bromine nuclear quadrupole coupling constants in gaseous state molecules, Journal of Molecular Structure, **651-653**, 2003, pp. 689 – 695.

[217] Chakrabarti, S.; Jaman, A. I., Microwave spectrum and quadrupole coupling constants of $^{13}CF_3Br$, Journal of Molecular Structure, **612**, 2002, pp. 103 – 108.

[218] Plyler, E. K.; Acquista, N., Infrared absorption spectra of five halomethanes, Journal of Research of the National Bureau of Standards, **48**, 1952, pp. 92 – 97.

[219] Polo, R. S.; Kent Wilson, M., The infrared spectra of CF_3Br and CF_3I, The Journal of Chemical Physics, **20**, 1952, pp. 1183 – 1184.

[220] Burczyk, K.; Burger, H.; Ruoff, A.; Pinson, A., Vibrational spectra and force constants of symmetric tops: rotational analysis of ν_1, $\nu_1 + \nu_6 - \nu_6$, and $\nu_1 + 2\nu_6 - 2\nu_6$ of $CF_3{}^{79}Br$ and $CF_3{}^{81}Br$ near 1100 cm^{-1}, Journal of Molecular Spectroscopy, **77**, 1979, pp. 109 – 116; Burczyk, K.; Bürger, H.; Schulz, P.; Ruoff, A., Das schwingungs-rotationsspektrum von $CF_3{}^{79}Br$ und $CF_3{}^{81}Br$ im bereich von ν_2, Zeitschrift für anorganische und allgemeine Chemie, **474**, 1981, pp. 74 – 82; Burczyk, K.; Bürger, H.; Ruoff, A.; Morillon-Chapey, M., Vibrational spectra and force constants of symmetric tops—XXII. Rotational analysis of $\nu_2 + \nu_3$ and $\nu_1 + \nu_2 + \nu_3$ of $CF_3{}^{79}Br$ and $CF_3{}^{81}Br$, Spectrochimica Acta, **37A**, 1981, pp. 615 – 626.

[221] Baldacci, A.; Passerini, A.; Ghersetti, S., Infrared absorption studies in the vapor phase of CF_3Br: Spectra between 1800 and 400 cm^{-1}, Journal of Molecular Spectroscopy, **91**, 1982, pp. 103 – 115.

[222] Bürger, H., Burczyk, K.; Hollenstein, H.; Quack, M., High resolution FTIR spectra of $^{12}CF_3I$, $^{13}CF_3I$ and $^{12}CF_3{}^{79}Br$ near 1050 cm^{-1} and 550 cm^{-1}, Molecular Physics, **55**, 1985, pp. 255 – 275.

[223] De Bekker, R.; Ebben, M.; Snels, M.; Stolte, S., High resolution spectroscopy of CF_3Br by diode laser in the frequency range 1070 – 1090 cm^{-1}, Laser Chemistry, **8**, 1988, pp. 61 – 78.

[224] Amrein, A.; Hollenstein, H.; Quack, M.; Schmitt, U., High resolution interferometric Fourier transform infrared spectrocopy in supersonic free jet expansions: N_2O, $CBrF_3$ and CF_3I, Infrared Physics, **29**, 1989, pp. 561 – 574.

[225] Snels, M., High-resolution infrared spectrum and analysis of the ν_2 band of CF_3Br, Journal of Molecular Spectroscopy, **138**, 1989, pp. 413 – 422.

[226] D'Amico, G.; Snels, M., Diode laser slit-jet spectra and analysis of the ν_{14} fundamental of 1-chloro-1,1-difluoroethane (HCFC-142b), Journal of Molecular Spectroscopy, **217**, 2003, pp. 72 – 78;

[227] Thompson, C. D.; Robertson, E. G.; McNaughton, D., Reading between the lines: exposing underlying features of high resolution infrared spectra ($CHClF_2$), Physical Chemistry Chemical Physics, **5**, 2003, pp. 1996 – 2000; Thompson, C. D.; Robertson, E. G.; McNaughton, D., Completing the picture in the rovibrational analysis of chlorodifluoromethane ($CHClF_2$): ν_3 and ν_8, Molecular Physics, **102**, 2004, pp. 1687 – 1695.

[228] Albert, S.; Keppler Albert, K.; Quack, M., Rovibrational analysis of the ν_4 and $\nu_5 + \nu_9$ bands of $CHCl_2F$, Journal of Molecular Structure, **695 – 696**, 2004, pp. 385 – 394; Albert, S.; Hollenstein, H.; Quack, M.; Willeke, M., Doppler-limited FTIR spectrum of the $\nu_3(a')/\nu_8(a'')$ *C*oriolis resonance dyad of $CHClF_2$: analysis and comparison with *ab initio* calculations, Molecular Physics, **102**, 2004, pp. 1671 – 1686; Albert, S.; Hollenstein, H.; Quack, M.; Willeke, M., Rovibrational analysis of the ν_4, $2\nu_6$ Fermi resonance band of $CH^{35}ClF_2$ by means of a polyad Hamiltonian involving the vibrational levels ν_4, $2\nu_6$, $\nu_6 + \nu_9$ and $2\nu_9$, and comparison with *ab initio* calculations, Molecular Physics, **104**, 2006, pp. 2719 – 2735; Albert, S.; Bauerecker, S.; Quack, M.; Steinlin, A., Rovibrational analysis of the $2\nu_3$, $3\nu_3$ and ν_1 bands of $CHCl_2F$ measured at 170 and 298 K by high-resolution FTIR spectroscopy, Molecular Physics, **105**, 2007, pp. 541 – 558.

[229] Pietropolli Charmet, A.; Stoppa, P.; Toninello, P.; Baldacci, A.; Giorgianni, S., Jet-cooled diode laser spectra of CF_3Br in the 9.2 μm region and rovibrational analysis of symmetric CF_3 stretching mode, Physical Chemistry Chemical Physics, **8**, 2006, pp. 2491 – 2498.

[230] Baldacci, A.; Giorgianni, S.; Visinoni, R.; Ghersetti, S., Analysis of the ν_1 band of trifluorobromomethane by diode laser spectroscopy, Journal of Molecular Spectroscoopy, **133**, 1989, pp. 36 – 44; Visinoni, R.; Baldacci, A.; Giorgianni, S.; Stoppa, P.; Ghersetti, S., Infrared study of $2\nu_5^0$ band of CF_3Br by diode laser spectroscopy, Journal of Molecular Spectroscopy, **140**, 1990, pp. 162 – 169;

[231] Baldacci, A.; Giorgianni, S.; Stoppa, P.; Ghersetti, S., Diode laser i.r. spectrum and rovibrational analysis of CF_3Br in the $\nu_2 + \nu_3$ region, Spectrochimica Acta, **45A**, 1989, pp. 329 – 334;

[232] Person, W. B.; Polo, S. R., Infrared intensities of the fundamental frequencies of CF_3Br, Spectrochimica Acta, **17A**, 1961, pp. 101 – 111.

[233] Varanasi, P.; Chudamani, S., Infrared intensities of some chlorofluorocarbons capable of perturbing the glabal climate, Journal of Geophysical Research, **93**, 1988, pp. 1666 – 1668.

[234] Orkin, V. L.; Guschin, A. G.; Larin, I. K.; Huie, R. E.; Kurylo, M. J., Measurements of the infrared absorption cross-sections of haloalkanes and their use in a simplified calculation

approach for estimating direct global warming potentials, Journal of Photochemistry and Photobiology A: Chemistry, **157**, 2003, pp. 211 – 222.

[235] Drage, E. A.; Jaksch, D.; Smith, K. M.; McPheat, R. A.; Vasekova, E.; Mason, N. J., FTIR spectroscopy and estimation of the global warming potential of CF_3Br and C_2F_4, Journal of Quantitative Spectroscopy and Radiative Transfer, **98**, 2006, pp. 44 – 56.

[236] Pickett, H. M., The fitting and prediction of vibration-rotation spectra with spin interactions, Journal of Molecular Spectroscopy, **148**, 1991, pp. 371 – 377.

[237] Pinnock, S.; Hurley, M. D.; Shine, K. P.; Wallington, T. J.; Smyth, T. J., Radiative forcing of climate by hydrochlorofluorocarbons and hydrofluorocarbons, Journal of Geophysical Research, **100**, 1995, pp. 23227 – 23238.

[238] Elrod, M. J., Greenhouse warming potentials from the infrared spectroscopy of atmospheric gases, Journal of Chemical Education, **76**, 1999, pp. 1702 – 1705.

[239] Kunde, V. G.; Conrath, B. J.; Hanel, R. A.; Maguire, W. C.; Prabhakara, C.; Salomonson, V. V., The Nimbus 4 infrared spectroscopy experiment 2. Comparison of observed and theoretical radiances from 425 – 1450 cm^{-1}, Journal of Geophysical Research, **79**, 1974, pp. 777 – 784.

[240] Berman, P. R., Speed-dependent collisional width and shift parameters in spectral profiles, Journal of Quantitative Spectroscopy and Radiative Transfer, **12**, 1972, pp. 1331 – 1342.

[241] Pickett, H. M., Effects of velocity averaging on the shapes of absorption lines, The Journal of Chemical Physics, **73**, 1980, pp. 6090 – 6094.

[242] Ward, J.; Cooper, J.; Smith, R. W., Correlation effects in the theory of combined Doppler and pressure broadening—I. Classical theory, Journal of Quantitative Spectroscopy and Radiative Transfer, **14**, 1972, pp. 555 – 576.

[243] D'Eu, F.-J.; Lemoine, B.; Rohart, F., Infrared HCN lineshapes as a test of Galatry and speed-dependent Voigt profiles, Journal of Molecular Spectroscopy, **212**, 2002, pp. 96 – 110.

[244] Brown, L. R.; Benner, D. C.; Malathy Devi, V.; Smith, M. A. H.; Toth, R. A., Line mixing in self- and foreign-broadened water vapor at 6 μm, Journal of Molecular Structure, **742**, 2005, pp. 111 – 122.

[245] Flower, D. R.; Bourhis, G.; Launay, J.-M., Molcol: a program for solving atomic and molecular collision problems, Computer Physics Communications, **131**, 2000, pp. 187 – 201.

[246] Thilbault, F.; Calil, B.; Boissoles, J.; Launay, J.-M., Experimental and theoretical CO_2–He pressure broadening cross sections, Physical Chemistry Chemical Physics, **2**, 2000, pp. 5404 – 5410.

[247] Johns, J. W. C.; McKellar, A. R. W.; Oka, T.; Römheld, M., Collision-induced Lamb dips in laser Stark spectroscopy, The Journal of Chemical Physics, **62**, 1975, pp. 1488 – 1496.

[248] Freund, S. M.; Johns, J. W. C.; McKellar, A. R. W.; Oka, T., Infrared-infrared double resonance experiments using a two-photon technique, The Journal of Chemical Physics, **59**, 1973, pp. 3445 – 3453.

[249] Blum, F. A.; Nill, K. W.; Kelley, P. L.; Calawa, A. R.; Harman, T. C., Tunable infrared laser spectroscopy of atmospheric water vapour, Science, **177**, 1972, pp. 694 – 695.

[250] Eng, R. S.; Calawa, A. R.; Harman, T. C.; Kelley, P. L.; Javan, A., Collisional narrowing of infrared water-vapor transitions, Applied Physics Letters, **21**, 1972, pp. 303 – 305.

[251] Eng, R. S.; Kelley, P. L.; Mooradian, A.; Calawa, A. R.; Harman, T. C., Tunable laser measurements of water vapor transitions in the vicinity of 5 μm, Chemical Physics Letters, **19**, 1973, pp. 524 – 528.

[252] Eng, R. S.; Kelley, P. L.; Calawa, A. R.; Harman, T. C.; Nill, K. W., Tunable diode laser measurements of water vapour absorption line parameters, Molecular Physics, **28**, 1974, pp. 653 – 664.

[253] Moretti, L.; Sasso, A.; Gianfrani, L.; Ciurlo, R., Collisional-broadened and Dicke-narrowed lineshapes of $H_2{}^{16}O$ and $H_2{}^{18}O$ transitions at 1.39 μm, Journal of Molecular Spectroscopy, **205**, 2001, pp. 20 – 27.

[254] Claveau, C.; Henry, A.; Lepère, M.; Valentin, A.; Hurtmans, D., Narrowing and broadening parameters for H_2O lines in the ν_2 band perturbed by nitrogen from Fourier transform and tunable diode laser spectroscopy, Journal of Molecular Spectroscopy, **212**, 2002, pp. 171 – 185.

[255] Lisak, D.; Rusciano, G.; Sasso, A., An accurate comparison of lineshape models on H_2O lines in the spectral region around 3 μm, Journal of Molecular Spectroscopy, **227**, 2004, pp. 162 – 171.

[256] Köhler, T.; Mäder, H., Measurement of speed dependent rotational relaxation rates using a microwave spectrometer with circular waveguide, Molecular Physics, **86**, 1995, pp. 287 – 300.

[257] Aroui, H.; Broquier, M.; Picard-Bersellini, A.; Bouanich, J.-P.; Chevalier, M.; Gherissi, S., Absorption intensities, pressure-broadening and line mixing parameters of some lines of NH_3 in the ν_4 band, Journal of Quantitative Spectroscopy and Radiative Transfer, **60**, 1998,

pp. 1011 – 1023; Aroui, H.; Picard-Bersellini, A.; Chevalier, M.; Broquier, M.; Ghersissi, S., Pressure-broadening and cross-relaxation rates of rotation–inversion transitions in the ν_4 band of NH_3 perturbed by CO_2, Journal of Molecular Spectroscopy, **176**, 1996, pp. 162 – 168.

[258] Toth, R. A., Line positions and strengths of CO_2 in the 1200 – 1400 cm^{-1} region, Applied Optics, **24**, 1985, pp. 261 – 274.

[259] Toth, R. A., N_2- and air-broadened linewidths and frequency-shifts of N_2O, Journal of Quantitative Spectroscopy and Radiative Transfer, **66**, 2000, pp. 285 – 304.

[260] Rothenberg, J. E.; Grischkowsky, D., Measurements of the phase of a frequency-swept ultrashort optical pulse, Journal of the Optical Society of America B: Optical Physics, **2**, 1985, pp. 626 – 633; Rothenberg, J. E.; Grischkowsky, D., Subpicosecond transient excitation of atomic vapor and the measurement of optical phase, Journal of the Optical Society of America B: Optical Physics, **3**, 1986, pp. 1235 – 1238.

[261] Rothenberg, J. E., Self-induced heterodyne: the interaction of a frequency-swept pulse with a resonant system, IEEE Journal of Quantum Electronics, **QE-22**, 1986, pp. 174 – 181.

[262] Mattick, A. T.; Sanchez, A.; Kurnit, N. A.; Javan, A., Velocity dependence of collision-broadening cross section observed in an infrared transition of NH_3 gas at room temperature, Applied Physics Letters, **23**, 1973, pp. 675 – 678; Mattick, A. T.; Kurnit, N. A.; Javan, A., Velocity dependence of collision broadening cross sections in NH_3, Chemical Physics Letters, **38**, 1976, pp. 176 – 180.

[263] Hopf, F. A.; Rhodes, C. K., Influence of vibrational, rotational and reorientational relaxation on pulse amplification in molecular amplifiers, Physical Review A, **8**, 1973, pp. 912 – 929.

[264] Matteson, W. H., De Lucia, F. C., Millimeter-wave studies of the $^{13}CH_3F$ laser: the effects of buffer gases and the spectroscopy of the laser states, Journal of the Optical Society of America B: Optical Physics, **2**, 1985, pp. 336 – 342.

[265] Peterson, K. I.; Klemperer, W., Structure and internal rotation of H_2O–CO_2, HDO–CO_2, and D_2O–CO_2 van der Waals complexes, The Journal of Chemical Physics, **80**, 1984, pp. 2439 – 2445.

[266] Jucks, K. W.; Huang, Z. S.; Miller, R. E.; Fraser, G. T.; Pine, A. S.; Lafferty, W. J., Structure and vibrational dynamics of the CO_2 dimer from sub-Doppler infrared spectraum of the 2.7 μm Fermi diad, The Journal of Chemical Physics, **88**, 1988, pp. 2185 – 2195.

[267] Huang, Z. S.; Miller, R. E., The structure of nitrous oxide dimer from sub-Doppler resolution infrared spectroscopy, The Journal of Chemical Physics, **89**, 1988, pp. 5408 – 5416.

[268] Dutton, C.; Sazonov, A.; Beaudet, R. A., High-resolution rovibrational absorption spectrum of CO_2–N_2O, The Journal of Physical Chemistry, **100**, 1996, pp. 17772 – 17779.

[269] Afshari, M.; Dehghany, M.; Moazzen-Ahmadi, N.; McKellar, A R. W., The torsional vibration of the CO_2–N_2O complex determined from its infrared spectrum, The Journal of Chemical Physics, **129**, 2008, pp. 74314 – 74319.

[270] Valdés, H.; Sordo, A. J., The $N_2O{\cdot}N_2O$, $N_2O{\cdot}SO_2$, and $(N_2O)_2{\cdot}SO_2$ van der Waals complexes: an ab initio theoretical analysis, The Journal of Physical Chemistry A, **108**, 2004, pp. 2062 – 2071.

[271] Nakayama, T.; Fukuda, H.; Sigita, A.; Hashimoto, S.; Kawasaki, M.; Aloisio, S.; Morino, I.; Inoue, G., Buffer-gas pressure broadening for the $(00^03) \leftarrow (00^00)$ band of N_2O measured with continuous-wave cavity ring-down spectroscopy, Chemical Physics, **334**, 2007, pp. 196 – 203.

[272] Hurst, G. J. B.; Fowler, P. W.; Stone, A. J.; Buckingham, A. D., Intermolecular forces in van der Waals dimers, International Journal of Quantum Chemistry, **29**, 2004, pp. 1223 – 1239.

[273] Millot, C.; Soetens, J.-C.; Martins Costa, M. T. C.; Hodges, M. P.; Stone, A. J., Revised anisotropic site potentials for the water dimer and calculated properties, The Journal of Physical Chemistry A, **102**, 1998, pp. 754 – 770.

[274] Zamith, S.; Degert, J.; Stock, S.; de Beauvoir, B.; Blanchet, V.; Bouchene, M. A.; Girard, B., Observation of coherent transients in ultrashort chirped excitation of an undamped two-level system, Physical Review Letters, **87**, 2003, pp. 33001 – 33004.

[275] Delagnes, J. C.; Blanchet, V.; Bouchene, M. A., Role of the radiated field in propagation of an ultra-short chirped pulse, Optics Communcations, **227**, 2003, pp. 125 – 131.

Appendix A. Contact Transformations

The method of contact transformation is based on the replacement of the original Hamiltonian by an equivalent but simpler Hamiltonian. The Schrödinger equation

$$\hat{H}\psi = E\psi$$

is transformed to

$$\tilde{H}\phi = E\phi, \qquad \tilde{H} = e^{i\hat{S}}\hat{H}e^{-i\hat{S}}, \qquad \phi = e^{i\hat{S}}\psi$$

where $\hat{S}$ is an Hermitian operator so that $e^{i\hat{S}}$ is unitary. Since the two Hamiltonians are connected by a unitary transformation, the eigenvalue spectrum and the normalization of wave function are preserved. If the transformed Hamiltonian $\tilde{H}$ is diagonal in some basis ϕ, then the diagonal elements E are the eigenvalues of $\hat{H}$ whose eigenfunctions are $\psi = e^{-i\hat{S}}\phi$.

More generally, the matrix $\tilde{H}$ may not be completely diagonal but has a block-diagonal form. In the procedure it is assumed that $\hat{H}$ is separated into terms of different order of magnitude with a book-keeping parameter λ, as

$$\hat{H} = \hat{H}_0 + \lambda\hat{H}_1 + \lambda^2\hat{H}_2 + \lambda^3\hat{H}_3 + ...$$

where λ can takes the values 0 or 1. A succession of contact transformations by the operators $e^{i\lambda\hat{S}_1}$, $e^{i\lambda^2\hat{S}_2}$,… is then performed. The first contact transformation gives the Hamiltonian $\tilde{H}^{(1)}$:

$$\tilde{H}^{(1)} = e^{i\lambda\hat{S}_1}\hat{H}e^{-i\lambda\hat{S}_1} = \tilde{H}_0^{(1)} + \lambda\tilde{H}_1^{(1)} + \lambda^2\tilde{H}_2^{(1)} + \lambda^3\tilde{H}_3^{(1)} + ...$$

In carrying out the transformation $\hat{S}_1$ is chosen so that $\tilde{H}_0^{(1)} = \hat{H}_0$ and $\tilde{H}_1^{(1)}$ is diagonal in the representation of the wave functions of $\hat{H}_0$ which are taken as basis function for the perturbation treatment. The procedure is then repeated by applying a second contact transformation on $\tilde{H}^{(1)}$:

$$\tilde{H}^{(2)} = e^{i\lambda^2\hat{S}_2}\tilde{H}^{(1)}e^{-i\lambda^2\hat{S}_2} = \tilde{H}_0^{(2)} + \lambda\tilde{H}_1^{(2)} + \lambda^2\tilde{H}_2^{(2)} + \lambda^3\tilde{H}_3^{(2)} + ...$$

where $\hat{S}_2$ is again chosen such that $\tilde{H}_0^{(2)} = \tilde{H}_0^{(1)} = \hat{H}_0$ and $\tilde{H}_0^{(2)} + \lambda\tilde{H}_1^{(2)} + \lambda^2\tilde{H}_2^{(2)}$ become diagonal.

The final result, $\tilde{H}^{(\infty)} = \tilde{H}$ is the block-diagonal Hamiltonian:

$$\tilde{H} = \tilde{H}_0 + \lambda\tilde{H}_1 + \lambda^2\tilde{H}_2 + \lambda^3\tilde{H}_3 + ...$$

where

$$\tilde{H}_0 = \hat{H}_0; \qquad \tilde{H}_1 = \hat{H}_1 + i\left[\hat{S}_1, \hat{H}_0\right]$$

$$\tilde{H}_2 = \hat{H}_1 + i\left[\hat{S}_2, \hat{H}_0\right] \qquad \tilde{H}_3 = \hat{H}_2 + i\left[\hat{S}_3, \hat{H}_0\right].$$

In this way the Hamiltonian is brought to a block-diagonal from.

Estratto per riassunto della tesi di dottorato

L'estratto (max. 1000 battute) deve essere redatto sia in lingua italiana che in lingua inglese e nella lingua straniera eventualmente indicata dal Collegio dei docenti.

L'estratto va firmato e rilegato come ultimo foglio della tesi.

Studente: NICOLA TASINATO matricola: 955380

Dottorato: SCIENZE CHIMICHE

Ciclo: *XXII*

Titolo della tesi[1] : INFRARED SPECTROSCOPY OF ATMOSPHERICAL AND ASTROPHYSICAL RELEVANT MOLECULES: SPECTRAL ANALYSIS, LINE PARAMETER RETRIEVALS AND STUDY OF COLLISIONAL DECAY PROCESSES

Abstract: This thesis encompasses different topics in the research field of IR spectroscopy, which includes line-by-line parameter and absorption cross sections retrievals, medium and high resolution analysis, and investigations about collisional processes. The research involving the line-by-line analysis has led to the development of a line-fitting software, VLSFP. Then, the line parameters of SO_2 and H_2C=CHF has been determined in the 8 – 9 μm atmospheric window by TDL spectroscopy. At medium resolution, the FT-IR spectrum of H_2C=CHF has been investigated experimentally and through CCSD(T) *ab-initio* calculations. At high resolution, the spectrum of CF_3Br, has been analysed in the $2\nu_5^0$ and $\nu_2 + \nu_3$ band regions. Absorption cross sections have been measured for SO_2, H_2C=CHF and CF_3Br. Finally, the physics of the interactions of chirped IR laser radiation with low pressure gases, H_2O, N_2O and CO_2, have been investigated by the frequency down-chirped radiation emitted by a QCL spectrometer employed in the intra-pulse method.

Questa tesi abbraccia diverse tematiche nell'ambito di ricerca della spettroscopia IR, che includono: la determinazione dei parametri di riga e delle sezioni d'urto d'assorbimento, le analisi a media e alta risoluzione e gli studi dei processi collisionali. Nella ricerca relativa all'analisi riga per riga, è stato implementato un programma per l'interpolazione delle righe spettrali, VLSFP. Mediante misure di spettroscopia a diodo laser, sono quindi stati determinati i parametri di riga dell'SO_2 e del H_2C=CHF nella regione della finestra atmosferica intorno agli 8 – 9 μm. A media risoluzione, lo spettro FT-IR del H_2C=CHF è stato studiato sperimentalmente e per mezzo di calcoli *ab-initio* CCSD(T). Ad alta risoluzione, lo spettro del CF_3Br, è stato analizzato in corrispondenza della bande $2\nu_5^0$ e $\nu_2 + \nu_3$. Sono inoltre state misurate le sezioni d'urto di SO_2, H_2C=CHF e CF_3Br. Infine, la fisica dell'interazione tra radiazione laser IR caratterizzata da "chirp" e gas a bassa pressione, H_2O, N_2O e CO_2, è stata investigata per mezzo della radiazione "frequency down-chirp" emessa da uno spettrometro QCL operante nel metodo "intra-pulse".

Firma dello studente

_____

[1] Il titolo deve essere quello definitivo, uguale a quello che risulta stampato sulla copertina dell'elaborato consegnato.